UNIVERSITÀ
DEGLI STUDI
FIRENZE

PhD in
Chemical Sciences

CYCLE XXXVI

COORDINATOR Prof. Anna Maria Papini

Development of Porphyrin-based two Qubits Quantum Logic Gates

Academic Discipline (SSD): Chim/03

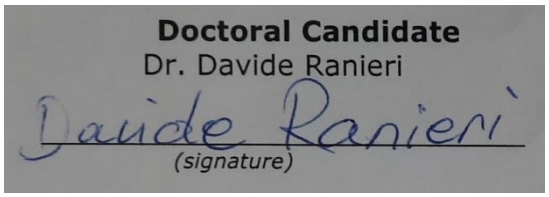

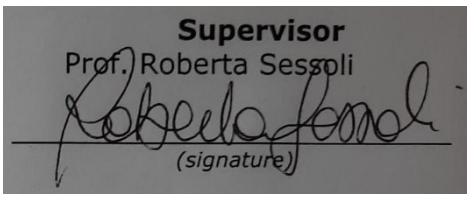

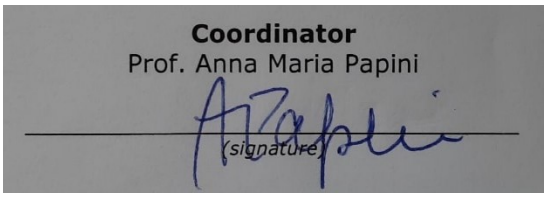

A few words

After almost six months of writing (yes, I started at the end of April...), I can finally say the work is done. My journey as a student began with no intention of pursuing a PhD. As a regular grad student at the University of Stuttgart in Germany, I initially aimed for an Erasmus+ internship. I chose Florence for two main reasons: A beautiful city and my growing interest in Molecular Magnetism.

During my internship in Prof. *Joris van Slageren's* research group at the University of Stuttgart, I was introduced to nanomagnets. A deeper dive into the field, along with the knowledge that Florence was a hub for molecular magnet research, changed the course of my academic journey. Interactions with the *van Slageren* group, who had connections with Florence, played an important role in this decision.

On November 28, 2019, I met Prof. *Roberta Sessoli* for the first time. Her remarkable attention to detail, passion, and scientific curiosity left an indelible mark. The competence, intelligence, and camaraderie of the research group convinced me to extend my stay. I decided to embark on a three-year PhD journey, hoping to reach their level of excellence.

Florence, 30.10.23

Summary

Paramagnetic molecular systems represent promising candidates for qubits, the fundamental components of quantum computers. Their chemical versatility allows for realizing two-qubit architectures and quantum logic gates. Key prerequisites for two-qubit gates include weak exchange coupling of the $S = 1/2$ centers, enabling the creation of four computational basis states. Distinguishable electron spin centers allow more complex quantum gates to be implemented, while a long coherence time is crucial for spin manipulation. Furthermore, the molecular spin qubit must be neutral and thermally stable, enabling deposition on various metal substrates to develop prototypical devices.

In this PhD Thesis, we show the potential of paramagnetic porphyrin compounds in quantum information research. We synthesized homometallic meso-meso linked $[VO]^{2+}$ porphyrins and heterometallic $[VO]^{2+}$-Cu^{2+} porphyrin dimers and solved their crystal structure using X-ray diffractometry. Electron paramagnetic resonance techniques were used to characterize their static and dynamic magnetic properties. In particular, the vanadyl porphyrin moiety was found to be a crucial building block. The results demonstrate that weakly exchange-coupled porphyrin systems provide the qubit-qubit interaction and the single spin addressability required to implement the controlled-NOT quantum gate. Additionally, we illustrate the ability to host paramagnetic porphyrin dimers within a matrix of diamagnetic dimers, yielding diluted single crystals. Beyond enhancing spectral resolution, magnetic diluted single crystals are crucial to implementing the proposed quantum gates through multi-frequency microwave pulses.

Our research further explored the chemical versatility of porphyrinic systems by extending the synthetic strategy to obtain porphyrin trimers with the perspective of employing photoexcitation to control the magnetic exchange. We also investigated the evaporability of porphyrin building blocks to deposit them on metallic surfaces.

This thesis underscores the versatility of paramagnetic porphyrins in quantum technologies based on molecular spins. Their electronic properties and thermal stability will facilitate their integration in more technologically relevant architectures.

Abbreviations of chemical compounds and reagents

Compounds	Abbreviation
Chapter 4	
maleonitriledithiolate	mnt
catechol	cat
phthalocyanine	Pc
tetrarkis(thiadiazole)porphyrazine	TTDPz
Chapter 5	
N-bromosuccinimide	NBS
5,10,15-triphenylporphyrin	H_2TrPP
10,20-diphenylporphyrin	H_2DPP
N-iodosuccinimide	NIS
phenyliodo-bis-trifluoroacetate	PIFA
silver(I)hexafluorophosphate	$AgPF_6$
pinacolborane	HBpin
scandium(III)triflate	$Sc(OTf)_3$
2,3-dichloro-5,6-dicyano-1,4-benzochinone	DDQ
Tris(4-bromophenyl)aminiumhexachloroantimonate	BAHA
acetylacetonate	acac
Chapter 6	
oxo-(5,10,15-triphenylporphyrinato)vanadium(IV)	**[VO(TrPP)]**
bis-oxo[(10,15,20-triphenylporphyrinato-5yl-)vanadium(IV)]	**$[VO(TrPP)]_2$**
Chapter 7	
oxo-(5,10,15-triphenylporphyrinato)titanium(IV)	**[TiO(TrPP)]**
bis-oxo(10,15,20-triphenylporphyrinato-5yl-)titanium(IV)	**$[TiO(TrPP)]_2$**
(5,10,15-triphenylporphyrinato)zinc(II)	**[Zn(TrPP)]**
bis-(10,15,20-triphenylporphyrinato-5yl-)zinc(II)	**$[Zn(TrPP)]_2$**
bis-5,10,15-triphenylporphyrin	**$[H_2(TrPP)]_2$**
magnetically diluted porphyrin	**$[VO_{(0.01)}H_{2(0.99)}(TrPP)]_2$**
Chapter 8	
(5-[10,20-diphenylporphyrinato-5-yl)copper(II)]-[oxo(10,20-diphenylporphyrinato)vanadium(IV)]	**$[VOCu(DPP)_2]$**
oxo-(10,20-diphenylporphyrinato)vanadium(IV)	**[VO(DPP)]**
(10,20-diphenylporphyrinato)copper(II)	**[Cu(DPP)]**
oxo-(5-iodo-10,20-diphenylporphyrinato)vanadium(IV)	**[VO(IDPP)]**
(5-iodo-10,20-diphenylporphyrinato)copper(II)	**[Cu(IDPP)]**
5-iodo-10,20-diphenylporphyrin	H_2IDPP
5-pinacolborane-10,20-diphenylporphyrin	BpinDPP
(5-[oxo(10,20-diphenylporphyrinato-5-yl)vanadium(IV)]-10,20-diphenylporphyrin	**$[VOH_2(DPP)]$**
(5-[(10,20-diphenylporphyrinato-5-yl)copper(II)]-10,20-diphenylporphyrin	**$[CuH_2(DPP)]$**
Chapter 9	
bis-5,15-iodo-10,20-diphenylporphyrin	**$[VO(I_2DPP)]$**
bis-5,15-pinacolborane-10,20-diphenylporphyrin	$Bpin_2$DPP
bis-(5-[oxo(10,20-diphenylporphyrinato-5-yl)vanadium(IV)]-10,20-diphenylporphyrin	**$[\{VO\}_2(DPP)_2(H_2DPP)]$**
oxo-(5-iodo-10,15,20-triphenylporphyrinato)vanadium(IV)	**[VO(ITrPP)]**
bis-(5-[oxo(10,15,20-triphenylporphyrinato-5-yl)vanadium(IV)]-10,20-diphenylporphyrin	**$[\{VO\}_2(TrPP)_2(H_2DPP)]$**

bis-(5-[oxo(10,15,20-triphenylporphyrinato-5-yl)vanadium(IV)]-10,20-diphenylporphyrin-5-yl-(10,15,20-triphenylporphyrinato)copper(II)	**[{VO}(TrPP){Cu}(TrPP)(H_2DPP)]**
(5-[oxo(10,20-triphenylporphyrinato-5-yl)vanadium(IV)]-10,20-diphenylporphyrin	**[VO(TrPP)(H_2DPP)]**
(5-[oxo(10,20-triphenylporphyrinato-5-yl)vanadium(IV)]-(15-iodo-10,20-diphenylporphyrin)	**[VO(TrPP)(H_2IDPP)]**
(5-pinacolborane-10,15,20-triphenylporphyrinato)copper(II)	**[Cu(BpinTrPP)]**
(5-bromo-10,15,20-triphenylporphyrinato)copper(II)	**[Cu(BrTrPP)]**
oxo(5-bromo-10,15,20-triphenylporphyrinato)vaandium(IV)	**[VO(BrTrPP)]**
5-bromo-10,15,20-triphenylporphyrin	H_2BrTrPP

List of acronyms

Full name	Abbreviation
Chapter 1	
Quantum information processing	QIP
negative-positive-negative-transistor	npn-transistor
control-not gate	CNOT-gate
Chapter 2	
continuous wave	cw
electron paramagnetic resonance	EPR
ferromagnetic	FM
antiferromagnetic	AF
Chapter 3	
spin-orbit coupling	SOC
free inductive decay	FID
Fourier-transformation	FT
Chapter 4 & 5	
Single molecule magnet	SMM
normal coordinate structural decomposition	NSD
oxidative ring closure	ODRC
Chapter 6,7,8	
broken symmetry	BS
ultra-high vacuum	UHV
X-ray photoelectronspectroscopy	XPS

Table of Contents

How chemistry can contribute to quantum technologies

The idea of using quantum physical phenomena in technological devices can be considered the beginning of the second quantum revolution [1,2] and dates back to the 1960s.[3] The interdisciplinary nature of the field of quantum information processing (QIP) has been growing since then and can be represented as shown in **Scheme 1**. Before the 1960s, technologies were not ready for a revolution, and many concepts remained written on paper. It was only through technological developments that quantum mechanical predictions and hypotheses became accessible, and the tools for creating quantum technologies became a reality. Among the great challenges in quantum technologies, realizing a quantum computer with its fundamental unit, the so-called quantum bit or qubit, is the most ambitious. Material scientists, engineers, and physicists got involved in finding a suitable candidate for a qubit.

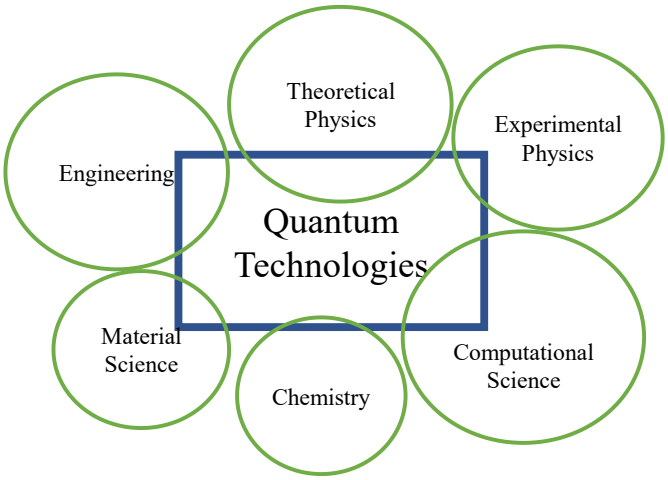

Scheme 1: Visualization of the interdisciplinary reality for developing quantum technologies. Chemistry makes only a little part of it.

Systems like superconducting qubits,[4] solid-state qubits,[5] or quantum dots[6,7] were proposed and studied. Indeed, multinational companies such as IBM[8,9] or Google[10]

developed quantum computers based on superconducting circuits. Much later, chemistry also got involved in finding a physical qubit. But what contributions can a chemist give in creating a qubit? The answer lies in the definition of quantum itself. As the word “quantum” suggests, the quantum bit is based on the laws of quantum physics as much as molecules do. By exploiting the quantum mechanical properties of a molecule, one might be able to create a qubit. Where physicists see rings, triangles, and chains, the chemist sees aromatic systems that can be functionalized, trimetallic frustrated transition metal complexes with peculiar magnetic behaviors, and chains of conjugated carbon tapes with unique electric properties. Not only can the chemist observe the molecule and determine its building blocks, but they can also develop new molecules better suited for performing a specific task and describe theoretically the intra- and intermolecular interactions of functionalized molecules. It is the ability to engineer molecular systems that make the chemist's work so interesting in the quantum technology universe to realize a so-called molecular spin qubit.[2,11–13]

This thesis focuses on engineering more complex molecular spin qubits that can be used as two-qubit quantum logic gates. These gates can be created with bimetallic transition metal complexes; therefore, most of the effort was dedicated to synthesizing new molecular systems specifically designed for this scope. In particular, homo- and hetero-metallic dimer complexes of paramagnetic spin 1/2 systems were synthesized. The focus was on aromatic and especially porphyrinic ligands since porphyrins have many suitable features for molecular spin qubits. The investigation of the magnetic properties of the synthesized complexes allowed us to determine the conformity of the molecule to be considered a molecular spin qubit gate, giving us insights into the magnetic spin-spin interactions of the molecule. This further solidified the understanding of the physics of such systems and helped us design further bimetallic paramagnetic spin 1/2 systems. First surface depositions were also conducted on the synthesized molecules and demonstrated the potential of porphyrinic systems for technologically relevant applications. The results obtained will have a significant impact when it comes to the development of further molecular spin qubits.

Chemistry can be helpful for quantum technologies, though on a much smaller scale. It can be considered as a part of the “bricks” (**Scheme 1**) that make up

the circle for the realization of the most important quantum technology of the future, the quantum computer. Theoretical physicists were the first to put the initial brick by creating the mathematical operations necessary for the implementation of the qubit, and they will also put the last brick, which is the final implementation of the algorithm. The final goal of this interdisciplinary research will be achieving quantum supremacy, i.e., the point beyond which a quantum computer is much more performant than a classical one.[1]

In this thesis, we will briefly provide a basic theoretical insight into qubits and quantum logic gates (Chapter 1) with an emphasis on the electron spin's similarity to qubits (Chapter 2) and the environmental effects altering its magnetic properties (Chapter 3) will be given. These topics are relevant to the molecular spin qubits discussed in Chapter 4. Chapter 5 introduces the physical and chemical properties of porphyrins. These concepts provide the necessary frame for the chemical and physical studies of the porphyrinic systems presented in this thesis (Chapters 6-9).

1 Basic concepts of quantum computation

Quantum computation is a vast research area that cannot be exhaustively treated in this thesis. This chapter aims to outline the most important concepts of quantum computation necessary for the realization of molecular spin qubits and will not cover the quantum algorithm part. The focus will be on the mathematical description of the qubit and the quantum logic gate. The mathematical description is, indeed, very important to understand why the electron spin is such a suitable candidate.

1.1 A brief history of quantum computation

This section will only give a brief chronological history of quantum computation. For the sake of brevity, this introduction will not cover all relevant aspects and contributors but is limited to providing the necessary frame in which this research has been developed.

The history of quantum computation can be considered the continuation of the history of quantum mechanics itself. While at the end of the 70s, most secrets of the nano-world had been discovered, other scientists were triggered by the idea of adapting quantum mechanical phenomena in computer science. It is difficult to say who started the process, but the research of *Charles Bennett* with his paper published in 1973[14] can be considered a milestone. *Bennett* was the first to demonstrate that it is possible to implement an algorithm using reversible quantum logic gates operation. As explained in the following sections, the reversibility of the QIP is crucial since only with a reversible process is it possible to retain the information in the single computational states. Nine years later, a paper published by *Richard Feynman*[15] showed that it is possible to describe the operations on a quantum computer by simple linear algebra. Furthermore, he proved that the laws of quantum physics enable the creation of new quantum logic gates which have no classical counterpart. With these new gates, information processing would become much faster, and calculation time would significantly decrease. Finally, in 1985, *David Deutsch*[16] introduced his

famous *Deutsch* algorithm, *i.e.*, an algorithm built with only qubit manipulations. In this article, he described the creation of a universal computer that completely worked by obeying the laws of quantum physics, and the information is contained in a single machine. Such computers would be built by combining the gates described by *Richard Feynman.*

To this day, many systems have been proposed as the basic unit of a quantum computer. Among them are molecular systems briefly mentioned in the introduction and will be discussed in detail in the next chapter. However, the quest to find the core units for these computers is still ongoing.

1.2 Bits and logic gates

To understand the nature of the qubit and how it is related to the quantum computer, we first must understand how a classical bit works. In modern computers, information is processed using electric currents.[17] In an electric circuit, specific devices are inserted that can change the electric potential while the current is passing through the device. One of these devices is the positive negative positive (npn)-transistor (**Scheme 1.1**, left). The npn-transistor consists of two main junctions: a collector (C), an emitter (E), and a base (B, see **Scheme 1.1**). If there is an electric circuit in which a potential of 1 V is applied to the transistor, the current "passes" the transistor at the C. The current only passes through the E if there is also a weak current at the B. Otherwise, the main current from C is "held" by the transistor. Thus, the transistor works as a switchable on/off device.[18]

In a computer, these differences in current can be used as signals for encoding and transporting information. The base of the transistor could be considered as the input signal, while the emitter gives the output. The transistor acts like a sort of gate that either lets the current pass or not. In a computational sense, the transistor is a NOT-gate (**Scheme 1.1**, middle). As shown in **Scheme 1.1** right, the input and output of the signal can be represented in a table (so-called truth table), with 1 being

the state when a current is measured and 0 if not. Note that the numbers 0 and 1 are labels that define the states and are not integers. The single states (0 and 1) are called bits, and a package of eight bits is called a byte.[17] These are the fundamental units of the computer and the source of information processing.

A bit is, therefore, the smallest package of information in the computational units. It must have a well-defined state and be distinguishable from its opposite state. By combining different transistors or changing the INPUT and OUTPUT positions, one can create other gates with different functions. A sequence of connections between different gates is used to write an algorithm the computer can translate to create a command.

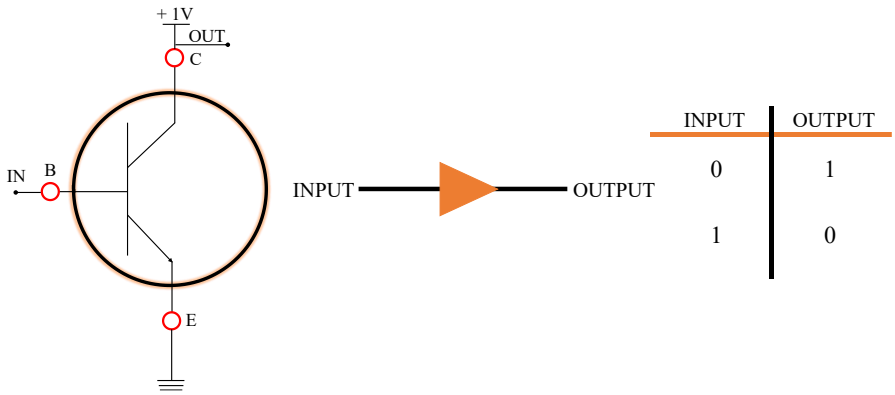

Scheme 1.1: The npn-transistor (left) is a possible device for creating a NOT-gate (middle), which satisfies the requirements of the truth table on the right. Note that in the electric circuit on the left, the resistances were omitted for clarity.

1.3 Qubits and quantum logic gates

If, instead of a current in the circuit, single electrons passing through the transistor are used, it is not possible to use a macroscopic quantity (such as a current or voltage in the previous example) to determine the computational states 0 and 1, but other distinguishable physical values are needed. The major issue, however, is that for single electrons, the laws of classical electrodynamics do not work, and the laws of quantum physics must be considered. Still, the principles of the computational theory

remain the same. While the fundamental unit in information processing is the bit, in QIP, these units turn to quantum bits or qubits[19] and the state manipulators (logic gates) are called quantum logic gates.[20,21] Indeed, when it comes to the representation of the qubit, it is not possible to express it in a trivial way like it is done with the classical bit. Since the laws of quantum mechanics apply to the qubit, the qubit must mathematically be described as a normalized vector that does not necessarily be a "pure" state (direction on the principal axis). The vector can point in any direction in space; thus, it could be described as a linear combination of two pure states. So, the direction can be used as a computational state. If the direction of the vector (*e.g.*, a 180° flip) is changed, another distinguishable and opposite computational state is created. Since, in this case, the computational basis states are also quantum states, the ket notation[22] is used. The two computational basis states used are denoted $|0\rangle$ and $|1\rangle$. An example of a vectorial representation of the $|0\rangle$ state is visible in **Scheme 1.2**. As for the gate, it must be able to change the direction of the qubit by switching its state from $|0\rangle$ to $|1\rangle$. In a mathematical sense, the quantum logic gate is nothing else than a matrix. The multiplication of a matrix by a vector gives rise to a new vector that can be considered a new computational basis state. In case of constructing a NOT-gate, the matrix is visible in **Scheme 1.2**.

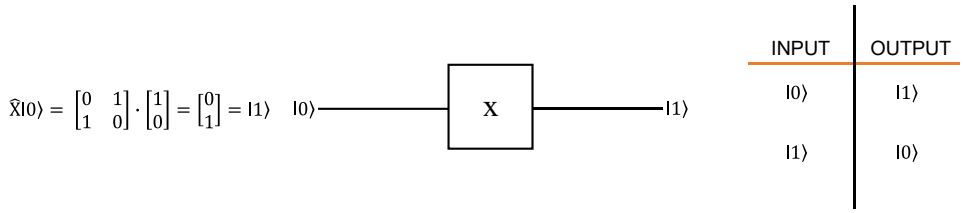

Scheme 1.2: The matrix (left) circuit (middle) and truth table (right) representation of a quantum NOT gate.

The quantum logic gate shown in **Scheme 1.2** is also called a *Pauli X*-gate and is represented as a square with a cross (X) in the middle or with the operator symbol $\hat{X}$. It can be considered the simplest quantum logic gate because it just flips the initial state like the classical NOT gate. Note that the matrix used for all qubit manipulations

must be a unitary matrix because only with unitary matrices it is possible to make reversible operations that fulfill the requirement of preservation of information.

The *Pauli* Gate is a simple example showing that it is theoretically possible to create a gate with a quantum system. But quantum logic gates offer further advantages when exploring the quantum mechanical phenomena of entanglement and quantum superposition.[23,24] The explanation of these phenomena is not simple, as they do not have a classical analogous and are difficult to imagine. One easy way to describe the superposition is by understanding the quantum interferometer. The simplified set-up of a quantum interferometer is visible in **Figure 1.1**, left. Let us take an example of a single quantum object that can be expressed by a wave function $|\Psi\rangle$ and is in the initial computational basis state $|0\rangle$. In this interferometer, the wave can take two paths, and each possible path can be labeled with the basis states $|0\rangle$ or $|1\rangle$. So, according to which path the wave takes, the basis state can either change or remain the same. Waves have a peculiar property of interfering and phase shifting, so waves are delocalized, and it is not possible to determine exactly the path they take. Since there is no information on where the wave is located inside the interferometer, the wave must be considered in both paths simultaneously.

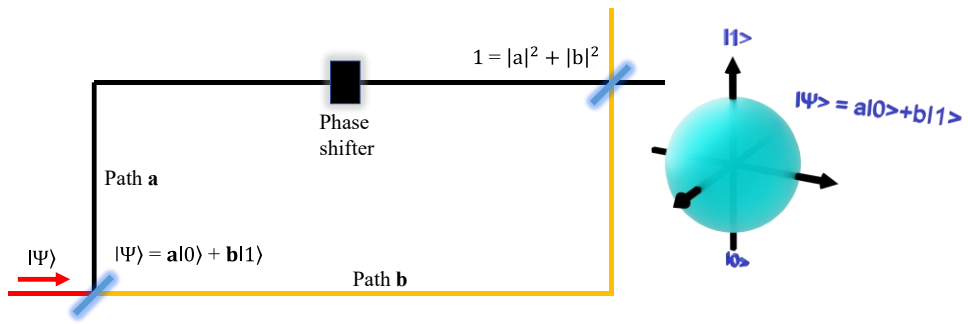

Figure 1.1: Left: Simplified scheme of a quantum interferometer. A single wave $|\Psi\rangle$ can either follow the black (**a**) or orange (**b**) path, thus creating a superposition. The probability of finding the qubit in the state $|0\rangle$ or $|1\rangle$ is given by the *Born* interpretation of quantum mechanics. Right: Representation of the qubit on a *Bloch* sphere.

According to quantum mechanics, the state must be written as

$$|\Psi\rangle = \frac{|0\rangle + |1\rangle}{\sqrt{2}} \tag{1.1}$$

Waves can also change their phase. If this is happening in one of the paths (*e.g.*, in path **a**, Figure 1.1), the basis states have to be rewritten considering the phase change as follows.

$$|\Psi\rangle = \frac{1}{\sqrt{2}}\left(|0\rangle + \mathrm{e}^{i\varphi}|1\rangle\right), \tag{1.2}$$

with φ being the phase shift. Further, other splittings in the path **a** will change the overall arbitrary state once again. Finally, the wave can be represented as follows:

$$|\Psi\rangle = \frac{1}{\sqrt{2}}\left(\frac{|0\rangle + |1\rangle}{\sqrt{2}} + \mathrm{e}^{i\varphi}\frac{|0\rangle - |1\rangle}{\sqrt{2}}\right). \tag{1.3}$$

The new state can be visualized more fashionably by using the *Euler* rules shown in formula (1.4)

$$|\Psi\rangle = \mathrm{e}^{\frac{i\varphi}{2}}\left[\cos\left(\frac{\varphi}{2}\right)|0\rangle - \mathrm{i}\sin\left(\frac{\varphi}{2}\right)|1\rangle\right]. \tag{1.4}$$

Formula (1.4) can be generalized by considering all possible outcomes and written as follows:

$$|\Psi\rangle = a|0\rangle + b|1\rangle, \tag{1.5}$$

with a and b being two complex numbers, also called amplitudes.[23] It is possible to visualize equation (1.5) graphically in a cartesian coordinate system, within a sphere also called the *Bloch* sphere[25] (**Figure 1.1**, right). A vector parallel or antiparallel to the z-axis describes the qubit in its pure basis states $|1\rangle$ or $|0\rangle$. Any other point on the surface of the *Bloch* sphere represents non-pure qubit states (**Figure 1.1**, right).

Returning to the quantum interferometer, one still needs to determine the outcome (output) of the qubit state at the end of the interferometer. The 5th postulate of quantum mechanics[26] says that a state in superposition, once measured, "collapses" to one of its two pure states. As evident from equation (1.4), the probability of whether path **a** or **b** is taken is not 50 % for each state like in a classical way, but due to the interference and phase shift, the probabilities of detecting either a $|0\rangle$ or $|1\rangle$ state are different and can be determined according to the *Born* interpretation of quantum mechanics.[26] Considering the superposition in equation (1.4), the probability of finding the qubit in either the $|0\rangle$ or $|1\rangle$ state is given by

$$P(|1\rangle) = |\langle 1|\Psi\rangle|^2 = \sin^2\frac{\varphi}{2}, \tag{1.6}$$

for the state $|1\rangle$, and

$$P(|0\rangle) = |\langle 0|\Psi\rangle|^2 = \cos^2\frac{\varphi}{2}, \tag{1.7}$$

for the state $|0\rangle$. Equations (1.6) and (1.7) can be summed and generalized to equation (1.8).

$$1 = |a|^2 + |b|^2. \tag{1.8}$$

From equation (1.8), it is also clear that the qubits in the states $|1\rangle$ or $|0\rangle$ must be orthogonal, and the two vectors form an orthonormal basis set.

The superposition makes it possible to create logic gates with no counterpart in classical computation science. As shown in **Scheme 1.3**, it is mathematically possible to induce the superposition in qubits while in their pure states. The quantum logic gate that acts on a single qubit and brings its pure state in an equal superposition of the two-basis state is called the Hadamard gate (). The quantum circuit notation and truth table of the Hadamard gate are shown in **Scheme 1.3**.

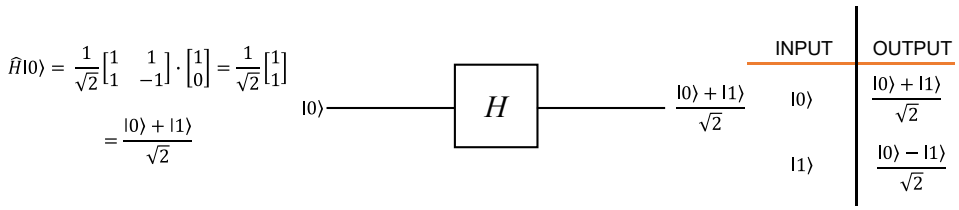

Scheme 1.3: The matrix (left) circuit (middle) and truth table (right) representation of a Hadamard gate that turns a qubit in its pure $|0\rangle$ or $|1\rangle$ state into a superposition state.

The phase shift of a qubit is also mathematically possible with a quantum gate. The matrix that is used in this case is visible in **Scheme 1.4**. In quantum computation, such a logic gate is represented with the letter *P* and is called a phase shift quantum gate.

$$\hat{P}|1\rangle = \begin{bmatrix} 1 & 0 \\ 0 & e^{i\varphi} \end{bmatrix} \cdot \begin{bmatrix} 0 \\ 1 \end{bmatrix} = \begin{bmatrix} 0 \\ e^{i\varphi} \end{bmatrix} = e^{i\varphi}|1\rangle$$

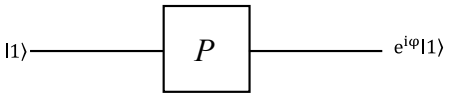

INPUT	OUTPUT
$\|0\rangle$	$\|0\rangle$
$\|1\rangle$	$e^{i\varphi}\|1\rangle$

Scheme 1.4: The matrix (left) circuit (middle) and truth table (right) representation of a phase shift quantum gate that turns a qubit in its pure $|1\rangle$ state into a phase-shifted $e^{i\varphi}$ state. Note that for$|\ 0\rangle$, the output is $|0\rangle$ itself.

The output from the quantum logic gates shown in **Scheme 1.3** and **Scheme 1.4** can be represented on a *Bloch* sphere, as shown in **Figure 1.2**.

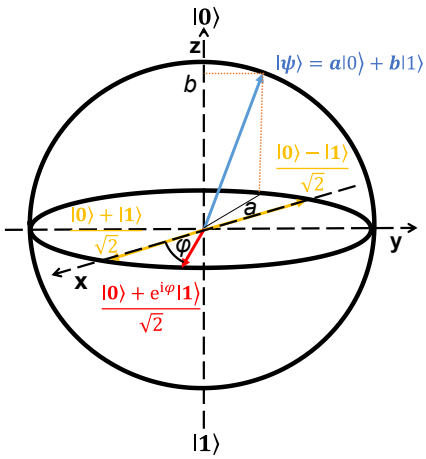

Figure 1.2: Graphical representation of a qubit on a *Bloch* sphere having an arbitrary superposition (blue arrow with blue formula), and after the manipulation of a pure state with a Hadamard gate (orange arrows with orange formula) or by a combined Hadamard and phase shift quantum gate (red arrow with red formula).

1.4 Two-qubit quantum logic gates

In all previous examples, the initial state was a pure computational basis state. Indeed, in quantum computation, it is important to have a well-defined initial state as an input because it facilitates the information processing. In 2000, *Di Vincenzo*[27] was the first

to present a set of seven requirements for systems to be used as qubits. The one mentioned above is the first requirement of the seven. Another important requirement is the possibility of creating multi-qubit systems. For this thesis, the focus will be only on two-qubit systems.

To describe a computational basis state $|\Psi\rangle$ as a two-qubit entity, it is necessary to create it from the composition of two individual qubits. According to the fourth postulate of quantum mechanics,[26] the new composite can be described by the tensor product of two-dimensional vectors (two single qubits). This will give a single vector in a four-dimensional space representative of a two-qubit system. Equation (1.9) shows the example for the $|0\rangle$ basis state. The tensor product will result in the new vector

$$|0\rangle \otimes |0\rangle = \begin{bmatrix}1\\0\end{bmatrix} \otimes \begin{bmatrix}1\\0\end{bmatrix} = \begin{bmatrix}1\\0\\0\\0\end{bmatrix} = |00\rangle, \tag{1.9}$$

where $|00\rangle$ is the computational basis state resulting from the tensor operation. The same treatment, as shown in equation (1.9), can be done with the pure state $|1\rangle$ that will result in $|11\rangle$. In two-qubit systems, it is also possible to compose a state by "admixing" the pure $|0\rangle$ and $|1\rangle$ states that result in the computational basis states

$$|0\rangle \otimes |1\rangle = \begin{bmatrix}1\\0\end{bmatrix} \otimes \begin{bmatrix}0\\1\end{bmatrix} = \begin{bmatrix}0\\1\\0\\0\end{bmatrix} = |01\rangle. \tag{1.10}$$

Note that the tensorial operations are not commutable, and therefore, the tensor product of $|1\rangle$ with $|0\rangle$ is not the same and results in the basis state $|10\rangle$. Like with the

single qubit, the two-qubit system can be brought into a superposition state, and the arbitrary superposition is described by expanding formula (1.5) to

$$|\Psi\rangle = a|00\rangle + b|01\rangle + c|10\rangle + d|11\rangle. \qquad (1.11)$$

As explained earlier, the qubit's superposition can be represented as a vector on the surface of a *Bloch* sphere in a *Hilbert* space. In some sources,[24] the graphical representation of equation (1.11) is done as shown in **Figure 1.3**.

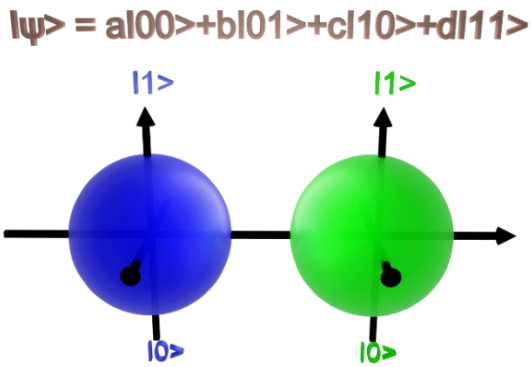

Figure 1.3: The representation of a two-qubit system results from a composition of two single qubits.

Note that the superposition of a two-qubit system should be represented in a four-dimensional *Hilbert* space, and the representation in **Figure 1.3** is just a way to better visualize the superposition of the complex two-qubit systems.

Like with a single qubit, a two-qubit system can also be manipulated. One important quantum logic gate used in quantum computation is the control-not (CNOT) gate. The CNOT gate has no classical counterpart, and the output we get follows the rules of quantum mechanics. In this gate, the “first” qubit is defined as the control (C) qubit and the “second” as the target (T) qubit. The state of the T-qubit is

modified (or not) by the gate depending on the state of the C-qubit. In **Scheme 1.5**, the example of a CNOT is given when the C-qubit is $|0\rangle$; the T-qubit does not change (see matrix-vector multiplication), while when the C-qubit is $|1\rangle$, the T-qubit is flipped. In this case, the CNOT gate is represented as a 4x4 unitary matrix, and the circuit representation is a composite of two circuits.

$$CNOT|10\rangle = \begin{bmatrix}1&0&0&0\\0&1&0&0\\0&0&0&1\\0&0&1&0\end{bmatrix} \cdot \begin{bmatrix}0\\0\\1\\0\end{bmatrix} = \begin{bmatrix}0\\0\\0\\1\end{bmatrix} = |11\rangle$$

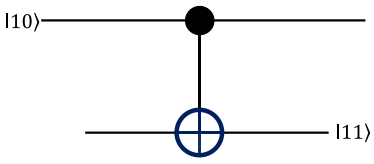

INPUT	OUTPUT
$\|00\rangle$	$\|00\rangle$
$\|01\rangle$	$\|01\rangle$
$\|10\rangle$	$\|11\rangle$
$\|11\rangle$	$\|10\rangle$

Scheme 1.5: The matrix (left) circuit (middle) and truth table (right) representation of a CNOT gate.

Interestingly, any set of a CNOT-gate combined with a one qubit gate is sufficient to create a universal quantum gate[28] that would allow an infinite amount of quantum computations. One of the simplest, but at the same time very important among these combinations, is the Hadamard gate combined with the CNOT gate. Since with two qubits we are working in a 4 x 4 space, the unitary matrix of the Hadamard gate changes according to equation (1.12). Therefore, when having a $|00\rangle$ initial state, the Hadamard gate will turn it in the superposition state shown in equation (1.12),

$$\widehat{H}|00\rangle = \frac{1}{\sqrt{2}}\begin{bmatrix}1&0&1&0\\0&1&0&1\\1&0&-1&0\\0&1&0&-1\end{bmatrix} \cdot \begin{bmatrix}1\\0\\0\\0\end{bmatrix} = \frac{1}{\sqrt{2}}\begin{bmatrix}1\\0\\1\\0\end{bmatrix} = \frac{|00\rangle + |10\rangle}{\sqrt{2}}, \quad (1.12)$$

and the CNOT gate will flip the T qubit only if the C qubit is $|1\rangle$. Note that the CNOT-gate also acts on 00 basis states only that this basis will not be affected by the CNOT-gate (see truth table **Scheme 1.6**)

$$CNOT\,\frac{|00\rangle + |10\rangle}{\sqrt{2}} = \begin{bmatrix} 1 & 0 & 0 & 0 \\ 0 & 1 & 0 & 0 \\ 0 & 0 & 0 & 1 \\ 0 & 0 & 1 & 0 \end{bmatrix} \cdot \frac{1}{\sqrt{2}} \begin{bmatrix} 1 \\ 0 \\ 1 \\ 0 \end{bmatrix} = \frac{1}{\sqrt{2}} \begin{bmatrix} 1 \\ 0 \\ 0 \\ 1 \end{bmatrix} = \frac{|00\rangle + |11\rangle}{\sqrt{2}}. \quad (1.13)$$

The resulting basis state obtained after the unitary operations in equations (1.12) and (1.13) are maximally correlated because the resulting C-and T-qubits are a combination of $|00\rangle$ and $|11\rangle$ basis states with the same amplitude. Further, it is not possible to factorize the output in equation (1.13) in terms of single-qubit states. Thus, the two qubits act like one unit: the result of the combined gate operation is, therefore, an entangled state.[23,24,29] **Scheme 1.6** shows the circuit representation of the combined unitary operations in equations (1.12) and (1.13) together with the truth table of all possible basis state outcomes. Interestingly, all four outputs are entangled states, so-called *Bell* states.[30]

These states are fundamental in the field of QIP because they are the key to quantum teleportation and superdense coding.[31]

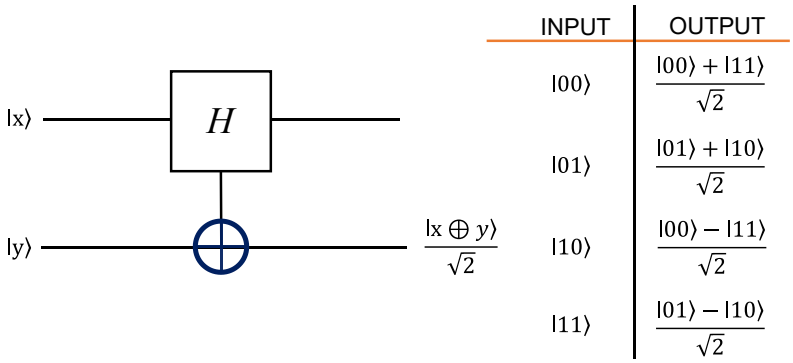

Scheme 1.6: The circuit representation (left) of a Hadamard Gate combined with a CNOT-gate that results in the formation of the four entangled *Bell*-states.

This concludes the basic explanation of the main mathematical concepts of quantum computing: in the next chapter, a possible candidate, the electron spin, will be presented, and all the benefits and drawbacks connected to QIP will be discussed.

2 The electron spin: A physical equivalent to the qubit

In the last chapter, it was briefly mentioned that the electron follows the rules of quantum mechanics. This means that all physical properties of the electrons are quantized; thus, only discrete energy values are allowed, and different energy states are populated at different temperatures according to the *Boltzmann* statistics. The electron has a magnetic moment, and the electron can be seen as a small magnetic dipole. The angular momentum correlated to the magnetic moment is also quantized. This angular momentum is called the spin. This chapter will illustrate why the electron spin can be considered a physical equivalent to the qubit. The best way to show the analogies between the electron spin and the qubit is by presenting the mathematical description of the spins while in a magnetic field (Section 2.1). Sections 2.2 and 2.3 will show how quantum decoherence is problematic in maintaining the superposition and how the exchange interaction can be used to create two-qubit quantum logic gates.

2.1 The electron spin in a magnetic field

As shown by the *Stern-Gerlach* experiment,[32] the electron spin takes two distinguished energy states (E_s) while in an external magnetic field. The energy of the spin system can be calculated using the Hamiltonian:

$$\hat{H} = g_e \cdot \mu_B \cdot \vec{B} \cdot \hat{S} \tag{2.1}$$

And solving this Hamiltonian, the following equation is obtained:

$$E_s = \pm m_s \cdot g_e \cdot \mu_B \cdot B_z, \tag{2.2}$$

With g_e being the electron g-factor, which has a value of 2.0023, μ_B the electron *Bohr*-magneton, B_z the external magnetic field parallel to the electron spin, and m_s being the magnetic electron quantum number with the value 1/2. For now, the g-factor will not be explained further but will be important in Chapter 3. The two spin states can either be called spin-up ($|\uparrow\rangle$)/spin-down ($|\downarrow\rangle$) states or α and β and are equivalent to the distinguishable pure computational basis states $|0\rangle$ and $|1\rangle$ (**Figure 2.1**). Speaking semi-classically, the spins start orientating parallel or antiparallel to this external magnetic field. The spins try to evade the force by applying a precession movement toward the magnetic field B_z. The frequency of this precession movement is called *Larmor*-frequency ω_0 and is described by equation (2.3)

$$\omega_0 = \gamma \cdot B_z. \tag{2.3}$$

with γ being the gyromagnetic ratio. If electromagnetic radiation with a magnetic component B_1 is applied perpendicular to the B_z field, the spins from the lower states are transferred to the state of higher energy when the frequency of the electromagnetic radiation has the same value as the *Larmor*-frequency. The selection rule for valid transitions is $\Delta m_s = \pm 1$. Absorption occurs if the frequency, *i.e.*, the energy of the electromagnetic radiation, is equal to the *Larmor*-frequency according to

$$\Delta E = h \cdot \nu = g_e \cdot \mu_B \cdot B. \tag{2.4}$$

This means that working with a 9.4 GHz microwave (mw), the resonance condition is achieved at the field of 335 mT. The spectroscopy art that can detect such absorption is continuous wave (cw) electron paramagnetic resonance spectroscopy (EPR). Indeed, this technique is crucial when it comes to the detection of unpaired electrons in various samples and is an essential part of this thesis. The instrumental set-up of the EPR-spectrometer will be explained in Chapter 11.

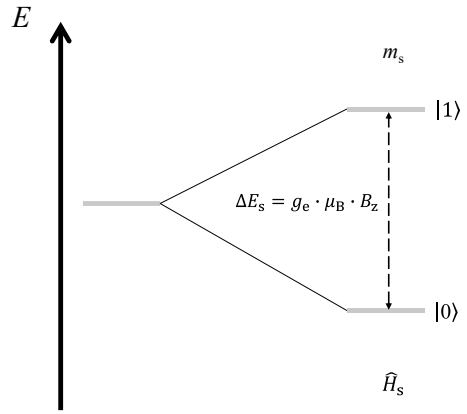

Figure 2.1: Qualitative energy scheme of an electron spin in an external magnetic field. The degenerated initial state is split into two new distinguishable states that can be represented as two computational basis states $|0\rangle$ and $|1\rangle$ necessary for quantum computation.

Some other similarities with the qubit can be seen if the Hamiltonian (2.1) is expressed with the basis m_s according to

$$E = \langle m_s | \hat{H} | m_s \rangle. \tag{2.5}$$

Rewriting (2.5) as a 2x2 matrix, we get

\	$\|1/2\rangle$	$\|-1/2\rangle$
$\|1/2\rangle$	E_1	
$\|-1/2\rangle$		E_2

(2.6)

The eigenvectors of the 2x2 matrix are the pure spin-states of the α or β spins. The 2-dimensional eigenvectors become:

$$S_{z,\alpha} = \begin{bmatrix} 0 \\ 1 \end{bmatrix}; S_{z,\beta} = \begin{bmatrix} 1 \\ 0 \end{bmatrix} \tag{2.7}$$

which are exactly the two-dimensional vector representations of the pure qubit $|0\rangle$ and $|1\rangle$ states. For a single $S = 1/2$ spin, the general spinor state[33] of the spin can be generalized as a linear combination of two $|\uparrow\rangle$ and $|\downarrow\rangle$ spins as shown in equation (2.8),

$$S = a|\uparrow\rangle + b|\downarrow\rangle = \begin{bmatrix} a \\ b \end{bmatrix}, \tag{2.8}$$

that form an orthonormal system, where the sum of the absolute square value of a and b must be 1. Equation (2.8) is mathematically the same representation of the qubit in superposition.

The operator that acts on the state of the electron spins is unitary, and Hermitian matrixes, also called *Pauli* matrixes,[33] are defined as follows:

$$\sigma_x = \begin{bmatrix} 0 & 1 \\ 1 & 0 \end{bmatrix}; \sigma_y = \begin{bmatrix} 0 & -i \\ i & 0 \end{bmatrix}; \sigma_z = \begin{bmatrix} 1 & 0 \\ 0 & -1 \end{bmatrix}. \tag{2.9}$$

Note that the first *Pauli* matrix σ_x equals the matrix operator of the *Pauli* X-gate (where the name *Pauli*-X gate comes from). The other two *Pauli* matrixes are equivalent to the *Pauli* Y and *Pauli* Z gates.

The matrix operators determine changes in the electron spin orientation in a magnetic field. These orientation changes can be physically induced by electromagnetic pulses perpendicular to the external magnetic field B_z that have the same frequency as the *Lamour* frequency of the spin ensemble. The sum of the

magnetic moments of the spin ensembles can be referred to as the magnetization (M), which, in this case, has only one B_z and generates only one magnetization in the z direction (M_z). After the mw-pulse, the magnetization is projected with an angle α to another direction in space, according to

$$\alpha = \gamma \cdot B_1 \cdot t, \tag{2.10}$$

where B_1 is the field perpendicular to B_z, and t is the pulse duration. The electromagnetic pulse works, therefore, as a quantum logic gate, and the pulse can induce a superposition state if α is anyhow different from 90° or 180°. The instrumental setup that makes the realization of spin manipulation in magnetic fields possible is pulsed-EPR spectroscopy.[34] The theory behind the pulsed-EPR spectroscopy will be discussed in Section 3.4.

So far, it was shown how the necessary ingredients for the physical equivalent of a qubit are present in the electron spin. But other requirements have to be taken into consideration as well. The *Di Vincenzo* requirements[27] give important indications for a physical system to be considered a proper qubit. The total requirements listed by *Di Vincenzo* are five, and the three most important ones will be presented in this thesis over time. Starting with the first and most important one the lifetime of the superposition, that is coupled with the ability of a quantum object to retain its coherence. The problem that occurs when working with the electron spin (and with all other quantum objects) is that they lose their quantum nature when they interact with the environment, which turns the quantum object into a classical one. The reason behind this behavior lies in the definition of coherence. In the next section, it will be explained how quantum coherence works and how to promote it.

2.2 Decoherence as a limiting factor for the superposition

Coherence can be explained with the density matrix.[35] The density matrix ρ is quantum mechanically defined as the product of a wavefunction Ψ with its complex conjugated wavefunction Ψ^*, as shown in the following equation:

$$\rho = |\Psi\rangle\langle\Psi|. \tag{2.11}$$

If we take as an example the wave function shown in equation (3.8) (that is, the wavefunction for the two spin states in an external magnetic field) and assume the Hadamard gate induced the superposition, then $|\Psi\rangle$ can be rewritten as

$$|\Psi\rangle = \frac{1}{\sqrt{2}}|\uparrow\rangle + \frac{1}{\sqrt{2}}|\downarrow\rangle. \tag{2.12}$$

Since the coefficients a and b are complex numbers, it is also possible to write equation (2.12) as

$$|\Psi\rangle = \frac{1}{\sqrt{2}}|\uparrow\rangle + e^{i\theta}\frac{1}{\sqrt{2}}|\downarrow\rangle, \tag{2.13}$$

with θ being the phase, that is a real number. The phase can be imagined as the angle between the spin superposition and the z-axis of the complex space. The density matrix corresponding to the wavefunction in equation (2.13) is therefore

$$\rho_\theta = \begin{pmatrix} \frac{1}{2} & \frac{1}{2}e^{-i\theta} \\ \frac{1}{2}e^{i\theta} & \frac{1}{2} \end{pmatrix}. \tag{2.14}$$

From an experimental point of view, it is the sum of many spins in superposition that gives rise to a detectable signal, and the sum of many superpositions corresponds to the averaging of θ. However, by averaging θ, the density matrix (2.13) turns to

$$\rho_0 = \begin{pmatrix} \frac{1}{2} & 0 \\ 0 & \frac{1}{2} \end{pmatrix}. \tag{2.15}$$

The matrix ρ_0 obtained is a diagonal matrix because by averaging all possible θ, one always gets 0 as a result. The diagonal entries of ρ resemble the probability of finding the electron in its spin-up or spin-down state after the measurement. Interestingly, ρ does not represent a quantum system anymore because the expression in equation (2.15) cannot be written as a product of wavefunctions. The initial state has lost its capability to make interference patterns, so no superposition is possible. When equation (2.15) is valid for a quantum system, decoherence occurs.[35]

The time that denotes the lifetime of the superposition state after a first interaction is called the coherence time (T_m). By now, it should be clear that long T_m is only possible if the qubit interacts as little as possible with its nearby environment. Therefore, the relaxation processes concerning the electron spins must be understood to limit the impact of decoherence (Section 3.5). For now, we will focus on another quantum phenomenon, the exchange interaction.

2.3 The exchange interaction: Turn on the communication between two spins

According to the *Di Vincenzo* rules,[27] a set of two communicating qubits is necessary to realize a two-qubit quantum logic gate. In Chapter 1, the concept of entanglement was introduced, and it is with entanglement that communicating qubits are created. A way to achieve this with electron spins is to bring two or more electrons to interact via exchange coupling.[36] This interaction has no classical counterpart. The exchange interaction occurs between two interacting spins that are locally in different places (*e.g.*, two different orbitals). In quantum chemistry books, the exchange interaction is introduced with the example of the H_2-molecule or the He atom,[26,37] where the exchange interaction is usually described as localized on two electron magnetic moments. In this thesis, however, the interaction between two $S = 1/2$ spins is important and is defined by the following Hamiltonian

$$\hat{H}_{Ex} = J \cdot \hat{S}_1 \cdot \hat{S}_2. \tag{2.16}$$

At this point, it must be clarified that in a more generalized system, the scalar J in equation (2.15) turns to a tensor **J**, consisting of an isotopic, an anisotropic, and an asymmetric part. The bimetallic complexes studied in this thesis could be described using only the isotropic exchange term, so the other two terms will not be mentioned further.

What will be discussed in more detail instead is the behavior of an exchange-coupled system in an external magnetic field. At the beginning of Chapter 2, it was shown that the energy degeneracy of a spin is removed when an external magnetic field is applied. The exchange interaction between two electron spins removes the degeneracy of the energy states even at $B = 0$. The separation in energy between the ground and the excited state is the exchange parameter J. Since the J value can take any positive or negative real number, two outcomes are possible. The two coupled spins could both be oriented parallel or antiparallel. This would result in

a spin system with $S = 1$ ground state. The other possibility is to have a spin system consisting of one parallel spin and one anti-parallel spin, thus leading to a $S = 0$ ground state. If the exchange coupling generates a $S = 1$ ground state, then the coupling is referred to as ferromagnetic (FM). The $S = 0$ case is called antiferromagnetic (AF) instead. There are various reasons for whether the spins show a FM or AF coupling. These reasons will be explained in more detail in Chapter 3. Generally, the states are also defined by their spin multiplicity, meaning that FM-coupled systems are called triplet states, while AF-coupled systems can be referred to as singlet states. The energies of these two possible outcomes can be calculated using equation (2.17):

$$E = \frac{J}{2} \cdot [S(S+1) - S_1(S_1+1) - S_2(S_2+1)]. \tag{2.17}$$

The energy for the ferromagnetic case is given by $S = 1$, and S_1, $S_2 = 1/2$, which leads to

$$E_{\mathrm{FM}} = \frac{1}{4}J. \tag{2.18}$$

The energy for the antiferromagnetic case is given by $S = 0$, and $S_1 = -1/2$, $S_2 = 1/2$, which leads to

$$E_{\mathrm{AF}} = -\frac{3}{4}J. \tag{2.19}$$

Once the field is applied, the triplet state splits into three energy levels, corresponding to $m_s = 0, \pm 1$, and the singlet state generates only one energy state with $m_s = 0$. In equations (2.18) and (2.19), it can be seen how the sign of J can vary the energies of E_{AF} or E_{FM}. For $J > 0$, the ground state consists of the singlet state, and the excited

state is the triplet one. For $J < 0$, the opposite is the case. Therefore, the ground state of a two-spin system could either have a FM ground state or an AF one, depending on how the spins interact with each other. For now, this question will be held open and discussed in greater detail in Chapter 3.

Figure 2.2 shows a qualitative energy diagram for an exchange coupled two-spin system when J is either negative (ferromagnetic) or positive (antiferromagnetic).

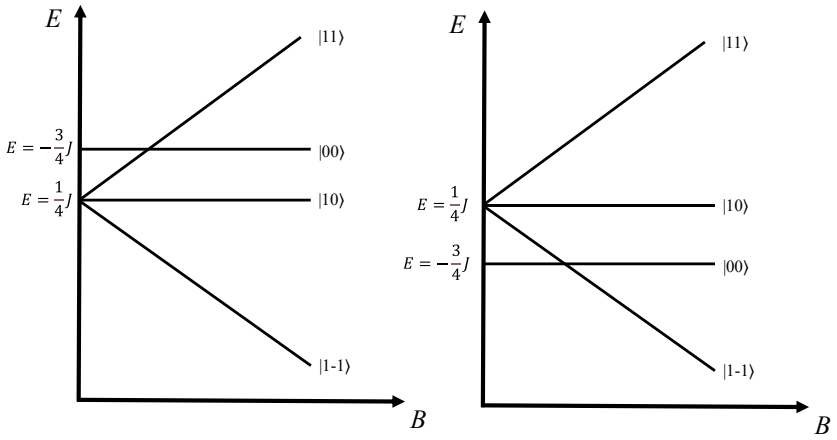

Figure 2.2: qualitative energy diagram for an exchange coupled two-spin system when J is smaller (ferromagnetic, left) or higher (antiferromagnetic, right) than 0.

If we consider an exchange-coupled system, the basis states could be written as[38]

$$\begin{aligned} |11\rangle &= |\uparrow\uparrow\rangle; \\ |10\rangle &= \frac{|\downarrow\uparrow\rangle + |\uparrow\downarrow\rangle}{\sqrt{2}}; \\ |1-1\rangle &= |\downarrow\downarrow\rangle; \\ |00\rangle &= \frac{|\downarrow\uparrow\rangle - |\uparrow\downarrow\rangle}{\sqrt{2}}. \end{aligned} \tag{2.20}$$

Note that the two $m_s = 0$ states look similar to the four-dimensional representation of a two-qubit system and, in particular, to the *Bell* states mentioned in Chapter 1. The energy states for the lowest and highest energy represent the two-qubit systems pure states. This becomes clearer when the eigenstates are represented as vectors:

$$\begin{aligned} |11\rangle &= \begin{bmatrix} 0 \\ 0 \\ 0 \\ 1 \end{bmatrix}; \\ |10\rangle &= \frac{1}{\sqrt{2}} \begin{bmatrix} 0 \\ -1 \\ -1 \\ 0 \end{bmatrix}; \\ |1-1\rangle &= \begin{bmatrix} 1 \\ 0 \\ 0 \\ 0 \end{bmatrix}; \\ |00\rangle &= \frac{1}{\sqrt{2}} \begin{bmatrix} 0 \\ -1 \\ 1 \\ 0 \end{bmatrix}. \end{aligned} \tag{2.21}$$

The eigenvalue energies of two exchange coupled spins can be represented by the following equations:

$$\begin{aligned} E_1 &= -g\mu_B B_Z + \frac{1}{4}J \\ E_2 &= \frac{1}{4}J \\ E_3 &= g\mu_B B_Z + \frac{1}{4}J \\ E_4 &= -\frac{3}{4}J. \end{aligned} \tag{2.22}$$

The eigenstates shown in equations (2.20) and (2.21) are equal for FM and AF coupled spins. Unfortunately, the description and presence of the four basis states are still not a satisfactory requirement for a two-qubit system. According to the third *Di Vincenzo* rule[27], single qubit manipulation must be possible because it would provide the necessary ingredients for realizing a quantum logic gate. However, single qubit manipulation is not possible in the example mentioned above. The reason lies in the possible transitions at a given field and mw-frequency. To better explain the issue, **Figure 2.3** will be used, in which the *Zeeman* plot of two FM coupled spins is shown with $\nu = 9.4$ GHz, $g_e = 2.0023$, and B_z between 0-600 mT at different J values. **Figure 2.3** left shows two coupled spins in the strong exchange coupling regime, whereas the right figure shows two spins in the low exchange coupling regime. Two spins are weakly coupled if the energy/frequency of the irradiating mw in the EPR experiment is higher than the absolute value of J. The opposite is the case for the strong coupling regime. This means that for a mw with $\nu = 9.4$ GHz, all J values lower than 9.4 GHz (or 0.3 cm^{-1}) will result in weak exchange coupled systems and vice versa.

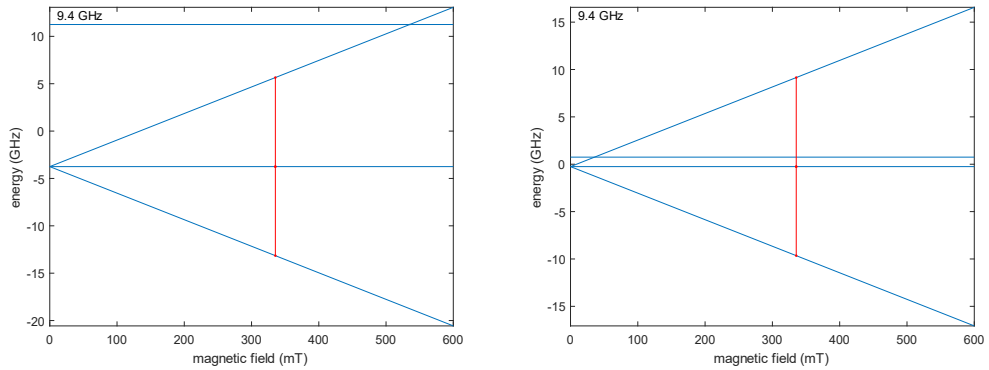

Figure 2.3: *Zeeman* plot simulated for two FM coupled electrons with $g_e = 2.0023$, $J = -15000$ MHz (left), and $J = -1000$ MHz (right) for $B = 340$ mT. Both plots were simulated using EasySpin.[39] all transitions are visualized as red arrows.

As can be seen in **Figure 2.3**, only two transitions, from $|1{-}1\rangle \rightarrow |10\rangle$ and $|10\rangle \rightarrow |11\rangle$, are possible at the given magnetic parameters for both the strong and weak exchange regime. Moreover, the transitions occur at the same magnetic field, so the states are not singly addressable. This is an expected result because the two electron spins are magnetically identical. To improve the system, one has to find a way to make the two spins distinguishable. This is the case if, *e.g.*, the *g*-values of the spins are different. **Figure 2.4** shows the *Zeeman* plot of two exchange-coupled spins with two different *g*-values (2.1 and 1.9) in the strong and weak exchange regimes.

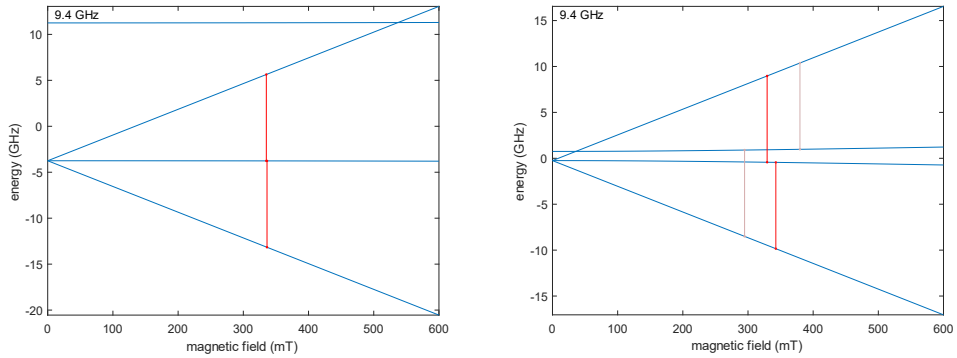

Figure 2.4: *Zeeman* plot simulated for two FM coupled electrons with $g_1 = 1.9$, $g_2 = 2.1$, $J = -15000$ MHz (left), and $J = -1000$ MHz (right). Both plots were simulated using EasySpin.[39] all transitions are visualized as red or cyan arrows.

The *Zeeman* plot on the left of **Figure 2.4** (strong exchange regime) is very similar to the one obtained, assuming equal *g*-values. However, if we look at the *Zeeman* plot for the weak exchange regime, four different energetically transitions are visible. A system with a similar *Zeeman* plot would be suitable for quantum computation. While the eigenstates of the example shown in **Figure 2.4** right are equal to the one shown in **Figure 2.3**, in the weak exchange regime, the different *g*-values change the eigenstates of the states $|00\rangle$ and $|10\rangle$ to

$$|10\rangle = \cos(\Phi)\frac{|\downarrow\uparrow\rangle + |\uparrow\downarrow\rangle}{\sqrt{2}} + \sin(\Phi)\frac{|\downarrow\uparrow\rangle - |\uparrow\downarrow\rangle}{\sqrt{2}};$$
$$|00\rangle = \cos(\Phi)\frac{|\downarrow\uparrow\rangle - |\uparrow\downarrow\rangle}{\sqrt{2}} - \sin(\Phi)\frac{|\downarrow\uparrow\rangle + |\uparrow\downarrow\rangle}{\sqrt{2}}, \quad (2.23)$$

with Φ being the admixing factor,[38] which depends on the strength of the exchange interaction and Δg like shown in equation (2.24):

$$\Phi = \frac{1}{2}\tan^{-1}\left(\frac{\Delta g \mu_B B_z}{2J}\right). \quad (2.24)$$

Until now, the through-space dipolar interaction (D_{Dip}) between the spins was neglected. However, in a real multi-spin system, the dipolar interaction is always present. The dipolar interaction can be represented as a 3x3 matrix (**D**) with the diagonal elements corresponding to the *D* values for each principal axis. The Hamiltonian of the dipolar interaction is

$$\hat{H}_{Dip} = \hat{S}_1 \cdot \boldsymbol{D} \cdot \hat{S}_2. \quad (2.25)$$

The dipolar interaction can be described by classical physics, and it is inversely proportional to the cube of the distance between the spins, which means that the *D*-value can be described as

$$D_{Dip} = \frac{\mu_B^2}{r^3} \cdot \left(g_1 \cdot g_2 - 3 \cdot \frac{(g_1 \cdot r) \cdot (g_2 \cdot r)}{r^2}\right), \quad (2.26)$$

with *r* being the distance between the two spins and g_1 and g_2 being the g-values of the two spins.[33] From a mathematical point of view, the dipolar interaction is described with the same Hamiltonian as the tensorial expression of **J**, which is why one interaction tensor is used in the Hamiltonian, that is, the sum of the **D** and **J** tensor, and considering the point dipole approximation results in:[40]

$$\mathbf{J} \approx J\mathbf{I} + \mathbf{D} = \begin{bmatrix} J + D_x & 0 & 0 \\ 0 & J + D_y & 0 \\ 0 & 0 & J + D_z \end{bmatrix}. \tag{2.27}$$

The *Zeeman* plot changes as shown in **Figure 2.5** left. The $|11\rangle$ and $|1{-}1\rangle$ basis states are shifted to higher energies for both antiferro-and ferromagnetic cases. The eigenvalues of $|10\rangle$ and $|00\rangle$ are only affected minimally by D_{Dip}, which is why, in the first approximation, the D_{Dip} term can be neglected in these two cases.[40] **Figure 2.5,** right, shows a simulated *Zeeman* plot of a two-spin system, having only dipolar but no exchange interaction. Four distinct transitions can be identified. However, the transitions are too close to each other and are probably not even detectable in cw-EPR experiments because of the spectral resolution. To achieve the four computational basis states, transitions in **Figure 2.5** must be more separated, requiring significant enhancement of the dipolar interaction. This is challenging, particularly for molecular spin systems, where the proximity of spins can result in a strong exchange coupling unsuitable for quantum computation (see Chapter 3).

Thus far, we have provided a comprehensive examination of electron interactions, raising important issues. Addressability poses a significant challenge due to the indistinguishable magnetic properties of electron spins. To solve this problem, it was just assumed that the *g*-values of the two spins were different, but it was not shown how to make them different. It is at this point that chemistry comes into the scene. The *g*-value is sensitive to the spin environment, meaning that an unpaired electron in a metal-ion does have different magnetic properties compared to the free electron and, therefore, also a different *g*-value. Indeed, *g*-values of approximately 1.9 and 2.1 can be found in common square pyramidal V^{4+}[41,42] and square planar Cu^{2+} complexes.[43,44] Good candidates are, therefore, bimetallic complexes containing weak exchange coupled spins. Consequently, the mathematical description in this chapter must adapt to this new spin system. The spin Hamiltonian requires expansion, and understanding the novel EPR-allowed transitions is essential. Further insights into

the impact of the chemical environment on the electron spin will be illustrated in Chapter 3.

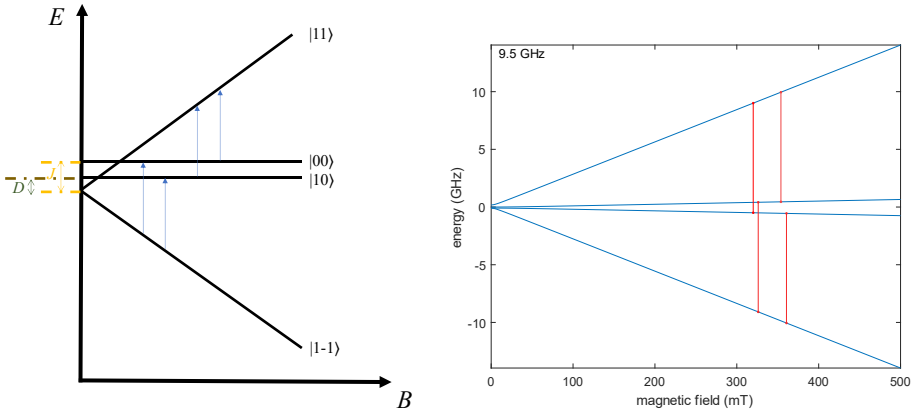

Figure 2.5: Qualitative *Zeeman* plot of a ferromagnetic exchange coupled system, also considering the dipolar interaction. The additional dipolar interaction does not significantly change the splitting. Only the$|11\rangle$ and $|1-1\rangle$ basis states are slightly shifted to higher energies (left). *Zeeman* plot simulated for two coupled electron spins with $g_1 = 1.9$, $g_2 = 2.1$, and $D = [180\ -360\ 180]$ MHz. The plots were simulated using EasySpin.[39] all transitions are visualized as red arrows (right).

3 Environmental effects on the EPR of electron spins

In the conclusion of Chapter 2, it was established that the feasibility of single spin addressability in molecular spin qubits arises from the different *g*-values associated with individual paramagnetic transition metal complexes. This differentiation originates from the orbital occupation with unpaired electrons dictated by the ligand field, consequently introducing changes in magnetic properties compared to the free electrons. The subsequent sections in this chapter will introduce and elucidate key parameters, beginning with the *g*-factor (Section 3.1), followed by an examination of the reasons behind the variance in *g*-values between unpaired electrons in metal ions and free electrons, along with their influence on the ground state of exchange-coupled systems (Section 3.2). An expansion of the spin Hamiltonian is necessary (Section 3.3), as is the introduction of experimental techniques enabling spin manipulation (Section 3.4) and its consequences on coherence and spin relaxation. These critical topics will be examined in greater detail in Sections 3.5 and 3.6.

3.1 The *g*-factor

First, the *g*-factor is anisotropic and should generally be described as a 3×3 tensor. The **g**-tensor describes the effective magnetic moment of a spin and its coupling with the magnetic field. It is the ratio between classically expected magnetic moments and observed moments. Paramagnetic molecules where the effect of the ligand field quenches the orbital angular momentum can still have *g*-values different from g_e anyhow because of spin-orbit coupling (SOC) present in the metal-ion that admixes the ground electronic state with the excited states. If we consider a free ion, that is, if one neglects the effect of ligands on the unpaired electrons of the paramagnetic ion, all atoms with more/less than half populated orbitals have non-zero total spins and angular momentum. The total spin angular momentum S and the total orbital angular momentum L can be combined in $(2L + 1)\ (2S + 1)$ ways. The combination of LS

results in a SOC, which leads to a splitting of the energy levels. The Hamiltonian is written as

$$\hat{H}_{\mathrm{SOC}} = \lambda \cdot \hat{L} \cdot \hat{S}. \tag{3.1}$$

$\hat{L}$ and $\hat{S}$ are the total orbital and spin operator, whereas λ is a parameter for the resulting energy, that can further be described as

$$\lambda = \pm \frac{\zeta}{2S}. \tag{3.2}$$

ζ is the spin orbit-coupling constant.[45] It increases with increasing atomic number and is negative for more than half-occupied d-orbitals and positive for less than half-occupied ones. The relation between SOC and the **g**-tensor is given by

$$\mathbf{g} = g_{\mathrm{e}}\mathbf{I} - 2\lambda\mathbf{\Lambda}, \tag{3.3}$$

with **I** being the identity matrix and **Λ** is described by equation (3.4)

$$\mathbf{\Lambda} = \sum_{\mathrm{n}} \frac{\langle \mathrm{g} \mid \hat{L} \mid \mathrm{n} \rangle \langle \mathrm{n} \mid \hat{L} \mid \mathrm{g} \rangle}{E_{\mathrm{n}} - E_{\mathrm{g}}}, \tag{3.4}$$

in which **Λ** is a tensor that considers the mixture of the ground and excited states mediated by the total angular momentum L of the unpaired electron.[45] $|\mathrm{g}\rangle$ and $|\mathrm{n}\rangle$ are the ground and excited states basis function with the energies E_{g} and E_{n}. By

considering transition metal complexes, d-orbitals containing n = 5 unpaired electrons have a g-value equal to g_e because no allowed transitions contribute to $\mathbf{\Lambda}$. Since $\mathbf{\Lambda}$ is always positive and λ can be positive or negative according to equation (3.4), with $n < 5$, the g-value is smaller than g_e, and for $n > 5$, the g-value is higher than g_e because of the change in the sign of λ.

We see that the g-value depends on the SOC, so now the question is which transition metal complex to use to realize the complex. Chemically stable $S = 1/2$ states in molecules are found in coordination compounds comprising quadratic planar Cu^{2+} complexes, like the d^9-system and the square pyramidal $V^{4+}O$ ion, a d^1-system also having a total spin of $S = 1/2$. The ligand field splitting of the d orbitals for the two ions in a tetragonal symmetry is shown graphically in **Figure 3.1**.

The reason why these two ions, in particular, are so interesting is not only the fact that they are both $S = 1/2$ systems but also because they have almost no orbital degeneracy and, therefore, a weak orbital contribution to g. These ions are preferred because the unpaired electron spin does not interact with the vibration of the crystal lattice of the molecular frame. The lattice of a crystal vibrates with a specific frequency ω and generates particles called phonons (q).[46–48] Their interaction with the spin degrees of freedom increases the relaxation times and thus promotes decoherence (Section 3.5).

The distance between the two metal ions is also important because the closer the ions are, the more they interact. Exchange interactions are promoted through orbital communication. More about the exchange coupling in metal ions can be found in the next section.

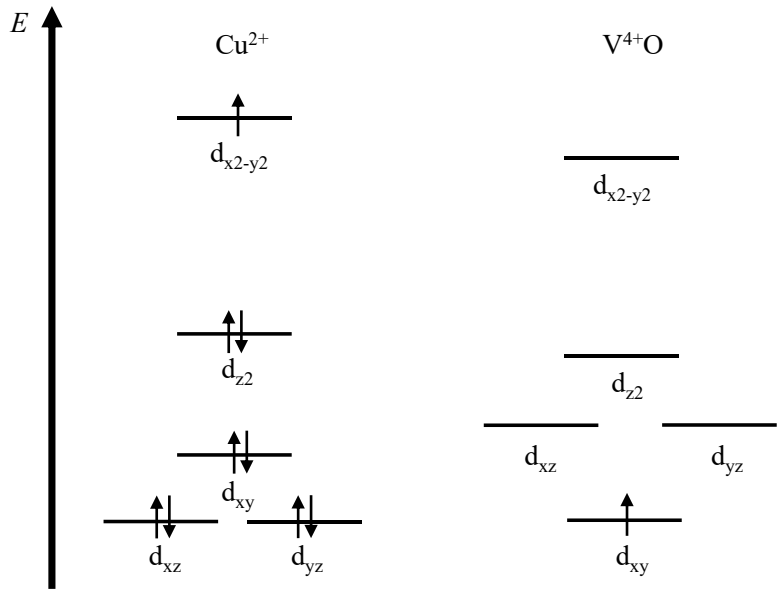

Figure 3.1: Ligand field splitting of Cu^{2+} (left) and $V^{4+}O$ (right) ions in a square planar and square pyramidal environment.

3.2 The ground state in exchange coupled systems

Orbital contributions have a significant impact on the nature of the exchange coupling. They determine whether the exchange coupling is FM or AF. Spin systems prefer singlet or triplet ground states depending on how the orbitals carrying the unpaired electrons, *i.e.*, the magnetic orbitals, can interact with each other. *Goodenough & Kanamori*[49–51] formulated three simple rules to predict and explain the different interactions in a bimetallic salt or complex. These rules are the following:

i. If the magnetic orbitals overlap directly through the presence of an auxiliary orbital, then the exchange coupling is antiferromagnetic.
ii. If the magnetic orbitals are orthogonal, the exchange interaction is ferromagnetic.
iii. If a magnetic orbital overlaps with an empty orbital, the exchange is ferromagnetic

The three rules are visualized with the orbitals in **Figure 3.2**.

It must be mentioned that the exchange interaction should be called superexchange interaction [52] because the interaction between the two electron spins is usually promoted by an "auxiliary" orbital that bridges the two metal ions. Direct exchange interactions where the magnetic orbitals directly overlap are known, but they fall beyond the scope of this thesis. From now on, the exchange interaction will refer to the superexchange interaction for simplicity.

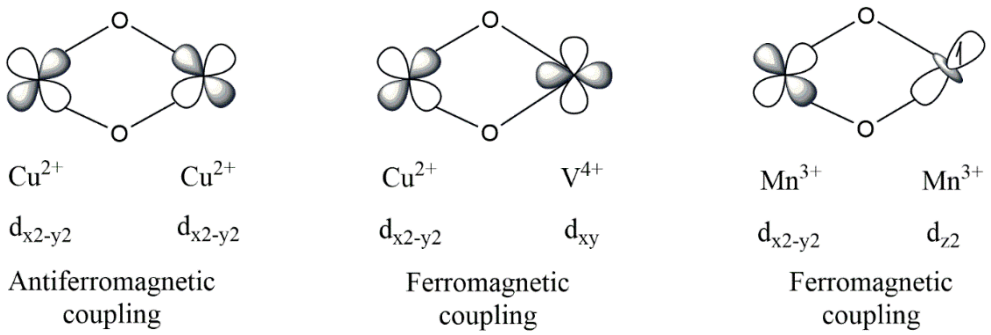

Figure 3.2: Three examples of bimetallic and O-bridged complexes where the first (left), second (middle), and third (right) *Goodenough & Kanamori* rules can be applied. The d-orbitals presented are all the magnetic orbitals except for the d_{x2-y2}-orbital of Mn^{3+} in an elongated octahedron, which is an empty orbital.

It is important to understand that similar systems like those shown in **Figure 3.2** are not interesting for quantum information because the exchange interaction is expected to be very strong.[52] The distance between the two metal centers must be enhanced while maintaining a degree of conjugation for entering the weak exchange regime. Another important aspect is that for quantum computation, the absolute value of J is more important than its sign. More details about the expanded spin Hamiltonian will be given in the following two sections.

3.3 The spin Hamiltonian for spin qubits

The *g*-value is not the only parameter that has to be introduced to describe the spin Hamiltonian of a paramagnetic complex. The metal nucleus can have a spin (so-called nuclear spin) interacting with the electron spin. The ligand also influences the magnetic anisotropy of the spin system. All these interactions impact the EPR of the spin qubit and QIP. The spin Hamiltonian, in the simplest case, would look like this:

$$\hat{H}_{\mathrm{S}} = \hat{H}_{\mathrm{EZ}} + \hat{H}_{\mathrm{NZ}} + \hat{H}_{\mathrm{Hyp}} = \mu_{\mathrm{B}} \cdot \vec{B} \cdot \mathbf{g} \cdot \hat{S} + \mu_{\mathrm{n}} \cdot \vec{B} \cdot \mathbf{g}_{\mathrm{n}} \cdot \hat{I} + \hat{S} \cdot \mathbf{A} \cdot \hat{I}. \qquad (3.5)$$

The first term of the spin Hamiltonian is the electron-*Zeeman* term ($\hat{H}_{\mathrm{EZ}}$), which was already introduced in Chapter 2. The electron-*Zeeman* term accounts for $2S + 1$ splitting of the degenerated energy states in a magnetic field $\vec{B}$.[53] Additionally, the *Zeeman* term consists of the total spin operator $\hat{S}$ and the **g**-tensor. The $\hat{H}_{\mathrm{EZ}}$ can be rewritten as

$$\hat{H}_{\mathrm{EZ}} = \mu_{\mathrm{B}} \cdot \begin{pmatrix} B_{\mathrm{x}} & B_{\mathrm{y}} & B_{\mathrm{z}} \end{pmatrix} \cdot \begin{pmatrix} g_{\mathrm{x}} & 0 & 0 \\ 0 & g_{\mathrm{y}} & 0 \\ 0 & 0 & g_{\mathrm{z}} \end{pmatrix} \cdot \begin{pmatrix} \hat{S}_{\mathrm{x}} \\ \hat{S}_{\mathrm{y}} \\ \hat{S}_{\mathrm{z}} \end{pmatrix}. \qquad (3.6)$$

In equation (3.6), the **g**-tensor is shown in its diagonalized form, with the diagonal elements being the *g*-values along the principal axis. This consideration can be done if the reference framework is the molecular system.

The second term of the spin Hamiltonian is the nucleus-*Zeeman* interaction ($\hat{H}_{\mathrm{NZ}}$). This interaction causes a $2I + 1$ splitting of the already split energy states created by the electron-*Zeeman* interaction.[53] Note that I is the nuclear spin quantum number. The nuclear-*Zeeman* interactions are usually neglected because they

are weak, and therefore, the fine structure of the EPR spectrum is given by the hyperfine interaction term ($\hat{H}_{\mathrm{Hyp}}$). This term accounts for the field-independent interactions between the nuclear spin I and the electron spin S in a molecule.[53] The hyperfine term in equation (3.5) can be rewritten as:

$$\hat{H}_{\mathrm{Hyp}} = \begin{pmatrix} \hat{S}_{\mathrm{x}} & \hat{S}_{\mathrm{y}} & \hat{S}_{\mathrm{z}} \end{pmatrix} \cdot \begin{pmatrix} A_{\mathrm{x}} & 0 & 0 \\ 0 & A_{\mathrm{y}} & 0 \\ 0 & 0 & A_{\mathrm{z}} \end{pmatrix} \cdot \begin{pmatrix} \hat{I}_{\mathrm{x}} \\ \hat{I}_{\mathrm{y}} \\ \hat{I}_{\mathrm{z}} \end{pmatrix}. \tag{3.7}$$

The **A**-tensor is shown in its diagonalized form, and the diagonal entries are the A-values along the principal axis. **Figure 3.3** shows the example of the energy levels of a paramagnetic molecule consisting of a Cu^{2+} ion that has I = 3/2 and one unpaired electron in d_{x2-y2} orbital (S = 1/2).

It is also possible to describe the energy states more quantitatively. This means one has to calculate the eigenvalue energies from the spin Hamiltonian shown in equation (3.5). The way to determine the energy for each level is to rewrite equation (3.5) in its matrix form.[35] The matrix is written in its magnetic quantum numbers m_{s} and m_{I} according to

$$E = \langle m_{\mathrm{s}}, m_{\mathrm{I}} | \hat{H}_{\mathrm{S}} | m_{\mathrm{s}}, m_{\mathrm{I}} \rangle. \tag{3.8}$$

If we take the Cu^{2+}ion as an example and assume we have only one Cu-isotope, we get the spin quantum numbers S = 1/2 and I = 3/2, meaning the possible basis values are m_{s} = ± 1/2 and m_{I} = ± 3/2; ± 1/2. The spin Hamiltonian matrix is an 8×8 matrix, with its diagonal elements corresponding to the energies of each energy level. Commonly found spin Hamiltonian parameters (g and A) for Cu^{2+} metal complexes are g = 2.105 and A = 360 MHz. Considering B = 340 mT and ν = 9.5 GHz. The

energies of each of the eight states can be described generally by the following eight equations:

$$
\begin{aligned}
E_1 &= \frac{1}{2} g_\mathrm{s} \cdot \mu_\mathrm{B} \cdot B_\mathrm{z} + \frac{3}{2} g_\mathrm{n} \cdot \mu_\mathrm{n} \cdot B_\mathrm{z} + \frac{3}{4} A \\
E_2 &= \frac{1}{2} g_\mathrm{s} \cdot \mu_\mathrm{B} \cdot B_\mathrm{z} + \frac{1}{2} g_\mathrm{n} \cdot \mu_\mathrm{n} \cdot B_\mathrm{z} + \frac{1}{4} A \\
E_3 &= \frac{1}{2} g_\mathrm{s} \cdot \mu_\mathrm{B} \cdot B_\mathrm{z} - \frac{1}{2} g_\mathrm{n} \cdot \mu_\mathrm{n} \cdot B_\mathrm{z} - \frac{1}{4} A \\
E_4 &= \frac{1}{2} g_\mathrm{s} \cdot \mu_\mathrm{B} \cdot B_\mathrm{z} - \frac{3}{2} g_\mathrm{n} \cdot \mu_\mathrm{n} \cdot B_\mathrm{z} - \frac{3}{4} A \\
E_5 &= -\frac{1}{2} g_\mathrm{s} \cdot \mu_\mathrm{B} \cdot B_\mathrm{z} + \frac{3}{2} g_\mathrm{n} \cdot \mu_\mathrm{n} \cdot B_\mathrm{z} + \frac{3}{4} A \\
E_6 &= -\frac{1}{2} g_\mathrm{s} \cdot \mu_\mathrm{B} \cdot B_\mathrm{z} + \frac{1}{2} g_\mathrm{n} \cdot \mu_\mathrm{n} \cdot B_\mathrm{z} + \frac{1}{4} A \\
E_7 &= -\frac{1}{2} g_\mathrm{s} \cdot \mu_\mathrm{B} \cdot B_\mathrm{z} - \frac{1}{2} g_\mathrm{n} \cdot \mu_\mathrm{n} \cdot B_\mathrm{z} - \frac{1}{4} A \\
E_8 &= -\frac{1}{2} g_\mathrm{s} \cdot \mu_\mathrm{B} \cdot B_\mathrm{z} - \frac{3}{2} g_\mathrm{n} \cdot \mu_\mathrm{n} \cdot B_\mathrm{z} - \frac{3}{4} A.
\end{aligned}
\tag{3.9}
$$

The general equations for the eight energies listed above correspond to the diagonal entries of the non-diagonalized matrix, which means that they are only the eigenvalues of the spin Hamiltonian if the *Zeeman* splitting is much larger than the hyperfine interaction. In that case, the out-of-diagonal elements can be neglected.[53] Generally, a matrix must be diagonalized so that the eigenvalues correspond to the energies of the energy states. Transitions are only allowed according to the *Fermi* golden rule.[54] Considering a perpendicular polarization of the mw radiation, they are as follows: $\Delta m_\mathrm{s} = \pm 1$; $\Delta m_\mathrm{I} = 0$. Therefore, the energy differences for the transitions are

$$\Delta E_{\mathrm{EZ}} = g_{\mathrm{s}} \cdot \mu_{\mathrm{B}} \cdot B_{\mathrm{z}}. \tag{3.10}$$

For the *Zeeman* splitting and

$$\begin{aligned} \Delta E_{\mathrm{Hyp},1} &= g_{\mathrm{s}} \cdot \mu_{\mathrm{B}} \cdot B_{\mathrm{z}} + \frac{3}{4}A \\ \Delta E_{\mathrm{Hyp},2} &= g_{\mathrm{s}} \cdot \mu_{\mathrm{B}} \cdot B_{\mathrm{z}} - \frac{3}{4}A \\ \Delta E_{\mathrm{Hyp},3} &= g_{\mathrm{s}} \cdot \mu_{\mathrm{B}} \cdot B_{\mathrm{z}} + \frac{1}{4}A \\ \Delta E_{\mathrm{Hyp},4} &= g_{\mathrm{s}} \cdot \mu_{\mathrm{B}} \cdot B_{\mathrm{z}} - \frac{1}{4}A \end{aligned} \tag{3.11}$$

For the hyperfine splitting (**Figure 3.3**). It is the $\hat{H}_{\mathrm{Hyp}}$ term that, therefore, is responsible for the additional transitions that are visible in the EPR spectrum. We already established that for a Cu^{2+}-ion, there are four transitions. In the case of a V^{4+} ion, the observed transitions would be eight because $I = 7/2$. Generally, the observable transitions in the EPR spectrum are $2I+1$.

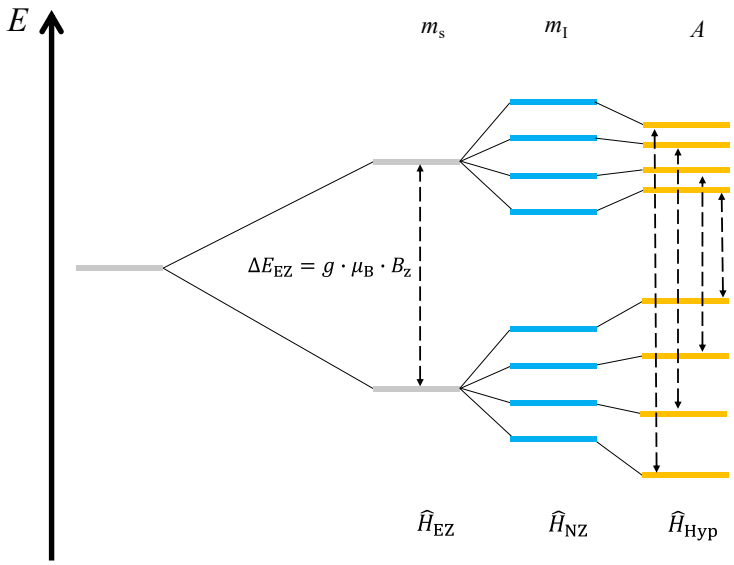

Figure 3.3: Energy scheme of a Cu^{2+} complex considering the spin Hamiltonian (4.5). Allowed transitions are shown by the black dotted arrows. Note that the energy states are not in scale and that the effect of the $\hat{H}_{NZ}$ term is less pronounced.

In the treatment done so far, the parameters g and A were considered as scalars and, therefore, isotropic. In reality, the spin Hamiltonian parameters can only be considered isotropic when the molecules are dynamic and fast-moving with respect to the microwave frequency timescale, *e.g.*, in solution. In frozen solutions or powders, however, the anisotropy of the Hamiltonian parameters can be detected.

It was already shown that **A** and **g** can be diagonalized, leading to three diagonal elements with three different values. If the **g**-tensor is taken as an example, the three possibilities that emerge are $g_x = g_y = g_z$ (isotropic system), $g_x = g_y \neq g_z$ (axial system), $g_x \neq g_y \neq g_z$ (rhombic system). The spectral shape in polycrystalline powders is caused by the random distribution of spins in the experimental framework while in the external magnetic field. Each orientation has a different g or A value with respect to the magnetic field. Fortunately, the EPR spectrum is dominated by the signals arising from species that have their molecular axes either parallel ($A_\parallel$, $g_\parallel$) or perpendicular ($A_\perp$, $g_\perp$) aligned parallel to the field if considering an axial system. The angular dependency of g is described by[53]

$$g(\theta) = \sqrt{g_{\perp}^2 \cdot \sin^2(\theta) + g_{\parallel}^2 \cdot \cos^2(\theta)}. \tag{3.12}$$

The cw-EPR spectra for the V^{4+} and Cu^{2+} will not be shown in this part of the thesis, but some examples of how simple cw-EPR spectra look are available in the experimental section (Section 11.5).

Equation (3.5) is the Hamiltonian that describes the magnetic properties of a single molecular spin qubit. The exchange term $\hat{H}_{ex}$ from Chapter 2 must be introduced while working with two communicating spin qubits and, therefore, a bimetallic metal complex. Equation (3.5) turns to

$$\begin{aligned}\hat{H}_S &= \hat{H}_{EZ,1} + \hat{H}_{EZ,2} + \hat{H}_{Hyp,1} + \hat{H}_{Hyp,2} + \hat{H}_{Ex} \\ &= \mu_B \cdot \vec{B} \cdot \mathbf{g}_1 \cdot \hat{S}_1 + \hat{S}_1 \cdot \mathbf{A}_1 \cdot \hat{I}_1 + \mu_B \cdot \vec{B} \cdot \mathbf{g}_2 \cdot \hat{S}_2 + \hat{S}_2 \cdot \mathbf{A}_2 \cdot \hat{I}_2 + \mathbf{J} \\ &\cdot \hat{S}_1 \cdot \hat{S}_2.\end{aligned} \tag{3.13}$$

With **J** being the interaction tensor introduced in Chapter 2 (see equation (2.27)).

Let us assume that the Hamiltonian (3.13) is sufficient to describe a bimetallic Cu^{2+} V^{4+} complex. Rewriting the spin Hamiltonian (3.13) in matrix form would lead to a 128×128 square matrix. Since the *Fermi* rules $\Delta m_s = \pm 1$, $\Delta m_I = 0$ are valid, the visible transitions at the given field and mw-frequency are 128, considering weak exchange interactions. Generally, one can write that there can be $4 \cdot (2I_1+1)(2I_2+1)$ allowed EPR transitions. At first, these might pose a problem, but for quantum computation, it is sufficient to have four distinguishable transitions between the m_s basis states. More importantly, one has to limit the simultaneous excitation of nearby m_I states with different projections. This means that the energy differences between each "sub"-state must be large enough.

Until now, the eigenstates of weak exchange coupled systems were not shown. The reason lies behind the complexity of the magnetic systems because all magnetic parameters and tensor orientations contribute to the mixing of all |01⟩ and |10⟩ states. The admixing factor Φ was introduced in Chapter 2 (see equation (2.24)). For the presented molecular systems, this admixing factor depends on **g**, **A**, **D**, J, and the tensor orientations. For isotropic and weak exchange coupled systems, such as spin-correlated radical pairs, the behavior of Φ is described in a review.[38]

3.4 Experimental spin manipulation and determination of the relaxation times

In this thesis, the spin relaxation mechanisms and pulsed EPR techniques will only be discussed generally referring to the literature for an exhaustive treatment[34] of the principles of pulsed EPR techniques. In contrast, more information on using pulsed EPR techniques in QIP can be found in the quoted review.[55] To explain the two defined relaxation times, one can start by introducing the *Bloch* equations.

Relaxation times are correlated to the external magnetic field and the *Zeeman* splitting mentioned before. It was already established that electron spins just interacting with an external magnetic field have two distinguishable energy states that are populated according to

$$\frac{N_\alpha}{N_\beta} = \exp - \left(\frac{g \cdot \mu_B \cdot B}{k_B \cdot T} \right). \qquad (3.14)$$

N_α and N_β are the number of spins populated in the two states, and k_b is the *Boltzmann* constant.[53] The α-spins only absorb energy when the resonance condition of equation (3.5) is set. Small perturbations of the magnetic field (*e.g.*, small oscillating magnetic field parallel to B) change the resonance condition, and ΔE also changes. The magnetization of a spin ensemble evolves with time after a perturbation modifies its

equilibrium value. This evolution follows, in general, an exponential law which can be described in a simple case by equation (3.15) that is

$$M(t) = M_0 \cdot \exp\ -\left(\frac{t}{\tau}\right), \tag{3.15}$$

with τ being the relaxation time[52] defined by the time the spins need to return to their thermal equilibrium state after the perturbation. More precisely, when considering the molecules with unpaired spins parallel to the magnetic field B_z, the evolution of M_z can be described by the first *Bloch* equation,[34] that is

$$\frac{\mathrm{d}M_z}{\mathrm{d}t} = -\frac{(M_z - M_0)}{T_1}, \tag{3.16}$$

and T_1 being the spin-lattice relaxation time. The *Bloch* equation described the time dependency of the magnetization along the *z*-direction. Note that the other two *Bloch* equations also describe the time dependency of M_x and M_y components of the magnetization. Considering an ensemble of spins in an external magnetic field B, T_2 is defined by the decay of the magnetization over time, orthogonal to this field. The time dependence of the orthogonal magnetizations can be represented by the *Bloch* equations[34] (3.17) and (3.18).

$$\frac{dM_x}{dt} = \gamma(B \times M)_x - \frac{M_x}{T_2}, \tag{3.17}$$

and,

$$\frac{dM_y}{dt} = \gamma(B \times M)_y - \frac{M_y}{T_2}. \qquad (3.18)$$

In equation (3.17) and (3.18), γ represents the gyromagnetic ratio.

The sample is introduced in a static magnetic field B_z, which is applied parallel to the experimental z-axis. Perpendicular to B_z, at the experimental x-axis, high-intensity mw-pulses of a few µs duration are radiated to the sample. These pulses either induce a transverse magnetization or flip the spin in the opposite direction, depending on the pulse duration. This transverse magnetization is detected at the y-axis by the detection coil. The observation of the transverse magnetization (see equation (3.7)) over time results in an exponentially decreasing magnetization, which is also called the free induction decay (FID) signal. The *Fourier* transform (FT) of this signal leads to the absorption spectrum.

To get a "cleaner" absorption spectrum and to preserve the detector from too intense mw-radiation, the relaxation times T_1 and T_m are usually extracted by performing more elaborate sequences of pulses involving the detection of an echo signal. To determine T_1, the Inversion-Recovery-sequence[34] is used (**Figure 3.4**, top). First, a 180° pulse in the x-direction rotates the spin ensemble (magnetization). Therefore, the magnetization changes from the z to the $-z$ direction. After manipulating the spins, they start relaxing back to their initial position. After a given time τ, a second 90° pulse rotates the spins to the y-direction where they are detected. Another 180° pulse in the y-direction after a time t produces the Echo signal. The Echo signal is caused by the relaxing spins. While the spins are transversely magnetized, their precession changes due to small magnetic field inhomogeneities. At a given time τ, the spins reach the point where they align again, and the signal intensity reaches its maximum. T_1 can be extracted from the Inversion Recovery experiment by modifying equation (3.15) to

$$I = a \cdot \mathrm{e}^{-\frac{\tau}{T_1}}, \tag{3.19}$$

Where a is a dimensionless factor, equation (3.19) shows the mono-exponential decay function for the experiment. Depending on the experimental data, sometimes it is helpful to fit the data with a bi-exponential function. Bi-exponential fitting occurs when the paramagnetic molecule is exposed to different environments, favoring different relaxation processes. As a result, two relaxation times can be detected, one being faster ($T_{1,\mathrm{f}}$) and the other being slower($T_{1,\mathrm{s}}$). In this case, two-dimensional factors for the slow (a_s) and fast (a_f) contribution have to be considered by turning equation (3.19) to

$$I = a_\mathrm{s} \cdot \mathrm{e}^{-\frac{\tau}{T_{1,s}}} + a_\mathrm{f} \cdot \mathrm{e}^{-\frac{t}{T_{1,f}}}. \tag{3.20}$$

The pulse sequence used for the determination of T_m is a 90°-τ-180°-τ sequence, also called the *Hahn*-Echo experiment (**Figure 3.4**, bottom).[34] Similar to the Inversion-Recovery experiment, an exponential decay is observed. This time, however, the magnetization in the z-direction is zero after the magnetization rotation into the xy-plane. After a given time t and another 180° pulse, the spins will eventually create the echo again. The decay of the magnetization is fitted with a stretched mono-exponential decay function:

$$I = a_\mathrm{s} \cdot \mathrm{e}^{\left(-\frac{2\tau}{T_{m,s}}\right)^{\beta}}, \tag{3.21}$$

with β being the stretching parameter. Note that for an ideal system, equation (3.19) should be valid.

Pulsed-EPR techniques can also be used to create quantum logic gates. The spin manipulation using mw-pulses is graphically represented in **Figure 3.5** on a *Bloch* sphere. Equation (2.5) can be rewritten in spherical coordinates to

$$|\Psi\rangle = \cos\frac{\theta}{2}|0\rangle + e^{i\varphi}\sin\frac{\theta}{2}|1\rangle. \tag{3.22}$$

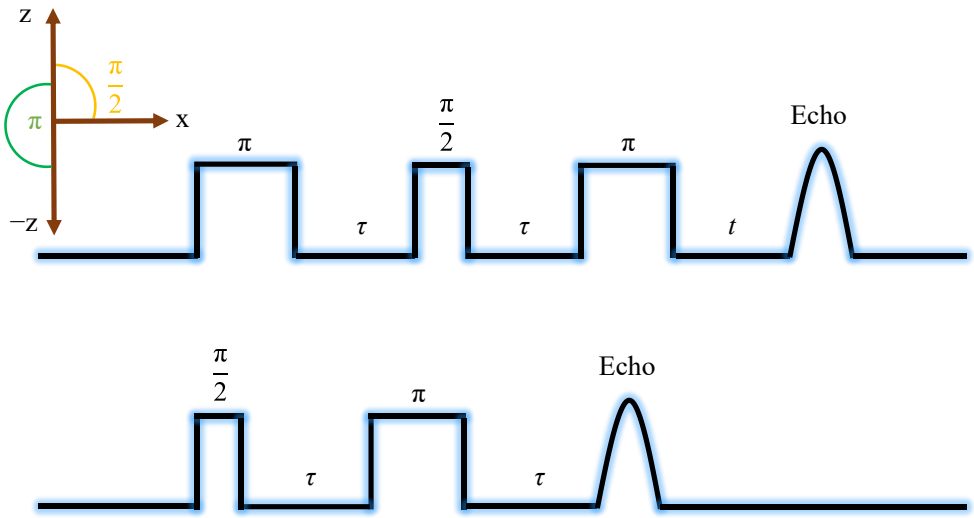

Figure 3.4: Inversion Recovery (top) and *Hahn*-Echo (bottom) experiment for the determination of T_1 and T_m shown graphically according to their pulse and time (t and τ) scheme.

The spin rotation in the z-direction described by the angle θ is induced by the pulse phase of the mw, whereas the rotation on the xy-plane is defined by the angle φ by the pulse power and duration.[55]

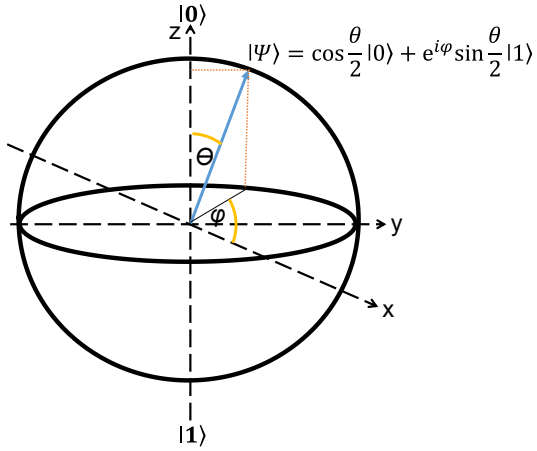

Figure 3.5: The representation of a molecular spin qubit on a *Bloch* sphere using spherical coordinates.

The unitary matrix of the Hadamard gate was introduced in Chapter 1, and it can be emulated with mw-pulses by a 180° rotation in the bisector of the x and *z*-coordinate on the *Bloch* sphere. Since in standard pulse EPR instruments, the mw-pulse is on the principal *y*-axis, the Hadamard gate has to be constructed by a sequence of two combined pulses. It was shown that a combined 90° pulse in the *y*-direction and a 180° pulse in the *x*-direction is indeed sufficient to describe the Hadamard gate. For a single qubit manipulation, the sequence for a Hadamard gate can be described in matrix form by:[55]

$$H = \frac{1}{\sqrt{2}}\begin{bmatrix}1 & 1\\ 1 & -1\end{bmatrix} = \sqrt{2}\begin{bmatrix}-\cos\frac{\pi}{2} & -i\cdot\sin\frac{\pi}{2}\\ -i\cdot\sin\frac{\pi}{2} & \cos\frac{\pi}{2}\end{bmatrix}\cdot\begin{bmatrix}\cos\frac{\pi}{4} & -\sin\frac{\pi}{4}\\ \sin\frac{\pi}{4} & \cos\frac{\pi}{4}\end{bmatrix} = i(\pi)_x\left(\frac{\pi}{2}\right)_y. \quad (3.23)$$

For the realization of two-qubit gates with mw-pulses, primary 180° pulses ($\pi_{x,y}$-rotations) are sufficient to realize the CNOT-gate. It was already explained in Chapter 1 that for the realization of a CNOT-gate, one qubit acts as a control (C) qubit, whereas the second one is a target (T) qubit. This means that the two spins involved in the

process must be individual and singly addressable with mw pulses. Furthermore, the coupling between the two spins must be fine-tuned. The following two sections will describe in more detail the processes involved in T_1 and T_2 and how the chemical design should be chosen to keep the relaxation times as high as possible.

3.5 Spin-lattice relaxation

Three main relaxation processes contribute to T_1, and they contribute differently depending on the temperature.[48] Figure 3.6 shows schematically the direct (left), *Raman* (middle), and *Orbach* (right) processes contributing to T_1. In a two-level spin system, the process that always occurs is the direct process (Figure 3.6, left). The direct process is a one-phonon process and arises from the interactions of the magnetic moments with the phonons created by the vibration of the crystal lattice. These vibrations can have different modes with different energies.

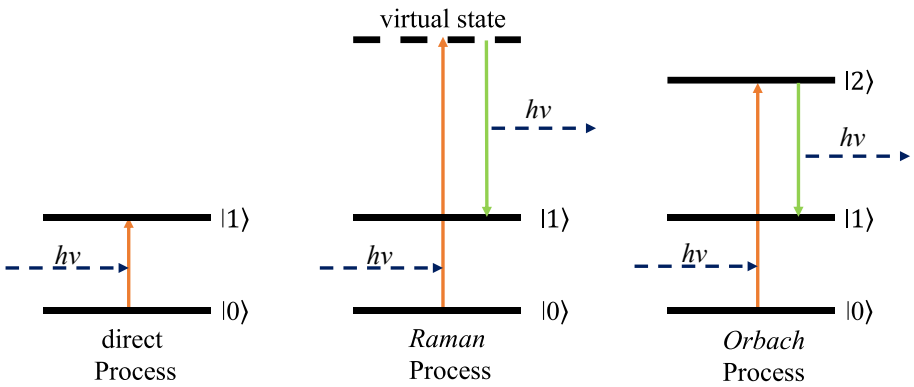

Figure 3.6 Schematic view of the direct process (left), *Raman* process (middle), and *Orbach* process (right) for the spin-lattice relaxation. Orange arrows highlight absorptions, whereas emissions are by dashed dark blue arrows. The green arrows represent the phonons relaxing to a state with lower energy.

According to the direct process, absorption is only possible if the phonons produced by the lattice vibration have an energy vibration that has the same ΔE as the energy difference between |0⟩ and |1⟩. As the *Zeeman* energy in magnetic fields accessible at the laboratory scale is small, the acoustic phonons are the ones that mainly contribute to the direct process. For *Kramers'* systems, so the systems with integer total spin,[56] T_1 is proportional to

$$T_1 = \frac{a_{\mathrm{dir}}}{B^4 \cdot T^{\mathrm{n}}}, \tag{3.24}$$

with B being the external applied magnetic field, T is the temperature, and a_{dir} a proportional constant. The exponent n at the temperature is between 1 and 2 for the direct process. Since vibrational modes of such low energy are the only ones populated at very low temperatures, the direct process is the dominant process at temperatures close to liquid hydrogen.

By increasing the temperature above liquid hydrogen (around 4 K), modes with higher frequencies, the so-called optical modes of a crystal, are accessible, and the *Raman* process (**Figure 3.6**, middle) starts to emerge. Contrary to the direct process, in the *Raman* process, phonons having a higher ΔE than the energy gap between |0⟩ and |1⟩ can be absorbed. In this case, a virtual state mediates forbidden transitions, and the spins relax to the state |1⟩. This mechanism makes the *Raman* process a two-phonon process[46] because once the spin is excited from |0⟩ to the virtual state, one spin from the virtual state falls back to state |1⟩. Note that the energy of the emitted phonon is lower than the absorbed one. For S = 1/2 systems, T_1 is proportional to

$$T_1 = \frac{a_{\mathrm{ram}}}{T^{\mathrm{n}}} \tag{3.25}$$

with *n* being reported to be between 7-9, though lower values are often encountered.[57]

The *Orbach* process is a special case of the *Raman* process. The *Orbach* process takes place in a multi-level system, and the excited state this time is a real state, not a virtual one. The energy of one phonon is high enough so that transitions from |0⟩ to |2⟩ (**Figure 3.6**, right) are possible. The phonon that is emitted afterward has a smaller energy than the absorbed one since it relaxes from |2⟩ to |1⟩. The *Orbach* process is the dominant process at temperatures where the probability of finding a phonon matching the transition from |0⟩ to |2⟩ is higher.[46] The process is dependent on the *Boltzmann* statistic, and therefore, for $S = 1/2$ systems, T_1 is proportional to

$$T_1 = a_{\mathrm{orb}} \left(\exp\left(\frac{-\Delta E_{|0\rangle,|1\rangle}}{k_b T} \right) \right)^{-1} \tag{3.26}$$

With $\exp\left(\frac{-\Delta E_{|0\rangle,|1\rangle}}{k_b T}\right)$ being the *Boltzmann* contribution term.

3.6 Spin-spin relaxation

Though connected to the spin-lattice relaxation, in QIP based on spin, the key parameter is the coherence time or the spin-spin relaxation time T_2. This relaxation time depends on other nuclear or electron spins surrounding the paramagnetic metal ion. Thus, a clever design of the coordination site and the surroundings is crucial to control it.

The spin-spin relaxation is dipolar in nature and is favored in environments with high nuclear spin diffusion when there is a continuous exchange of energy between nuclear spins.[58] Many processes contribute to T_2, but in particular, the flip-flop has a strong impact on the decoherence of spins.[34] The flip-flop process orientates a spin-up electron to a spin-down electron. The energy released is then used

to induce an orientation change of a spin-down electron to a spin-up electron. If taken the relation $T_2 \leq T_1$[34] and introducing the relaxation time associated to the flip-flop, T_2', we get for T_2 the relation

$$\frac{1}{T_2} = \frac{1}{T_2'} + \frac{1}{2T_1}. \tag{3.27}$$

It is challenging to detect T_2 experimentally because other processes also cause the loss of the spin phase, which is why the coherence time T_m is introduced as an effective, measurable parameter. T_2 can be seen as an upper limit for T_m. Contributions that lead to the lowering of T_m in a molecular environment are dipolar interactions of the unpaired electron spin with other unpaired electrons/nuclear spins. Using nuclear-spin-free solvents or reducing the nuclear magnetic moment, *e.g.*, replacing hydrogen with deuterium, on the other hand, enhances T_m.[58,59] Another effect that influences T_m is the presence of unsaturated side groups containing nuclear spins in the ligand that surrounds the unpaired electron. Hydrocarbon side chains tend to rotate in solution or vibrate with many modes in the solid state, the effective field felt by the electron oscillates with time. In particular, side groups containing active nuclei like methyl groups will shorten T_m.[60] Most effort was put into designing ligands with little or zero nuclear spin contribution, with a rigid structure to reach high T_1 even at room temperature and T_m up to 1 μs below room temperature.

This Chapter highlighted the importance of metal and ligand interaction with the unpaired electron. The next chapter will show some examples of literature-reported molecular spin qubits.

4 Molecular spin qubits

The preceding four chapters laid the foundation for this overview of molecular spin qubits. This chapter is divided into two sections: the first section addresses single and two-molecular spin qubit systems, while the second delves into the potential of porphyrin-based molecular spin qubits.

4.1 Examples of molecular spin qubits

After describing the coherence and exchange properties in spin qubits, it is time to present some examples of metal complexes in the literature that were proposed as possible candidates for molecular spin qubits. Herein, it is important to start with a bit of history. The idea of using magnetic molecules for information processing dates back to the early 90s. Magnetic measurements on the peculiar $[Mn_{12}O_{12}(O_2CCH_3)_{16}(H_2O)_4]$ (**Figure 4.1** left, abbreviated as $Mn_{12}(OAc)_{16}$) complex,[61] evidenced that these molecules behave like permanent magnets at very low temperatures ($T < 1.8$ K). The mixed valence Mn^{3+} and Mn^{4+} cluster (ground state $S = 10$) builds the core unit of the complex. In contrast, the acetate ligands surround the core unit, thus creating a "protective shield" against the molecule's nearby environment. The presence of Jahn-Teller distorted Mn^{3+} ions originate the strong, easy-axis magnetic anisotropy that made it the first example of a single molecule magnet (SMM). Moreover, the small but crucial non-axial anisotropy present in $Mn_{12}(OAc)_{16}$ makes it possible to overcome the energy barrier between the m_s $-m_s$ basis states by means of quantum tunneling.[61] The physical properties found in this complex made it legitimate to ask if it was possible to store information at a molecular level and exploit at the same time its quantum features. As a matter of fact, the multi-level nature of the $Mn_{12}(OAc)_{16}$ looked very promising for quantum computation. This idea was proposed by *Leuenberger & Loss*.[62] This question prompted the research community to synthesize similar transition-metal-based clusters[63] along

with lanthanide-based ones,[64] with similar physical properties but at higher temperatures. However, the strong magnetic anisotropy present in $Mn_{12}(OAc)_{16}$ and other SMMs promotes strong orbital contributions as well, thus having a negative impact on the coherence properties. Therefore, other multi-level systems with weaker magnetic anisotropy had to be found.

One particular class of transition metal complexes is considered a breakthrough in the quantum information field; these were the octa-member rings of the type $[\{R_2NH_2\}Cr_7MF_8(O_2CCMe_3)_{16}\}]$ (abbreviated as Cr_7Ni-ring, **Figure 4.1**, right).[65] These rings consist of seven Cr^{3+} and one M^{2+} (usually Ni^{2+}) octahedral coordinated ions that are antiferromagnetically coupled, forming an $S = 1/2$ ground state. Like the $Mn_{12}(OAc)_{16}$, the metal ions are bridged by carboxylate (usually trimethylacetate) and fluorine ions. The ring has one negative charge and presents an amine cation that sits right in the center of the ring. While SMM resembles a much smaller version of a bit, the Cr_7Ni-rings resemble the essence of the qubits.[66,67] These rings have two distinguishable energy states suitable for quantum computation and a unique chemical design that makes them very versatile from a chemical point of view. It was shown that T_m could be enhanced in two ways: firstly, by changing the organic amine cation with Cs^+, then substituting all hydrogens from the trimethylacetate ligand with deuterium,[68] secondly, by diluting the Cr_7Ni-rings in a diamagnetic matrix with a similar structure like Cr_7Ga-rings.[69] Coherence times up to 15 µs were achieved using the abovementioned chemical methods. Moreover, it was shown that by successfully functionalizing the ligand, it was possible to couple the Cr_7Ni-rings with each other. This was chemically done by simply replacing the fluorine—anions with a polyalcohol (*N*-ethyl-D-glucamine) that coordinates upon five Cr^{3+}-ions but leaves the Ni^{2+}-ion with a loose H_2O molecule ligand, that can be easily replaced with *e.g.*, pyrazine, therefore creating the Cr_7Ni-dimer.[70] Finally, it was shown that by substituting the carboxylate ligand with a thiophencarboxylate[71] or long-chain carboxylate,[72] it was possible to graft the Cr_7Ni-rings on Au(111) or graphene surfaces. It was demonstrated that the magnetic properties of the surface-grafted Cr7Ni-rings do not change significantly.

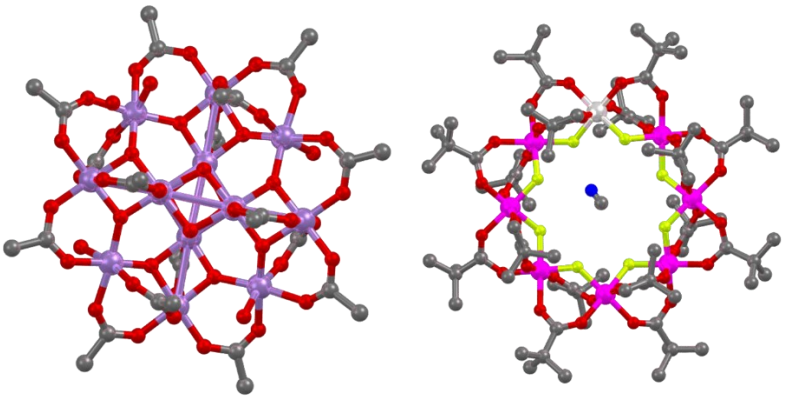

Figure 4.1: Crystal structure of the $Mn_{12}(OAc)_{16}$[73] (left) and Cr_7Ni-ring[70] (right), both shown along the crystallographic *c*-axis. These complexes were the first to be proposed as alternative bits or qubits. Color code: red = O, blue = N, dark grey = C, green = F, magenta = Cr^{3+}, pink = $Mn^{3+/4+}$, light grey = Ni^{2+}. H atoms were omitted for clarity.

We can already see that the Cr_7Ni-rings are perfectly suited for the realization of a first prototypical device where spin manipulation could potentially be done on the substrate.[74] However, there are some drawbacks to mention regarding the Cr_7Ni-rings. Cr_7Ni-rings have an S =3/2 first excited state at a few tens of K, potentially limiting T_m. Moreover, the Cr_7Ni-rings present many bulky side groups, which were already mentioned as the primary cause of limiting T_1. Indeed, T_m up to 15 µs was achieved at temperatures below 2 K, but with an increase in the temperature, the relaxation times decreased significantly.

The new quest was to find metal complexes that were much simpler from the magnetic point of view and showed a more rigid structure. Thus, attention was addressed to the aforementioned square planar Cu^{2+} and square pyramidal V^{4+}-complexes. Record relaxation times could be detected on a maleonitriledithiolate-Cu^{2+} complex ($(PPh_4)_2[Cu(mnt)_2]$), while diluted in $(PPh_4)_2[Ni(mnt)_2]$). The T_m measured was up to 9.2 µs at 7 K (**Figure 4.2a**).[75] Moreover, the relaxation times decrease at a much lower rate than expected, reaching a T_m of 0.6 ns at 300 K. By replacing all hydrogens from the counterion $(PPh_4)^+$ with deuterium, the relaxation time at 7 K was 68 µs and even 1 µs at room temperature. V^{4+}-complexes turned out to be even better.

The first systems are a series of dithiolate complexes of octahedral V^{4+}-ions.[76] Especially the $\{d_{20}\text{-}PPh_4\}_2[V(C_3S_5)_3]$ complex (**Figure 5.2b**) displayed remarkable millisecond T_m at 10 K in a frozen solution of CS_2.

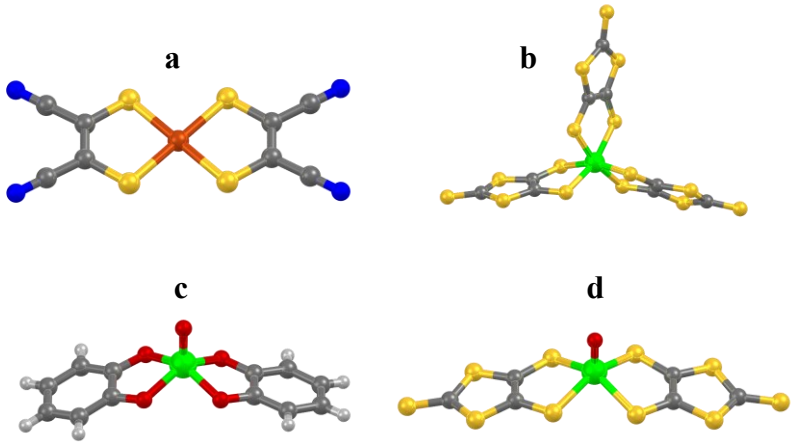

Figure 4.2: Simple S = 1/2 Cu^{2+} and V^{4+} transition metal complexes proposed as molecular spin qubits because of their long coherence times. The molecules presented are $[Cu(mnt)_2]^{2-}$ (**a**)[77], $[V(C_3S_5)_3]^{2-}$ (**b**)[76], $[VO(cat)_2]^{2-}$ (**c**), and $[VO(dmit)_2]^{2-}$ (**d**). The $(PPh_4)^+$ counterion was omitted for all four complexes. Color codes: dark grey = C, yellow = S, blue = N, white = H, red = O, brown = Cu^{2+}, green = V^{4+}.

Better than octahedral V^{4+}-ions are square pyramidal vanadyl ($[VO]^{2+}$)-ions. These complexes, in general, show lower T_m, but the relaxation times decrease less by increasing the temperature.[46,78–80] The square pyramidal $[VO]^{2+}$ catechol complex ($[VO(cat)_2]$) (**Figure 4.2c**) showed that in a temperature range between 4-100 K, T_m up to 4-6 µs could be achieved in a frozen solution.[78] Similar results were obtained by studying the dynamic magnetic properties of the square pyramidal $[VO]^{2+}$ dithiolate complex ($[VO(dmit)_2]$) (**Figure 4.2d**).[80]

All the studies on the Cu^{2+} and $[VO]^{2+}$-complexes showed how to enhance relaxation times in molecular spin qubits. However, these ligands do not allow engineering the molecular architecture to create multi-qubit systems, and alternative strategies were developed. Two notable examples of square pyramidal $[VO]^{2+}$ complexes are presented. The first homometallic $[VO]^{2+}$ complex is based on the *N*,*N*‘-Bis(2,3-dihydroxybenzoyl)-1,4-phenylenediamine ligand.[81] This ligand can

be seen as a di-catechol, which can coordinate two $[VO]^{2+}$ units (**Figure 4.3a**). The interatomic vanadyl-vanadyl distance is around 10 Å (though the real distance is not measurable as no crystal structure is available), and the exchange interaction is neglectable as no direct connection between the two vanadyl ions is present. The EPR spectrum does, however, show some characteristic features of dipolar coupled systems. The two vanadyl ions are not distinguishable, but it was proposed that a simple quantum simulation is possible with this dimer by exploiting the vanadium nuclear spins. Next on the chronological list is the bis-hydroxyphenylpyrazolyl ligand, which was used to create a two-qubit molecular system coordinating two vanadyl ions (**Figure 4.3b**), again non-distinguishable.[82] In principle, identical paramagnetic centers can be individually addressed if their tensors are oriented differently in space. This was also experimentally confirmed by the two-qubit architecture of organic nitroxide radicals.[83] Lanthanide complexes showed promising results for the realization of heterometallic dimers. The $[Ce^{3+}Er^{3+}O]$ hybrid complex reported in **Figure 4.3c**, built on the 6-(3-oxo-3-(2-hydroxyphenyl)propionyl)pyridine-2-carboxylic acid is very promising for quantum computation (**Figure 4.3d**).[84] The realization of heterometallic lanthanide dimers is enabled by the unique structure of the ligand that presents pockets that can selectively accommodate ions with different dimensions. Using two different lanthanides with two different ion-radii, the smaller ion (in this case Er^{3+}) will coordinate at position **1,** and the larger ion (in this case Ce^{3}) will coordinate at position **2** (see **Figure 4.3d**). It was concluded from specific heat data experiments that a finite exchange interaction was present in the complex, though it was impossible to determine the exact value.[84] The exchange turned out to be ferromagnetic, and it was proven that a simple CNOT gate could be constructed using the $[Ce^{3+}Er^{3+}](L)_3(Pyr)(NO_3)(H_2O)]$ complex. Additionally, the ligand could even be expanded to realize a three-qubit architecture.[85]

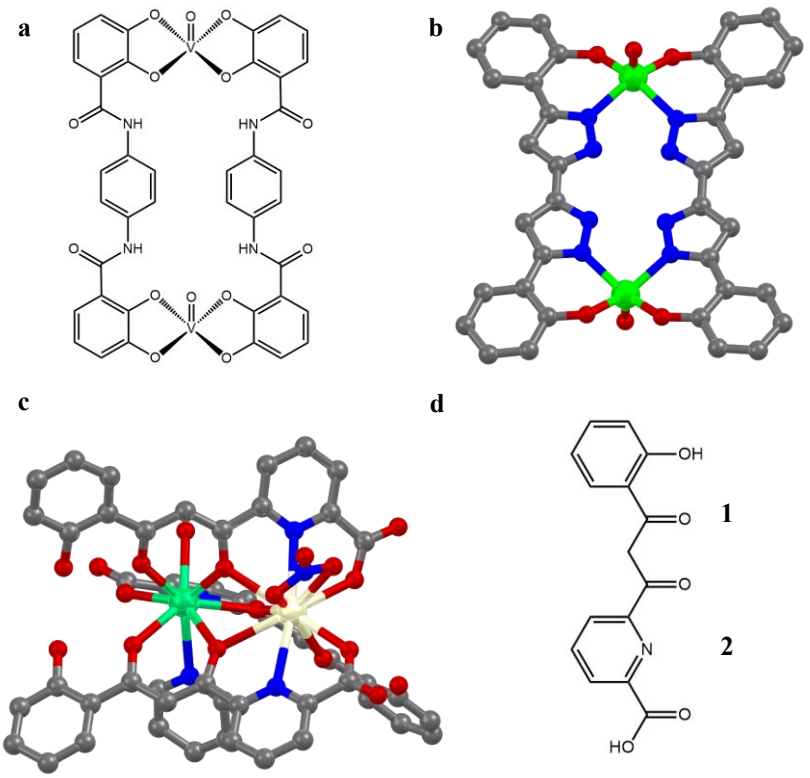

Figure 4.3: Coordination of the vanadyl-ion with either *N*,*N*'-Bis(2,3-dihydroxybenzoyl)-1,4-phenylenediamine (**a**) or hydroxyphenylpyrazolyl (**b**) leads to a bimetallic $[VO]^{2+}$-complex. These complexes were proposed as potential quantum simulators.[81,82] $[Ce^{3+}Er^{3+}]$ Heterometallic lanthanide-based complexes (**c**) can be synthesized by using a ligand (**d**), which is able to coordinate smaller (**1**) and bigger (**2**) ions selectively into the same ligand position. These lanthanide complexes showed energy levels that could be used to implement a CNOT-gate.[84] Color codes: dark grey = C, blue = N, red = O, green = V^{4+}, pale green = Ce^{3+}, white = Er^{3+}.

4.2 Porphyrin-based molecular spin qubits

Other promising classes of ligands are porphyrin and phthalocyanine ligands (Figure 4.4). Even simple and common porphyrinoids have unique spin properties, as they show good relaxation times, are chemically versatile, and can be deposited on metallic surfaces by thermal sublimation at low pressure. First experiments conducted on a 1 % diluted thin film of copperphthalocyanine[86] (**[Cu(Pc)]**, Figure 4.4**a**) evidenced that T_m of 10 µs at 80 K could be reached and that T_m is weakly dependent on

temperature. Even better results could be obtained with the vanadylphthalocyanine (**[VO(Pc)]**, Figure 4.4**b**) complex, which showed room temperature coherence times of 1 µs.[57]

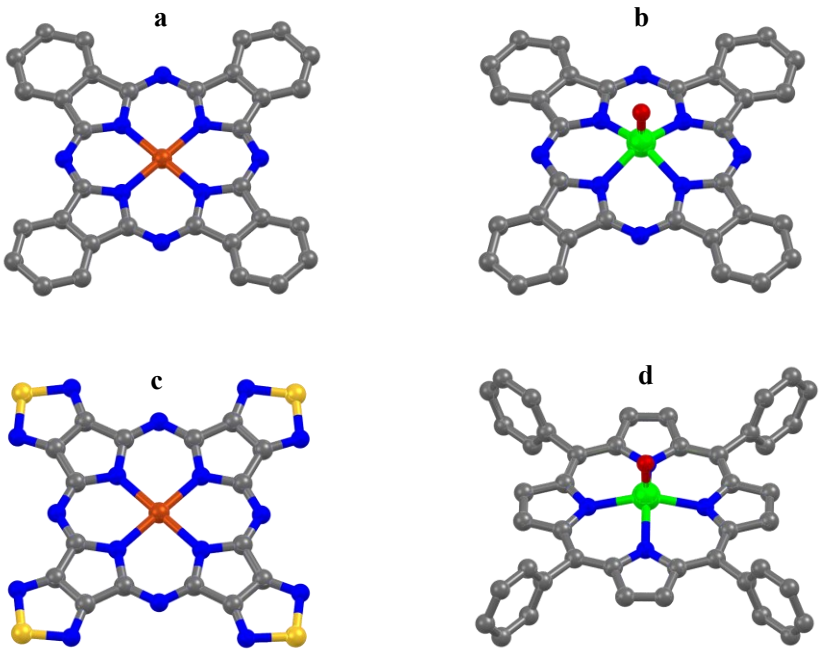

Figure 4.4: The porphyrinic Cu^{2+} and $[VO]^{2+}$ systems [Cu(Pc)][87] (**a**), [VO(Pc)][88] (**b**), [Cu(TTDPz)][89] (**c**), and [VO(TPP)][90] (**d**), are very promising molecular spin qubits due to their good coherence properties, and surface stability after sublimation. Especially porphyrins have a lot of potential because the ligand can be functionalized to make multi-qubit systems color code: dark grey = C, blue = N, red = O, green = V^{4+}, brown = Cu^{2+}. Hydrogens are omitted.

Surface depositions were also possible with **[VO(Pc)]** molecules[91–93], though the vanadyl unit adsorbs either with the O atom pointing towards the substrate or facing away from it.[94,95] This feature is also encountered on non-metallic decoupling layers.[92,93] Hydrogen-free porphyrinoids like the coppertetrakis(thiadiazole)porphyrazine (**[Cu(TTDPz)]**, Figure 4.4**c**)[96] showed slightly better T_m than **[Cu(Pc)]**, but due to their low solubility and crystallinity, no real advantages were visible after removing hydrogen atoms. Indeed, the hydrogen-

rich vanadyltetraphenylporphyrin **([VO(TPP)]** **Figure 4.4d**) turned out to almost match the quantum coherence properties of the above-mentioned porphyrinoid systems.[97] Presumably, the limiting factor in porphyrinoid systems regarding coherence is the presence of the coordinating nitrogen atoms of the core porphyrin ring.

Since porphyrins offer the advantage of being more soluble and versatile from a chemical point of view than phthalocyanines, they became an interesting system to synthesize and study. It is possible to functionalize porphyrins at various positions in the ligand.[98] The chemical functionalization of porphyrins will be described in more detail in Chapter 5. Concerning complexes carrying more than one paramagnetic center, tree hybrid Cu^{2+}-porphyrin, and Ti^{3+}pentacarbonyl bimetallic complex[99] with an oligo-*p*-phenyleneethylynylene spacer showed only a very small exchange interaction. On the other hand, quantum state tomography experiments revealed that coherence times are governed by nearby nuclear spins and not the electron spins of the other paramagnetic site. This suggests that one can shorten the intramolecular spin-spin distance in a bimetallic complex to enhance the exchange interaction without worrying about decreasing too much T_m. The nearest Cu^{2+}-Ti^{3+} intramolecular distance is about 11.6 Å in the complex with the shortest *p*-phenyleneethylynylene spacer.

Directly linked porphyrin dimers show an intramolecular metal-metal distance from 8.4 to 9.6 Å, and some paramagnetic bi-metallic porphyrins have already been studied.[100,101] To clarify things, in **Figure 4.5**, the chemical structure of five possible directly linked porphyrin dimers is shown. The monomeric porphyrin core unit consists of three positions on the carbon in which a direct linkage to another porphyrin is possible.

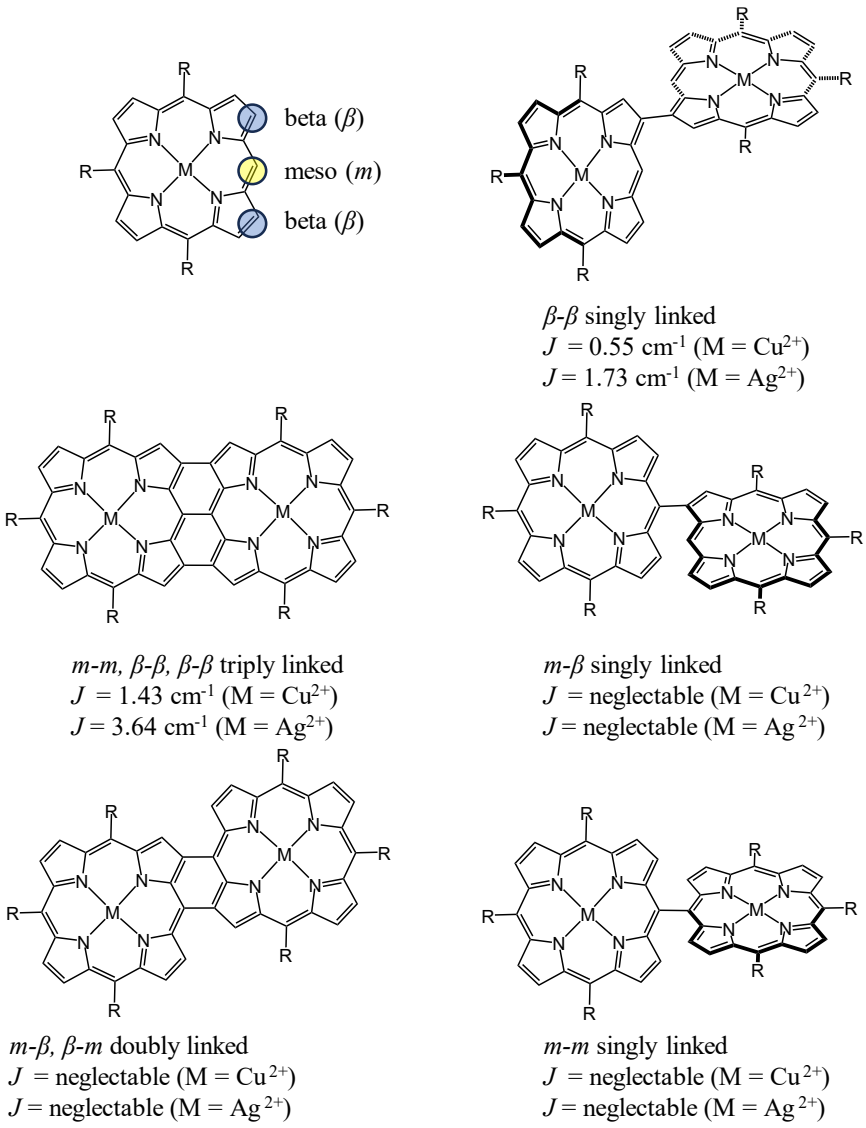

Figure 4.5: Five variations of directly linked porphyrin dimers, in which either complete flat (left) or tilted (right) dimers are obtained. The exchange parameter also depends on the metal center and the overall orientation of the single porphyrin units. The listed *J*-values were taken from.[101]

The beta (*β*) carbons are the two carbons of the pyrrolic unit of the porphyrin, whereas the meso (*m*) carbon is the bridging carbon between two pyrrolic units (see **Figure 4.5**). Synthetically accessible dimers are either singly linked and tilted *m-m*, *m-β*, *β-β* porphyrins, or flat *m-β*, *β-m* doubly linked porphyrins, along with triply linked *m-m*,

β-β, *β-β*, porphyrins (**Figure 4.5**). As it turns out, the coordination center and the linkage are crucial in tuning the intramolecular spin-spin interactions, as evidenced by *Osuka* and co-workers.[101] In their study, they synthesized both homometallic Cu^{2+} and Ag^{2+} dimers in all five linkage variations and determined their exchange interaction by static magnetic measurements. These measurements showed that measurable *J*'s are only obtained when the two *β*-carbons of each porphyrin unit are bonded. Negligible interactions are observed for singly linked *m-m* and *m- β* porphyrins and doubly linked *m-β*, *β-m* porphyrins. DFT calculations highlighted the influence of the magnetic orbitals in determining the strength of *J*.[101] The magnetic orbitals in both square planar Cu^{2+} and Ag^{2+}-complexes are the d_{x2-y2} orbitals. These orbitals point at the four pyrrolic nitrogen of the porphyrin core, meaning they can promote the delocalization of the unpaired electrons into the porphyrinic core unit through σ-bonding. Due to the closer proximity of the d_{x2-y2} orbital at the *β*-position in the porphyrin, spin density from the unpaired electron was only found at these positions but not at the *m* one. Interestingly, Ag^{2+} porphyrin dimers show stronger *J* than the analogous Cu^{2+} dimers. The exact values of *J* are listed in **Figure 4.5**. The authors explained the different *J*'s by means of metal-ion size. The larger is the metal ion, the higher is the value of *J*.

It should be noted that the directly linked porphyrin dimers presented here were not proposed as potential two-qubit systems, but it is clear how much potential they have because of their magnetic properties. However, further studies on the exchange coupling in paramagnetic porphyrin dimers are necessary. A better understanding can be achieved if the crystal structures are available. Also, paramagnetic dimers with other metal ions (like $[VO]^{2+}$) could be explored since the magnetic orbital differs from the d_{x2-y2} orbital. Other delocalization pathways between metal-center and porphyrin core units might be exploited. Very little is known about paramagnetic heterometallic porphyrin dimers. The unexplored potential of these systems motivated the research conducted in this PhD thesis work aimed at synthesizing and characterizing magnetic porphyrin dimers, hoping to identify the molecule that could be operated as a quantum gate. Efforts along this line and the

results obtained will be discussed in the following chapters, briefly introducing the properties of this class of ligands first.

5 Porphyrins: The promising ligand for a possible breakthrough

The porphyrin ligand is a macrocycle containing 22-π electrons. From the chemical point of view, porphyrin is a cyclic tetrapyrrole linked together by four methine bridges. Further, the ring closure produces two pyrrolic and two imidic nitrogens. This leaves the inner core of the porphyrin with two pyrrolic hydrogens, which can be released to metalize the porphyrin with various metals. This chapter is divided into two major sections. In the first section, we will delve into the structure and physical properties of porphyrins. Porphyrins are not flat as might be expected for an aromatic system. We will emphasize the impact of porphyrin plane deformation on their physical properties and examine how the coordinating metal alters their structural characteristics. The metalation and chemical functionalization of porphyrins will be discussed in Section 5.2.

5.1 Structures and physical properties of porphyrins

Electronic repulsion caused by spin densities from the coordinating metal-ion or core ring substituent leads to both an in-plane and out-of-plane porphyrin distortion. The deformation of the porphyrin plane can be classified according to the dominant out-of-plane normal mode. **Figure 5.1** shows the four most common out-of-plane distortion types found in monomeric porphyrin systems. Note that this section will give only a brief overview of the deformation of porphyrins since only some aspects of the porphyrin distortions are important for the magnetic properties of their complexes. A more detailed discussion regarding porphyrin distortion can be found in the literature.[102–106] The saddle-like distortion (**Figure 5.1a**) is common in highly substituted porphyrins, *i.e.*, both functionalized in the *m* and *β* positions. The saddle-like distortion in porphyrins, observed in both free base and some metalated forms, increases with a greater number of substitutions, with free base porphyrins typically

exhibiting a higher degree of distortion than metalated ones. Ruffle-shaped porphyrins (**Figure 5.1b**) can be promoted by inserting small metal ions in the porphyrin core, such as Ni^{2+} ions. Large metal ions, like lanthanides, on the other hand, promote the creation of dome-shaped porphyrins (**Figure 5.1c**). When two M^{+} type ions are inserted into the porphyrin core, a distinct porphyrin shape emerges, where one imidic and one pyrrolic nitrogen coordinate with one metal while the other two nitrogens coordinate with the other metal, causing two nitrogens to rise and the other two to lower, resulting in a wave-like porphyrin shape (**Figure 5.1d**).

An elegant way for quantifying porphyrin deformations is using the normal coordinate structural decomposition (NSD) analysis[102,105,106] presented in **Figure 5.1** right. Using NSD, one can see a reoccurring pattern for each dominant vibrational mode. In other words, the NSD analysis allows one to convert the atom position from a cartesian coordinate to a cylindrical one. The *y*-axis represents the *z*-position of the C or N atoms in the porphyrin; thus, when plotted against the cylindrical coordinate, it shows the porphyrin unit as a linear tetrapyrrole. The positions are given as a difference between the coordinates of the analyzed porphyrin and a reference, copper tetraphenylporphyrin (**[Cu(TPP)]**), which is flat.[107] This means that the z-position values correspond to the deviation (in Å) from a perfect plane. Even though the porphyrin plane distortion was studied extensively, it is still impossible to predict a porphyrin's shape because the crystallization conditions also determine the porphyrin shape. Polymorph metalloporphyrins can have different forms, even though they are chemically identical. One example is the aforementioned **[Cu(TPP)]** molecule, which can show a perfectly flat porphyrin plane[107] or saddle-like distortion.[108]

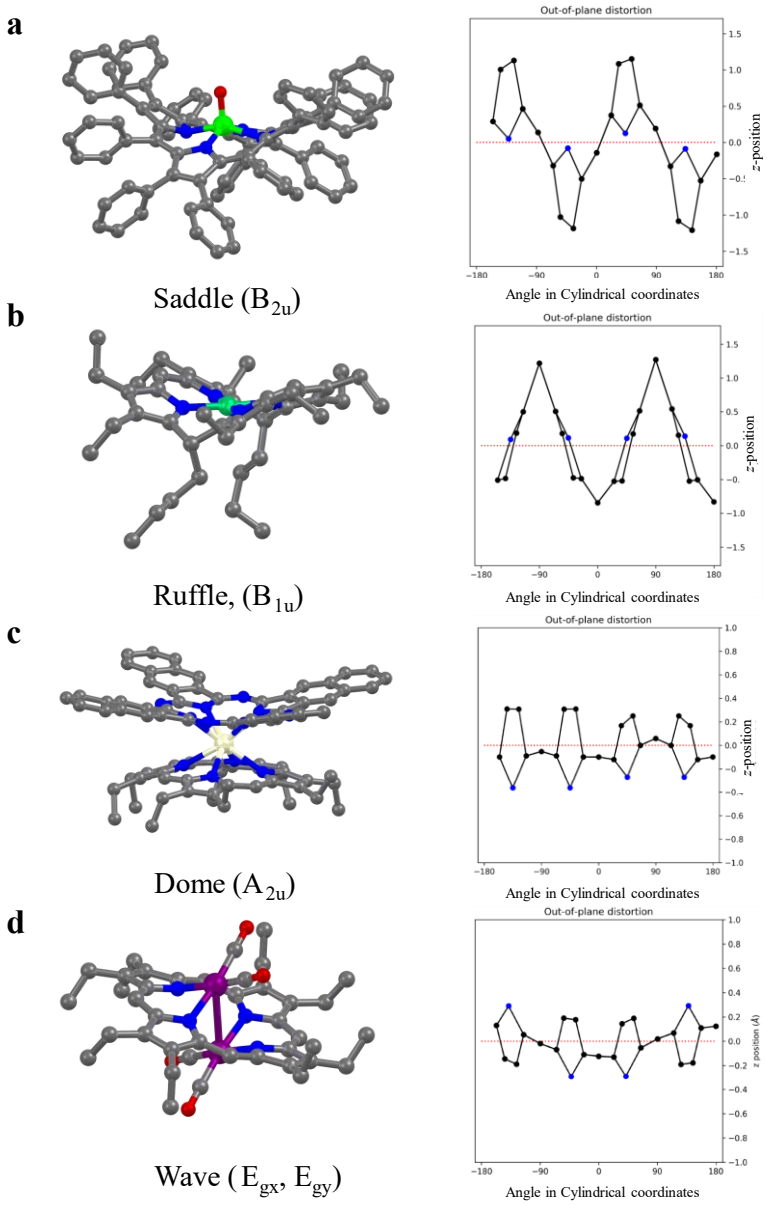

Figure 5.1: Examples of the four most dominant out-of-plane modes shown on a vanadylporphyrin[109] (Saddle B_{2u}, **a**), nickelporphyrin[110] (Ruffle B_{1u}, **b**) ceriumporphyrin[111] (Dome A_{2u}, **c**), and rutheniumporhyrin[112] (Wave A_{gx}, **d**). When plotting the position of the atom coordinates against the angle in cylindrical coordinates, the four out-of-plane contributions can be quantitatively distinguished (right). The dotted line visible in all four graphs is the *z*-position of the reference porphyrin [Cu(TPP)]. Color code: dark grey = C, red = O, blue = N, green = V^{4+}, dark green = Ni^{2+}, white = Ce^{4+}, violet = Ru^{1+}. Hydrogens are omitted for clarity.

The out-of-plane distortion brings several changes in the chemical and physical properties of porphyrins. For instance, the pyrrolic hydrogens in strong saddle-distorted porphyrins show highly catalytic properties.[113] The changes in electronic properties are visible even with the naked eye. Porphyrin monomers usually have a strong purple color in various apolar and polar solvents. But when porphyrin planes are highly distorted, the color of porphyrin solutions changes to green, indicating a change in electronic properties.[109]

To understand the electron properties in porphyrins, it is worth studying electronic transitions with UV/Vis spectroscopy. **Figure 5.2** shows the UV/Vis spectra of a free base (left) and metalated porphyrin (right). Characteristic in both free-base and metalloporphyrin is the B-(also called *Soret*) band visible in the wavelength range from 380 to 430 nm.[114] This band is caused by the transitions from the electronic singlet ground state to the second singlet excited state ($S_0 \rightarrow S_2$) that involves π and π*-molecular orbitals, abundant in the porphyrin aromatic system. The second region of interest in the porphyrin UV/Vis spectrum is the Q-band region, which lies between 500-700 nm in most porphyrin systems.[114] The bands are caused by the $S_0 \rightarrow S_1$ transitions. These transitions are much broader and lower in intensity than the *Soret* transition. When comparing the Q-band region of a free-base and metalated porphyrin (**Figure 5.2**), one can see that four bands are visible in the first case, while only two bands can be seen in the second case.

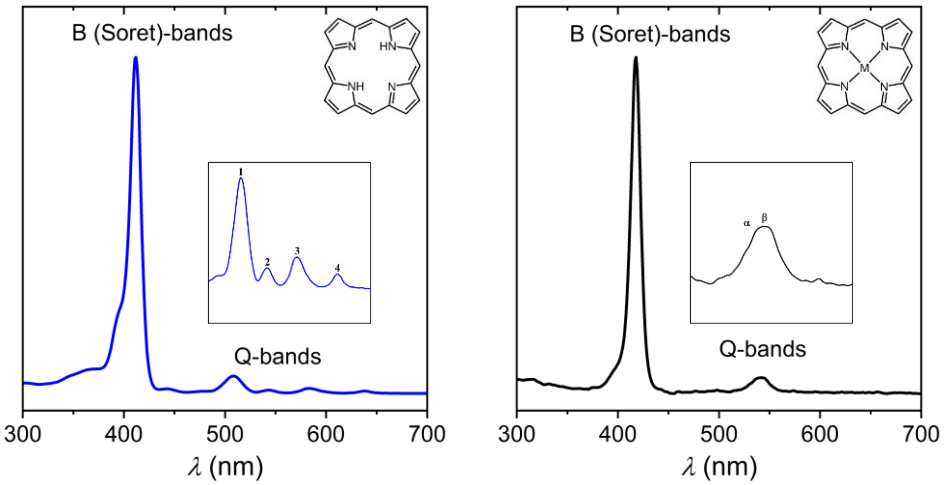

Figure 5.2: UV/Vis spectra of a free base (left, blue line) and metalized (right, black line) porphyrin. The B-band (also called *Soret*-band, between 400-450 nm) and the Q-band region (between 500-700 nm) are marked in the spectra. In the free base porphyrin, four transitions are visible due to the N-H bond symmetry break. The symmetry is restored by removing the pyrrolic hydrogens, which turn the visible bands into one (metalated porphyrin, right spectrum).

A simple consideration of molecular symmetry can explain these differences. While a perfectly flat porphyrin has a D_{4h} symmetry, the steric repulsion caused by the pyrrolic nitrogens induces a saddle-like distortion, thus reducing the symmetry to C_{2v}.[115] This enables the probability of transitions between more vibration energy states due to the removed degeneracy of the states. In highly distorted porphyrins, the removal of degeneration is much more pronounced, making the redshift even larger, thus leading to a change in color. The insertion of the metal inside the porphyrin ring enhances the symmetry once again, thus reducing transition probabilities. The transitions in D_{4h} porphyrins can be graphically described with *Gouterman's* four orbital models.[116,117] *Gouterman's* diagram is shown in **Figure 5.3**. This model focuses on the two highest occupied and two lowest unoccupied molecular orbitals of the porphyrins. The HOMO and HOMO-1 orbitals are the A_{1u} and A_{2u} orbitals, whereas the LUMO and LUMO+1 are the E_{gx} and E_{gy} molecular orbitals. As shown in **Figure 5.3**, transitions occur between the $A_{1u} \rightarrow E_g$ orbitals that give rise to the *Soret* bands, and the $A_{2u} \rightarrow E_g$ transitions give rise to the Q-bands.

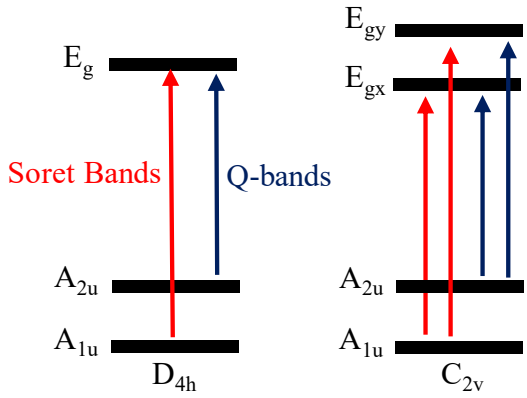

Figure 5.3: The four orbital models proposed by *Gouterman* to explain the *Soret* (red line) and Q-bands (dark blue line) in a flat porphyrin with D_{4h} symmetry (left) and C_{2v} symmetry (right). In porphyrin dimers or highly distorted porphyrins, the splitting in the E_g states is more pronounced.

Two *Soret* and four Q-bands should be visible in a C_{2v} symmetrical porphyrin (**Figure 5.2**, free base porphyrin UV/Vis spectrum). Due to spectral resolution, in most cases, the second Soret is not visible. In tilted and directly linked porphyrin dimers, where symmetry effects and the different transition dipole moments affect the electronic transitions of the second titled porphyrin unit, the *Gouterman* model only partially explains the electronic transitions. The result of the tilted porphyrin unit on the UV/Vis spectrum is shown in **Figure 5.4**. The second *Soret*-band is visible now, and indeed, singly directly linked porphyrin dimer solutions are orange. *M. Kasha*[118] was the first to predict that two excitons (in this case, two porphyrin units) in close proximity will result in an exciton coupling, and thus, electronic excitation will be delocalized between the two units. This exciton coupling will give rise to two nondegenerate excited states in porphyrin dimers, which results in the formation of parallel and colinear transition dipoles.[119–122] Although the *Gouterman* four orbital model fashionably describes the Soret and Q-bands, it does not predict the intensities of the UV/Vis signals. Indeed, according to the *Gouterman* four orbital model, the UV/Vis signal intensities should be the same. The discrepancy between experimental intensities and expected intensities can be explained by orbital mixing. The orbital

mixing partially cancels the transition dipole moment for the $A_{2u} \rightarrow E_g$ transitions, whereas the $A_{1u} \rightarrow E_g$ transitions are reinforced.

The overall easy manipulation of the electronic states in a porphyrin by simple additional functionalization or metal insertion allows to fully exploit the electronic properties of porphyrins. Porphyrins account for many biological activities and porphyrin derivate chlorophyll as the essential molecule for photosynthesis. Artificial multiporphyrin systems are proposed as electronic tapes,[123] as polarons in organic photovoltaic devices,[124] and as optical wires.[125] However, the research on the magnetic properties of porphyrins still lacks impactful contributions. The tuning of porphyrin distortion and linkage might also induce a change in the magnetic properties of the porphyrin. There are only a few publications regarding the magnetic properties of paramagnetic porphyrins,[44,96,97,126] especially paramagnetic porphyrin dimers.[99–101] But these studies are only a fraction of what was published about their electronic properties. Next, we will discuss the chemical functionalization and the mechanism of porphyrin metalation.

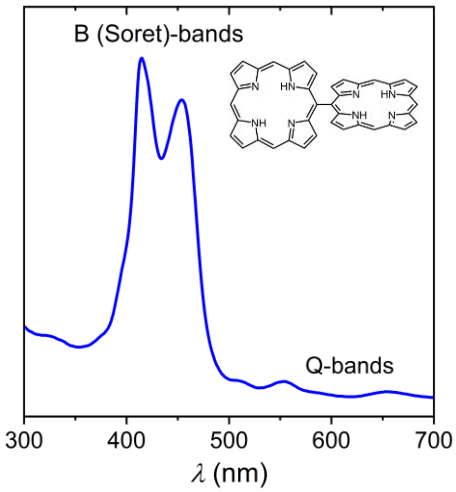

Figure 5.4: UV/Vis spectrum of a free base *m-m* linked porphyrin dimer. According to the *Gouterman* four orbital model, the Soret-band is split whereas four Q-bands should be visible. Note that for the wrong resolution, only two out of four Q-bands can be seen in the spectrum above.

5.2 Metalation and peripherical functionalization of porphyrins

In this section, we will present some important chemical reactions for synthesizing the novel porphyrins reported in this thesis. First, we are going to investigate the metalation of porphyrin cores.

There are two types of mechanisms involved in the complexation of porphyrins. The first one is the *Lewis* acid-base complexation, suggested by *Lavallee,* [127] *Hambright*,[128] and *Tanaka*,[129] which is supported by various kinetic experiments. The first step is a deformation of the porphyrin ring caused by the interaction with a nearby metal salt.

$$H_2P \rightleftharpoons H_2P^*, \tag{5.1}$$

Which subsequently turns into an outer-sphere complexation according to the reaction

$$ML_6 + H_2P^* \rightleftharpoons [ML_6, H_2P^*]^{2+} \tag{5.2}$$

followed by the ligand dissociation, connected with a first and second metal-nitrogen bond formation.

$$[ML_6, H_2P^*]^{2+} \rightleftharpoons [ML_5\text{-}L\text{-}H_2P]^{2+} \rightleftharpoons L5M\text{-}H_2P^{2+}, \tag{5.3}$$

$$L_5M\text{-}H_2P^{2+} \rightleftharpoons L_nM{=}H_2P^{2+} + (5{-}n)L. \tag{5.4}$$

This yields the metalloporphyrin.

$$L_nM{=}H_2P^{2+} \rightleftharpoons MP + L_n + 2H^+. \tag{5.5}$$

These kinetic studies were performed in highly polar solvents, such as DMF, and with bivalent metal cations. Usually, porphyrins are rather apolar and soluble in CH_2Cl_2. Reactions employing DMF are only used when high temperatures are needed to perform reactions.[130] However, metalation reactions with Cu^{2+} and Zn^{2+} can be completed in mild conditions.[131] When possible, attempts are made to avoid DMF, preferring the solvent mixture CH_2Cl_2/CH_3OH. The polar solvent is needed to solubilize the metal salt and, at the same time, to create the solvated M^{2+} complex.[127] Ligand dissociation turned out to be necessary for the coordination of the M^{2+}-ion.

Without delving too much into the details, the second metal-insertion mechanism is based on a redox mechanism.[132] The core hydrogens are reduced, whereas the metal-ion with a positive charge different from 2+ will be oxidized. These reactions are relatively slow, and the exact mechanism has not been fully understood yet. However, there is an interpretation of a metalation redox mechanism on a metal surface (also called direct-metalation).[133]

It is also possible to remove the metal in the porphyrin ring. Theoretically, this can be done by introducing an acid into the metalloporphyrin solution.[127] The strength of the acid needed for the demetallation depends on the metal ion. It was shown that a metal-ion in one of its reduced forms is more likely to dissociate from the porphyrin ring, while metal ions with strong ligand field stabilization tend to form more stable complexes.[127] This is why alkaline metal porphyrins immediately hydrolyze in water. The Zn^{2+} porphyrin complex is much more stable than its alkaline earth counterpart. In this case, the larger charge/radius ratio also plays a vital role in stabilizing the metal complex. However, Zn^{2+} porphyrins are easily demetallized by weak acids because of the lack of crystal field stabilization. However, if a faster reaction is to be performed, trifluoroacetate (TFA) is generally used, as this acid is readily soluble in apolar organic solvents. More stable Ni^{2+} or Cu^{2+} porphyrins need strong acids such as H_2SO_4 to be demetallized.[131]

To discuss the functionalization of the porphyrin core, an introduction to the numbering of the porphyrin carbon rings is needed. In porphyrins, all four *m*-positions are numbered with 5, 10, 15, and 20, whereas the additional β-positions are

labeled with 2, 3, 7, 8, 12, 13, 17, and 18. All hydrogen-free carbons are called *α*-carbons and are labeled as 1, 4, 6, 9, 11, 14, 16, and 19 (see **Scheme 5.1a**).[134] The porphyrin ring has, in principle, four *m* and eight *β* positions that can be functionalized. When it comes to the halogenation of the porphyrin ring, the mechanism is an electrophilic aromatic substitution, following the same reaction as the halogenation of other aromatic systems. Bromination reactions are widely exploited and can be performed both at the *m* or *β*-position, with the first one being the more reactive position. The higher reactivity of the *m*-position can be explained by the Fleischer-Webb (F-B) hypothesis,[135] which suggests that the *β*-positions are rather olefinic than aromatic, making an electrophilic aromatic substitution quite challenging. The *m* bromination, therefore, works quite smoothly without much synthetic effort. Problems may arise during the purification. **Scheme 5.1** shows the bromination reaction of a 5,15-diphenyporphyrin (H_2DPP) using various bromination reagents. The best results for the *m*-bromination were achieved by using N-bromosuccinimide (NBS) as the bromination agent in chloroform at 0°C (**Scheme 5.1b**).[136] Pyridine is added to act as an H^+ scavenger. With two equivalents of NBS, a mixture of mono- and dibrominated species is obtained, with the monobromated ones making up 50 % of the product. The yield of the dibrominated species is usually much lower (20 %), and some unreacted porphyrin is also present. Enhancing the reaction times or using more than 4 eq. of NBS, the fully dibrominated species is obtained with almost quantitative yields.[136,137] Using 10, 15, 20-triphenylporphyrin (H_2TrPP) leads selectively to forming 5-bromo-10,15,20-triphenylporphyrin in quantitative yields. Metal complexes of porphyrins do not show any significant change in the reactivity compared to their free-base counterpart, as similar yields are achieved with various metalated porphyrins.[136–138]

For the realization of *β*-substituted brominated porphyrins, Br_2 is employed instead of NBS.[139] The reaction with Br_2 is not very selective, and one obtains the fully brominated porphyrin species as the main product. This strategy is used for tetraphenylporphyrins (H_2TPP, **Scheme 5.1**) to obtain a tetrabromo-tetraphenyl porphyrin (**4**, **Scheme 5.1**).[139] Selective monobromination in H_2TPP can be achieved with NBS (**3**, **Scheme 5.1**).[140] In this case, however, the reaction mixture

is brought into reflux. The same solvent and acid scavenger are used for the bromination in *m*-position.

Iodination reactions are also possible in the *m* or *β*-position of the porphyrin. Reactions with iodine are usually characterized by lower yield, whether a mono- or poly-iodinated porphyrin is desired.[141] The formation of iodoaromatics, starting from I_2, leads to the formation of HI, a strong reducing agent, thus reverting the iodination reaction. Oxidizing agents are therefore needed to limit the reducing effect of IH. Using more electrophilic iodine compounds or the presence of acids in the reaction mixture (for creating the I^+ ion) also promotes the iodination reaction. There are only a few examples available on porphyrin iodination in the literature. Still, the procedures are mainly similar to those reported for the bromination, only that N-iodosuccinimide (NIS) is used instead of NBS.[142] Moreover for faster reactions with higher yield it is possible to use I_2 powders for the iodination, in addition to an oxidative agent like phenyliodo-bis-trifluoroacetate (PIFA)[142] or silver(I)hexafluorophosphate ($AgPF_6$).[143] While bromination in *β*-position is easily possible, using iodine poses problems. Fully iodinated porphyrins are synthesized from scratch, meaning that tetraiodoporphyrin are obtained from the condensation of pyrrole unit that has at least one iodine unit in its meso position.[144] Selectively, iodination in *β*-position is achieved using iodine salts combined with H_2O_2.[145]

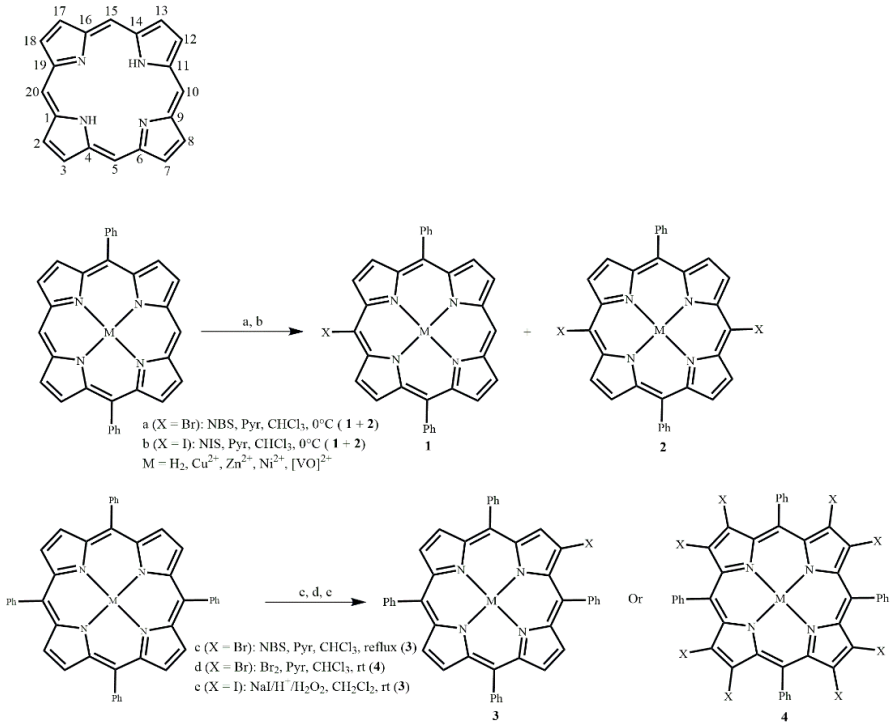

Scheme 5.1: Numbering carbon atoms in the porphyrin ring (top). Various porphyrin halogenations in *m* (middle) and *β*-position (bottom) are reported in the literature.

In any case, the functionalization of porphyrins with halogens brings many advantages. For instance, starting from them, it is possible to exploit other reaction paths to further functionalize the porphyrin. *M. J. Therien*'s working group exploited the reactivity of halogenated porphyrins and synthesized so-called *Suzuki*-porphyrins, the first pinacolborane-based porphyrins.[146] The porphyrins were realized via a *Suzuki-Miyaura*-coupling reaction.[147] It is well known that Pd^0 catalyzes reactions between halogenated and borylated organic compounds (alkyl or aromatic), forming a C-C bond linkage. Functionalizing porphyrin with pinacolborane (HBin, **Scheme 5.2**) will, therefore, result in the possibility of the creation of directly linked porphyrins in both *m* and *β*-positions. Indeed, some years later, after the discovery of the *Suzuki*-porphyrins, the working group of *Osuka* started to develop porphyrin dimers via a *Suzuki* cross-coupling reaction (**Scheme 5.3**).[148,149] The reaction mechanism follows the exact path reported in *Miyaura* and *Suzuki's* original

paper.[147] Cross-coupling reactions at the *β*-positions are also reported.[150,151] These porphyrin dimers might be relevant for electro-chiral applications, as one introduces axial chirality into the porphyrin.[152]

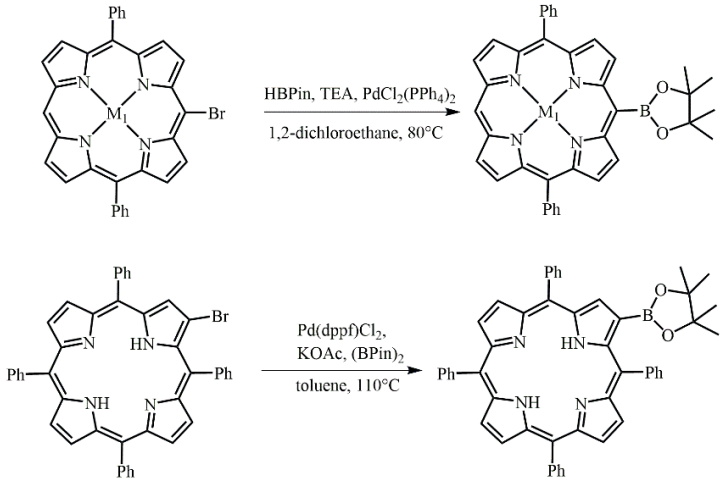

Scheme 5.2: Examples of *Suzuki-Miyaura* cross-couplings on monomeric porphyrin species at *m* and *β*-position found in literature.

Osuka's working group also developed different approaches for realizing porphyrin dimers. These reactions were based on the oxidative coupling between two porphyrins not functionalized in the peripherical positions (**Scheme 5.3**). The coupling reactions were extremely efficient when working with Cu^{2+}, Ni^{2+}, and especially Zn^{2+}-porphyrins. These types of reactions require an oxidative coupling reagent.[153] The first paper on directly linked *m-m*-bonded porphyrins was published in 1997, where $AgPF_6$ was used as an oxidative coupling agent on a 5,15-diaryl-Zn^{2+}-porphyrin (**Scheme 5.3**).[154] The trimer, tetramer, and other oligomeric species of the directly linked *m-m* porphyrins were isolated after purification with size-exclusion chromatography. These oligomers turned out to be very interesting for further studies of the electronic properties of complex porphyrinic systems because they offered the opportunity to gain insight into the energy-transfer mechanism of linear porphyrins.[148,155,156] Upon exploring other oxidizing agents, *Osuka's* working group

found that the use of scandiumtriflate ($Sc(OTf)_3$) combined with 2,3-dichloro-5,6-dicyano-1,4-benzoquinone (DDQ) leads to the formation of triply linked porphyrins (**Scheme 5.4**)[157,158], like the one mentioned in Chapter 4 (see **Figure 4.5**). Doubly linked porphyrins are also obtained by using tris(4-bromophenyl)aminium hexachloroantimonate (BAHA) (**Scheme 5.4**).[159] These doubly linked porphyrins fall beyond the scope of this thesis, so they will be mentioned but will not be discussed further.

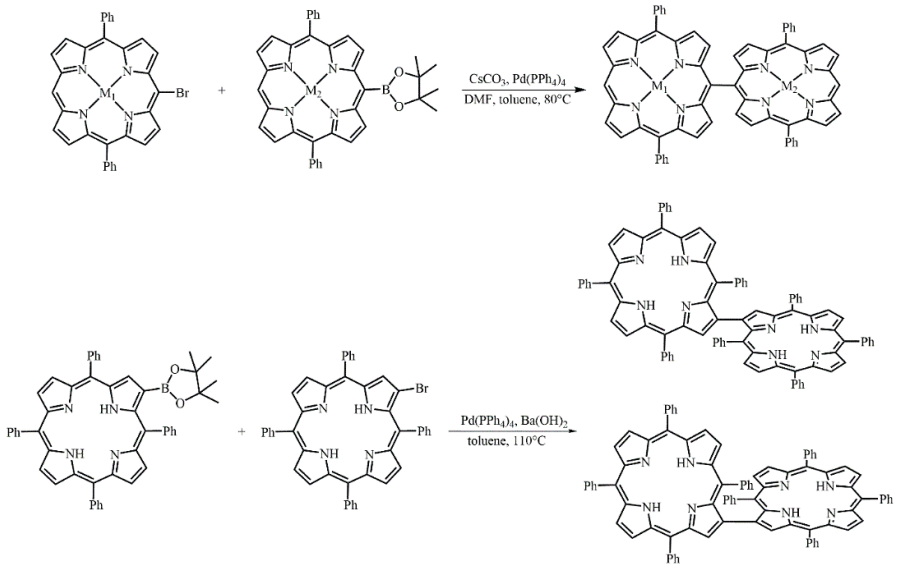

Scheme 5.3: *Suzuki-Miyaura* cross-couplings on dimeric porphyrins at the *m* (top) and *β*-positions (bottom). These kinds of reactions have many advantages since they can be used to selectively synthesis the singly linked porphyrins, and it is possible to create homometallic porphyrin dimers. The *β*-*β* linked porphyrin dimers are axially chiral.

Similar results are obtained using nonmetallic oxidizing agents like the PIFA molecule containing hypervalent I^{3+}.[160,161] PIFA offers the advantage of being non-toxic, soluble in apolar and polar solvents, and relatively stable. The formation of singly *m*-*β* or *m*-*m* turned out to be metal-dependent.[158,161] This implies that local electron density in various positions is a key factor. In the oxidative coupling

mechanism, the first step forms a radical cation at the porphyrin ring. The newly formed radical cation will show a HOMO with orbital symmetry, either A_{1u} or A_{2u}. A_{1u} HOMOs show a node at the meso position, whereas the A_{2u} HOMO has a significant spin density at the *m* position but almost no spin density at the *β*-positions.[157,158,161,162] Cu^{2+}, Ni^{2+}, and Pd^{2+} porphyrin complexes consist of A_{1u}-HOMOs, and therefore *β*, linked porphyrin dimers are favored during an oxidative coupling reaction.[158] On the other hand, Mg^{2+} or $Zn^{2+,}$ having A_{2u}-HOMOs instead, form mostly *m*-*m* linked porphyrin dimers under the abovementioned conditions.[158] Interestingly, some kinds of Zn^{2+}-porphyrins show a mixture of *m*-*β* and *m*-*m* linked porphyrin dimers under the reaction with Ag^{+}-salts[163] because, in the case of Zn^{2+}-porphyrins, the energy states of the A_{1u} and A_{2u} orbitals are very close in energy. Upon the introduction of electron-donating groups, the selective formation of *m*-*m* linked porphyrins is observed.[163] These results suggest that introducing the appropriate functional group can affect the HOMO energy levels, leading to changes in the reactivity of peripheral positions.

The conversion from singly linked porphyrins to triply linked ones follows the reaction mechanism of an oxidative ring closure (ODRC).[164] This conversion is possible if the metalloporphyrin shows a low first oxidation potential and the oxidation agent is strong enough.[161] In particular, the hybrid $Sc(OTf)_3$/DDQ oxidation approach is very efficient in creating triply-linked flat porphyrin dimers.[158] This lies in the enhanced oxidation ability of DDQ when its ion interacts with $Sc(OTf)_3$.[157] Similar results can be obtained when an excess of PIFA is used for the oxidation coupling reaction. It was shown that Zn^{2+}-porphyrins are easily converted to triply linked porphyrins upon treatment of the reaction mixture with an excess of PIFA in CH_2Cl_2 at −78°C (**Scheme 5.4**). Other metalloporphyrins (Ni^{2+}, Cu^{2+}, and Pd^{2+}) resulted in the formation of only *m*-*m*-singly linked porphyrins[161] in the conditions specified above. The selective synthesis of doubly or triply linked porphyrins was only achieved by modifying the previously introduced reaction by adding $BF_3{\cdot}Et_2O$ to the reaction mixture.[165]

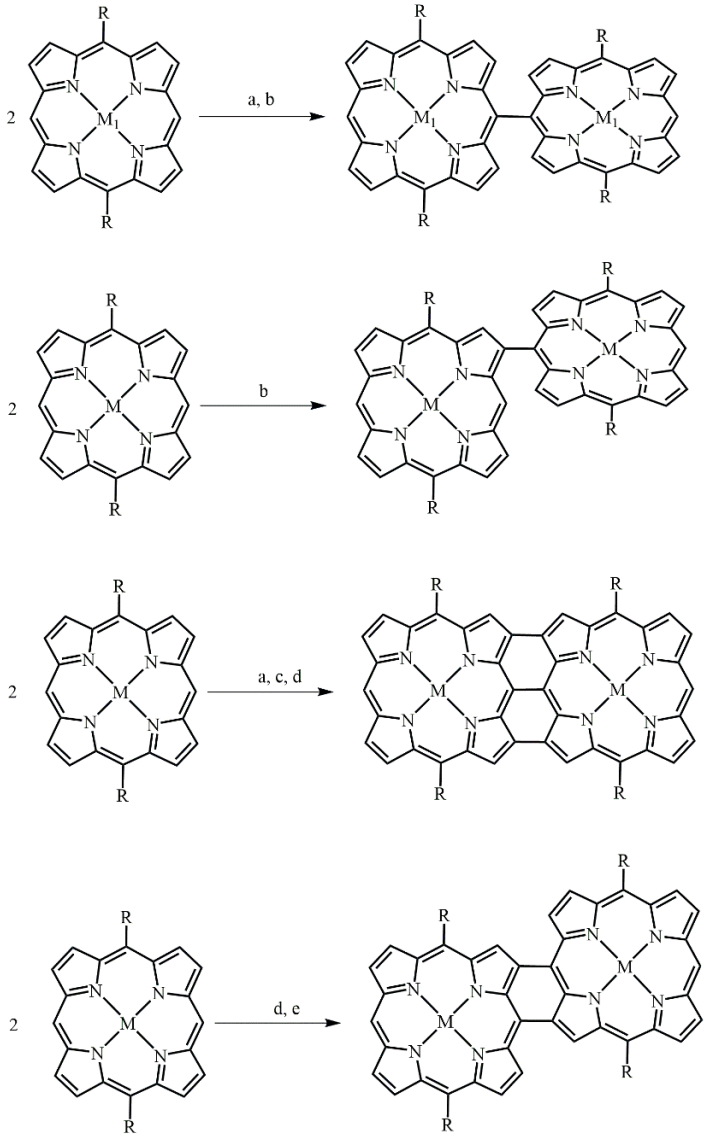

Scheme 5.4: Oxidative coupling reactions reported in the literature[150,158,159,162,165] of various metalloporphyrins for realizing homometallic singly, doubly, or triply linked porphyrins.

Coupling reactions can also be generated on the surface (**Scheme 5.5**). It was shown that *Ullman*-couplings (reductive coupling reaction) on surfaces using bromo-porphyrins are possible.[166] Thus, following the deposition of a porphyrin building block, the coupling reaction on the surface can be induced via thermal annealing. Moreover, it was shown that coupling with unfactionalized porphyrins is also possible on the surface,[167] though the generation of radical species might be possible if a cyclodehydrogenation reaction occurs. This would lead to the formation of an open-shell porphyrin with one delocalized radical that might change the magnetic properties of the deposited porphyrin.[168–170]

Overall, thanks to the various possibilities of functionalizing the porphyrinic peripheric positions, porphyrins are suitable for many applications. This versatility also makes them relevant to the field of QIP. To the best of our knowledge, the chemistry of vanadyl and porphyrins, along with their magnetic properties, has been described only in a few papers.[171,172] The following four chapters will present the most relevant results in this direction obtained during the three years of this PhD.

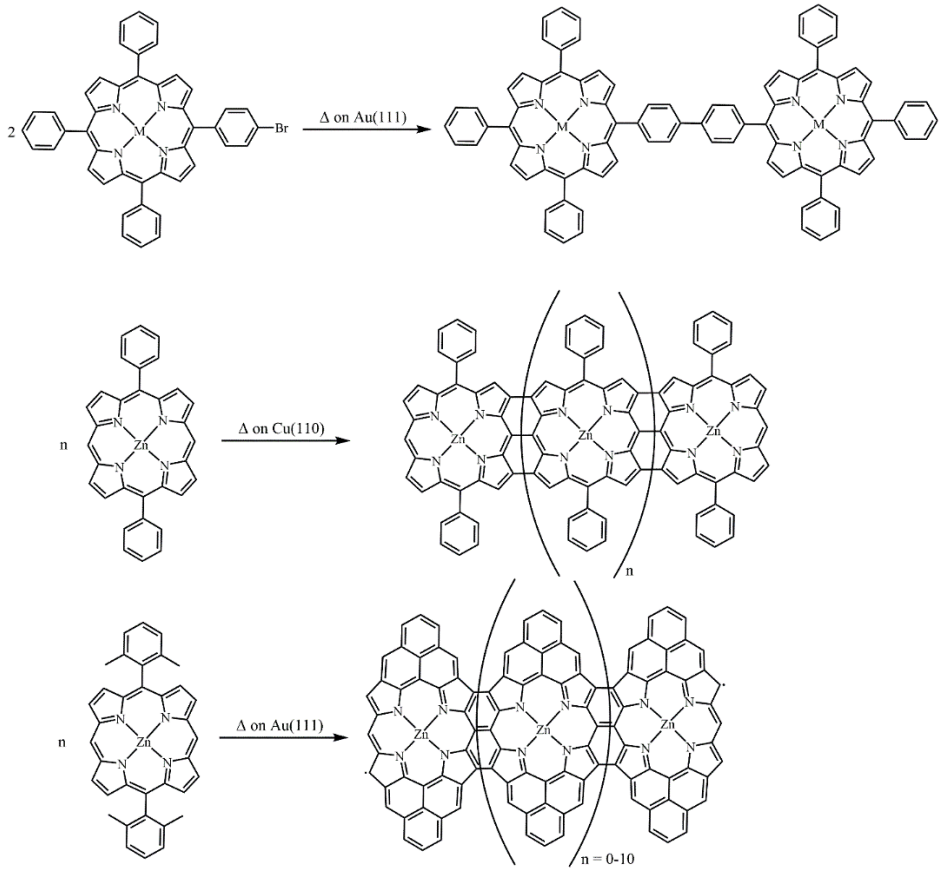

Scheme 5.5: Examples of surface-induced coupling reactions after thermal annealing. Thermal annealing of Bromo-tetraphenylporphyrins (top) induces an *Ullman*-coupling.[166] Diphenylporphyrins (middle) will react after thermal annealing thanks to a surface-mediated organometallic bond.[167] The presence of sp^3-carbons on a peripherical position of the porphyrins (bottom) will give rise to a cyclodehydrogenation that leads to the creation of surface stabilized radicals.[169]

6 **[VO(TrPP)]$_2$**: A homometallic porphyrin dimer as a promising candidate for a two-qubit quantum gate

In the previous chapters, it was shown that for a two-qubit architecture, weak exchange coupled bimetallic complexes that maintain a long coherence time and single spin addressability are interesting. In this framework, dimeric porphyrin-ligands and their metal complexes are potential candidates to take into consideration because porphyrin metal complexes have been reported to have considerable decoherence times,[57,97,126,173] and the two macrocycle units in directly linked porphyrin dimers adopt a tilted geometry which can allow single spin addressability by exploiting the anisotropy of single ion magnetic interactions. On the other hand, the exchange interaction in these systems has been studied only moderately in the literature. It was therefore decided to synthesize and investigate a novel bisporphyrin vanadyl complexes (bis-oxo(10,15,20-triphenylporphyrinato-5yl-)vanadium(IV) (**[VO(TrPP)]$_2$**), to combine the interesting properties of porphyrins with the good coherence times characteristic of their vanadyl complexes in an exchange-coupled system.[97,174]

Sections 6.1 to 6.6 will show the synthesis, crystallographic characterization, EPR, and DFT-calculations performed on the synthesized **[VO(TrPP)]$_2$** complex, along with identifying transitions, allowing individual addressing of the spins.

6.1 Synthesis of **[VO(TrPP)]$_2$**

The realization of homometallic porphyrin dimers follows a synthetic two-step approach, in which we first have to synthesize the monomeric oxo-(5,10,15-triphenylporphyrinato)vanadium(IV) (**[VO(TrPP)]**) compound. **[VO(TrPP)]** was synthesized by slightly modifying a previously reported procedure.[97] The reaction of the free H_2TrPP ligand with the vanadyl precursor [VO(acac)$_2$] (acac =

acetylacetonate) was conducted in phenol (PhOH) as reported in **Scheme 6.1a**. The dimer **[VO(TrPP)]$_2$** was then obtained by performing an oxidative coupling reaction on **[VO(TrPP)]**, in analogy to literature reports for other metal derivatives.[161] Detailed synthetic procedures with all characterizations can be found in Chapter 11. Among the different strategies reported in the literature to obtain *m-m* linked metal porphyrin complexes,[101,175] the use of (bis(trifluoroacetoxy)iodo)benzene (PIFA) as an oxidative coupling reagent recently turned out to be a good alternative to commonly used silver(I) hexafluorophosphate ($AgPF_6$),[154] Sc^{3+}-triflate ($Sc(OTf)_3$),[157] and Au^{3+} chloride/Ag^+ triflate ($AuCl_3$/AgOTf) mixtures.[163] Indeed, the PIFA reactant is cheaper, and, being metal-free, it does not interfere with the magnetic characterization of the final product. Previous studies showed that PIFA leads to highly selective reactions characterized by almost quantitative yields in the case of the reaction of Zn^{2+} and Ni^{2+} porphyrin dimers.[161] The reaction reported in **Scheme 6.1b** was then conducted in dry CH_2Cl_2 under an inert atmosphere by adding PIFA. The reactivity, selectivity, and mechanism of the reaction were explained in Section 5.2 and will not be further discussed here. For the first attempts, it was tried to optimize the reaction by changing the quantity of PIFA used in the reaction. **Table 6.1** shows the list of yields obtained, while different equivalents of PIFA were used for the reaction. Note that for all reactions, the **[VO(TrPP)]** solution at the beginning of the reaction was 2.5 mM.

As explained in Chapter 5, porphyrin monomer solutions are violet and tilted porphyrin dimers appear orange (**Figure 6.1**, left). At first, we tried to follow the reaction just by checking the color of the reaction mixture. However, this method was too inaccurate since porphyrin monomers show a higher molar extinction coefficient (ε) than porphyrin dimers.[158,176] A better monitoring technique consists of either TLC examinations or measuring UV/Vis spectra of the reaction mixture. For the monitoring, a small amount of solution of the reaction mixture was taken, quenched with $NaBH_4$, and then a first TLC-check was performed. If the TLC-check did not result in a clear or satisfactory result, UV/Vis spectra were recorded additionally to clarify the results.

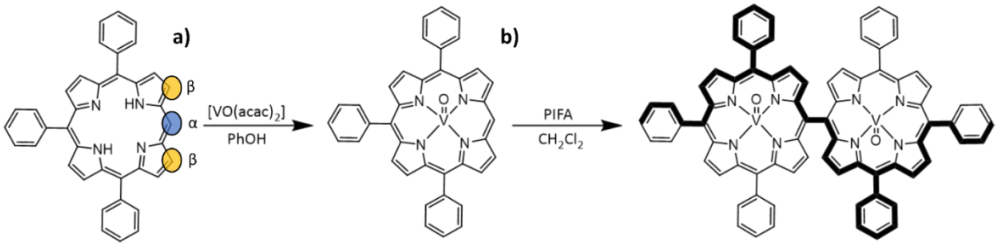

Scheme 6.1. Sketch of the reaction strategies to obtain **[VO(TrPP)] a)** and **[VO(TrPP)]$_2$ b)**. **a)** in PhOH, 165 °C, N_2, 12 h; **b)** anhydrous CH_2Cl_2, -78°C to room temperature, N_2, 40 mins. The ellipsoids on the porphyrin rings highlight the carbons where oxidative coupling reactions are possible in *β* (orange) and *m* (blue) positions.

The first attempt was made by using 0.5 equivalents of PIFA because one PIFA molecule can produce two radical cation porphyrins. However, **[VO(TrPP)]** turned out to be less reactive regarding oxidative couplings than its Zn-porphyrin counterpart.[160,161] Even after five hours of reaction time, according to TLC monitoring, only a small amount of monomer is converted to the desired product. Leaving the reaction mixture stirring overnight at rt did not enhance the yield but led to the decomposition of the porphyrins. Indeed, a growing green spot at the base of the TLC was visible upon enhancing the reaction time, and the reaction mixture turned green. The reasons for this decomposition are still unclear. While PIFA decomposition yields two molecules of TFA, a potent organic acid, there is no literature report of TFA causing demetallation of $[VO]^{2+}$-porphyrins. It is possible that the resulting radical cation is exceptionally stable and does not promote dimer formation. Nonetheless, this shows that the porphyrin should not be left for a long time reacting with PIFA. Radicalized porphyrins could be quenched with the use of a weak base.[177] In this case, however, the addition of a weak base ($NaHCO_3$ or NH_4OH) resulted in the formation of a fine brownish precipitate, insoluble in any organic solvent (CH_3OH, CH_3CN, CH_2Cl_2 Et_2O, etc.). Differences in reactivity were also observed when PIFA was added as a solid or dropwise while solubilized in dry CH_2Cl_2. Optimally, PIFA should be added with the latter method to the **[VO(TrPP)]** solution because it limits the formation of green radical cation porphyrins.

Next, it was tried to use one equivalent of PIFA, and it was shown that the amount of porphyrin dimer in the solution was enhanced. The reaction was quenched after four hours, and the mixture was purified with column chromatography. Most reported literature procedures[160,161] use $CHCl_3$ as an eluent. However, in our case, this did not separate the monomer and dimer porphyrin very well. This might be due to the commercial $CHCl_3$ being stabilized with 1 % ethanol, which changes the polarity of the eluent solution and limits the separation capability of $CHCl_3$ regarding monomer/dimer porphyrin mixtures. Using CH_2Cl_2 instead of $CHCl_3$ helped separate monomer and dimer, but the retention time of the two species remained quite similar. Enhancing the apolarity using hexane/ CH_2Cl_2 mixtures did not improve the separation much. Finally, toluene proved to be the best eluent that was able to separate monomer and dimer (**Figure 6.1**, middle) in a flash silica column (R_f(**[VO(TrPP)]**) = 0.45, R_f (**[VO(TrPP)]$_2$**) = 0.52). The final yield obtained was around 10 % while starting from 20 mg of **[VO(TrPP)]**.

By raising the equivalents of PIFA to 1.5, the final yield was increased to 70 %. This required stopping the reaction after four hours to recover the unreacted monomer before preventing porphyrin decomposition from occurring.

Table 6.1: Attempts of obtaining **[VO(TrPP)]$_2$** from **[VO(TrPP)]** by an oxidative coupling reaction, using various amounts of PIFA. **[VO(TrPP)]** was kept constant at 2.5 mM for each reaction.

[VO(TrPP)]-mass (mg)	Equivalents PIFA	Reaction time (h)	Yield (%)
20	0.5	16	Traces of **[VO(TrPP)]$_2$**,
20	1	4	10
20	1.5	4	70
10	2	2	96

The best results were obtained by using two equivalents of PIFA and stirring the reaction for two h at rt. No reaction with more than two equivalents was tried, though

they might be interesting because they could induce the formation of doubly or triply linked vanadyl porphyrins.

Figure 6.1: Separating funnel showing the water phase (transparent) and organic phase (orange) containing the porphyrin dimer (left). SiO_2-TLC of a mixture of **[VO(TrPP)]$_2$** (orange spot) and **-[VO(TrPP)]** (violet spot) using toluene as eluent (middle). Column packed with flash SiO_2 in which **[VO(TrPP)]$_2$** is purified using toluene as eluent (right).

6.2 Crystal structures of **[VO(TrPP)]** and **[VO(TrPP)]$_2$**

Details of the X-ray diffractometry characterization on single crystals of **[VO(TrPP)]** and **[VO(TrPP)]$_2$** is reported in Section 11.1.

Needle-shaped X-ray quality crystals of the monomeric unit **[VO(TrPP)]** were grown by slow evaporation of a CH_2Cl_2/CH_3CN (98:2) solution. This system crystallizes in the *P2$_1$/c* space group (n. 14) with two pairs of centrosymmetrically related molecules per unit cell (Chapter 11). The asymmetric unit is a single **[VO(TrPP)]** molecular complex in which V^{4+} presents a square pyramidal coordination geometry comprising the four porphyrins N atoms and the apical O atom of the V=O moiety. To better characterize the porphyrin plane distortion modes, the

normal-coordinate structure decomposition (NSD) tool was used.[102,178] The porphyrin ring assumes a distorted ruffle shape,[109,178] B_{1u}. This ruffle shape distortion differs from the planar structure of some *m*- and *β* substituted vanadyl-porphyrin complexes.[97,179–181] Conversely, the distance of the V atom from the plane individuated by the four N atoms, 0.51 Å, is the same as that observed in tetraphenyl derivatives.[28] The mean V-N and V-O distances of 2.06 Å and 1.58 Å are comparable with those observed in similar vanadyl complexes, while the shortest intermolecular VO-VO distance is 9.42 Å. This is about 1.2 Å shorter than the tetraphenyl analogous, as expected for the reduced hindering.

Single crystals of **[VO(TrPP)]$_2$** suitable for X-ray measurements were obtained using two strategies involving toluene as a crystallization solvent. Prism-shaped red to violet crystals were grown by very slow evaporation (~ 1 month) of a toluene solution dispersed in Sephadex® gel. In this case, the dimer (hereafter, **m-[VO(TrPP)]$_2$**) crystallizes in the monoclinic *C2/c* space group (n. 15), with three crystallization toluene molecules per dimer molecule. The molecular structure comprises two **[VO(TrPP)]** units, symmetry-related by the C_2 axis. The asymmetric unit is thus composed of half a dimer unit, one disordered toluene molecule, and half of a disordered toluene molecule lying in a special position (**Figure 6.2b** and **Figure 6.3**). The dihedral angle *θ*, formed by the planes passing through C1-C2-C2' and C2-C2'-C3' (see **Figure 6.2a**) at the porphyrin ring, is about 69° (**Figure 6.2b**). The molecular structure presents an intrinsic disorder of the vanadyl moieties below and above the porphyrin planes, not observed for **[VO(TrPP)]**, with occupancy factors of 85:15. The V1-O1-O1'-V1' tilting angle, *δ*, is ca. 64° (red dashed line in **Figure 6.2b**).

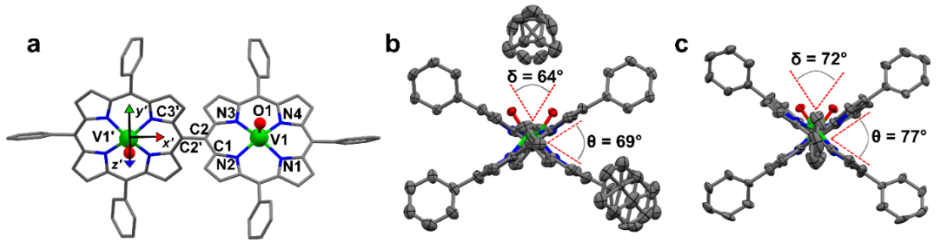

Figure 6.2. **a** Molecular structure of **[VO(TrPP)]$_2$** with labeled atoms. The local *xyz* (not shown for clarity's sake) and *x'y'z'* reference frames are those diagonalizing *g*- and *A*- tensors of the two vanadyl moieties. Primed labels indicate atoms related by the C_2 symmetry axis bisecting the *m-m* bond to non-primed ones b, c View along the *m-m* bond of the **m-[VO(TrPP)]$_2$** and **o-[VO(TrPP)]$_2$** molecules. The dihedral angle, θ, among the porphyrin planes and the torsion angle, δ, between the vanadyl moieties' directions are highlighted by red dashed lines; Atoms in **b**, **c** are represented as thermal ellipsoids at 50 % probability level. Color code: C = gray; N = blue; V = green; O = red. Only the majority configuration of the V=O groups is reported. H-atoms are omitted for clarity.

The intramolecular VO-VO distance is 8.37 Å, while the minimum intermolecular VO-VO distance of 9.70 Å is found between parallel molecules on adjacent layers (Figure 6.4). The porphyrin molecules in **m-[VO(TrPP)]$_2$** are not aligned to any crystallographic axes.

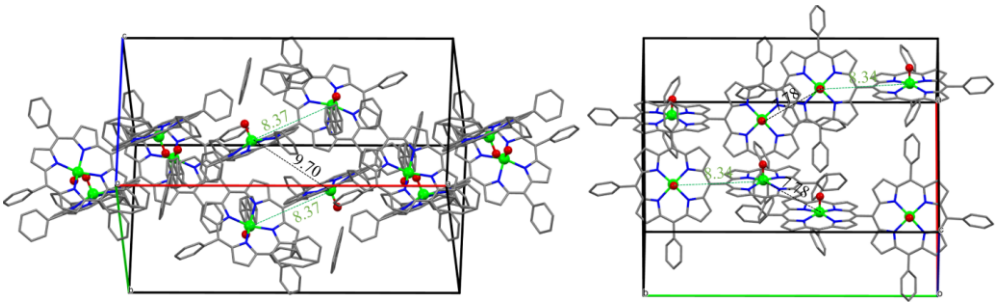

Figure 6.3. Unit cell content of **m-[VO(TrPP)]$_2$** (left) and **o-[VO(TrPP)]$_2$** (right) with the shortest inter (green dashed lines)-and intramolecular (black dashed lines) V-V distances in the crystal labeled. Color code: C = gray; N = blue; V = green; O = red.

As a second crystallization strategy, X-ray quality crystals of **[VO(TrPP)]$_2$** were grown by very slow evaporation of an acetone/toluene (95:5) solution. These crystals were similar in shape, size, and color to those grown in toluene. Still, the system crystallized in the acentric orthorhombic *Ccc2* (n. 37) space group without cocrystallized solvent molecules (hereafter **o-[VO(TrPP)]$_2$**, Figures 6.2**c** and Figure 6.3). Even in this case, the asymmetric unit is composed of one vanadyl-porphyrin unit, and the dimer is generated by the C_2 axis parallel to *c* and perpendicular to the C2-C2' meso-bridging bond. The absence of significative residual electron density suggests an intrinsic porous nature of the material. The molecules are oriented with the C2-C2' bridging bond direction along the crystallographic *b*-axis. An intrinsic disorder in the VO center is also observed in this case, with estimated occupancy factors of 75:25. The tilting of the two porphyrin moieties is higher in **o-[VO(TrPP)]$_2$**, as indicated by both θ and δ angle of about 77° and 72°, respectively. On the other hand, the first coordination sphere does not present any significant difference with respect to **m-[VO(TrPP)]$_2$**, and the intramolecular VO-VO distance (8.37 Å) is also comparable. The closest intermolecular contact for the **o-[VO(TrPP)]$_2$**, *i.e.*, average distance of 7.78 Å considering the VO disorder (Figure 6.3), is shorter than in the previous case, most likely due to the absence of crystallization solvent molecules.

The dominant distortion mode in **m-[VO(TrPP)]$_2$** is the ruffle distortion B_{1u}, and B_{2u} (saddle) for **o-[VO(TrPP)]$_2$** is also found in other A3B type porphyrins.[182–184] The average dihedral angle among the pyrrole planes is 7.41° for **o-[VO(TrPP)]$_2$**, while it is 4.36° for **m-[VO(TrPP)]$_2$** indicating a larger deviation from planarity and a higher degree of distortion in the solvent-free crystal structure **o-[VO(TrPP)]$_2$** than in **m-[VO(TrPP)]$_2$** (Scheme 6.2). The observation of tilting angles significantly different from 90° is not unprecedented in linked porphyrins. At least two reported structures of pentacoordinated Zn^{2+}-porphyrin dimers, including bulky *t*-Bu groups on peripheral positions, are characterized by a dihedral angle of about 72°.[185,186] The dihedral angle, however, cannot be directly correlated to the coordination number of the central ion since at least one previous result reports a pentacoordinated Zn^{2+} system showing a dihedral angle of about 90°.[187]

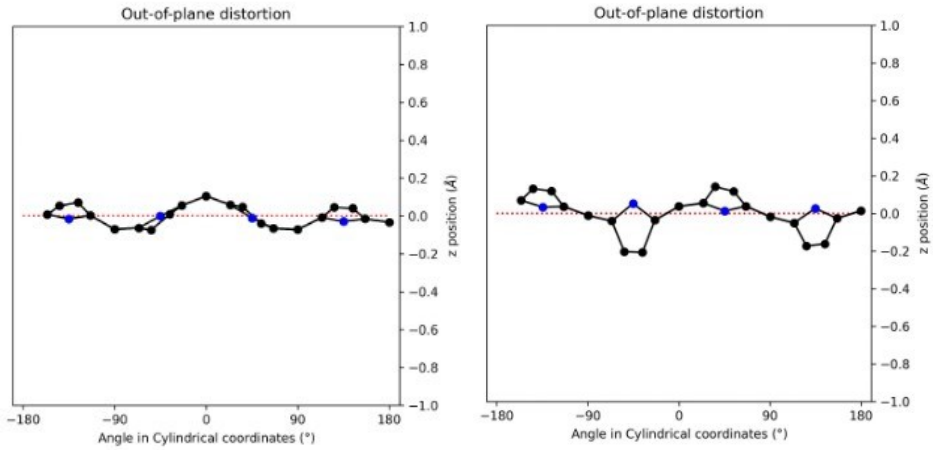

Scheme 6.2: NSD-analysis[102] of **m-[VO(TrPP)]$_2$**(left) and **o-[VO(TrPP)]$_2$** (right). The plot shown for **m-[VO(TrPP)]$_2$** is similar to a ruffle-shaped porphyrin, while **o-[VO(TrPP)]$_2$** shows a saddle-like distortion mode.

6.3 EPR experiments in frozen solutions

The electronic structure and magnetic interactions in both **[VO(TrPP)]** and **[VO(TrPP)]$_2$** compounds were investigated by using EPR spectroscopy. The low temperature (T = 30 K) cw-EPR X-band spectrum of a 1 mM toluene frozen solution of the monomer **[VO(TrPP)]** is shown in Figure 6.4**a** (black trace), while the Q-band (ν = 33.8 GHz) Electron Spin Echo (ESE) detected EPR spectrum, corresponding to the absorption spectrum, is shown in Figure 6.4**b** (black trace). Both spectra show the characteristic EPR powder pattern due to the anisotropic hyperfine coupling of the electron spin to the I = 7/2 nuclear spin of ^{51}V. Spectral simulations, shown in Figure 6.4**a** and 6.4**b**, were performed based on the following spin Hamiltonian:[39]

$$\hat{H}_{[\boldsymbol{VO(TrPP)}]} = \mu_B \vec{B} \cdot \boldsymbol{g} \cdot \hat{S} + \hat{S} \cdot \boldsymbol{A} \cdot \hat{I} \qquad (6.1)$$

assuming collinear and axial g and A tensors, indicating, within the spectral resolution, a local C_{4v} symmetry. The spin-Hamiltonian parameters extracted from the

simulations of the spectra recorded at the two frequencies are listed in Table 6.2 and closely match those already reported in the literature for $[VO]^{2+}$ porphyrins consistently with a magnetic d_{xy} vanadium orbital.[97] The X-band cw-EPR spectrum of the **[VO(TrPP)]$_2$** dimer (blue trace in Figure 6.4**a**), recorded under the same conditions, shows a complex hyperfine pattern, incompatible with two identical, non-interacting **[VO(TrPP)]** units, thereby indicating the presence of magnetic interactions between the two VO units.

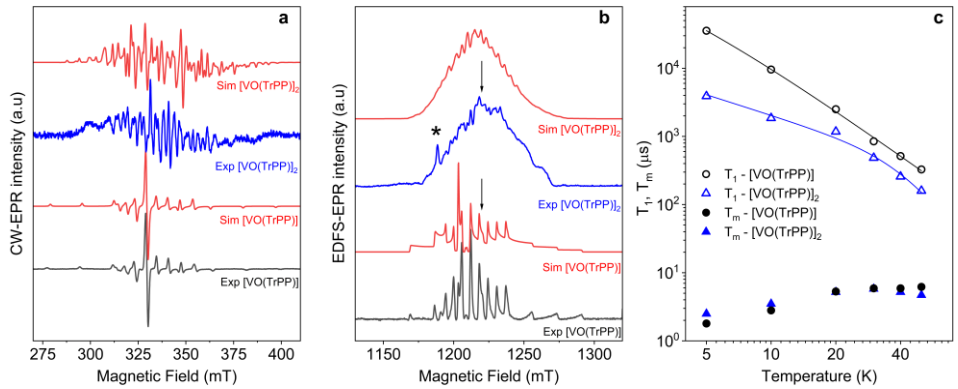

Figure 6.4: **a** X-band (ν = 9.40 GHz) cw-EPR spectra of **[VO(TrPP)]** and **[VO(TrPP)]$_2$** in frozen toluene solution (T = 30 K) together with their best simulations obtained using Spin Hamiltonian parameters reported in **Table 6.4**. **b** Q-band (ν = 33.8 GHz) ESE-EPR spectra of **[VO(TrPP)]** and **[VO(TrPP)]$_2$** in frozen -toluene/CH_2Cl_2 1:1 solution (T = 5 K). The arrows indicate the magnetic field settings at which pulse EPR experiments were performed. The asterisk indicates the signal of background impurities. **c** Temperature dependence of T_1 (open symbols) and T_m (full symbols) for **[VO(TrPP)]** (circles) and **[VO(TrPP)]$_2$** (squares) measured at 1214 mT at Q-band frequency in a 0.5 mM frozen d_8-toluene solution. Error bars are within the size of the symbols. The continuous lines represent the best-fit curves obtained using the model and parameters reported in the text.

The same complex spectral profile is observed in Q-band ESE-EPR experiments (blue trace in Figure 6.4**b**) and suggests that the two vanadyl units in **[VO(TrPP)]$_2$** are coupled through an exchange interaction smaller than the microwave quantum of energy ($h\nu \approx 0.3$ cm^{-1} for X-band). Under these circumstances, magnetic coupling of the two S = 1/2 electron spins results in four states, which are neither pure "triplet"

nor pure "singlet," leading to $4(2I_1+1)(2I_2+1)=256$ $\Delta M_s = 1$ allowed EPR transitions, where $I_1 = I_2 = 7/2$ are the nuclear spin quantum numbers of the two coupled ^{51}V nuclei.[188] In the case of a randomly oriented sample (frozen solution), the spectrum will contain overlapping peaks from those orientations corresponding to $\partial B/\partial\theta = 0$ or $\partial B/\partial\varphi = 0$. Such conditions occur along principal directions, although extra peaks may arise in other orientations (off-axis turning points),[189] leading to the intricate spectral pattern reported in **Figures 6.4a** and **6.4b**.

Inversion recovery and echo decay experiments at Q-band frequency were performed to get insight into the temperature dependence (T = 5-50 K) of the spin-lattice relaxation time T_1 and the coherence time T_m, respectively. The experimental data of both experiments were fitted using the stretched-exponential equation reported in Chapter 3, equation (3.21). The parameters obtained from the fit are listed in **Table 6.2**. In **Figure 6.4c** and **Table 6.3**, we report the T_1 and T_m values for both **[VO(TrPP)]** and **[VO(TrPP)]$_2$** in 0.5 mM deuterated d_8-toluene obtained from the fit of the inversion recovery and echo decay traces. The temperature dependence of T_1 shows a slight divergence between the monomer and the dimer below 20 K but is in essential agreement with previous reports of T_1 in vanadyl porphyrins. The temperature-dependent data for T_1 were fitted by assuming a combination of direct and *Raman* processes:

$$T_1^{-1} = aT + bT^n \qquad (6.2)$$

The best-fit parameters (**Table 6.3**) suggest that the direct process is more efficient in the dimer than in the monomer and that the *Raman* processes show low values of the exponent n (2.2 for **[VO(TrPP)]** and 4.2 for **[VO(TrPP)]$_2$**), in the range reported for vanadyl complexes.[78,80,126,190] We note, however, that due to the limited temperature range in which the investigation is possible, the number of experimental points is small compared to the number of parameters of equation (6.2). The numerical values of the obtained best-fit parameters should then be considered with caution. The

experimental coherence times T_m are very similar for the two samples and of the order of a few μs in the 5 – 50 K range; the slight decrease in T_m observed on decreasing temperature has already been reported for other S = 1/2 molecular species.[78] The decoherence times reported here are comparable to or even higher than those reported for weakly interacting vanadyl moieties[16,25] or molecular dimers based on either Cr_7Ni rings[192] or lanthanide complexes.[84]

Table 6.2: Experimental relaxation times (T_1, T_m, and corresponding stretch parameters b_1, b_m) for **[VO(TrPP]** and **[VO(TrPP)]$_2$** obtained from stretched-exponential fits of the Inversion Recovery experiment (T_1) and the Hahn Echo experiment (T_m). All samples were measured in a frozen solution (0.5 mM d_8-toluene).

	[VO(TrPP]				**[VO(TrPP)]$_2$**			
***T* (K)**	T_1 (μs)	b_1	T_m (μs)	b_m	T_1 (μs)	b_1	T_m (μs)	b_m
5	35500	0.65	1.8	0.7	3890	0.5	2.5	1
10	9578	0.66	2.8	0.8	1854	0.5	3.5	0.9
20	2504	0.6	5.3	1.5	1174	0.6	5.2	1
30	847	0.7	5.9	2.0	485	0.6	5.8	1
40	514	0.8	5.9	2.4	257	0.67	5.2	1
50	328	0.8	6.2	1.8	159	0.7	4.7	0.96

Table 6.3: Best fit parameters and uncertainties for the temperature dependence of T_1 obtained using equation (7.2).

	[VO(TrPP]		**[VO(TrPP)]$_2$**	
	Value	**Uncertainty**	**Value**	**Uncertainty**
a ($s^{-1}K^{-1}$)	2.1	1.5	49	5
b ($s^{-1}K^{-n}$)	0.5	0.3	$2.8 \cdot 10^{-4}$	$1.5 \cdot 10^{-3}$
n	2.2	0.2	4.2	1.4

6.4 Single-crystal cw-EPR experiments: determination of the exchange coupling

cw-EPR measurements on large single crystals of **[VO(TrPP)]$_2$** dimers were performed to determine the spin-Hamiltonian parameters precisely. Collecting single crystal spectra offers an elegant solution to reducing the intrinsic disorder and parameter distribution obtained in frozen solutions, which might affect coherence and addressability for molecular spin qubits. The angular dependence of the EPR spectra on both the **m-[VO(TrPP)]$_2$** and **o-[VO(TrPP)]$_2$** crystals was studied by performing crystal rotations along three orthogonal axes.

For the monoclinic case, the rotations were performed along the crystallographic *b*-axis (Rot1) and two orthogonal axes (Rot 2, 3) in the *ac** plane, clockwise tilted by 14° with respect to the *a* and *c** axes (**Figure 6.5**). For the orthorhombic crystal, the rotations were performed along directions collinear to the crystallographic *a*, *b*, and *c* axes.

The experimental EPR spectra of the two forms are characterized by a different linewidth, most likely attributable to other intermolecular through-space dipolar coupling in the two crystals. The spectra were simulated based on the spin Hamiltonian shown in equation (6.3):

$$\widehat{H}_{[\boldsymbol{VO(TrPP)}]_2} = \sum_{\boldsymbol{i=1,1'}} \mu_B \vec{\boldsymbol{B}} \cdot \boldsymbol{g}^{\boldsymbol{V_i}} \cdot \hat{S}^{V_i} + \sum_{\boldsymbol{i=1,1'}} \left(\hat{S}^{V_i} \cdot \boldsymbol{A}^{\boldsymbol{V_i}} \cdot \hat{I}^{V_i} + \hat{S}^{V_i} \cdot J \cdot \hat{S}^{V_i} \right) \tag{6.3}$$

This includes the Zeeman and hyperfine interaction terms for both VO porphyrin units (first and second term) and an interaction term described by a general matrix *J*,[193] which comprises the isotropic component *J* of the exchange interaction and a through-space dipolar coupling *D* (equation 6.4):

$$\mathbf{J} \approx J\mathbf{I} + \mathbf{D} = \begin{bmatrix} J + D_x & 0 & 0 \\ 0 & J + D_y & 0 \\ 0 & 0 & J + D_z \end{bmatrix} \tag{6.4}$$

Intramolecular dipolar interaction was fixed at the value calculated by point-dipole approximation (see **Table 6.4**). The antisymmetric and the anisotropic exchange contribution to the *J* matrix were neglected since both are expected to be small due to the small orbital contribution to the magnetism of vanadyl ions.[193] Based on the results of the crystallographic study, two different tilting angles between the magnetic tensors of the two VO units were considered for **m-[VO(TrPP)]$_2$** and **o-[VO(TrPP)]$_2$**, of 64° and 72° respectively. The molecular reference framework we adopted for the simulation has the Z-axis parallel to the C_2 axis of the molecule (*b*-axis), the Y-axis parallel to the *m-m* bond direction, and the X-axis perpendicular to these two directions (red arrows **Figure 6.5**).

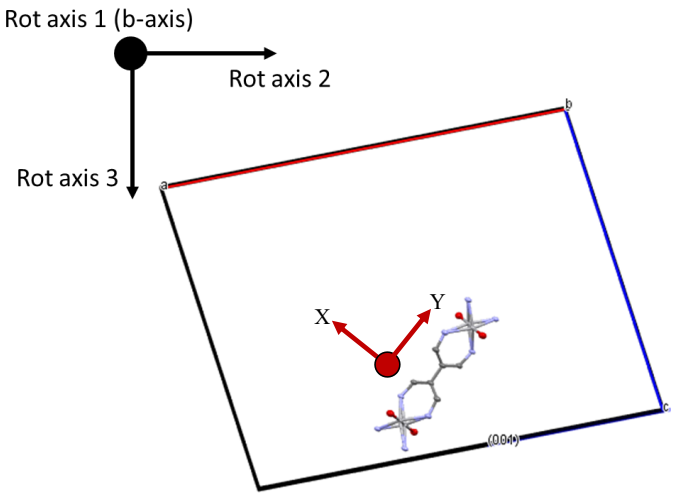

Figure 6.5: Rotations axes for the angular dependent cw-EPR spectra of the **m-[VO(TrPP)]$_2$** crystal. Clockwise rotations were performed. Rotation axis 1 is parallel to the *b*-axis of the crystal. Rotation axis 2 is on the *ac* plane and is clockwise tilted by 14° with respect to the *-a* axis. Rotation axis 3 is on the *ac* plane and is clockwise tilted by 14° with respect to the *c*-axis.

The principal values of the **g** and **A** tensors of the two vanadyl centers were kept fixed to the values obtained by the best simulation of the **[VO(TrPP)]** monomer, with their local *z-direction* oriented along the V=O bond. Intermolecular through-space dipolar interactions were included as a broadening of the linewidth. The simulated spectra are shown in **Figures 6.6a** and **6.6b** (red traces), while the extracted spin-Hamiltonian parameters are listed in **Table 6.4**.

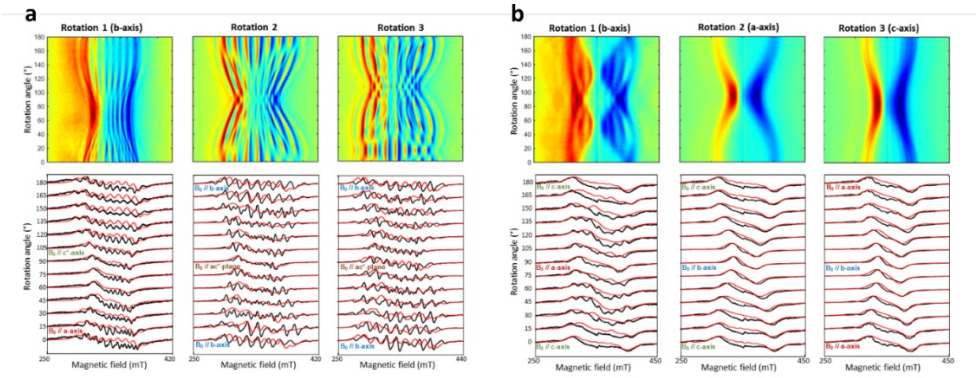

Figure 6.6. Room temperature angular-dependent cw-EPR X-band spectra of (**a**) **m-[VO(TrPP)]$_2$** and (**b**) **o-[VO(TrPP)]$_2$** for crystal rotations around three orthogonal axes. For both panels, the upper row shows the 2D experimental EPR contour plots for the three rotations, acquired with a 3° step; the lower row shows representative EPR spectra (black lines) for the three rotations from 0° to 180° every 15° together with the best spectral simulations (red lines), obtained by using $|J|$=0.01 (0.005) cm^{-1} and $|J|$=0.05 (0.01) cm^{-1} for (**a**) and (**b**) respectively. Experimental frequency: 9.40 GHz for (**a**), 9.87 GHz for (**b**).

Specifically, we used a peak-to-peak Lorentzian linewidth of 8 mT for **m-[VO(TrPP)]$_2$** and 13 mT for **o-[VO(TrPP)]$_2$**, which highlights a stronger dipolar interaction in the latter, consistent with the shorter intermolecular distance. We survey simulated EPR spectra for the two crystals to assess the effect of $|J|$ magnitudes ranging from $1.0 \cdot 10^{-5}$ to 1 cm^{-1} (see Chapter 11). Our analysis shows that for **m-[VO(TrPP)]$_2$**, the $|J|$ value that best simulates the angular dependence of the EPR spectra is about 0.01 (0.005) cm^{-1}, while for **o-[VO(TrPP)]$_2$** $|J|$ is about 0.05 (0.01) cm^{-1}.

Table 6.4: Spin-Hamiltonian parameters for **[VO(TrPP)]** and **[VO(TrPP)]$_2$** obtained from the simulation of frozen solution and single crystal experimental EPR spectra. For the simulation of the frozen solution spectra, a VO-VO tilting angle δ = 64°, corresponding to the monoclinic structure, has been considered.

Simulation Parameters	**[VO(TrPP)]**	**Single crystal [VO(TrPP)]$_2$**	**Frozen solution [VO(TrPP)]$_2$**
g_z	1.962 (1)	1.962	1.962
$g_{x,y}$	1.985 (1)	1.985	1.985
A_z (MHz)	480 (2)	480	480
$A_{x,y}$ (MHz)	168 (2)	168	168
J (cm^{-1})		$\|1.0(5)\cdot10^{-2}\|$ (**m-**) $\|5(1)\cdot10^{-2}\|$ (**o-**)	$>\|1.0\cdot10^{-2}\|$
D (cm^{-1})		[2.8 −5.6 2.8] 10^{-3}	[2.8 −5.6 2.8] 10^{-3}

The same parameters provide a convincing simulation of the frozen solution spectra at both X- and Q-band frequencies (**Figures 6.4a**, **6.4b**, and **Table 6.4**), confirming the consistency of the determined values. A survey of the simulation parameters allows defining a lower limit of $|J| = 10^{-2}$ cm^{-1} to simulate the spectra, consistent with the spanned range in the crystalline phases.

6.5 DFT-calculations

It is interesting to highlight two counterintuitive results of our investigation. First, the exchange interaction is larger in vanadyl than in copper *m-m* linked dimers [100] despite the weaker overlap (π v. σ interaction) of the metal ion magnetic orbital with the ligand scaffold. Notably, for triply linked dimers, the exchange is stronger in the copper derivative, as expected.[24,25] Second, the exchange interaction increases with the porphyrin tilting angle, which is counterintuitive when considering the extent of conjugation between the two porphyrin units.

To elucidate the nature of the observed exchange interaction and establish magneto-structural correlations, we performed DFT Broken-Symmetry (BS) calculations.[194] Ab initio calculations were performed with the ORCA 5.0.3 package[195] with the B3LYP functional[178,196] and D3 as atom-pairwise dispersion correction[197,198] were tested employing all-electron basis sets: def2-TZVP basis set for the Cu, V, O, N, and C atoms and def2-SVP for H atoms. The Broken Symmetry (BS) approach has been used to calculate the isotropic exchange parameters, *J*, within the full projection method[194,199,200] by using equation (6.5)

$$J = \frac{[E(HS) - E(BS)]}{2S_1S_2}, \tag{6.5}$$

where *E*(*HS*) and *E*(*BS*) correspond to the energies computed for the ferro- and antiferromagnetically coupled spins of the V^{4+} ions.

To verify the accuracy of the adopted method, a similar system for which the sign and the magnitude of the *J* value were experimentally determined was chosen: the triply linked Cu^{2+}-porphyrin dimer **f-CuP2**,[100] with a *J* value of 3.84 cm^{-1}. The application of the computational protocol selected led to a computed value of *J* of 5.63 cm^{-1}, confirming the accuracy in sign and order of magnitude requested to investigate the **[VO(TrPP)]$_2$** dimers. For the correspondent *m-m* linked derivative, **CuP2**,[100] the exchange interaction was too weak to be experimentally determined.

The X-ray structures have been used for both **o-** and **m-[VO(TrPP)]$_2$** and **f-CuP2**. Magneto-structural correlations were computed for the **o-[VO(TrPP)]$_2$**, varying the θ dihedral angle from 17° to 157°. For 17° ≤ θ < 90°, the two VO groups lay both above(below) the plane of the porphyrin, while one above and the other below 90° < θ ≤ 157°.

First, we focus on the crystallographic structures: the computed *J* values for **m-** and **o-[VO(TrPP)]$_2$** are both antiferromagnetic and in striking agreement with their experimental estimated magnitude: $1.4 \cdot 10^{-2}$ and $4.7 \cdot 10^{-2}$ cm^{-1}, respectively.

The computed magnetic orbitals (labeled according to the standard reference system for vanadyls) for both derivatives) are localized on the V^{4+} centers (d_{xy}) with in-plane π contributions from the N-$C_{2,5}$ *sp* components of each of the four pyrrole subunits (**Figure 6.7**). Next, we investigated the *J* variation as a function of the dihedral angle θ, keeping the other structural parameters fixed to that of the orthorhombic structure. The results (see **Figure 6.8**) show an asymmetric double-well behavior with the absolute minimum for $\theta \sim 60°$ and a less pronounced one for $\theta \sim 125°$. The double-well asymmetry originates from the non-planarity of each vanadyl-porphyrin moiety, which alters the overlap between their π-π systems for the clock- and the anti-clockwise rotation around $\theta = 90$.

The highest *J* values were computed for the smallest and largest accessible θ values (θ = 17° and 157°), *i.e.*, close to coplanarity where the largest overlap between two out-of-plane π porphyrins systems is expected. The relative maximum for $\theta \sim 90°$ is achieved when the overlap between the *sp* system of one porphyrin and the out-of-plane π system of the other is largest. The computed angular dependence is, however, not sufficient to justify the different *J* magnitude in the two derivatives, otherwise well reproduced when using the real structures. This observation points to the key role of the saddle distortion of the single porphyrin unit that alters the mixing of the local *sp* (in-plane) and delocalized π (out-of-plane) contributions: indeed, the average dihedral angle between pyrrole planes is larger for the *o*- than the *m*- derivative (7.4° vs. 4.4°, see Section 6.1).

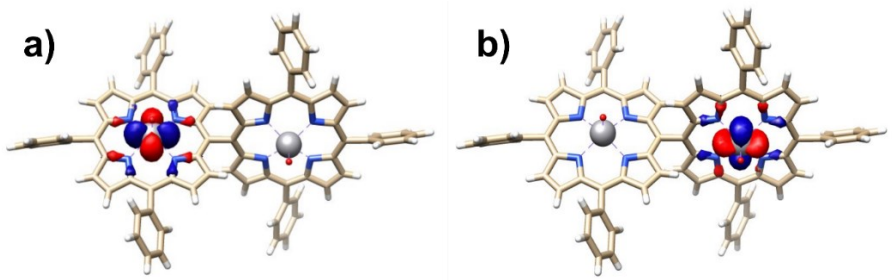

Figure 6.7: Magnetic orbitals computed for the **m-[VO(TrPP)]$_2$** with θ_{exp} (cutoff 0.03 au **a)** spin α; **b)** spin β.

As discussed in other works,[104,201,202] the distortion of the porphyrin plane indeed alters their chemical and physical properties. The change in electronic properties of the porphyrins is reflected by the redshift of the Q and B-bands in the UV/Vis spectrum and their respective broadening, which is also visible in our spectra (see Chapter 11). Although the red shift in the UV/Vis spectrum can be exclusively attributed to the plane distortion, in porphyrin dimers, the conjugation between two porphyrin rings might be the dominant cause.[202,203] Discrimination between these two hypotheses would require more detailed calculations, which are beyond the scope of this study.

The DFT analysis confirmed the magnitude of the interaction and allowed us to disclose its antiferromagnetic nature and explain the reason for the more significant coupling in the orthorhombic form.

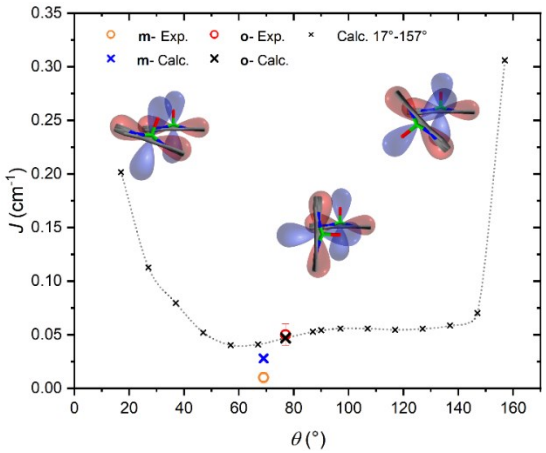

Figure 6.8: Magneto-structural correlation of the exchange parameter J (cm^{-1}) vs θ(°). The in-plane *sp* and out-of-plane π densities of the two porphyrins are sketched by red and blue lobes, respectively. The black line across the red density indicates the porphyrin planes. Large crosses refer to values computed for the two crystallographic structures, while small crosses refer to simulated geometries obtained varying the tilting angle in **o-[VO(TrPP)]$_2$**.

The deviation from the planarity of the single porphyrin units and the vanadyl magnetic orbital lying slightly above/below the porphyrin plane is responsible for the

not negligible *J* value. These geometrical features contribute to the involvement of the out-of-plane π systems, providing a more efficient superexchange interaction. These considerations also explain the negligible exchange coupling recently observed for the similar *m-m* linked Cu-porphyrin dimer.[100] That system is indeed characterized by the high planarity of the porphyrins and the in-plane nature of the magnetic orbitals. Moreover, in **[VO(TrPP)]$_2$**, access to the out-of-plane π system can occur via spin polarization processes through the oxygen atom in the VO group, as witnessed by a non-negligible spin density on it. Therefore, the VO systems present intrinsic properties that make them more appealing than the copper ones for their exploitation as multi-qubit systems in *m-m* systems.

6.6 Computational states

As a final step, it will be illustrated that **[VO(TrPP)]$_2$** fulfills the conditions that allow individual addressing of the spins. The presence of a sizeable exchange interaction and the small homogeneous line widths estimated by the measured T_m indicates that selective excitation is possible, *i.e.*, at a given field, the frequency difference between spin transitions on the two electronic sites is larger than the decoherence rate.

To analyze this issue in more detail, we performed simulations of frequency-swept EPR spectra of an oriented crystal of **o-[VO(TrPP)]$_2$**. We assumed a static magnetic field of 1.3 T applied along the local *z*-direction of **A** and **g** tensors of one of the vanadyl moieties (**Figure 6.9**) and swept the frequency in the Q-band region. This configuration has been chosen to maximize the difference between the resonant frequencies of the two sites. However, the operative conditions in two-frequency experiments implementing logic gates can be easily matched by aligning the field closer to the two-fold symmetry axis of the dimer. To better reproduce the initialization process of our system, we performed our simulation at 10 mK.

The direction of the field establishes the so-called “target” (T) qubit, while the other unit, tilted by 72°, is defined as the “control” (C). Under these

conditions the ground state of the system is given by $|m_S^T, m_S^C, m_I^T, m_I^C\rangle = \left|-\frac{1}{2}, -\frac{1}{2}, +\frac{7}{2}, +\frac{7}{2}\right\rangle$ (with minor contributions from states with different m_I), and the system is initialized as $|00\rangle$. We selected spin transitions among almost completely factorized states following the selection rules $\Delta m_s = \pm 1$ and $\Delta m_I = 0$, so that the computational basis can be roughly defined by the electronic spin states of the two moieties (i.e., $|0\rangle = |-\frac{1}{2}\rangle$ and $|1\rangle = |+\frac{1}{2}\rangle$). This option guarantees a unique computational basis for the two-qubit architecture given by the four states $|00\rangle$, $|10\rangle$, $|01\rangle$ and $|11\rangle$, where the first label indicates C and the second T.

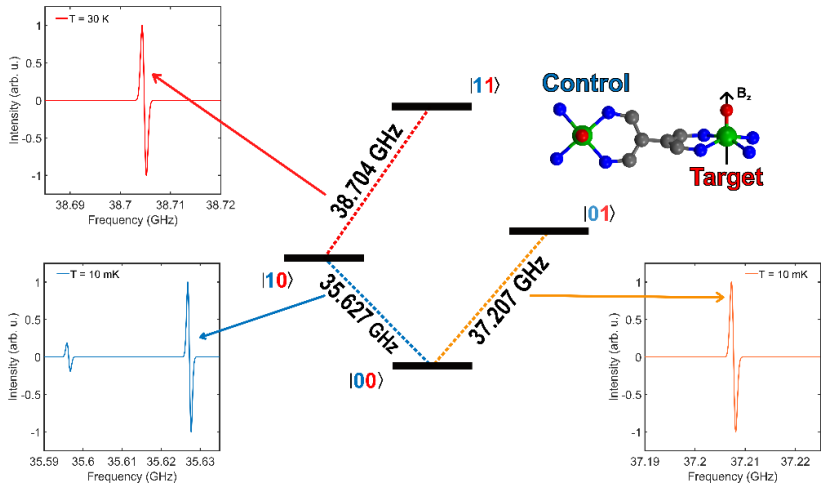

Figure 6.9: Plots of the calculated frequency-swept spectra with a magnetic field of 1.3 T applied along the local *z-axis* of the target vanadyl moiety in three different regions, corresponding to inverting the electronic spin of the control (blue line, bottom left corner), of the target without inverting the control (orange plot, bottom right corner) and of the target once the control is inverted (red plot, upper left corner). A temperature of 10 mK is employed to simulate thermal initialization in the ground state. In contrast, T=30 K is used to have a sizeable intensity of the transition of the target once the control is flipped(red).

A scheme of the transitions involved in the quantum computing process, together with the zoom on the spectral region of interest, is visible in **Figure 6.9**. By using the Spin Hamiltonian parameters reported in **Table 6.4**, the transition $|00\rangle \rightarrow |10\rangle$ and $|00\rangle \rightarrow |01\rangle$ are separated by an energy of 1.575 GHz, far exceeding the decoherence rate.

Furthermore, no other transitions are visible close to the $|00\rangle \rightarrow |01\rangle$ (**Figure 6.9**, bottom right corner), while a much less intense peak is observed in proximity of $|00\rangle \rightarrow |10\rangle$. However, this minor transition involves a higher-lying initial state, with different nuclear spin projections than those of $|00\rangle$; thus, this would not interfere with the quantum computational process. This means it is possible to excite selectively either C or T moiety once the system is properly initialized in the $|00\rangle$ state.

The computational process requires that the spin state of T must be selectively changed only when C is set to $|1\rangle$, i.e., the spin transition $|10\rangle \rightarrow |11\rangle$ must be selectively probed. This implies to first excite our system from $|00\rangle \rightarrow |10\rangle$ and only then to invert the target spin by promoting the transition $|10\rangle \rightarrow |11\rangle$. Our simulation, performed at 30 K to obtain a reasonable population of the excited $|10\rangle$ state, indicates that the transition occurs at 38.704 GHz (red dashed lines in **Figure 6.9**). This is the only allowed transition in the probed frequency range, and it can be selectively excited without involving side transitions, thus demonstrating the appeal of our system as a potential Quantum information processing unit.

We notice here that, on increasing temperature from 10 mK, further nuclear transitions would appear because of the 16x16 dimension of the electronuclear spin space. While this might be seen as detrimental for Quantum Information applications, exploiting the nuclear spin degrees of freedom has been highlighted as a further advantage of vanadyl over other systems.[174,204]

Concluding this section, **[VO(TrPP)]$_2$** shows strong potential in the quantum computational research field due to its weak exchange coupling and the presence of two individually addressable spins. The study of these dimers in different pseudo-polymorphs (**o-[VO(TrPP)]$_2$** and **m-[VO(TrPP)]$_2$**) allowed us to gain valuable insights into the exchange interaction, including the impact of porphyrin tilting angle and out-of-plane distortion. Our findings, supported by DFT calculations, confirm the antiferromagnetic nature of the exchange interaction. Moreover, the anisotropic hyperfine interaction enables individual addressability of the exchange-coupled vanadyl units, a crucial requirement for quantum logic gate implementation.

With the added advantage of porphyrin system evaporability, these dimers hold significant promise for applications in quantum information processing.

PhD author contribution:

Results discussed in this chapter are published in: *Chem. Sci.* **2023**, *14*, 61–69, and the full paper can be found in the appendix.

The author of this Thesis contributed to the synthesis of all molecules studied and contributed to the single crystal preparation and structure determination (helped significantly by Dr. Fabio Santanni). The author of this thesis also simulated the cw-EPR spectrum of **[VO(TrPP)]** and contributed to finding the computational states (helped by Fabio Santanni and Prof. Roberta Sessoli).

7 The quest of finding a suitable diamagnetic dilutant for **[VO(TrPP)]$_2$**

The importance of diluting molecular spin qubits in a diamagnetic matrix to enhance spectral resolution and facilitate spin addressability in single crystals was explained in Chapter 4. It was shown there that typical isostructural diamagnetic diluent for $[VO]^{2+}$-complexes are the homologous $[TiO]^{2+}$-complexes. Hence, it becomes evident that to acquire an appropriate diamagnetic diluent for **[VO(TrPP)]$_2$**, we need to develop a method for synthesizing bis-oxo(10,15,20-tetraphenylporphyrinato-5yl-)titanium(IV) (**[TiO(TrPP)]$_2$**). However, in the case of porphyrins, the use of (bis-[(10,15,20-tetraphenylporphyrinato-5yl-)zinc(II)] (**[Zn(TrPP)]$_2$**), or the metal-free bis-5,10,15-triphenylporphyrin (**[H$_2$TrPP)]$_2$**) can also be considered as valid alternatives.[126,205] Identifying the optimal candidate involves evaluating two primary criteria. Firstly, the synthesis should result in a high overall yield of the dimer. Secondly, the dimer should provide large and good-quality crystals. In Section 7.1, the synthetic and crystallographic studies on the three diamagnetic porphyrin dimers will be presented, while in Section 7.2, we will discuss some preliminary EPR studies.

7.1 Synthesis and crystal structures of diamagnetic **[M(TrPP)]$_2$** porphyrin dimers

For the synthesis of the diamagnetic *m*-*m* linked **[M(TrPP)]$_2$** (M = $[TiO]^{2+}$, Zn^{2+}, H_2) homometallic porphyrin dimers, the same oxidative coupling reaction of **[VO(TrPP)]$_2$** was used, with PIFA as oxidative coupling reactant (see **Scheme 7.1**). While a detailed description of the synthesis of all mentioned compounds will be given in Chapter 11, we report here the most salient problems and differences observed with respect to the synthesis of **[VO(TrPP)]$_2$**.

7.1.1 Synthesis of the titanyl porphyrin derivates

The synthesis of (**[TiO(TrPP)]**) was performed by metalation of H_2TrPP with a titanyl(IV)acetylacetonate ($TiO(acac)_2$) salt. High boiling solvents, such as phenol (PhOH), must be used to synthesize titanylporphyrins, as described in the literature.[97] After heating the reaction mixture in a nitrogen atmosphere for 48 h, the reaction was stopped.

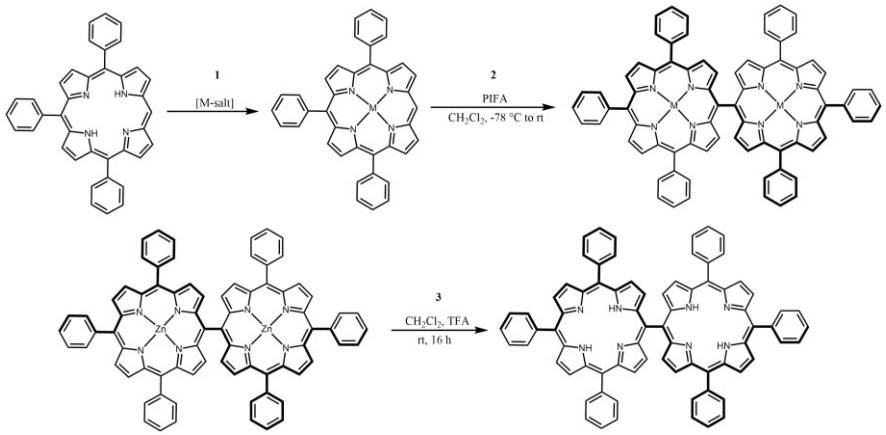

[TiO(TrPP)]$_2$: **1** $TiO(acac)_2$; PhOH, 48 h, 180°C, (~5 %) **[Zn(TrPP)]$_2$:** **1** $Zn(AcO)_2$; $CHCl_3$/MeOH 2/1, 2 h, rt, (90 %)
2 PIFA (5 eq.), 16 h, (95 %) **2** PIFA (0.5 eq.), 6 min, (96 %)
[H_2(TrPP)]$_2$: **3** **[Zn(TrPP)]$_2$**; TFA/CH_2Cl_2 1/4, 16 h, rt, $NaHCO_3$ (90 %)

Scheme 7.1: Reaction schemes for the realization of diamagnetic porphyrin dimers, starting from the metalized porphyrin monomers **[TiO(TrPP)]** and **[Zn(TrPP)]** (**1**), that were subsequently coupled using PIFA (**2**) to obtain **[TiO(TrPP)]$_2$** and **[Zn(TrPP)]$_2$**. The synthesis of **[H_2(TrPP)]$_2$** required an additional step (**3**), which was the demetallation of **[Zn(TrPP)]$_2$** with TFA.

A black insoluble solid, probably carbonized porphyrin/acetylacetonate, is produced during the reaction. No extraction procedure (including Soxhlet extraction with CH_2Cl_2, CH_3OH, and EtOAc) helped in solubilizing the black solid, though some porphyrin (both free base and metalated) was recollected. Attempts were made to lower the temperature to 150°C and to enhance the reaction time up to 5 d, but the

black insoluble solid always formed. An increased quantity of PhOH was used to prevent the formation of the black solid. Nevertheless, no significant change was observed. The reaction mixture was distilled to remove PhOH, and the crude product was purified with column chromatography (flash SiO_2, CH_2Cl_2) to separate non-metalized ligand and residual PhOH from the **[TiO(TrPP)]** crude product**.** Figure 7.1 shows the ^{1}H-NMR-spectrum of **[TiO(TrPP)]**. Some residual solid PhOH is probably present in the **[TiO(TrPP)]** powders after column chromatography because some aromatic signals not allocable to **[TiO(TrPP)]** were found in the ^{1}H-NMR-spectrum of **[TiO(TrPP)]** (Figure 7.1, signals marked with *). The removal of solid PhOH from the final product was difficult. The very similar R_f-values of PhOH and **[TiO(TrPP)]** in various eluent mixtures probed and on both flash-SiO_2 or Al_2O_3 made it impossible to separate PhOH from **[TiO(TrPP)]**. This is quite different from what was observed in the vanadyl derivative. Thanks to the fact that PhOH is soluble in acetonitrile, whereas **[TiO(TrPP)]** is only partially soluble, the best way to remove PhOH turned out to be recrystallization of **[TiO(TrPP)]** in a CH_2Cl_2/acetonitrile mixture, which resulted in the formation of dark purple and needle-like crystals. These were identified after X-ray crystallography as **[TiO(TrPP)]** (Figure 7.2).

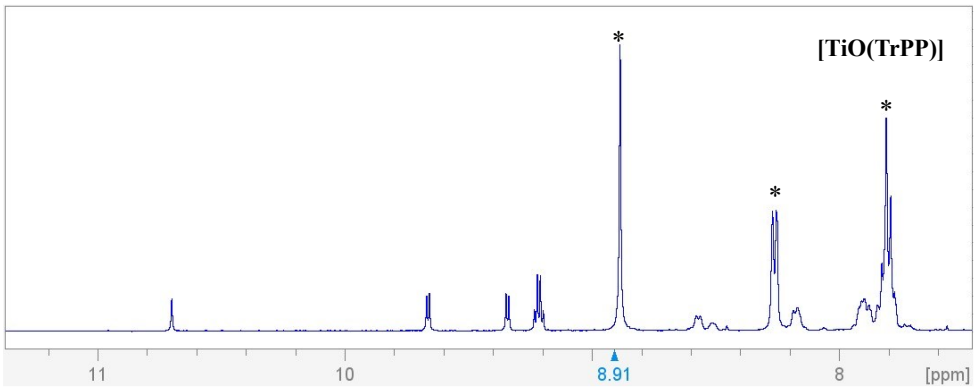

Figure 7.1: ^{1}H-NMR spectrum of **[TiO(TrPP)]** (blue) in the aromatic region (7.5-11.3 ppm). Signals marked as asterisks are the aromatic contaminant present in the sample.

The low yield obtained for this reaction (~ 5%) was somehow deceiving, so we looked for possible causes and solutions to this issue. We noted that an identical reaction for the synthesis of (**[TiO(TPP)]**) gave the product in good yields,[97] suggesting a larger stability due either to the complete substitution in *m*-positions or to the symmetry of the porphyrin. To investigate if the latter is the case, we devised a new strategy in which a novel oxo(5,15-diphenylporphyrinato)titanium(IV)(**[TiO(DPP)]**) monomer was synthesized, and subsequently one meso position functionalized with a phenyl ring using phenyllithium.[206] The last step of the reaction is reported to result in the formation of **[M(TrPP)]** porphyrins in good yields. However, this reaction step has never been studied because the metalation of H_2DPP with $TiO(acac)_2$ in PhOH failed again.

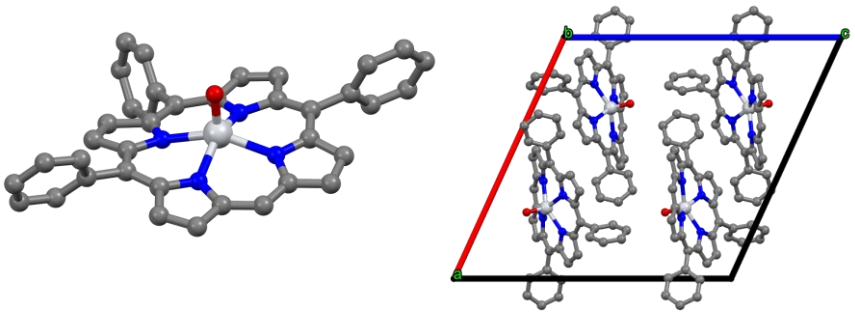

Figure 7.2: Ball and stick model of the asymmetric unit in the **[TiO(TrPP)]** crystal structure (left) and the unit cell of **[TiO(TrPP)]** viewed along the crystallographic *b*-axis (right). Color code: C = dark grey, N = blue, O = red, Ti = silver. Hydrogens are omitted for clarity.

As a final attempt to increase the yield, we substituted PhOH with other high-boiling solvents, such as DMF or toluene. We used $TiCl_4$ as a metalating agent, as reported for synthesizing **[TiO(TPP)]**.[155,207,208] However, even after 4 d and continuous adding of $TiCl_4$, no reaction occurred. Other high boiling solvents, such as cyclohexanone, o-xylene, and 1,2-dichlorobenzene, did not result in a metalation. It was, therefore, decided not to optimize the reaction any further but to concentrate the efforts on synthesizing **[TiO(TrPP)]$_2$**.

[TiO(TrPP)] turned out to be more inert than **[VO(TrPP)]** regarding oxidative coupling on the *m*-positions. Indeed, to obtain quantitative yields, 10 eq. of PIFA and reaction times up to 16 h were needed. Other differences in the synthesis were noticed while quenching the reaction mixture. When using 10 eq. of $NaBH_4$ (like for the synthesis of **[VO(TrPP)]$_2$**), it was observed that a decomplexation occurred. This could be avoided if only 5 eq. of $NaBH_4$ were used or if the reaction was quenched with sat. $NaHCO_3$ instead. Residual monomeric species could be separated using Et_2O, while metal-free porphyrin dimer was separated using flash-SiO_2 hexane/CH_2Cl_2 1/1. Since **[TiO(TrPP)]** might be contaminated with PhOH, it is possible that some PIFA reacted with PhOH, thus forming a bis-phenyl compound. Reactions like these are reported in the literature and likely also happened in this case.[209] Indeed, another aromatic impurity could be detected by ^{1}H-NMR spectroscopy (Figure 7.3 blue line).

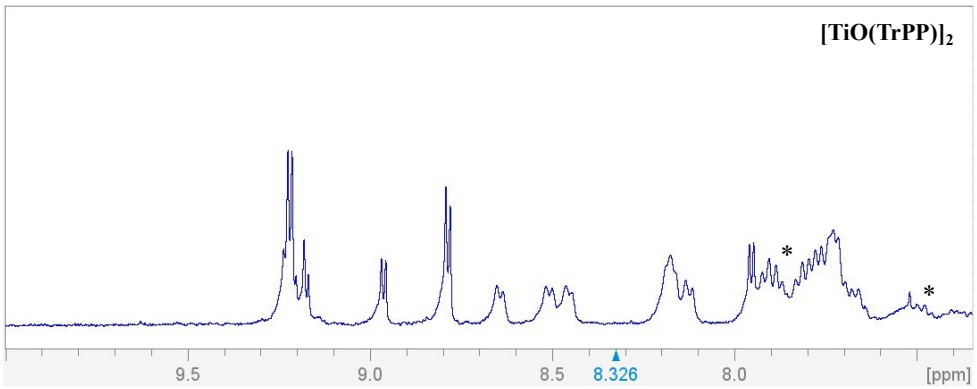

Figure 7.3: ^{1}H-NMR spectrum of **[TiO(TrPP)]$_2$** in the aromatic region (7.4-10.0 ppm). Signals marked as asterisks are the aromatic contaminant present in the sample.

Like its vanadyl counterpart, **[TiO(TrPP)]$_2$** is very soluble in most organic solvents, such as toluene, chlorinated solvents, ethers, and even semi-soluble in liquid alkanes. Nonetheless, it was not possible to grow single crystals. Even **[TiO(TrPP)]$_2$** powders are amorphous, though under the microscope, they have a plate-like shape (see Figure 7.4) and shine under the light.

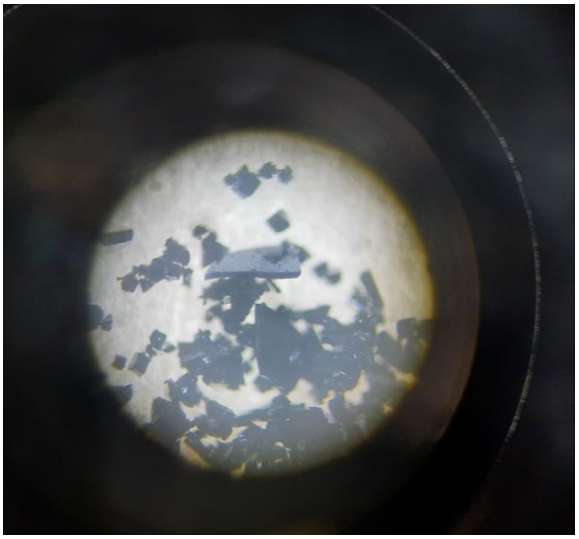

Figure 7.4: [TiO(TrPP)]$_2$ powders under the light microscope. These plate-like powders are amorph.

7.1.2 Synthesis of the zinc porphyrin derivates

While **[TiO(TrPP)]$_2$** dimers may appear ideal as magnetic dilutants for **[VO(TrPP)]$_2$**, they are challenging to purify, lack crystallinity, and are obtained in overall low yields. Hence, we opted to explore *m-m* linked **[Zn(TrPP)]$_2$** as a more accessible magnetic dilutant due to its reported synthesis in the literature.[160,161]

The synthesis of **[Zn(TrPP)]** is performed by simple metalation of H_2TrPP with zinc(II)acetate ($Zn(OAc)_2$) in a mixture of $CHCl_3$/CH_3OH that yields **[Zn(TrPP)]** quantitatively. Other than the **[VO(TrPP)]** and **[TiO(TrPP)]** monomers, **[Zn(TrPP)]** does not require any column chromatography for purification since the byproduct of the reaction (acetic acid and excess of $Zn(OAc)_2$) can be removed with water. This allowed us to obtain very pure **[Zn(TrPP)]** powders (see ^{1}H-NMR spectrum **Figure 7.5,** blue line). The obtainment of very pure **[Zn(TrPP)]** makes it possible to start the synthesis of **[Zn(TrPP)]$_2$**.

The synthesis of **[Zn(TrPP)]$_2$** in almost quantitative yields required the use of 0.5 eq of PIFA (as reported in the literature[160]) in the oxidative coupling reaction of **[Zn(TrPP)]**, at variance with the 2 eq. used for the vanadyl derivative. Furthermore, the oxidative reaction involving **[Zn(TrPP)]** is much faster than for **[VO(TrPP)]** (6 min instead of 2 h) and column chromatography (flash-SiO_2 hexane/CH_2Cl_2/TEA 1/1/0.01, **Figure 7.6**) evidences the presence of four different fractions which were characterized. The desired product was the fourth and last fraction in the column. Interestingly, the second band in the column (**Figure 7.6**, left) was orange in color, which indicates the presence of another porphyrin dimer different from **[Zn(TrPP)]$_2$**. MALDI-Orbitrap analysis (**Figure 7.6**, right) indicated that the molecular mass of the second fraction coincides with that of the hybrid dimer 5-[10,20-triphenylporphyrinato-5-yl)zinc(II)]-10,20-triphenylporphyrin (**[Zn(TrPP)(H$_2$TrPP)]**, hereafter indicated as **[ZnH$_2$(TrPP)$_2$]** for simplicity). Given these results, vanadyl porphyrins display higher stability and chemical selectivity than Zn^{2+}-porphyrins. The ^{1}H-NMR spectrum of **[Zn(TrPP)]$_2$** (**Figure 7.5**, red line) reveals no contamination peaks in the phenyl region (from 7.7 to 8.5 ppm). Furthermore, the ^{1}H-NMR signal at 10.28 ppm allocable to hydrogens in meso positions is visible, and therefore, the monomeric porphyrin is present. This reflects the difficulties in separating monomer from dimer using column chromatography.

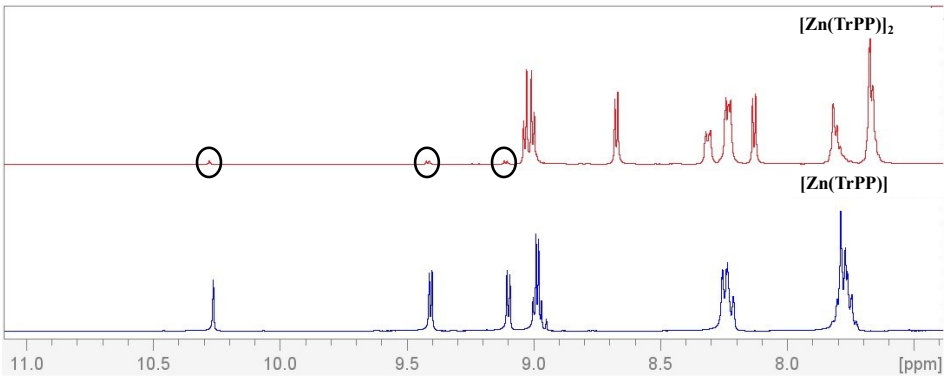

Figure 7.5: ^{1}H-NMR spectra of **[Zn(TrPP)]** (blue) and **[Zn(TrPP)]$_2$** (red) in the aromatic region (7.4-11 ppm). Signals highlighted with the black circle are residual **[Zn(TrPP)]** monomers still present in the signal of the dimer after purification.

We then attempted to separate the dimer from the monomer using recrystallization techniques: by using coordinating solvents, which are known to favor the crystallization of Zn^{2+}-porphyrins,[185–187] single crystals suitable for X-ray diffraction measurements were obtained.

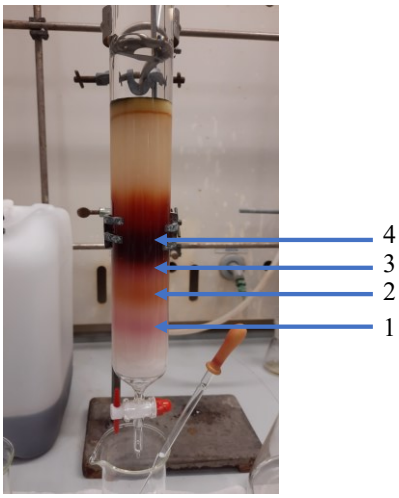

1 = **H_2TrPP**
2 = **[ZnH_2(TrPP)$_2$]** (see MALDI on the right)
3 = **ZnTrPP** (not yet visible)
4 = **[Zn(TrPP)]$_2$** (mayor fraction 96 % yield)

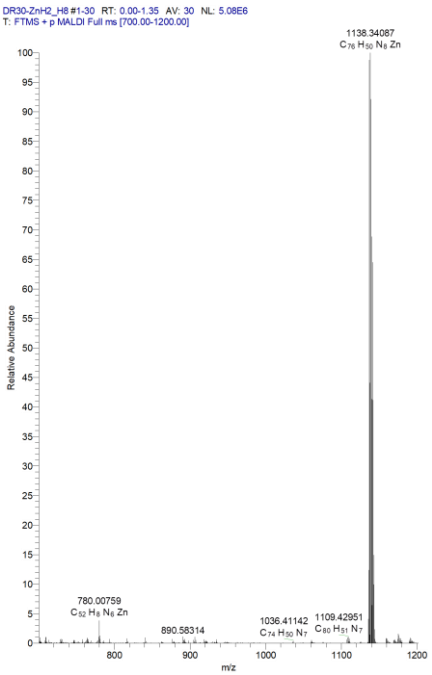

Figure 7.6: Column chromatography of the crude product **[Zn(TrPP)]$_2$** (flash-SiO_2 hexane/CH_2Cl_2/TEA 1/1/0.01, left). MALDI-Orbitrap spectrum of the second band of the column, which resulted in **[ZnH_2(TrPP)$_2$]** (right).

The corresponding structures obtained using either methanol or pyridine as solvent are reported in Figure 7.7. In both systems, the Zn^{2+}-ion is coordinated by the solvent.

Consequently, two different complexes with coordinating molecules were obtained using other polar solvents for the recrystallization. The use of solvents that coordinate the metal **Figure 7.7** shows the crystal structures of the two different **[Zn(TrPP)]$_2$** molecules, where the Zn^{2+}-ion is either coordinated by methanol (Figure 7.7, left) or pyridine (Figure 7.7, right). The methanol derivative, hereafter

[Zn(TrPP)]$_2$-MeOH, is obtained after slow evaporation of a CH_2Cl_2/CH_3OH 1:4 mixture and crystallizes in the $P2_1/n$ monoclinic space group. Its crystals are dark purple in color, have a needle-like shape, and the asymmetric unit consists of two **[Zn(TrPP)]$_2$** molecules containing six CH_3OH molecules. Four of the CH_3OH molecules coordinate with each of the four Zn^{2+}-ions present in the asymmetric unit, while the other two are non-coordinating. Additionally, two molecules of water are present as a co-crystallization solvent. The chemical composition of the asymmetric unit, containing two dimeric units, is **[Zn(TrPP)(CH_3OH)]$_4$·2CH_3OH·2H_2O**.

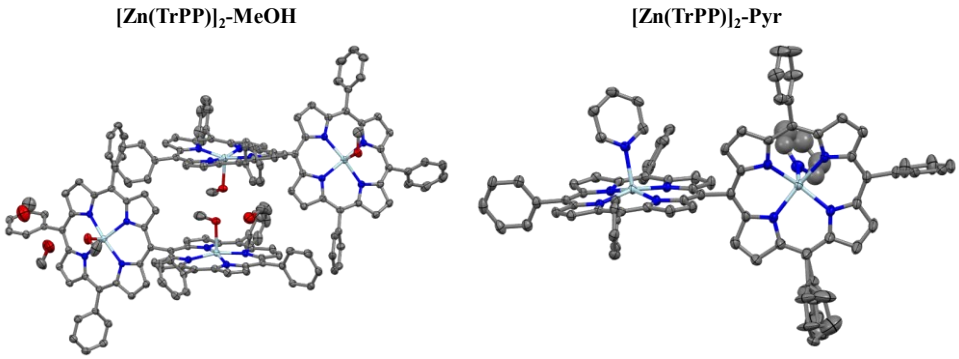

Figure 7.7: Asymmetric unit of two **[Zn(TrPP)]$_2$** complexes. When crystallized in a DCM/MeOH 1:4 mixture, **[Zn(TrPP)]$_2$-MeOH** is obtained (left), while when crystalized in a DCM/MeOH/Pyr 1:4:0.1 mixture, **[Zn(TrPP)]$_2$-Pyr** is obtained (right). Color code: C = dark grey, N = blue, O = red, Zn = white. Hydrogens are omitted for clarity. Atoms are shown as thermal ellipsoids (50 % occupancy).

The additional coordination leads to a higher deformation of the porphyrin plane because the central Zn^{2+}-ion is now sitting slightly atop the plane of the porphyrin instead of being directly on the plane, which would be the case if a non-coordinating molecule was present.[210] Within the unit cell, two different **[Zn(TrPP)]$_2$** are present, with one unit being more distorted than the other. This leads to two different Zn-Zn intramolecular distances, which are 8.38 Å for the more distorted dimer and 8.41 Å for the less distorted one. The tilting angle between the two linked porphyrin units (determined as discussed in Section 6.1 for **[VO(TrPP)]$_2$**) is 77° in the more distorted

[Zn(TrPP)]$_2$ molecule and 76° in the less distorted one. The intermolecular distance between the two closest Zn^{2+}-ions is 6.4 Å. A list of the most important experimental and structural parameters is shown in Chapter 11.

The second derivative, noted **[Zn(TrPP)]$_2$-Pyr,** was obtained after slow evaporation of a CH_2Cl_2/CH_3OH/pyridine 1:4:0.1 mixture. It crystallizes in the monoclinic space group $P2_1/c$, and its asymmetric unit consists of a Zn^{2+} porphyrin dimer where each Zn^{2+}-ion is coordinated by a pyridine, thus creating a square pyramidal environment. Additionally, four co-crystallized water molecules are present in the unit cell. The chemical formula of the complex is then **[Zn(TrPP)(C_5H_5N)]$_2$·4H_2O.** Interestingly, each porphyrin unit plane in the dimer is deformed differently, which is somewhat atypical for a porphyrin dimer. The intramolecular Zn-Zn distance is 8.32 Å and is, therefore, very similar to the one found in **[Zn(TrPP)]$_2$-MeOH**. The closest intermolecular Zn-Zn distance is 8.63 Å, similar to the intramolecular distance. The two porphyrin units are tilted by 82°, 5° more than in **[Zn(TrPP)]$_2$-MeOH**.

7.1.3 Synthesis of the free base porphyrin dimer

The analysis of the structures of these two **[Zn(TrPP)]$_2$** derivatives makes it clear that the presence of the coordinating solvent molecules would hamper the magnetic dilution, since it is incompatible with the structure of **[VO(TrPP)]$_2$**. We therefore decided to start the synthesis of a metal-free porphyrin dimer, namely bis-5,10,15-triphenylporphyrin ($(H_2TrPP)_2$, hereafter **[H_2(TrPP)]$_2$**).

Since oxidative couplings starting from H_2TrPP are not possible, this dimer was synthesized by demetallation of the previously obtained **[Zn(TrPP)]$_2$** porphyrin with TFA in CH_2Cl_2. ^{1}H-NMR-spectrum, reported in **Figure 7.8** in comparison to that of **[Zn(TrPP)]$_2$** (red line), evidences a singlet signal at −2.2 ppm (dark blue ellipsoid in **Figure 7.8**), which is originated by the pyrrolic nitrogens (N-H) of the two porphyrin units. This indicates that the demetallation was successful.

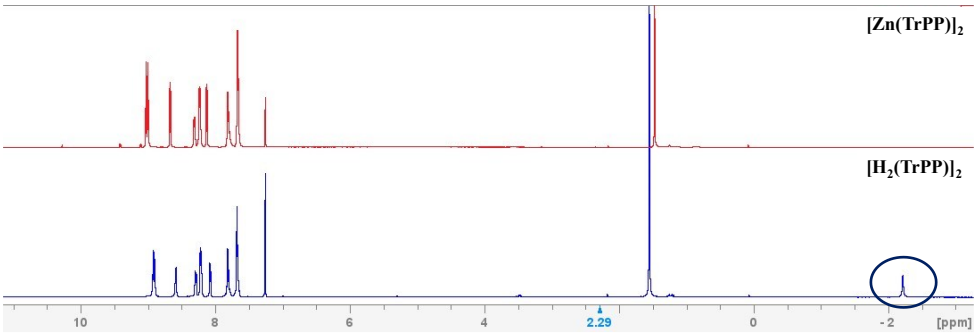

Figure 7.8: Full region ^{1}H-NMR spectra of **[Zn(TrPP)]$_2$** (red) and **[H$_2$(TrPP)]$_2$** (blue). The Signal highlighted with the dark blue ellipsoid is the singlet form of the four pyrrolic hydrogens.

Slow evaporation of different solvent mixtures led to the formation of single crystals of sufficient quality for X-ray diffraction experiments despite being of lower quality than those of **[Zn(TrPP)]$_2$**. After slow evaporation of a CH_2Cl_2/CH_3OH/Pyr (1:4:0.1) mixture in different batches, dark purple crystals were obtained; however, the shapes of the crystals in the two different batches were different. Interestingly, X-ray diffraction analysis showed that in one of these plate-like crystals, hereafter **[H$_2$(TrPP)]$_2$-DCM** (Figure 7.9, left), the porphyrin dimer crystallizes with one CH_2Cl_2 per molecule of porphyrin dimer, whereas in the other one (needle-like crystals, hereafter **[H$_2$(TrPP)]$_2$-H$_2$O**, Figure 7.9) up to two molecules of water per porphyrin dimer are present. Since the solvent and ratio of the mixture were the same for both solutions, we suggest that both dimer concentration and temperature play a key role in preferring one or the other solvatomorph. The two solvatomorphs crystallize in the same space group (monoclinic, P2/n), though with different cell parameters (see Table 7.1). At the same time, the tilting angle between the two porphyrin units varies drastically (80° for **[H$_2$(TrPP)]$_2$-H$_2$O** vs 68° for **[H$_2$(TrPP)]$_2$-DCM**). The difference in tilting angle is explained by the bulkier co-crystallized solvent molecules that tend to reduce the tilting angle. A similar phenomenon was observed in the **[VO(TrPP)]$_2$** crystals (see Section 6.1).

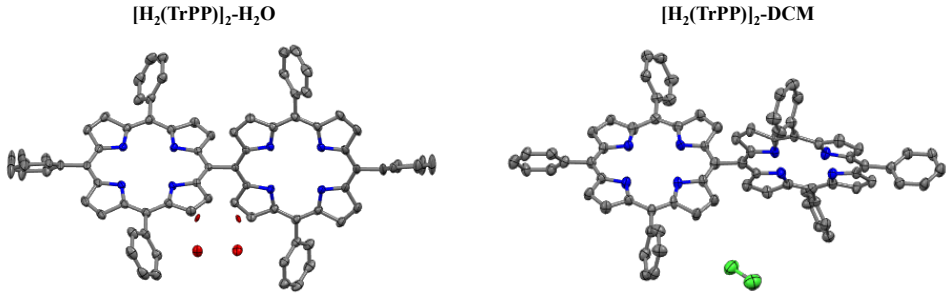

Figure 7.9: Crystal structure of the two **[H$_2$(TrPP)]$_2$** polymorphs **[H$_2$(TrPP)]$_2$-H$_2$O** (left) and **[H$_2$(TrPP)]$_2$-DCM** (right). Color code: C = dark grey, N = blue, O = red, Cl = green. Hydrogens are omitted for clarity. Atoms are shown as thermal ellipsoids (50 % occupancy).

To improve the quality of the obtained crystals, we devised a crystallization method in which most parameters were kept as constant as they could (see Chapter 11). A 1.5 mM **[H$_2$(TrPP)]** solution in CH_2Cl_2 was prepared, in which CH_3OH and pyridine were added. Three different batches of these solutions were prepared and stored in the chemistry laboratory at a temperature between 16-18°C. After 5-6 days, needle-like crystals were visible. The evaporation of CH_2Cl_2 from the vial was stopped by closing the screw cap and taping the border (cap and glass) with parafilm® and with a black friction tape. This was done to avoid the complete loss of solvent and to prevent crystal degradation. Despite the low quality of the crystals, as evidenced by the relatively high R(Int) value and their tendency to lose crystallinity when not in the mother liquor, it was possible to solve the structure by collecting X-ray diffractometry data on the crystal shown in **Figure 7.10** right, which belongs to P2/n space group. The structure obtained is graphically reported in **Figure 7.10** left, and evidence that the obtained solvatomorph, hereafter **[H$_2$(TrPP)]$_2$-Pyr,** consists of one co-crystallization molecule of pyridine per porphyrin dimer. Unlike **[Zn(TrPP)]$_2$-Pyr**, the uncoordinated pyridine molecules in **[H$_2$(TrPP)]$_2$-Pyr** do not significantly disturb a possible magnetic dilution. Further, the tilting angle between the two porphyrin units is 79°, thus very similar to the 77° torsion angle measured in **o-[VO(TrPP)]$_2$** (see Section 6.1). Finally,

the same crystal structure was measured for all the batches prepared in this way, which indicates this crystallization method is quite reproducible.

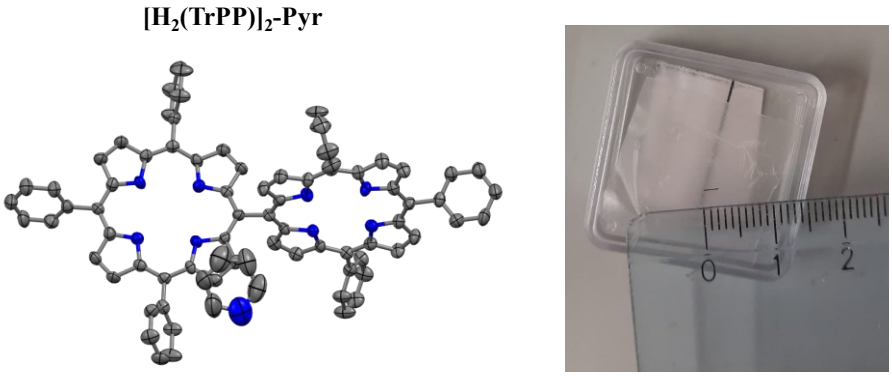

Figure 7.10: Molecular structure of **[H$_2$(TrPP)]$_2$-Pyr** (left). This structure was solved using a needle-like single crystal that had a length of approximately 3 mm (right).

7.2 Preparation and characterization of the diluted samples

The **[H$_2$(TrPP)]$_2$** crystal thus looks promising as a dilutant crystal for **[VO(TrPP)]$_2$**. As a good compromise between signal detection and low spin-spin interaction, we first attempted to obtain samples with 1 % of **[VOTrPP]$_2$** dilution, both in single crystal and powder forms.

7.2.1 Preparation of the diluted powders

The first dilution experiments were performed with polycrystalline powders. **[H$_2$(TrPP)]$_2$** and **[VO(TrPP)]$_2$** were dissolved in CH_2Cl_2, with the correct stoichiometric ratio. A few mL of methanol and a few drops of pyridine were added to the solution. After fast evaporation under the rotatory evaporator, a precipitate formed, yielding the 1 % diluted powders (from now on called

[VO$_{(0.01)}$H$_{2(0.99)}$(TrPP)]$_2$), which were subsequently filtered and dried. Since the yield of this synthesis was quantitative, we can assume that the concentration of $[VO]^{2+}$ centers in the powder is 1mol%.

Figure 7.11 shows the PXRD-pattern of fast precipitating **[VO$_{(0.01)}$H$_{2(0.99)}$(TrPP)]$_2$** powders (black patterns), compared with the simulated PXRD-pattern obtained from the single crystal structures of **m-[VO(TrPP)]$_2$** (orange pattern, Figure 7.11 right) **[H$_2$(TrPP)]$_2$-H$_2$O** (blue pattern, Figure 7.11 right), **[H$_2$(TrPP)]$_2$-Pyr** (red pattern, Figure 7.11 right), and **[H$_2$(TrPP)]$_2$-DCM** (turquoise pattern, Figure 7.11 right).

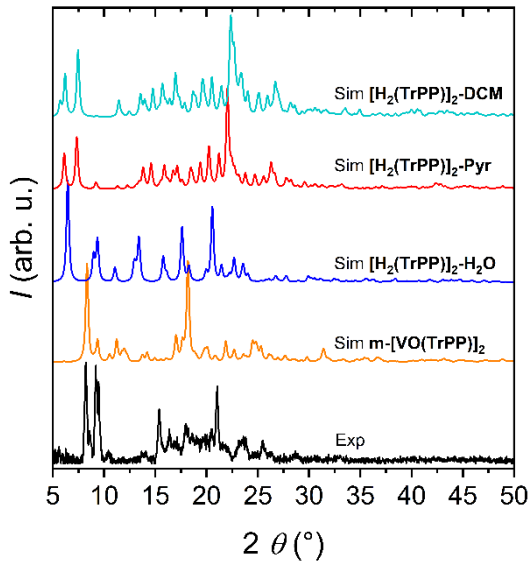

Figure 7.11: PXRD-pattern of the fast precipitated powder of **[VO$_{(0.01)}$H$_{2(0.99)}$(TrPP)]$_2$** (black pattern) compared with the simulated PXRD-pattern of the crystal structures of **m-[VO(TrPP)]$_2$** (orange pattern) **[H$_2$(TrPP)]$_2$-H$_2$O** (blue pattern), **[H$_2$(TrPP)]$_2$-Pyr** (red pattern, right figure), and **[H$_2$(TrPP)]$_2$-DCM** (turquoise pattern)

The results show that the **[VO$_{(0.01)}$H$_{2(0.99)}$(TrPP)]$_2$** sample is indeed polycrystalline, but a significant amount of amorph sample is present as well. Indeed, the FWHM of each reflection is much broader than expected for an ideal polycrystalline powder.

More importantly, the PXRD pattern does not correspond with either the simulated **[VO(TrPP)]$_2$** or **[H$_2$(TrPP)]$_2$** crystal structures. This indicates that the polycrystalline phase obtained is probably another polymorph generated upon fast precipitation of the powders. Consequently, it is plausible that the distortion of the porphyrin plane and the tilting angle in the powders of this phase may deviate from those observed in **[H2(TrPP)]$_2$-Pyr** single crystals.

7.2.2 Preparation of the diluted single crystal

Since this uncertainty might pose some problems for the more advanced experiments, we switched to a slower crystallization procedure to obtain single crystals of the solid solution. The synthesis followed the procedure designed for getting **[H$_2$(TrPP)]$_2$-Pyr** single crystals, with the only difference being that a solution of **[VO(TrPP)]$_2$** solved in CH_2Cl_2 was added to the mixture. After 5 d, needle-like crystals precipitated, and the cell parameters and space group were confirmed to be equal to those of **[H$_2$(TrPP)]$_2$-Pyr**.

The concentration of the $[VO]^{2+}$ in the doped crystals was too low to be quantified by X-ray single crystal analysis, and therefore, the only possible way to see if incorporation of **[VO(TrPP)]$_2$** in **[H$_2$(TrPP)]$_2$-Pyr** occurred was by cw-EPR spectroscopy. Cw-EPR spectroscopy will only provide a qualitative analysis (indicating the presence of diluted paramagnetic centers). However, quantifying the concentration of $[VO]^{2+}$ is challenging due to low signal and concentration.

Table 7.1: Crystal data and structure refinement parameters for the **[H$_2$(TrPP)]$_2$-H$_2$O**, **[H$_2$(TrPP)]$_2$-DCM**, **[H$_2$(TrPP)]$_2$-Pyr**, polymorphs and **[TiO(TrPP)]** molecule.

Empirical formula	$C_{38}H_{25}N_4O_{1.50}$ **([H$_2$(TrPP)]$_2$-H$_2$O)**	$C_{77}H_{52}N_8Cl_2$ **([H$_2$(TrPP)]$_2$-DCM)**	$C_{43}H_{30}N_5O_{0.5}$ **([H$_2$(TrPP)]$_2$-Pyr)**
Formula weight	561.62	1160.22	624.72
Temperature	293(2)	100	100
Wavelength	1.54184 Å	1.54184 Å	1.54178 Å
Crystal system	monoclinic	monoclinic	monoclinic
Space group	P2/n	$P2_1/m$	P2/n
Unit cell dimensions (Å)	a = 16.8535(4) b = 11.7103(3) c = 16.8684(4) α = γ = 90° β = 108.4890(10)°	a = 19.046(3) b = 6.9519(10) c = 23.779(4) α = γ = 90° β = 94.777(12)	a = 19.2338(7) b = 7.0288(2) c = 24.1574(8) α = γ = 90° β = 94.693(2)°
Volume	3157.30 Å^3	3137.5(9) Å^3	3254.90 Å^3
Z	4	4	4
Density (calculated)	1.182 g cm^{-3}	-	1.275 g cm^{-3}
Absorption coefficient	0.58 mm^{-1}	-	0.602 mm^{-1}
F(000)	1172	-	1308
Crystal size	0.04x0.04x0.02 mm^3	-	0.06x0.04x0.01 mm^3
Theta range for data collection	3.775° to 72.237°	5.718° to 114.112°	3.06° to 68.12°
Index ranges	−20≤h≤20, −14≤k≤14, −20≤l≤20	-	−19≤h≤23, −8≤k≤6, −29≤l≤29
Reflections collected	59414	52668	23135
Independent reflections	6201 [R(int) = 0.065]	1333	6848
Completeness to theta = 63.898°	99.3 %	99.5 %	99.5 %
Absorption correction	Multi-scan	Multi-scan	Multi-scan
Refinement method	Full-matrix least-squares on F^2	Full-matrix least-squares on F^2	Full-matrix least-squares on F^2
Goodness-of-fit on F^2	1.157	1.102	1.018
Final R indices [I>2σ(I)]	R1 = 0.0671, wR2 = 0.1954	-	R1 = 0.0580, wR2 = 0.15270
R indices (all data)	R1 = 0.0650, wR2 = 0.1932	-	R1 = 0.0804, wR2 = 0.1717

7.2.3 Cw-EPR investigations on magnetically diluted **[VO(TrPP)]$_2$**

The experimental cw-EPR spectrum of **[VO$_{(0.01)}$H$_{2(0.99)}$(TrPP)]$_2$** powders is plotted in Figure 7.12 (black lines) and shows a clear signal which can be attributed to weakly exchange coupled $[VO]^{2+}$-units. Furthermore, the line width of this spectrum is much

smaller than for the powder spectra of pure **[VO(TrPP)]$_2$** (blue line, Figure 7.12) and even smaller compared to the frozen solution spectra (pink line, Figure 7.12). We can attribute this behavior to the successful dilution of **[VO(TrPP)]$_2$** molecules inside a **[H$_2$(TrPP)]$_2$** crystal matrix. In both cases, the spin-spin interactions are strongly reduced: while in frozen solution, distribution of various titling angles θ can be expected, in polycrystalline powders, only one θ is present, thus justifying the reduced line width. However, given the different PXRD-pattern of the diluted phase with respect to both **[VO(TrPP)]$_2$** and any **[H$_2$(TrPP)]$_2$** solvatomorph, it is impossible to obtain exact information on the tilting angle between the porphyrin units.

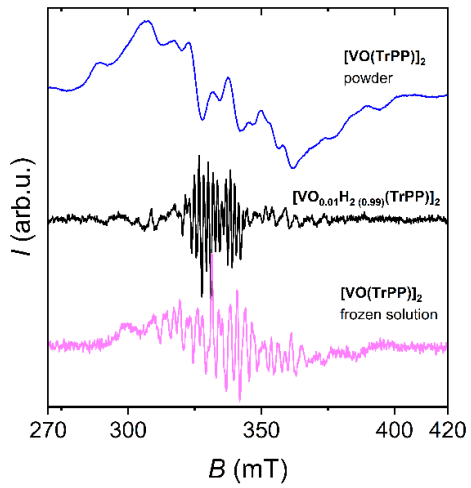

Figure 7.12: comparison between the three experimental cw-EPR spectra of **[VO$_{(0.01)}$H$_{2(0.99)}$(TrPP)]$_2$** diluted powders (black line), **[VO(TrPP)]$_2$** frozen solutions (pink line), and powders (blue line). The cw-EPR spectrum of **[VO$_{(0.01)}$H$_{2(0.99)}$(TrPP)]$_2$** was recorded at T = 10 K (ν = 9.417 GHz), whereas the spectra of the frozen solution (ν = 9.448 GHz) and powders (ν = 9.403 GHz) were recorded at T = 30 K.

For this reason, we moved to study single crystals of **[VO$_{(0.01)}$H$_{2(0.99)}$(TrPP)]$_2$** dilutions, which have the same cell parameters as **[H$_2$(TrPP)]$_2$-Pyr**. A good diffracting crystal was found, with an approximate size of (0.025, 0.04, 0.05) mm. The crystal was placed on the acetate film (see Figure 7.13, right). The crystal was

mounted on the sample holder for the single crystal measurements on the EPR spectrometer by keeping the *b*-axis parallel to the static magnetic field. The corresponding EPR spectrum is reported in **Figure 7.13**, left, whereas in **Figure 7.13,** right, a sketch of the measured crystal shape and orientation is shown. The observed signal is extremely weak, in agreement with the low mass of the crystal and the 1% dilution of the paramagnetic molecules. Despite this, the results are promising since narrow lines clearly indicate the successful obtainment of a diluted single crystal of **[VO$_{(0.01)}$H$_{2(0.99)}$(TrPP)]$_2$**. These findings pave the way for experiments with non-conventional and more sensitive EPR spectrometers. Ongoing experiments on oriented and diluted single crystals using multiple frequency pulses and milli-kelvin temperatures are in progress in Prof. *Fernando Luis's* research group at the Universidad de Zaragoza, Aragòn, Spain.

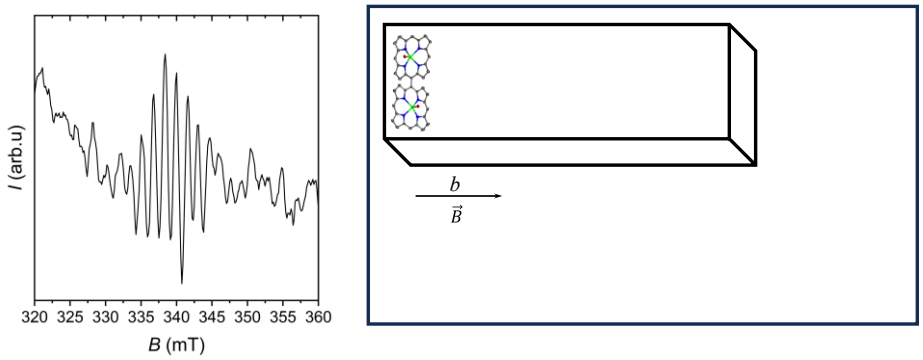

Figure 7.13: Experimental X-band cw-EPR spectrum (ν = 9.394 GHz, T = 30 K) on a diluted single crystal of **[VO$_{(0.01)}$H$_{2(0.99)}$(TrPP)]$_2$** recorded parallel to the crystallographic *b*-axis and external magnetic field (left). Sketch of the needle-like single crystal of **[VO$_{(0.01)}$H$_{2(0.99)}$(TrPP)]$_2$** on the thin acetate film that was used for the cw-EPR experiment.

Contribution from the author of this PhD thesis:

The author of this thesis synthesized and prepared all molecules/samples used for the experiments. He solved the crystal structure of **[TiO(TrPP)]** (helped by Dr. Samuele Ciattini) and measured all the PXRD patterns.

8 **[VOCu(DPP)$_2$]**: The heterometallic version of a two-qubit quantum logic gate

After having synthesized and studied the **[VO(TrPP)]$_2$** dimer, the realization of a novel heterometallic $[VO]^{2+}$-Cu^{2+} *m-m* singly linked dimer was the next goal. The open question was whether the vanadyl unit is able to promote a significant magnetic exchange interaction even when coupled to a different paramagnetic center. Moreover, heterometallic singly linked dimers could be more interesting from an applicational point of view because, upon the surface deposition, the porphyrin tilting angle is expected to get smaller on the surface. This would result in the loss of single spin addressability in homometallic porphyrin dimers, achieved because of the different orientations of the magnetic tensors. On the contrary, a heterometallic dimer would have distinguishable spins even if their magnetic anisotropy axes are aligned in space, as long as the exchange interaction strength is not too large. Moreover, the addressability will be retained for most orientations of the external magnetic field. The two metals chosen to realize these dimers were the $[VO]^{2+}$ and Cu^{2+} ions because the Δg is large enough to achieve spin addressability (see Chapter 3) and the single units are expected to show reasonable coherence times.

In the following sections, we will first present the primary outcome of the synthesis of (5-[10,20-diphenylporphyrinato-5-yl)copper(II)]-[oxo(10,20-diphenylporphyrinato) vanadium(IV), **[VOCu(DPP)$_2$]**. Then, in Section 8.2, we will delve into the EPR investigation of the **[VOCu(DPP)$_2$]** complex. Possible computational states for quantum information will be explored and outlined in Section 8.3. Finally, the experimental spin Hamiltonian parameters will be validated through DFT calculations in Section 8.4.

8.1 Synthesis and crystal structures of the porphyrin monomers and hybrid porphyrin dimers

At variance with homometallic porphyrin dimers that can be readily synthesized using a two-step approach, a challenging multi-step synthetic procedure is required to obtain heterometallic porphyrin dimers. This is necessary because the two monomers that need to react to form the dimer must be functionalized differently to prevent the formation of homometallic species. This requires a deep knowledge of the porphyrin reactivity. For this reason, the synthesis of the hybrid $[VO]^{2+}$-Cu^{2+}porphyrin dimer was developed during my research at the Laboratory of Tetrapyrroles of the Biomedical Institute of Trinity College Dublin.

We started by considering that hybrid porphyrin dimers such as **[VOCu(DPP)$_2$]** could be synthesized by a *Suzuki-Miyaura* coupling[211] between a borylated and halogenated porphyrin monomer (**Scheme 8.1**).[149] It was thus necessary to synthesize these "*Suzuki*" porphyrins first.

Following the *Suzuki-Miyaura* coupling approach, the monomeric porphyrin complexes (**Scheme 8.1**) were synthesized by reacting H_2DPP with $VO(acac)_2$[97] or $Cu(AcO)_2$[212] to yield the respective metalloporphyrin **[VO(DPP)]** or **[Cu(DPP)]** (**Scheme 8.1a**). The H_2DPP porphyrin ligand was selected as a compromise between solubility and decoherence induced by hydrogen magnetic nuclei on the ligand. Moreover, this choice represents a good building block for extended arrays of porphyrin rings and might be more suitable for surface deposition experiments using the PVD technique. Additionally, we focused on singly-linked porphyrins to avoid the stronger coupling promoted by triply-linked porphyrins.[100] In contrast to O*suka's* procedure, a better-leaving group (iodine rather than bromine) for the oxidative coupling step in the dimerization procedure had to be used since the coupling employing brominated porphyrins did not yield the dimer.[213] The difference between the results of *Osuka* and co-workers might be due to the different metals employed here.

Monomer **[VO(DPP)]** was used to obtain the iodinated derivative **[VO(IDPP)]** (Scheme 8.1**a**). To obtain the iodinated Cu^{2+} monomer (**[Cu(IDPP)]**), the free base H_2DPP was first iodinated to get H_2IDPP and subsequently metalated with $Cu(OAc)_2$. All iodinated compounds were obtained by following published procedures.[142,213] The yield of the iodination did not change significantly upon using various oxidative agents such as $CuCl_2$, PIFA, or $AgPF_6$. Nonetheless, PIFA was chosen as the oxidizing agent to reduce metal contamination of the final products purified by column chromatography. The borylated compound (BpinDPP, Scheme 8.1**a**) was synthesized using a literature procedure.[213] The synthesis of compounds **[VO(IDPP)]**, **[Cu(IDPP)]**, and BpinDPP allowed an entry into the hybrid porphyrin dimers. For the synthesis of the hybrid dimers of the type **[M(DPP)(H$_2$DPP)]** (hereafter abbreviated as **[VOH$_2$(DPP)$_2$]** and **[CuH$_2$(DPP)$_2$]**, Scheme 8.1**b**), a *Suzuki-Miyaura* coupling[211] was performed between the pinacolborane and iodinated porphyrins **[VO(IDPP)]** or **[Cu(IDPP)]** (Scheme 8.1**b**).[214,215] Finally, the metalation of the free base porphyrin unit in compound **[VOH$_2$(DPP)$_2$]** with $Cu(acac)_2$ in $CHCl_3$ at room temperature afforded the desired compound **[VOCu(DPP)$_2$]** (Scheme 8.1**c**). Metalation of **[VOH$_2$(DPP)$_2$]** was preferred over **[CuH$_2$(DPP)$_2$]** to obtain **[VOCu(DPP)$_2$]** due to milder reaction conditions for insertion of Cu^{2+} than $[VO]^{2+}$ into the porphyrin-free base.

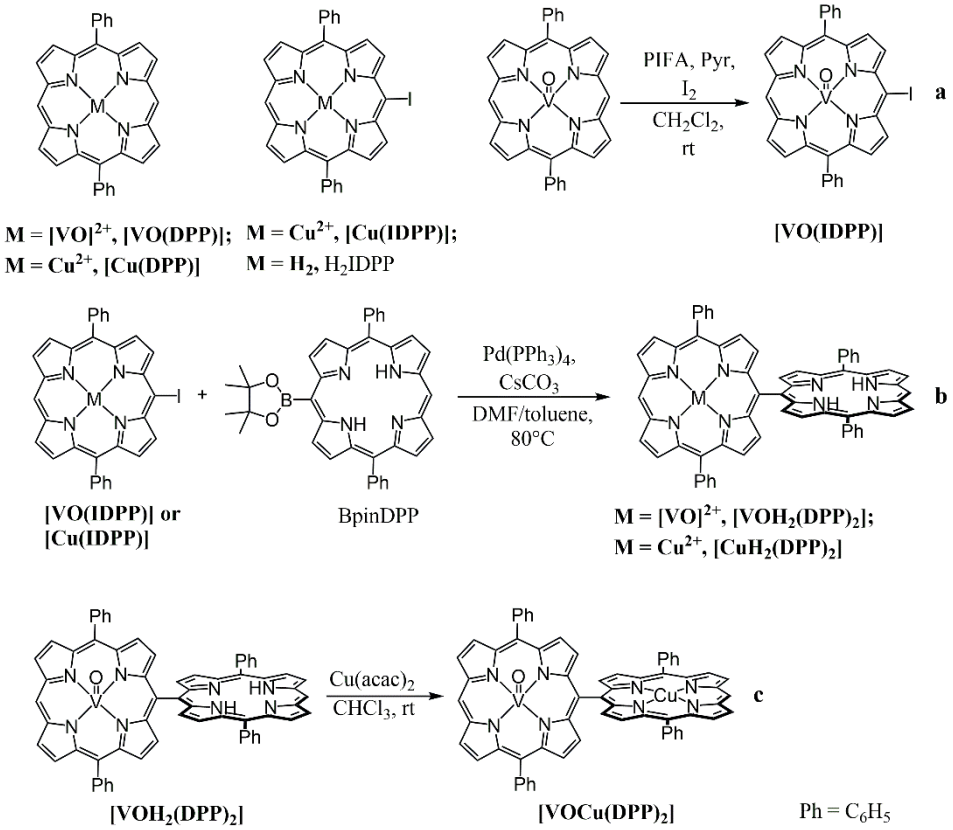

Scheme 8.1: (**a**) Chemical structures of the synthesized monomeric porphyrins, along with the synthesis of **[VO(IDPP)]**. (**b**) Reaction scheme for the reaction of the iodinated $[VO]^{2+}$ (**[VO(IDPP)]**) or Cu^{2+} (**[Cu(IDPP)]**) porphyrin with the borylated porphyrin (BpinDPP) to obtain hybrid porphyrin dimers **[VOH$_2$(DPP)$_2$]** or **[CuH$_2$(DPP)$_2$]**. (**c**) The free base porphyrin unit in **[VOH$_2$(DPP)$_2$]** can be metalated with $Cu(acac)_2$ to yield the heterometallic porphyrin dimer **[VOCu(DPP)$_2$]**.

Purple needle-like single crystals of monomers **[VO(DPP)]** and **[Cu(DPP)]** were obtained by slow evaporation of a CH_2Cl_2/MeCN (10:1) mixture and a $CHCl_3$/heptane (7:1) mixture, respectively. Both compounds crystallized in the monoclinic space group $P2_1/c$ (see Section 11.3). For **[VO(DPP)]**, the asymmetric unit is half of the molecule, the V=O group being disordered over inversion above and below the porphyrin plane (**Figure 8.1a**).[216] For **[Cu(DPP)]**, the asymmetric unit includes the porphyrin unit with one $CHCl_3$ molecule of solvation (**Figure 8.1b**). In **[Cu(DPP)]**, the porphyrin plane exhibits out-of-plane ruffled distortion.

Crystallization of all dimers shown in **Scheme 8.1** was hampered by their low solubility in toluene and ethers and only limited solubility in $CHCl_3$ or CH_2Cl_2. This resulted in fast precipitation during the slow evaporation process, thus limiting the sizes of the crystals obtained and the quality of the data collection. However, the basic features of the molecular structures were obtained, providing crucial information on the chemical identity, connectivity of the complexes, and the tilting angle between the two moieties. In the case of **[CuH$_2$(DPP)$_2$],** attempts to get single crystals were unsuccessful.

[VOH$_2$(DPP)$_2$] crystallized in the tetragonal space group P4cc (**Figure 8.1c**), and the refined structure evidences a high degree of disorder. The asymmetric unit consists of one porphyrin moiety with 50% metal occupancy, the dimer showing a C_2-axis perpendicular to the meso-meso bond. The resulting tilting angle between the porphyrin planes θ, defined as the dihedral angle about the meso-meso bond, is 78°, close to that observed in a homometallic $V^{IV}O$-dimer;[217] a similar saddle-like distortion is also observed.

The shortest intermolecular VO-VO distance is around 8.5 Å. **[VOCu(DPP)$_2$]** crystallizes in the tetragonal space group P4/ncc (**Figure 8.1d**). The asymmetric unit is half a porphyrin unit, with partial $[VO]^{2+}$ and Cu^{2+} occupancy, and the former being disordered above and below the porphyrin plane. A C_2-axis passing through the meso carbon atoms and an S_4-axis bisecting the meso-meso bond generates the dimeric unit. The tilting angle θ between porphyrin planes is around 78° (**Figure 8.1e**), and the intramolecular V-Cu distance is around 8.44 Å, which compares well with the 8.37 Å observed in the homometallic vanadyl dimer.[217] Despite the low quality of the crystal structure, the simulated PXRD pattern compares well with the experimental one (see Section 11.3).

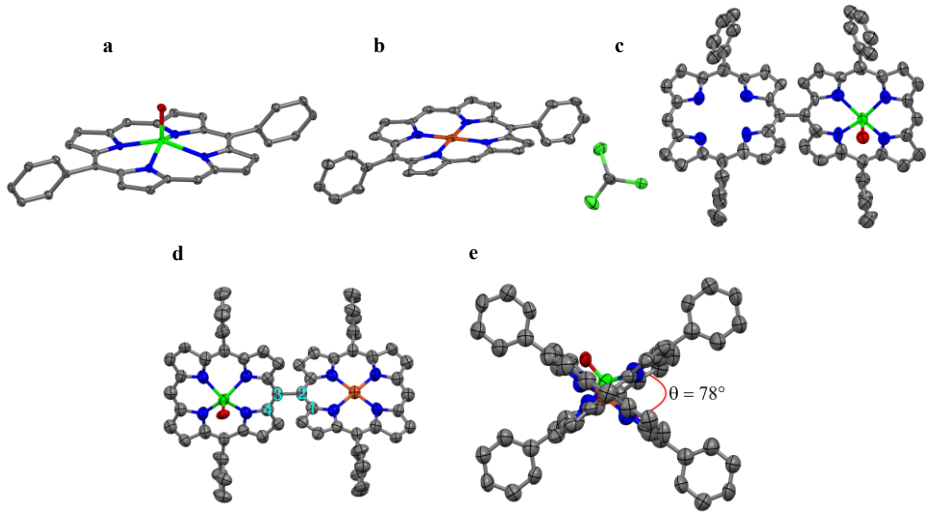

Figure 8.1: Molecular structure of **[VO(DPP)]** (**a**), **[Cu(DPP)]** (**b**), **[VOH$_2$(DPP)$_2$]** (**c**), and **[VOCu(DPP)$_2$]** (**d**) in the crystal. Molecular structure of **[VOCu(DPP)$_2$]** viewed along the meso-meso linkage (**e**). The angle *θ,* describing the tilting between the porphyrin units, is defined as the dihedral angle between the carbon atoms 1-4 labeled in **d**.

8.2 EPR investigation

In this section, the X-band cw-EPR measurements of both the two monomers (**[VO(DPP)]** and **[Cu(DPP)]**) and the three hybrid porphyrin dimers (**[VOH$_2$(DPP)$_2$]**, **[CuH$_2$(DPP)$_2$]**, **[VOCu(DPP)$_2$]**) will be shown and discussed. We will start the discussion with the simplest EPR spectra, which are the ones obtained from the two monomers and the metal-free base dimers. All spectra were recorded in a frozen solution of toluene: CH_2Cl_2 1:1 mixture at 30 K. **[VOH$_2$(DPP)$_2$]** and **[CuH$_2$(DPP)$_2$]** solutions were measured with a known concentration (0.2 mM), whereas **[VO(DPP)]** and **[Cu(DPP)]** monomers concentrations were not determined. The porphyrin EPR spectra shown in Figure 8.2 were simulated according to the following spin Hamiltonian:[39]

$$\hat{H}_{\mathrm{M}} = \mu_{\mathrm{B}}\vec{B}\cdot\mathbf{g}_{\mathrm{M}}\cdot\hat{S}_{\mathrm{M}}\cdot\mathbf{A_M}\cdot\hat{I}_{\mathrm{M}} + \sum_{i=1}^{4}\hat{S}_{\mathrm{M}}\cdot A_{\mathrm{N}}\cdot\hat{I}_{\mathrm{N,i}} \qquad (8.1)$$

where $\mathbf{g}_{\mathrm{M}}$ is the g-tensor of the metal porphyrin, $\mathbf{A}_{\mathrm{M}}$ and $\mathbf{A}_{\mathrm{N}}$ are the hyperfine coupling tensors for the metal and the pyrrolic nitrogen nuclei. Figure 8.2 left shows the experimental cw-EPR spectrum of **[VO(DPP)]** (green line) and **[VOH$_2$(DPP)$_2$]** (turquoise line), with the corresponding simulations (orange lines).

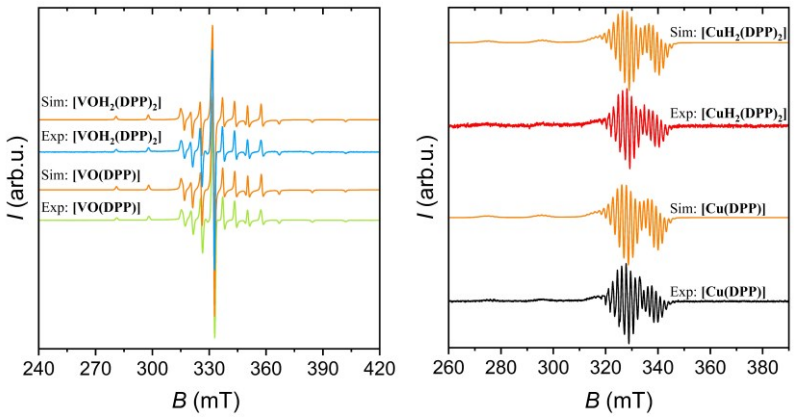

Figure 8.2: Experimental X-band cw-EPR spectra of **[VO(DPP)]** (green line, ν = 9.395 GHz), and **[VOH$_2$(DPP)$_2$]** (turquoise line, ν = 9.392 GHz) (left). Experimental X-band cw-EPR spectra of **[Cu(DPP)]** (black line, ν = 9.393 GHz), and **[CuH$_2$(DPP)$_2$]** (red line, ν = 9.402 GHz GHz) (right).Simulated cw-EPR spectra are shown as orange lines. All experimental spectra were measured at T = 30 K.

Both **[VO(DPP)]** and **[VOH$_2$(DPP)$_2$]** spectra show the characteristic EPR frozen solution pattern of vanadyl porphyrins due to the anisotropic hyperfine coupling of the electron spin with the ^{51}V (I = 7/2) nucleus. No sign of coupling with the four nearby nitrogen atoms of the porphyrin unit is observed since the d_{xy} magnetic orbital of the vanadyl ion is not pointing directly toward the nitrogen donors. The last term of the Hamiltonian (8.1) can therefore be neglected. The simulations assumed a local electronic C4v symmetry with the $\mathbf{g_M}$ and $\mathbf{A_M}$ tensors collinear and axial.

Similarly, the spectra of **[Cu(DPP)]** and **[CuH$_2$(DPP)$_2$]** (see Figure 8.2 right show the typical pattern of Cu^{2+} porphyrins due to the anisotropic hyperfine interaction of the electron spin with nuclei of Cu (^{63}Cu, natural abundance, NA = 69.17%; ^{65}Cu, NA =30.83%; both I = 3/2) and the four coordinated ^{14}N (I = 1). The simulation parameters for all the monometallic porphyrins agree with the values in the literature.[43,44,97]

Notably, the monomers and mono-metalated dimers spectra are very similar. This highlights that after introducing an additional porphyrin unit, both $\mathbf{A_M}$ and $\mathbf{g_M}$ tensors remain axial within the spectral resolution of X-band cw-EPR spectroscopy. All the spin Hamiltonian parameters extracted from the spectra shown in Figure 8.2 are listed in Table 8.1.

The X-band cw-EPR spectrum of **[VOCu(DPP)$_2$]** was also recorded in frozen solution (toluene: CH_2Cl_2 1:1 mixture 0.2 mM at 30 K), and it is shown in Figure 8.3.

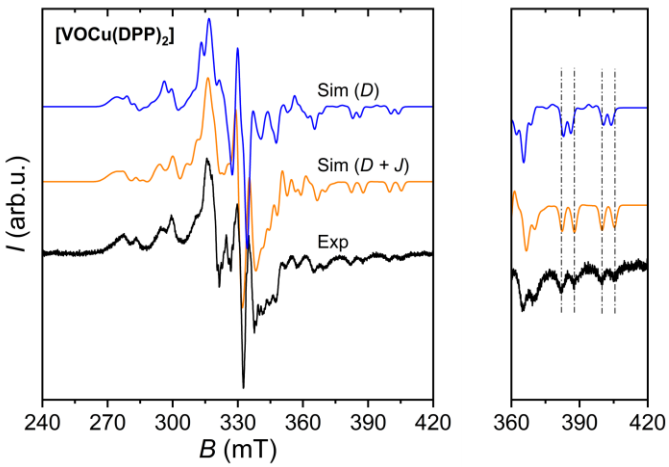

Figure 8.3: Left: Experimental X-band cw-EPR spectra (T = 30 K, frozen solution 0.2 mM in 1:1 toluene/CH_2Cl_2) of **[VOCu(DPP)$_2$]** (ν = 9.394 GHz, black line) together with two relevant spectral simulations of **[VOCu(DPP)$_2$]**. The reported simulations were performed at two different values of J (0 and $-8.0 \cdot 10^{-3}$ cm^{-1}) by keeping the dipolar interaction and θ = 78° constant to highlight the effect of the exchange interaction. Middle: magnification of the high fields spectral region to appreciate the impact of the exchange interaction. The parameters of the simulations are reported in Table 8.1.

The EPR spectrum of **[VOCu(DPP)$_2$]** differs from the superposition of the contribution of the two different metal ions. It is characterized by a larger linewidth than the monometallic dimers, most likely attributable to the dipolar coupling interaction between the two unpaired electron spins of the dyad and a possible distribution of dihedral angles between the two porphyrin units in the frozen solution. The EPR spectrum was simulated based on the following spin-Hamiltonian:

$$\hat{H}_{\mathrm{V-Cu}} = \mu_B \vec{B} \cdot \mathbf{g}_{\mathrm{V}} \cdot \hat{S}_{\mathrm{VO}} + \hat{S}_{\mathrm{VO}} \cdot \mathbf{A}_{\mathbf{V}} \cdot \hat{\mathbf{I}}_{\mathbf{V}} + \mu_{\mathrm{B}} \vec{B} \cdot \mathbf{g}_{\mathrm{Cu}} \cdot \hat{S}_{\mathbf{Cu}} + \hat{S}_{\mathrm{Cu}} \cdot \mathbf{A}_{\mathrm{Cu}} \cdot \hat{\mathbf{I}}_{\mathrm{Cu}} + \sum_{i=1}^{4} \hat{S}_{\mathrm{Cu}} \cdot \mathbf{A}_{\mathrm{N},i} \cdot \hat{I}_{\mathrm{N}} + \hat{S}_{\mathrm{VO}} \cdot \mathbf{J}_{\mathrm{V-Cu}} \cdot \hat{S}_{\mathrm{Cu}} \quad (8.2)$$

which adds to the Zeeman and hyperfine interaction terms of the single centers the interaction contribution described by the matrix $\boldsymbol{J}_{V\text{-}Cu}$. The latter comprises the isotropic component of the exchange interaction J and the through-space dipolar coupling **D,** while we neglected the antisymmetric term:[193]

$$\mathbf{J} \approx J\mathbf{I} + \mathbf{D} = \begin{bmatrix} J + D_x & 0 & 0 \\ 0 & J + D_y & 0 \\ 0 & 0 & J + D_z \end{bmatrix} \quad (8.3)$$

To reduce the number of free parameters, the $\mathbf{g}_{\mathbf{M}}$ and **A** tensor's principal values were fixed at those of their respective monometallic dimers, and their local z-axis was assumed to be perpendicular to the porphyrin planes. Further, the tilting angle between the two porphyrin units was fixed at the experimental value of θ = 78°, and **D** was calculated in the point-dipole approximation using the X-ray data and relative **g**-tensor orientations.[217] Due to the relatively small g-anisotropy, the calculated **D** tensor is essentially axial, with the main axis being directed along the V-Cu direction. Thus, it

is not affected by variation of the dihedral angle.[193] Consequently, the only variable parameter was the exchange interaction *J*.

From a technical point of view, given the large dimension of the problem to be treated, simulations were performed by using the '*hybrid*' option in EasySpin[39], where the nuclear spins of the metal ions were treated exactly while the contribution of the nitrogen nuclei perturbatively. This procedure allowed us to reduce calculation times and the occurrence of simulation artifacts in the central part of the spectrum. In addition, two separate simulations for the Cu isotopes, namely ^{63}Cu and ^{65}Cu, were performed and summed considering their relative natural abundance (0.6915 vs. 0.3085, respectively). Finally, to improve the number of orientations of the powder simulation and the quality of the simulated spectra, simulations as a function of the tilting angle θ and fixed *J* were obtained as the sum of single crystal spectra with orientation and weights defined by the EasySpin function *sphgrid* with 200 knots (ca. 80000 spectra).

A first qualitative analysis of the spectra indicates that the splitting of the outermost lines, corresponding to the parallel transitions of the $V^{IV}O$ unit, can provide a first clue as to the magnitude of the exchange interaction. The splitting simulated assuming a purely dipolar coupling (i.e., $J = 0$, **Figure 8.3**, blue line) is clearly smaller than the experimental results. A preliminary survey (**Figure 8.4**) indicates that the correct splitting of those lines can be obtained with either $J = 2 \cdot 10^{-3}$ (antiferromagnetic) or $J = -8 \cdot 10^{-3}$ cm^{-1} (ferromagnetic). These values differ because when aligning the field along the V=O bond (*i.e.*, the parallel transitions), the dipolar interaction with the copper spin is AF. FM exchange interactions larger than AF ones are therefore necessary to obtain the same splitting, which is proportional to $|J+D_z|$. The survey further shows that the central part of the spectrum is much better reproduced using $J = -8 \cdot 10^{-3}$ cm^{-1} than $J = +2 \cdot 10^{-3}$ cm^{-1}. The best simulation is reported in **Figure 8.3**.

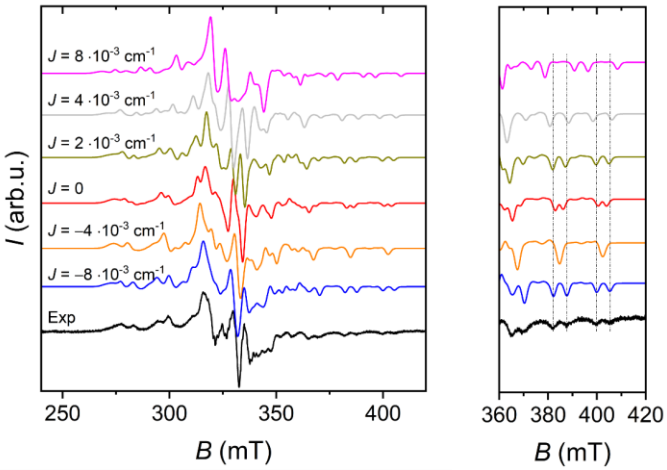

Figure 8.4: X-band cw-EPR spectrum of compound **[VOCu(DPP)$_2$]** simulated with various J (in cm^{-1}) by keeping the same A, g, parameters as **[VOH$_2$(DPP)$_2$]** and **[CuH$_2$(DPP)$_2$]** and fixing **D** as calculated in point dipole approximation. The ***g***-tensors were considered to be 78° tilted to each other. The default *EasySpin*[39] option for the mapping of the sphere was used (*Opt.nKnots = 19)*.

Notably, in contrast to the homometallic vanadyl dimer,[217] the simulated spectra of the heterometallic dimer do not change significantly by varying the $\mathbf{g}_M$ and $\mathbf{A}_M$-tensors tilting angle (i.e., the porphyrin twisting angle), as shown in **Figure 8.5**.

The EPR data clearly show that the VO-Cu exchange coupling is weakly ferromagnetic. Its magnitude falls between those reported for structurally similar meso-meso linked Cu-Cu[100] and VO-VO [217] homometallic dimers, being of opposite sign. This confirms our prediction, based on the deformations brought in by $[VO]^{2+}$ coordination, that local sp (in-plane) and delocalized π (out-of-plane) contributions are responsible for the super-exchange interaction.[23] A comparison between the UV/Vis spectra of **[VOCu(DPP)$_2$]** and **[VO(TrPP)]$_2$** dimers shows for the latter a larger line broadening and more red-shifted Q-bands (Section 11.3)[202,203] confirming the higher conjugation.

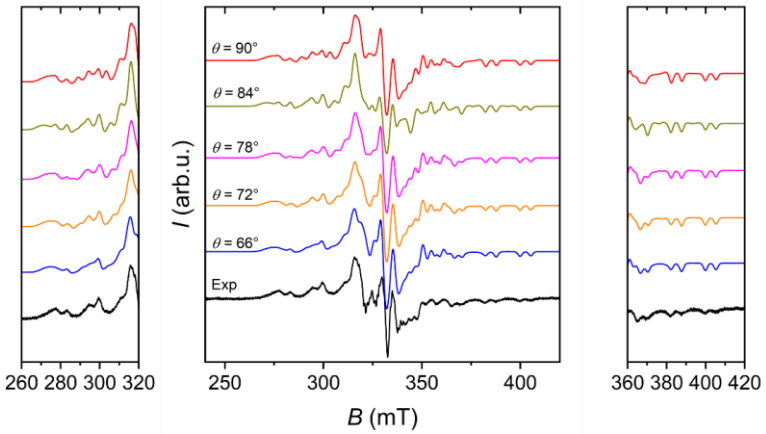

Figure 8.5: X-band cw-EPR spectrum of **[VOCu(DPP)$_2$]** (ν = 9.394 GHz) simulated considering various tilting angles θ, and keeping the same A, g, parameters as **[VOH$_2$(DPP)$_2$]** and **[CuH$_2$(DPP)$_2$]**. J was kept constant at $-8\cdot10^{-3}$ cm^{-1} for all simulations, and **D** was fixed at the value calculated in point dipole approximation. The high (right) and low field (left) regions are plotted in separate graphs to make the slight differences in the simulations visible.

The spin relaxation properties of the compounds **[VOH$_2$(DPP)$_2$]**, **[CuH$_2$(DPP)$_2$],** and **[VOCu(DPP)$_2$]** were studied by pulsed EPR spectroscopy at X-band frequency (**Figure 8.6**). Temperature-dependent inversion recovery and primary echo decay experiments were used to determine T_1 and T_m between 7 and 120 K. The samples were dissolved in d_8-toluene (0.2 mM) and measured as frozen solutions. All measurements were performed at a magnetic field setting corresponding to the maximum intensity of the echo-detected EPR spectrum. T_m values were extracted by fitting the experimental decay traces using a stretched exponential function (Chapter 3, equation 3.21). In contrast, T_1 values were obtained by a bi-exponential fitting (Chapter 3, equation 3.20) of the inversion recovery traces. In **Figure 8.6**, only the slow component of the bi-exponential fit, usually taken to represent the spin-lattice relaxation (T_1), is plotted; the fast component[173,218] is not shown because it is associated with spectral diffusion effects[173,218] (*i.e.*, excitation bandwidth smaller than the spectral width). A list of all parameters extracted from the inversion recovery and primary echo decay experiments can be seen in **Table 8.2**, **8.3**, and **8.4**.

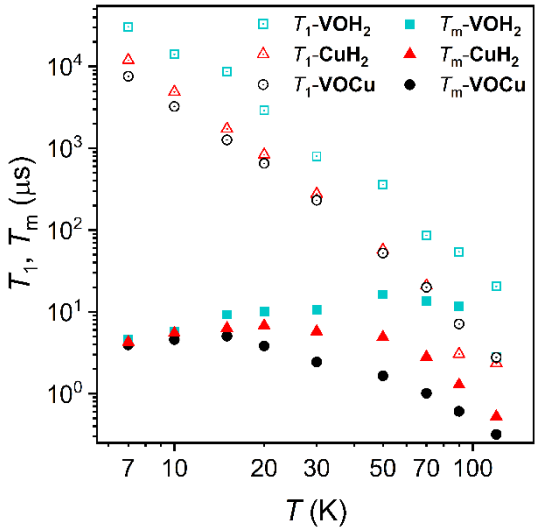

Figure 8.6: Temperature dependence of T_1 (left) and T_m (right) for compounds **[VOH$_2$(DPP)$_2$]** (turquoise squares, **VOH$_2$**), **[CuH$_2$(DPP)$_2$]** (red triangles, **CuH$_2$**), and **[VOCu(DPP)$_2$]** (black circles, **VOCu**) measured at 340 mT at X-band frequency in a 0.2 mM frozen d_8-toluene solution.

[VOH$_2$(DPP)$_2$] has T_1 and T_m values longer than **[CuH$_2$(DPP)$_2$]**. In both cases, these values are comparable with the relaxation times of other monomeric $[VO]^{2+}$[57,97,126] or Cu^{2+} complexes.[86,96,126] The faster spin-lattice relaxation of Cu^{2+} can be attributed to the larger spin-orbit coupling that makes the spin system more sensitive to molecular vibrations. **[VOCu(DPP)$_2$]** has T_1 values very similar to **[CuH$_2$(DPP)$_2$]**, suggesting that the presence of the nearby slower relaxing vanadyl unit does not negatively impact the spin-lattice relaxation. T_m values of **[VOCu(DPP)$_2$]** are instead slightly faster than those of **[VOH$_2$(DPP)$_2$]** and **[CuH$_2$(DPP)$_2$]** and also lower than those reported for dimeric $[VO]^{2+}$ bimetallic complexes, including the homometallic vanadyl porphyrin dimer **[VO(TrPP)]$_2$**.[78,82,99,219]

Table 8.1: Principal values of the Spin-Hamiltonian tensors for compounds **[VO(DPP)]**, **[Cu(DPP)]**, **[VOH$_2$(DPP)$_2$]**, **[CuH$_2$(DPP)$_2$]**, and **[VOCu(DPP)$_2$]**, obtained from the simulation of frozen solution samples. For the simulation of the spectra of **[VOCu(DPP)$_2$]**, a tilting angle of 78° was assumed between Cu^{2+} and V^{4+} tensors. **D** has been calculated in the point-dipole approximation with *z* perpendicular to the Cu-porphyrin plane and *y* along the meso-meso bond.

		[VO(DPP)]	**[Cu(DPP)]**	**[VOH$_2$(DPP)]**	**[CuH$_2$(DPP)]**	**[VOCu(DPP)$_2$]**	
M		V	Cu	V	Cu	V	Cu
$\mathbf{g}_M$	*x* *y* *z*	1.985 1.985 1.964	2.051 2.051 2.195	1.985 1.985 1.964	2.051 2.051 2.195	1.985 1.985 1.964	2.051 2.051 2.195
$\mathbf{A}_M$ (MHz)	*x* *y* *z*	162 162 475	60 60 626	162 162 476	60 60 626	162 162 476	60 60 626
$\mathbf{A}_N$ (MHz)	*x* *y* *z*	- - -	54 43 45	- - -	54 43 45	- - -	54 43 45
J (cm^{-1})						$-8 \cdot 10^{-3}$	
D (cm^{-1})	*x* *y* *z*					$3.0 \cdot 10^{-3}$ $-6.2 \cdot 10^{-3}$ $3.2 \cdot 10^{-3}$	

Table 8.2: Parameters of bi-/stretched exponential fit functions for inversion recovery and primary echo decay experiments for **[VOH$_2$(DPP)$_2$]**. The sample was measured in frozen solution (0.2 mM, d_8-toluene).

T (K)	A_s	$T_{1,s}$ (µs)	A_f	$T_{1,f}$ (µs)	T_m (µs)	β
7	12864	58141	16962	9439	2.52	0.53
10	11836	22391	9513	3689	2.95	0.51
15	1737	8668	1737	8667	8.71	0.88
20	4575	4928	3630	357	6.47	0.58
30	6530	1733	8259	57	9.71	0.83
50	186	404	6158	359	17.15	1.14
70	89	86	3483	85	13.36	0.97
90	410	58	2567	53	11.67	0.99
120	12149	27	4234	1	1.43	0.51

Table 8.3: Parameters of bi-/stretched exponential fit functions for inversion recovery and primary echo decay experiments for **[CuH$_2$(DPP)$_2$]**. The Sample was measured in frozen solution (0.2 mM, d_8-toluene).

T (K)	A_s	$T_{1,s}$ (µs)	A_f	$T_{1,f}$ (µs)	T_m (µs)	β
7	32633	18328	22954	2881	2.3	0.52
10	16807	7129	10504	1282	3.4	0.57
15	14186	2212	5073	368	4.5	0.64
20	10972	1000	3260	269	5.7	0.75
30	15190	323	3842	93	5.0	0.77
50	78914	65	16703	19	3.5	0.63
70	7209	25	1697	6	1.7	0.55
90	17159	8	38240	0.6	0.8	0.56
120	20207	3	4440	0.02	0.5	0.79

Table 8.4: Parameters of bi-/stretched exponential fit functions for inversion recovery and primary echo decay experiments for **[VOCu(DPP)$_2$]**. The Sample was measured in frozen solution (0.2 mM, d_8-toluene).

T (K)	A_s	$T_{1,s}$ (µs)	A_f	$T_{1,f}$ (µs)	T_m (µs)	β
7	13313	14083	15811	2140	2.47	0.57
10	23247	5369	20810	848	2.65	0.54
15	15229	2018	12306	335	3.54	0.63
20	13236	983	9831	207	2.69	0.63
30	8642	339	6138	78	1.53	0.58
50	24206	101	41813	24	1.77	1.23
70	53177	26	20581	5	1.12	1.54
90	89060	8.8	23500	1	0.68	3.39
120	20408	2.8	20408	2.8	0.35	1.49

8.3 Computational states

The accurate determination of the Spin-Hamiltonian parameters of **[VOCu(DPP)$_2$]** allowed us to envision the microwave operation of the dimeric unit as a controlled-NOT quantum gate. This gate is fundamental for realizing a universal quantum computer. We defined the computation states by choosing the ^{51}V electronic spin as the control qubit and the ^{65}Cu spin as the target one (**Figure 8.7a**). By applying a field of 1.3 T, the nuclear and electronic spin states are factorized, and the microwave radiation in the Q-band range (ca. 30 GHz) induces a transition from the $m_s = -1/2$ to the $m_s = +1/2$ states (labeled as computational states in **Figure 8.7b**).

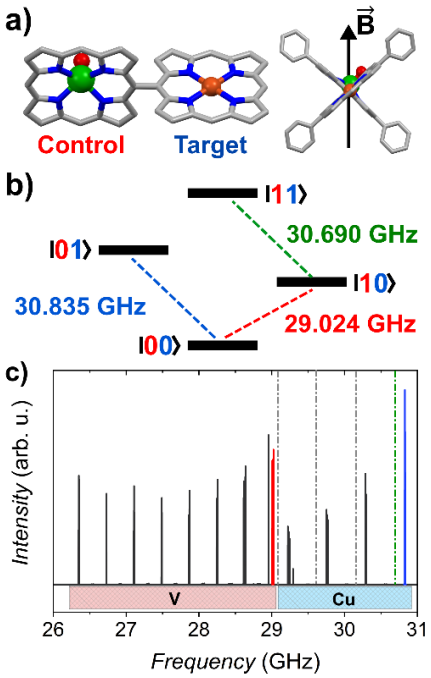

Figure 8.7: a) Orientation of the static magnetic field with respect to the control and target qubits; **b**) Computed energy differences between states involving control (red) and target qubit (blue and green) electronic spin transitions highlighted with the same color in the frequency-swept absorption spectrum (**c**) simulated for B=1.3 T, T=100 mK and the Spin-Hamiltonian parameters reported in **Table 8.1**. Gray dashed lines refer to other possible choices of hyperfine levels of the target.

In difference to the homometallic vanadyl dimer, addressability of the two spins in **[VOCu(DPP)$_2$]** is warranted for most orientations of the static magnetic field, including along the bisector of the two porphyrin planes. **Figure 8.7c** shows the frequency-swept absorption spectrum computed for this orientation at 100 mK. The spectrum can be divided into a low-frequency region where the eight hyperfine transitions of the ^{51}V are visible and a high-frequency region where four transitions (shown only for the ^{65}Cu isotope for clarity) can be identified. The nuclear spins are not polarized at this temperature, and the intensity is almost equally distributed over the different hyperfine lines. Focusing on the highest hyperfine transition of the target qubit, we computed that the transition occurs at 30.835 GHz if the control qubit is in its ground state ($|00\rangle \rightarrow |01\rangle$, the blue line in **Figure 8.7b** and **Figure 8.7c**. Upon excitation of the control qubit – for instance, irradiating at 29.024 GHz (red line) – microwaves at 30.690 GHz can be absorbed, corresponding to $|10\rangle \rightarrow |11\rangle$ (green line). Different hyperfine lines of the target can be selected to reduce the frequency separation between the control and the target absorptions while maintaining ca. 200 MHz of separation induced by the control (gray dashed lines in **Figure 8.7c**, as commercial low-Q cavities have a bandwidth of ca. 400 MHz.

Interestingly, the scenario described in **Figure 8.7** is rather robust against different operating conditions. To demonstrate this, we repeated the analysis for different magnetic field orientations. If the static magnetic field is aligned along the target *z*-axis, the target and control transitions are slightly more separated in frequency (see **Figure 8.8**), while a separation similar to that in **Figure 8.7c** is observed upon reduction of the tilting angle between the two porphyrin units (**Figure 8.9**).

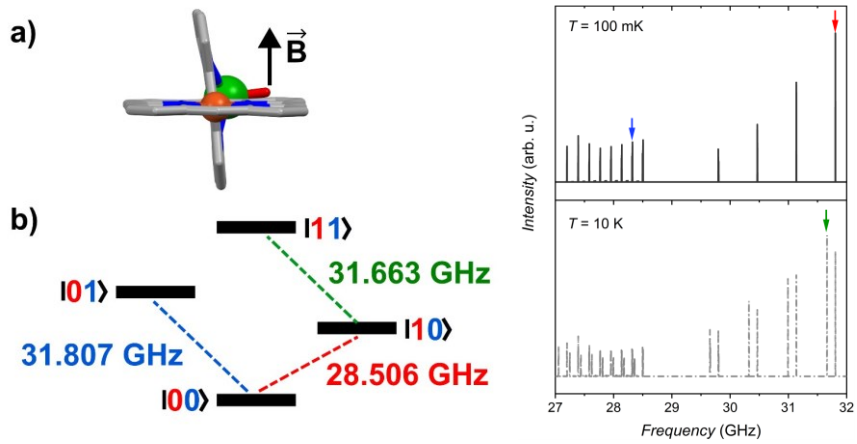

Figure 8.8: **a**) Molecular sketch with the orientation of the *B* parallel to the target z-axis, *i.e.*, perpendicular to the Cu^{2+} porphyrin unit. The tilting angle between the porphyrin units is set to 78°. **b**) Computed energy differences between states involving control (red) and target qubit (blue and green) electronic spin transitions highlighted with the same color in the frequency-swept absorption spectrum (right) simulated for *B*=1.3 T, *T* = 100 mK and the Spin-Hamiltonian parameters reported in Table 8.1.

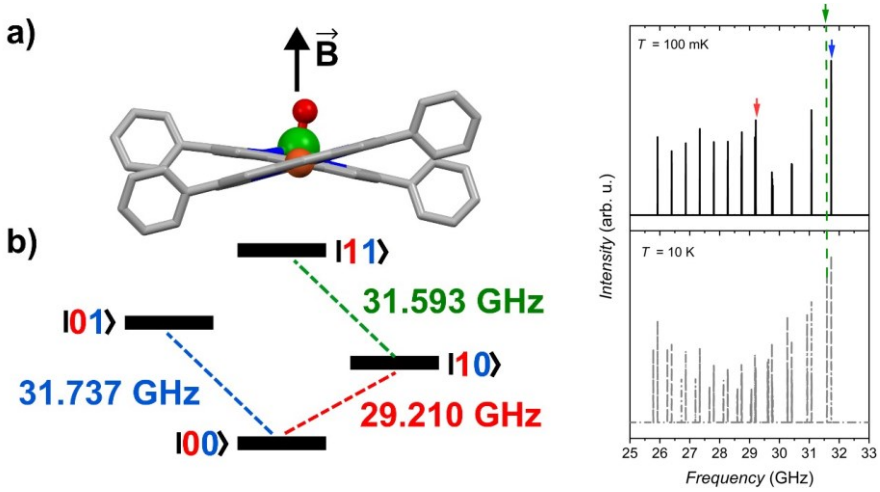

Figure 8.9: **a**) Molecular sketch with the orientation of *B* parallel to the bisector of the two porphyrin planes. The tilting angle between the porphyrin planes is set to 20°. **b**) Computed energy differences between states involving control (red) and target qubit (blue and green) electronic spin transitions highlighted with the same color in the frequency-swept absorption spectrum (right) simulated for *B* = 1.3 T, *T* = 100 mK and the Spin-Hamiltonian parameters reported in Table 8.1.

8.4 DFT calculations

DFT geometry optimization in gas-phase was carried out to shed light on the structural properties of the compound **[VOCu(DPP)$_2$]** because of the low quality of the experimental structure determination. The tilting angle computed for the optimized structure, θ ~84°, is close to the value θ ~78° of the X-ray structure. To calculate the isotropic exchange parameters *J*, we used the Broken Symmetry (BS) approach within the full projected formula,[194,199,200] as already presented in Chapter 6. The corresponding calculated *J* value ($-1.2\cdot10^{-2}$ cm^{-1}) is in very good agreement with the one estimated from the EPR simulations. It confirms the trend expected upon substituting vanadyl with copper ions in singly-linked porphyrin dimers, *i.e.*, a reduction in the magnitude of the coupling and a change of the nature from antiferromagnetic to ferromagnetic.[217]

This observation corresponds to the behavior of the seminal copper/vanadyl dimer reported by Kahn *et al.*,[41] but at a different level of complexity. The magnetic orbitals of the Cu^{2+}($d_{x^2-y^2}$) and $[VO]^{2+}$ (d_{xy}) ions are orthogonal by symmetry (see **Figure 8.10**), justifying the ferromagnetic nature of the interaction in **[VOCu(DPP)$_2$]** and its smaller value in comparison to **[VO(TrPP)]$_2$**.[217] Moreover, as the Cu^{2+} ion lies in the porphyrin ligand's plane, the magnetic orbital overlap with the porphyrin out-of-plane orbitals (π-system) is minimal. This significantly reduces the antiferromagnetic contributions that are active when the porphyrin rings are tilted.

To analyze this point in more depth, we performed single-point *J*-value calculations on two additional geometries. The first corresponds to the tilting angle set to the value determined by single crystal X-ray analysis. In contrast, the second represents a possible critical point where the tilting angle is set to 90°. No significant difference in *J* is computed for the X-ray or optimized structures, while a small reduction in the magnitude of *J* is derived for θ = 90. We have seen in Chapter 6 that for **[VO(TrPP)]$_2$** angles close to 90° correspond to a relative maximum of $|J|$. The presence of two pathways - the ferromagnetic one through σ porphyrin orbitals and the antiferromagnetic one involving π orbitals - nicely explains the different angular

dependence of the computed exchange interaction in hetero- and homo-metallic dimers. The exchange interaction mediated by out-of-porphyrin-plane orbitals is expected to be antiferromagnetic and maximum at $\theta = 90°$, where the overlap with the in-plane orbital of the metal unit is highest. In the case of **[VOCu(DPP)$_2$]**, this antiferromagnetic contribution adds to the ferromagnetic one with the opposite sign, thus slightly reducing $|J|$ for $\theta = 90°$.

We also computed the exchange coupling for an optimized structure of a triply fused dimer (**Figure 8.11**). As expected, a much stronger ferromagnetic coupling of $J = -0.36$ cm^{-1} is calculated, which would hamper the single spin addressability. Similar to the singly linked case, the sign of the coupling is consistent with Kahn's model. Its magnitude is intermediate between that of triply-fused Cu[100] and VO homometallic dimers[219], the former being the largest one.

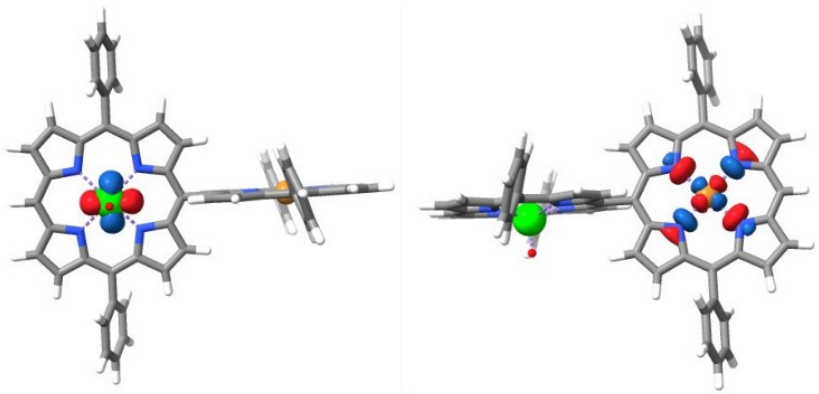

Figure 8.10: Two orthogonal views of the isodensity (ψ = 0.05 (e bohr^{-3})$^{1/2}$) surfaces of magnetic orbitals for compound **[VOCu(DPP)$_2$]** computed at the B3LYP level. The code color is V (green), Cu (orange), N (blue), O (red), C (gray), and H (white).

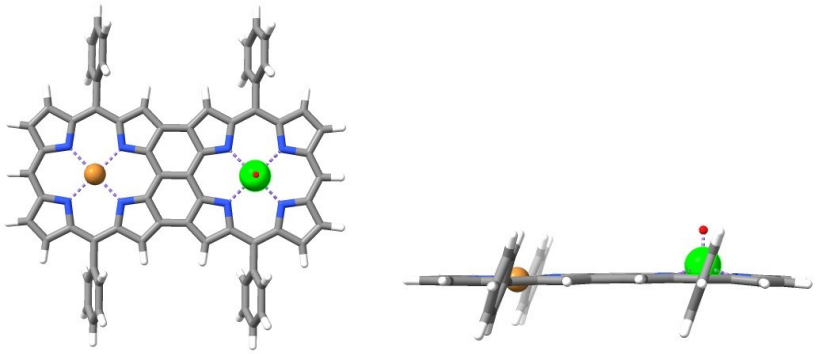

Figure 8.11: Two orthogonal views of the optimized structure of the compound assuming triply linked **[VOCu(DPP)$_2$]**. The code color: V (green), Cu (orange), N (blue), O (red), C (grey), and H (white).

The combined results in Chapter 6 and Chapter 8 show that paramagnetic bimetallic $[VO]^{2+}$ bisporphyrins are promising candidates for developing two-qubit quantum gates.

The exchange and coherence properties of this system form a sound starting point for further investigations that are presented in the next chapter.

PhD author contribution:

Results discussed in this chapter are published in: *Angew. Chem. Int. Ed.* **2023**, DOI 10.1002/anie.202312936., and the full paper can be found in the appendix.

The author of this Thesis contributed to the synthesis of all molecules studied and simulated all cw-EPR spectra present in this Chapter (helped significantly by Prof. Lorenzo Sorace, Dr Alberto Privitera & Prof. Roberta Sessoli).

9 The chemical versatility of porphyrins

The last three chapters have showcased the primary outcomes and findings of this PhD thesis, but other porphyrinic systems were studied as well. While ongoing investigations into these porphyrinic systems remain incomplete, it is worthwhile to include these preliminary results to emphasize the versatility of porphyrinic systems. In Section 9.1, we present a linear porphyrin trimer with the potential for inducing a two-qubit gate through photoexcitation of the central moiety. In Section 9.2, we present porphyrin building blocks deposited onto an Au(111) single crystal, which have the potential to react on the metal surface upon annealing, thus forming dimers directly on the surface.

9.1 Towards light controlled molecular spin qubits: A study on vanadyl(IV) porphyrin trimers

In Chapters 6 and 8, it was shown that one of the key capabilities of porphyrin complexes is their ability to create weakly exchange coupled paramagnetic systems. This feature can be exploited to develop two-qubit quantum gates. The next step is to improve such systems by introducing a physical switch in the quantum logic gate that can promote or disrupt the communication between the two electron spins. Some possible implementations of this physical switch have been proposed for dimeric Cr_7Ni-rings connected with an acetate-bridged copper(II)-ion[220] and a redox switchable Ru_2Co complex.[221]

These two examples required, however, quite “uncontrollable” perturbations to modify the switch state (temperature and an external potential) and thus to operate the gate. For this reason, the focus was recently shifted to photo-excitable linkers to control the exchange interaction between two radicals.[222] One option for a switchable exchange interaction molecule is a paramagnetic molecule containing a diamagnetic unit that interacts with the paramagnetic part upon photoexcitation, forming weakly exchange-coupled systems.[38,223,224] Porphyrin

dimers are among these systems,[225–227] but none reported in literature are directly linked. The photoswitchable linker must form a triplet state upon photoexcitation, which should interact with the paramagnetic unit, thus populating a quartet state. It was shown that zinc(II) diamagnetic units are more propitious to populate the quartet states due to enhanced intersystem crossing (ISC). In contrast, free-base porphyrin units only showed weak exchange coupling.[224]

Based on these results, we decided to extend the possibility of photoexciting diamagnetic porphyrin units by introducing such a unit between two vanadyl porphyrins. The exchange interaction between the two vanadyl units might be turned on by the photoexcitation of the central porphyrin. These kinds of linear trimers would be an improved version of the aforementioned **[VO(TrPP)]$_2$** (Chapter 6).

To realize the linear *m*-*m* linked trimer (**Scheme 9.1**), we chose a free-base porphyrin as the central unit. This might contrast with what was explained earlier, but because of optical selectivity, the free-base porphyrin might be more suitable in linear, directly linked porphyrin systems. This is evident when comparing the UV/Vis absorption spectra in the Q-band region of free-base and metalated porphyrins (see Chapter 5). Metalation of the free-base porphyrin can anyhow be achieved easily if no exchange interaction is measured for the free-base version of the trimer.

Hybrid porphyrin trimers are synthesized via *Suzuki-Miyaura* coupling in much the same way as reported for the hybrid porphyrin dimers described in Chapter 8. The key difference is that the reactant, which will form the central free-base porphyrin, must be functionalized on both *m*-positions. Good starting materials are bis-iodo porphyrins (**[VO(I$_2$DPP)]**, **Scheme 9.1**) or bis-borylated porphyrins (Bpin$_2$DPP, **Scheme 9.1**). Bis-borylated porphyrins are preferred over bis-iodinated ones due to their better solubility in the DMF/toluene solvent mixture used for this reaction. Consequently, the mono-iodinated vanadyl porphyrin is selected as the porphyrin unit for constructing the trimer's peripherals. The reaction between **[VO(IDPP)]** and Bpin$_2$(DPP) yields the linear porphyrin trimer (**[{VO}$_2$(DPP)$_2$(H$_2$DPP)]**, **Scheme 9.1**).

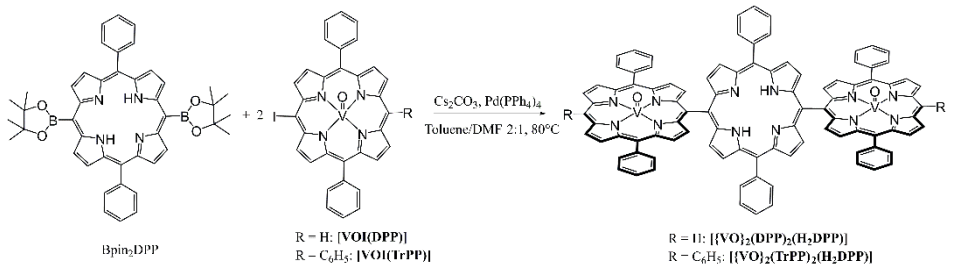

Scheme 9.1: Reaction scheme for the realization of either **[{VO}$_2$(DPP)$_2$(H$_2$DPP)]** (R = H) or **[{VO}$_2$(TrPP)$_2$(H$_2$DPP)]** (R = C_6H_5).

The purification of the crude product was done with column chromatography (flash SiO_2 petroleum ether: CH_2Cl_2:NEt_3 1:1:0.01). Four main fractions were detected and separated during the column. According to UV/Vis analysis, the last fraction was the hybrid **[{VO}$_2$(DPP)$_2$(H$_2$DPP)]** trimer. The MALDI-Orbitrap analysis also revealed that the **[{VO}$_2$(DPP)$_2$(H$_2$DPP)]** fraction is contaminated with a linear porphyrin tetramer (**Figure 9.1**) that was not possible to separate using the selected eluent mixture. The formation of the tetramer is likely caused by contamination of **[VO(I$_2$DPP)]** that is formed during the iodination reaction and cannot be separated with column chromatography or recrystallization.

A second column chromatography on flash SiO_2 was performed, using as an eluent mixture hexane: CH_2Cl_2 1:2. As seen from **Figure 9.2** left; two orange bands were visible during the column elution. The first fraction (with the lowest retention time) was confirmed to be the pure **[{VO}$_2$(DPP)$_2$(H$_2$DPP)]** molecule, according to MALDI-Orbitrap analysis (**Figure 9.2**, right).

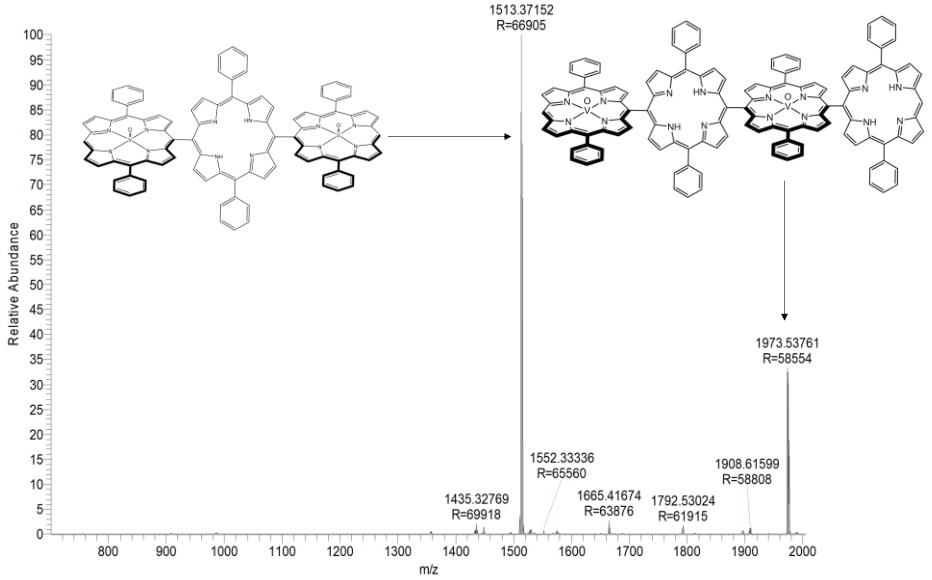

Figure 9.1: MALDI-Orbitrap spectra of the fourth fraction of the column chromatography on the crude **[{VO}$_2$(DPP)$_2$(H$_2$DPP)]** powders. Another m/z signal of 1973.53761 is allocable to a linear porphyrin tetramer contaminant.

The final purification step significantly reduced the yields. After the first column, a yield of 52% was obtained for the impure **[{VO}$_2$(DPP)$_2$(H$_2$DPP)]** powders, but a substantial amount of the desired product still cannot be separated from the second fraction of the column, mainly containing tetramer molecules. Therefore, the overall yield is reduced to 15%. Furthermore, bands become broader during the column, leading to more than half of the first fraction mixing with the second. To mitigate this issue, it is necessary to column only a small amount of crude product and use larger columns to prevent band aggregation during elution. Attempts to obtain crystals of **[{VO}$_2$(DPP)$_2$(H$_2$DPP)]** were unsuccessful.

For this reason, the halogenated starting reactant was changed to **[VO(ITrPP)]**. The [**VO(ITrPP)]** molecule has one *m*-position blocked by the phenyl substituent, thus not allowing a di-iodination even if iodine is used in excess. [**VO(ITrPP)]** was synthesized following the same procedure as **[VO(IDPP)]**.

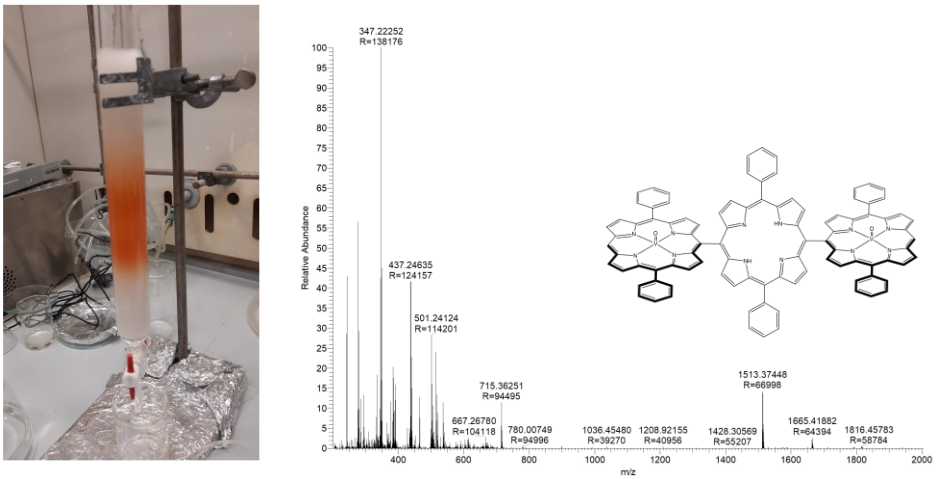

Figure 9.2: Second column chromatography purification of **[{VO}$_2$(DPP)$_2$(H$_2$DPP)]** powders that was performed to remove the porphyrin tetramer impurity. The faster (first band) corresponds to **[{VO}$_2$(DPP)$_2$(H$_2$DPP)]**, whereas the slower (second band) corresponds to the tetramer impurity (left). MALDI-Orbitrap analysis (right) confirmed that the tetramer was removed from the final product.

The *Suzuki-Miyaura* coupling with Bpin$_2$(DPP) (see Chapter 11 for full synthetic procedure) resulted in the formation with **[{VO}$_2$(TrPP)$_2$(H$_2$DPP)]** (**Scheme 9.1**). **Figure 9.3** left shows the column chromatography of crude **[{VO}$_2$(TrPP)$_2$(H$_2$DPP)]** product, and **Figure 9.3** right shows the MALDI-Orbitrap patterns obtained from the third and slowest fraction of the column, which turned out to be **[{VO}$_2$(TrPP)$_2$(H$_2$DPP)]**. The overall yield of **[{VO}$_2$(TrPP)$_2$(H$_2$DPP)]** was 60 %. Part of the product is lost because of the formation of **[VO(TrPP)(H$_2$DPP)]** that was confirmed by UV/Vis analysis and was isolated in 20 % yield. Additional side reactions are porphyrin radicalization and loss of the functional groups of the iodinated or borylated porphyrins during the reaction process, forming **[VO(DPP)]** or H$_2$TrPP monomers. This problem can, in principle, be resolved by using less base for the reaction (2 equivalents instead of 4). Optimization of the synthetic procedure in this direction is still ongoing. Moreover, **[{VO}$_2$(TrPP)$_2$(H$_2$DPP)]** crystals were still not obtained.

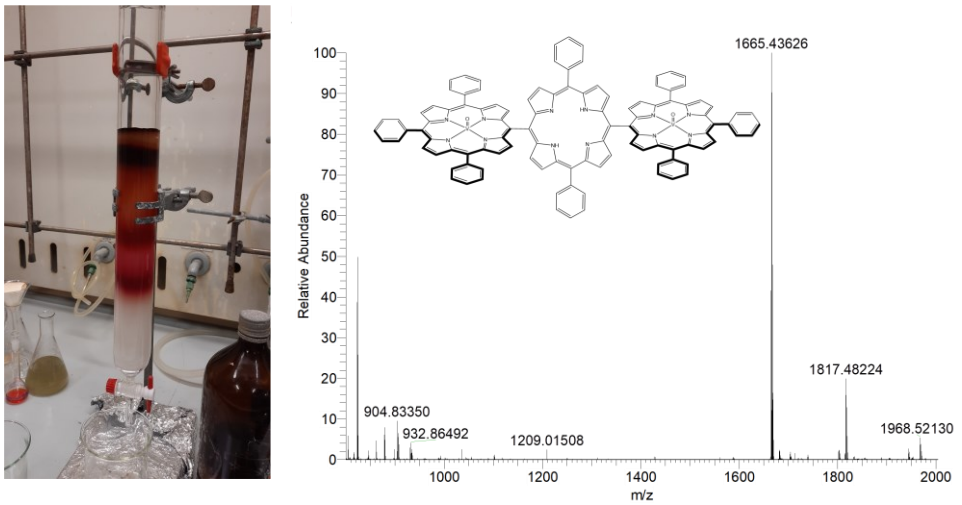

Figure 9.3: column chromatography purification of **[{VO}2(TrPP)2(H2DPP)]** powders (left). The faster (first band) corresponds to either H_2DPP or **[VO(TrPP)]** monomer, whereas the second band is a VO-H_2 hybrid porphyrin dimer, according to ESI-MS. The third fraction is the desired **[{VO}$_2$(TrPP)$_2$(H$_2$DPP)]** trimer. MALDI-Orbitrap analysis (right) of **[{VO}$_2$(TrPP)$_2$(H$_2$DPP)]**.

After the purification of the two linear porphyrin trimers, their magnetic properties were studied by means of X-band cw-EPR spectroscopy and as frozen solutions (toluene: CH_2Cl_2 1:1). Figure 9.4 shows both the experimental and simulated spectra of **[{VO}$_2$(DPP)$_2$(H$_2$DPP)]** and **[{VO}$_2$(TrPP)$_2$(H$_2$DPP)]**. Since the experimental spectra of both trimers are very similar to monomeric **[VO(TPP)]**,[97] and **[VO(TrPP)]**[217] they were simulated by considering two-non interacting spin centers, according to the spin-Hamiltonian (6.1)[39]

The best simulation *g*- and *A*-values (see Figure 9.4 and Table 9.1) are similar to the mentioned porphyrin vanadyl(IV) monomers. This result is unsurprising because the spin-spin distance is too long to allow a dipolar or exchange interaction detectable in a cw-EPR spectrometer at low temperatures. However, this is precisely our goal, as the interaction must be off when the central porphyrin is not photoexcited.

Time-resolved EPR spectroscopy, which records the absorption/emission of microwaves after a light pulse, is the key technique to

characterize the spin interactions mediated by the photoexcited porphyrin in the triplet state. These experiments will be performed at Northwestern University in Evanston, IL (United States) in the frame of a collaboration with Prof. *Michael R. Wasielewski* after the submission of this thesis.

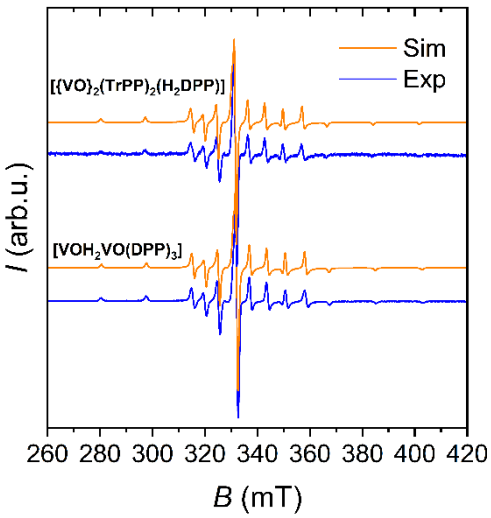

Figure 9.4: simulated (orange line) and experimental (blue line) X-band cw-EPR spectra of **[{VO}$_2$(DPP)$_2$(H$_2$DPP)]** (c = 0.2 mM, ν = 9.398 GHz) and **[{VO}$_2$(TrPP)$_2$(H$_2$DPP)]** (c = 0.1 mM, ν = 9.375 GHz) frozen solutions (CH_2Cl_2:toluene 1:1). Both spectra were measured at T = 30 K.

Table 9.1: Best spin-Hamiltonian parameters obtained for **[VOH$_2$VO(DPP)$_3$]** and **[{VO}$_2$(TrPP)$_2$(H$_2$DPP)]** frozen solutions in the X-band region of the cw-EPR.

Samples	g	A (MHz)
[{VO}$_2$(DPP)$_2$(H$_2$DPP)]	g_x = 1.987 g_y = 1.987 g_z = 1.964	A_x = 168 A_y = 168 A_z = 480
[{VO}$_2$(TrPP)$_2$(H$_2$DPP)]	g_x = 1.986 g_y = 1.986 g_z = 1.963	A_x = 165 A_y = 165 A_z = 477

On the assumption that the outcomes of the experiments show that photoexcitation of the central porphyrin does result in a weak exchange coupled system, we can expect

a further increase in interest in linear porphyrinic systems. The linear trimer synthesized may feature two identical, spatially aligned vanadyl units not tilted relative to each other. This design is not optimal for quantum computation as the two vanadyl units must be distinguishable. However, this study was meant to show and optimize the photoexcitation of the central porphyrin. We, therefore, opted to start with a simpler system and concentrate on the photophysical studies before beginning to move on to a more suitable complex. Once an exchange coupling is confirmed and understood, the design of a hybrid $[VO]^{2+}$-H_2-Cu trimer (**[{VO}(TrPP){Cu}(TrPP)(H_2DPP)]**) should be undertaken. Such trimers could synthetically be achieved, as shown in **Scheme 9.2**, and have two distinguishable spins, separated by the free-base or Zn^{2+}-porphyrin, which makes this kind of porphyrin class even more interesting than hybrid porphyrin dimers. Indeed, we can expect an increasing interest in such systems in the quantum computing community.

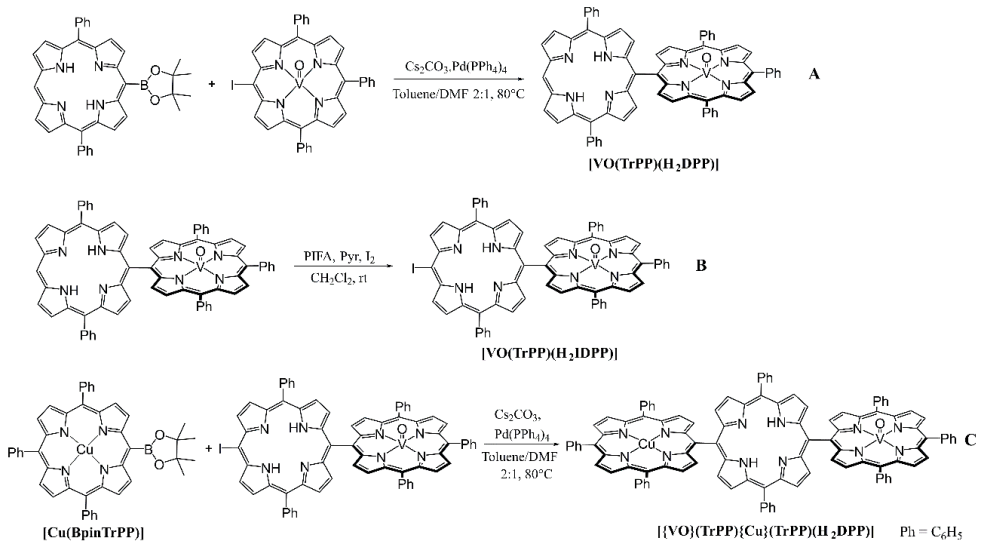

Scheme 9.2: Possible reaction routes for obtaining a hybrid $[VO]^{2+}$-H_2-Cu trimer. *Suzuki-Miyaura* coupling between a BPin(DPP) and **[VO(ITrPP)]** yields an asymmetric hybrid $[VO]^{2+}$-H_2 dimer **[VO(TrPP)(H_2DPP)]** (**A**). This dimer is then iodinated to obtain **[VO(TrPP)(H_2IDPP)]** (**B**), which can be used for another *Suzuki-Miyaura* coupling with **[Cu(BpinTrPP)]** to obtain the final hybrid linear trimer **[{VO}(TrPP){Cu}(TrPP)(H_2DPP)]** (**C**).

9.2 Synthesis and surface deposition of **[M(BrTrPP)]** building blocks

Throughout this thesis, we have repeatedly emphasized one key advantage of porphyrinic systems, *i.e.*, their neutral character and thermal stability that open the possibility of depositing them on a wide range of metal substrates with thermal sublimation. This feature may, in principle, enable the development of prototypical devices, particularly when harnessing porphyrin dimers with two interacting paramagnetic centers. In this thesis, after having characterized the properties of porphyrin homo- and hetero- dimers in bulk phases, we took the initial steps toward characterizing the targeted dimeric molecular species after their deposition onto a metal surface. The latter can be achieved by two strategies: by depositing dimeric species hosting two metal centers or by creating dimers on the surface starting from the deposition of molecular building blocks. During my PhD, I contributed to the synthesis and preliminary experiments that explored this second route. We started from the deposition of brominated type **[M(BrTrPP)]** (M = $[VO]^{2+}$, Cu^{2+}) porphyrin building blocks. We explored the possibility of fabricating dimers by *Ullman* reactions achieved by thermal annealing the monomers on the surface.[166]

Scheme 9.3 shows the synthesis of the two porphyrins that were used as building blocks (**[Cu(BrTrPP)]** and **[VO(BrTrPP)]** respectively); the third row represents the cross-coupling reaction on the surface to be performed once the successful deposition of the monomers has been achieved.

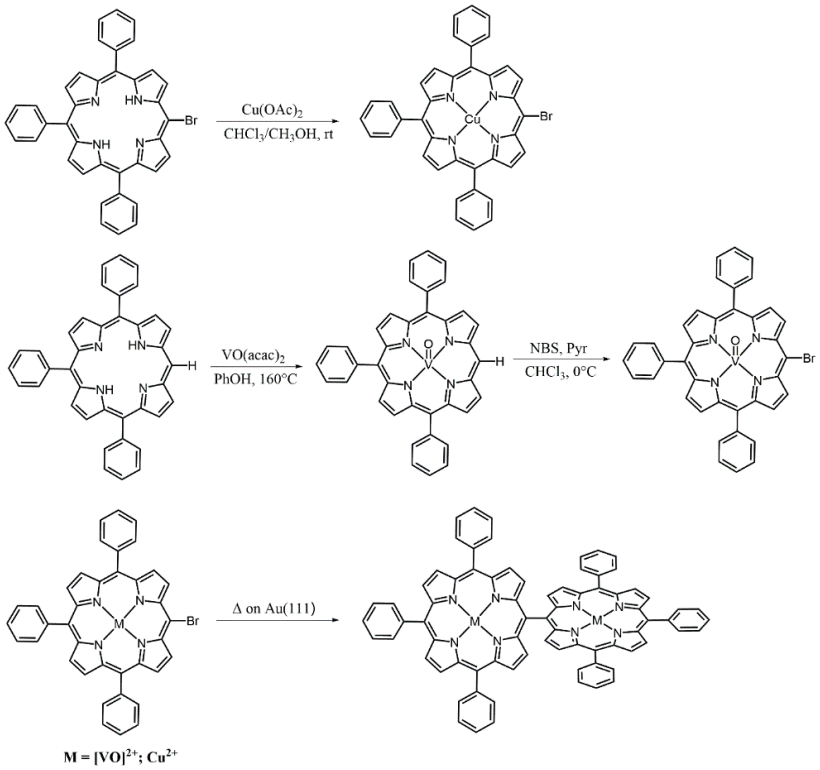

Scheme 9.3: Synthesis of the building blocks **[Cu(BrTrPP)]** (top) and **[VO(BrTrPP)]** (middle) that are capable of reacting on a metal substrate after being sublimated to form **[M(BrTrPP)]$_2$** dimers (bottom).

The synthesis of the bromo-functionalized porphyrins along with the Cu^{2+} or $[VO]^{2+}$ metalations was performed according to previously published procedures.[127,137,228] In detail, while **[Cu(BrTrPP)]** is synthesized by simple metalation of a 5-bromo-10,15,20-triphenylporphyrin (H_2BrTrPP) with $Cu(OAc)_2$, **[VO(BrTrPP)]** must be synthesized using a two-step approach. First, $[VO]^{2+}$ is inserted in the free base H_2TrPP ligand, yielding **[VO(TrPP)]**. As a second step, **[VO(TrPP)]** is brominated to yield **[VO(BrTrPP)]** (Scheme 9.3). This procedure is necessary because H_2BrTrPP decomposes due to the harsh thermal conditions during the $[VO]^{2+}$ metalation.

Once the two porphyrin building blocks were synthesized and fully characterized, the first deposition experiments were performed. All samples were

deposited on Au(111) single crystals in UHV. This is a chemically inert metal well-suited for successive *Ullman*-coupling reactions.[166] The results of this step were evaluated by XPS by fitting the components according to what was reported in the literature for similar porphyrin systems.

Figure 9.5 shows the XPS-spectra of the **[VO(BrTrPP)]** deposit in the C*1s* (**a**), N*1s* (**b**), Br*3p* (**c**), and VO*2p* O*1s* (**d**) regions. The main signal in the C*1s* region (Figure 9.5**a**) comprises three different components. The main component (cyan area) is attributed to the C=C bonds (284.7 eV),[229,230] the second component (orange area) is attributed to the C=N bonds (284.6 eV),[229,230] and the smallest component (red area) attributed to the C-Br bond (286.2 eV).[231]

In Figure 9.5**b**, the N*1s* signals are fitted with two components: a primary one at 398.5 eV (cyan area) and a shake-up component at 401.8 eV (orange area).[230,232,233] These components indicate no demetallation of the porphyrin on the surface.

The two Br*3p* signal positions (Figure 9.5**c**) are also in accordance with literature reports of bromine atoms bound to sp^2 carbon.[234] However, the presence of two smaller signals (red and green area, Figure 9.5**c**) might indicate the presence of bromine ions on the surface,[234] which suggests that some porphyrin molecules might lose their bromine functional group during the sublimation process.

The main components in the VO*2p* O*1s* regions (Figure 9.5**d**) correspond to V^{4+} signals, and the positions of the $V_{p1/2}$ (red area, 524.0 eV) and $V_{p3/2}$ (cyan area, 516.8 eV) signals are in good agreement for deposited **[VO(Pc)]** molecules[92,94,230,235] and indicate the presence of V^{4+} ions. Also, the O*1s* signal (orange area, 532.3 eV) aligns with literature values.[92,94,230,235]

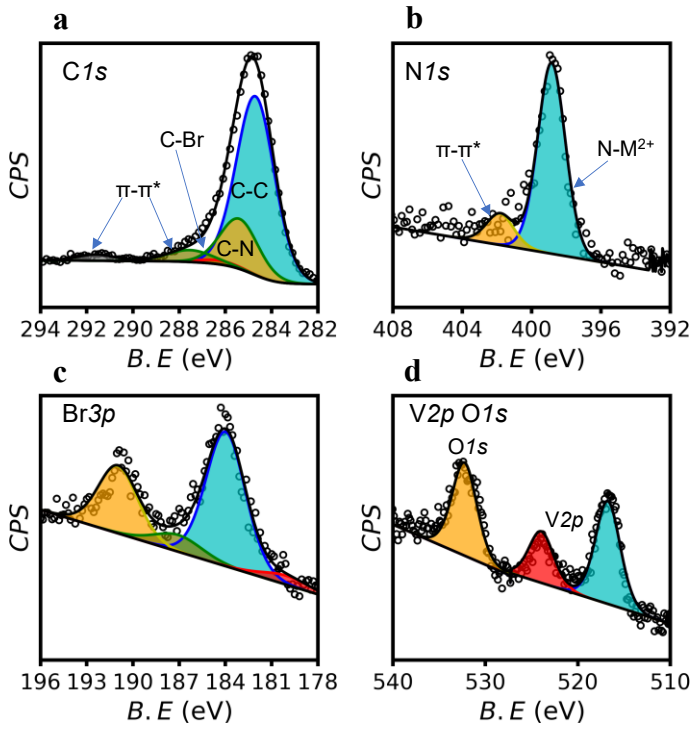

Figure 9.5: XPS-spectra of the C*1s* (**a**), N*1s* (**b**) Br*3p* (**c**), and VO*2p* O*1s* (**d**) regions of the **[VO(BrTrPP)]** molecules deposited on Au(111) single crystals.

Overall, the results of the XPS characterization of the **[VO(BrTrPP)]** deposits, reported in tabulated form in Tables 9.2-9.5, are very promising because they demonstrate that bromine functionalized porphyrin building blocks are stable enough to be deposited with thermal sublimation.

Similar conclusions can be drawn for the XPS characterization of **[Cu(BrTrPP)]** deposits on Au(111) single crystal (Figure 9.6), which points to molecule intactness on the surface.

Having confirmed the building blocks intactness on the surface, the *Ullman* reaction on the surface was attempted on this deposit by thermal annealing of the substrate at 220 °C. The comparison between the **[Cu(BrTrPP)]** deposit before and after the annealing is shown in Figure 9.6.

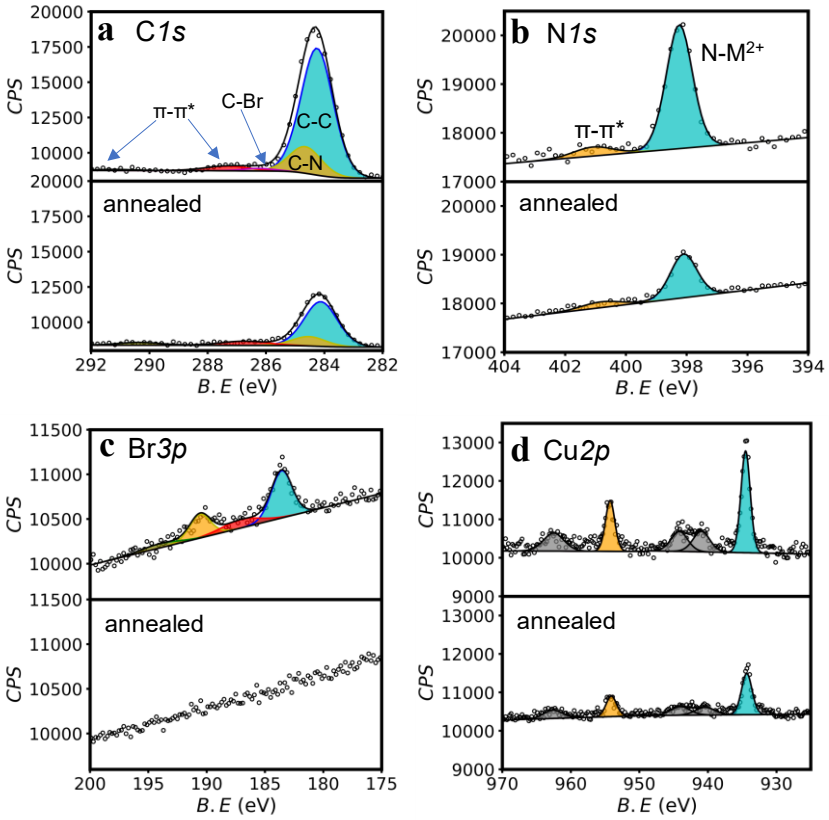

Figure 9.6: XPS-spectra of the C*1s* (**a**), N*1s* (**b**) Br*3p* (**c**), and Cu*2p* (**d**) regions of the **[Cu (BrTrPP)]** molecules deposited on Au(111) single crystals. The spectra shown at the top of each graph correspond to non-annealed **[Cu (BrTrPP)]** deposits, while at the bottom of each graph, the **[Cu (BrTrPP)]** deposit spectra after the annealing at 220°C can be seen.

The CPS of each region decreased following annealing, suggesting that some **[Cu(BrTrPP)]** molecules desorbed from the surface. Furthermore, the Br*3p* signal vanished entirely after annealing. The question remains whether this disappearance resulted from a coupling process leading to the formation of **[Cu(BrTrPP)]$_2$** or by simply a debromination. Further in-depth XPS investigations flanked by synchrotron measurements are still ongoing. Though informative, these techniques are not sufficient for comprehensive deposit characterization. Microscopy techniques, such as atomic force microscopy (AFM) and scanning tunneling microscopy (STM), are necessary to offer deeper insights into the nature of the deposit.

The successful deposition of **[M(BrTrPP)]** building blocks represents, however, a promising initial step toward realizing two-qubit quantum logic gates directly on surfaces. These studies are not only crucial for delving into on-surface porphyrin chemistry but also serve as a valuable tool for constructing complex porphyrin structures starting from simple building blocks.

Future studies should focus on optimizing the annealing process for porphyrin building blocks. With the proper annealing methods, the realization of singly, doubly, or triply linked porphyrins could become possible. If surface couplings enabling m-m or even *β*-*β* linked porphyrin dimers become attainable, it may spark heightened interest in the quantum computational research field for these building blocks. This would open doors for further investigations into implementing gates directly on the surface and two-qubit quantum logic gates.

The work presented in this section marks only the initial stride toward realizing functional two-qubit quantum logic gates on surfaces. A further crucial step is to investigate the impact of the metal surface on the magnetic properties of porphyrins. Will these properties, particularly the spin coherence, remain consistent with those in the bulk? Current research using STM coupled with pulsed EPR has, for the moment, focused on metal phthalocyanine with promising results.[236,237] Preliminary experiments on **[VO(TPP)]** are currently carried out in collaboration with the group of Prof. *Andrea Heinrich,* director of the Center of Quantum Nanoscience in Seoul.

Table 9.2: C*1s*, N*1s*, Br*3p*, Cu*2p*, and V*2p* O*1s* regions of the analyzed samples **[Cu(BrTrPP)]**, **[VO(BrTrPP)]**, and **[Cu(BrTrPP)]**-annealed. For clarity, the shake-ups of the Cu*2p* regions will not be given.

Sample	C*1s* (eV)	N*1s* (ev)	Br*3p* (eV)	Cu*2p*/V*2p* O*1s* (eV)
[Cu(BrTrPP)]	Main components: 284.2 (C-C) 284.6 (C-N) 286.3 (C-Br) Shake-ups: 287.3; 291.2	Main components: 398.2 Shake-ups: 401.1	Main components: 183.7 (Br3$p_{3/2}$) 190.7 (Br3$p_{1/2}$)	Main components: [233,238,239] 934.5 (Cu2$p_{3/2}$) 954.3 (Cu2$p_{1/2}$)
[VO(BrTrPP)]	Main components: 284.7 (C-C) 285.4 (C-N) 286.3 (C-Br) Shake-ups: 287.5; 291.6	Main components: 398.5 Shake-ups: 401.8	Main components: 184.0 (Br3$p_{3/2}$) 191.0 (Br3$p_{1/2}$)	Main components: 516.8 (V2$p_{3/2}$) 524.0 (V2$p_{1/2}$) 532.3 (O*1s*)
[Cu(BrTrPP)]-annealed	Main components: 284.1 (C-C) 284.5 (C-N) Shake-ups: 286.7; 290.3	Main components: 398.1 Shake-ups: 400.8	Main components: - - - -	Main components: 934.4 (Cu2$p_{3/2}$) 954.2 (Cu2$p_{1/2}$)

Table 9.3: semi-quantitative elemental analysis of **[Cu(BrTrPP)]** and **[VO(BrTrPP)]** deposits. Errors were estimated to be 5 % of the absolute value of the element XPS signal area contribution to the XPS spectrum.

Sample	C (%)	N (%)	Br (%)	Cu or VO (%)
[Cu(BrTrPP)] (exp)	89.30 ± 4.46	7.41 ± 0.37	1.86 ± 0.09	1.43 ± 0.07
[Cu(BrTrPP)] (calc)	86.36	9.09	2.27	2.27
[VO(BrTrPP)] (exp)	83.03 ± 4.15	8.41 ± 0.42	2.27 ± 0.11	2.12 ± 0.11 (V) 4.18 ± 0.21 (O)
[VO(BrTrPP)] (calc)	84.44	8.89	2.22	2.22 (V) 2.22 (O)
[Cu(BrTrPP)]-annealed (exp)	88.07 ± 4.39	9.02 ± 0.45	-	2.92 ± 0.16
Cu(BrTrPP)]-annealed (calc)	88.37	9.30	-	2.33

Table 9.4: Signal ratio of the different regions in the spectrum for the **[Cu(BrTrPP)]** deposits. The error was assumed to be 5% of the experimental value. The signal ratio containing the C areas (in the case of **[Cu(BrTrPP)]**) has a large error margin because they are probably contaminated with adventitious carbon.[240]

Sample	Ratio	C/N	C/Br	C/Cu	N/Br	Cu/N	Cu/Br
[Cu(BrTrPP)]	exp	14.02± 0.70	38.5 ± 1.92	51.24 ± 2.56	2.75 ± 0.14	0.27 ± 0.01	0.75 ± 0.04
	theoretic	9.50	38.00	38.00	4.00	0.25	1.00
Cu(BrTrPP)]-annealed	exp	9.77 ± 0.49	-	28.03 ± 1.40	-	0.35 ± 0.02	-
	theoretic	9.50	-	38.00	-	0.25	-

Table 9.5: Signal ratio of the different regions in the spectrum for the **[VO(BrTrPP)]** deposits. The error was assumed to be 5% of the experimental value.

Ratio	C/N	C/Br	C/V	N/Br	V/N	V/Br	V/O
exp	9.87 ± 0.49	36.56 ± 1.83	39.15 ± 1.96	3.70 ± 0.19	0.25 ± 0.01	0.93 ± 0.05	0.50 ± 0.03
calc	9.50	38.00	38.00	4.00	0.25	1.00	1.00

Contribution from the author of this PhD thesis:

The author of this thesis synthesized all molecules/samples used for the experiments. The author of this thesis also simulated all the EPR spectra present in this chapter and performed the XPS analysis under the guidance of Dr. Giulia Serrano.

10 Conclusion & perspectives

This research project was undertaken to design bimetallic paramagnetic complexes and evaluate their suitability as two-qubit quantum logic gates using EPR techniques. A pivotal aspect of this molecular design is the control of the exchange coupling between paramagnetic centers in a specifically defined range. The exchange coupling between the two metal ions of the dimer should be in the range of 10^{-2} cm^{-1} to 10^{-3} cm^{-1} to allow the admixing of their electron spin states while preserving their individual addressability at X-band and Q-band EPR frequencies. Furthermore, the spin system should maintain a coherence time (T_m) in the order of 1 µs at low temperatures. Additionally, the complex should be neutral and evaporable with thermal sublimation in an ultra-high vacuum. My thesis work has shown that all these requirements are potentially satisfied in paramagnetic complexes of porphyrin dimers.

Indeed, the synthesis and magnetic measurements of a homometallic m-m singly linked porphyrin dimer, **[VO(TrPP)]$_2$**, revealed a weak exchange coupling in the range needed to implement two-qubit logic gates. Interestingly, this had not been reported before for paramagnetic homometallic *m-m* linked porphyrin dimers containing Cu^{2+} or Ag^{2+} metal ions.[100,101] Experimental results were supported by DFT calculations, which also allowed exploring the correlation between porphyrin structure and metal center in promoting magnetic superexchange interactions. These investigations unveiled the significant influence of the vanadyl moiety on the porphyrin's magnetic properties, laying the foundation for implementing a CNOT-gate. Notably, the square pyramidal coordination of the V^{4+} ion, slightly above the porphyrin plane, fosters the overlap of the magnetic orbital with the out-of-plane π-system, thus promoting the delocalization and the exchange interaction.

Furthermore, we could determine both theoretically and experimentally the influence of the porphyrin out-of-plane deformations and the dihedral angle between the two porphyrin planes on the strength of the exchange interaction in porphyrin dimers. This was made possible by solving the X-ray structures of the two pseudo polymorphs of **[VO(TrPP)]$_2$** and correlating the structural parameters with

the magnetic properties. Solid-state X-band cw-EPR measurements revealed that the two polymorphs exhibit distinct *J* values, with the more distorted and tilted polymorph, **o-[VO(TrPP)]$_2$**, displaying a stronger *J*. This discovery underscores the pivotal role of saddle-like distortion in facilitating the transfer of spin density from the magnetic orbital into the π-system of the porphyrin. Prior to this study, no hints were available on how the distortion of porphyrin affects the magnetic interactions in porphyrin dimers.

The relevance of the $[VO]^{2+}$ unit in promoting exchange coupling was confirmed by studying a heterometallic m-m linked $[VO]^{2+}$-Cu^{2+} porphyrin dimer (**[VOCu(DPP)$_2$]**) that also showed weak exchange coupling in the order of 10^{-2} cm^{-1}, thus making it suitable as a CNOT-gate. The addressability of the two individual spins is made possible by the different **g**-tensors of V^{4+} and Cu^{2+}-ions, in contrast to homometallic dimers where tilting of the porphyrin planes plays a key role. Therefore, single-spin addressability in the heterometallic dimer can be maintained even with small tilting angles, as expected when deposited on the surface, unlocking the full potential of molecular quantum gates for practical applications. These findings suggest that weak exchange couplings can be achieved with any m-m linked paramagnetic $[VO]^{2+}$-M^{2+} porphyrin dimers, implying that a vast platform of two-qubit systems can be probed using vanadyl units. Further studies are required to improve crystallinity since obtaining large diffracting single crystals was not successful with these systems. The use of H_2TrPP ligands instead of H_2DPP may aid in enhancing crystallinity. However, employing bulkier porphyrin ligands like tetra-4-tertbutylphenylporphyrin is not recommended as it could negatively affect relaxation times and thermal sublimation ability.

The significance of diluting paramagnetic porphyrin dimers within a diamagnetic crystalline matrix is crucial for improving spectral resolution and simplifying spin addressability in single crystals. However, the synthetic work conducted in this thesis demonstrated that acquiring diamagnetic analogs for dimeric porphyrin complexes is not a straightforward task. In the case of **[VO(TrPP)]$_2$**, the optimal diamagnetic counterpart was found to be **[H$_2$(TrPP)]$_2$**, as opposed to the more similar **[TiO(TrPP)]$_2$** dimer. The former is preferable because it can be obtained in a

pure form, with good overall yields, and more importantly, allows the growth of single crystals.

In perspective, one study will exploit the photophysical properties of the porphyrins by introducing a free base porphyrin chemically in between two vanadyl porphyrins. These synthesized linear *m-m* linked porphyrin trimers (**[$VOH_2VO(DPP)_3$]** and **[$\{VO\}_2(TrPP)_2(H_2DPP)$]**) show no sign of exchange interaction in cw-EPR experiments. However, the exchange interaction could potentially be induced by photoexciting the free-base porphyrin, thus creating an open shell excited state that will switch on the communication between the two vanadyl porphyrin units. These studies are still ongoing, but if successful, they will demonstrate the vast opportunities that paramagnetic porphyrins have in the quantum information field. Indeed, it would make realizing photo-switchable two-qubit quantum logic gates possible.

We also started to explore an alternative approach for realizing porphyrin dimers. It involved depositing porphyrin building blocks (**[Cu(BrTrPP)]** and **[VO(BrTrPP)]**) onto Au(111) single crystals using thermal sublimation. The objective was to anneal the substrates to create either **$[Cu(TrPP)]_2$** or **$[VO(TrPP)]_2$** dimers on the surface. XPS analysis of both building block deposits confirmed the presence of intact porphyrins on the surface post-sublimation. After annealing **[Cu(BrTrPP)]** deposits, the disappearance of the Br*3p* signal in the XPS spectrum indicates that the initial step (debromination) of the surface reaction took place. Further analysis using synchrotron facilities and scanning microscopies is required to examine the magnetic properties of the deposit and confirm the presence of **$[Cu(TrPP)]_2$** dimers on the surface.

Overall, the synthesis and study of bimetallic weak exchange coupled complexes is a very interesting research area with great potential for the future. The inherent advantage of bimetallic molecular spin qubits is their chemical versatility, which allows, e.g., precise tuning of exchange interactions. This thesis demonstrates that porphyrin dimers represent an ideal platform for achieving this tuning due to the remarkable chemical adaptability of porphyrins. It is worth noting that other aromatic

systems may also hold similar potential, and their exploration and study could yield promising discoveries in the future. Lastly, it is important to note that applying molecular spin qubits in a working quantum computer faces challenges, particularly in terms of scalability, entangling multiple qubits, and ensuring a sufficiently long T_m. These factors are critical for implementing quantum algorithms essential for achieving quantum supremacy.

This manuscript opens with a description of the bricks that make up the world of quantum technology to highlight the interdisciplinary character of this research area. This thesis contributes to showcasing the potential of the molecular spin qubit field thanks to the investigation of a versatile and promising 'chemistry brick'. It is my hope that the field will continue to grow, ultimately playing a significant role in advancing the broader quantum technology landscape.

11 Detailed synthetic procedures & characterizations

11.1 SI: **[VO(TrPP)]$_2$**: A homometallic porphyrin dimer as a promising candidate for a two-qubit quantum gate

Synthesis of [VO(TrPP)]: The general synthesis was readapted from the literature.[97] Phenol (PhOH, 2 g) was heated to 80 °C and degassed by vacuum/N2 cycles in a pre-dried flask. H_2TrPP (80 mg, 0.15 mmol) and $VO(acac)_2$ (40 mg, 0.15 mmol) were added to the PhOH solution, and the reaction mixture was heated to 165 °C under N_2 for 12 h. The reaction was checked by TLC (CH_2Cl_2/Pet. ether 1:1) and UV/Vis (**Figure 11.1**). Afterward, PhOH was removed by distillation under a constant N2 flow while the temperature was kept at 140 °C – 150 °C. The crude product was then solved in 200 mL of CH_2Cl_2, filtered, and purified by column chromatography (flash silica gel, CH_2Cl_2/Pet. ether 1:1). The overall process yielded 50 mg (0.08 mmol) of a microcrystalline powder identified as the target **[VO(TrPP)]** product (final yield = 55%). R_f (CH_2Cl_2/Pet. ether 1:1) = 74%; λ_{max}(CH_2Cl_2) = 417 nm, 541 nm, 576 nm; ν_{max}/cm^{-1}: 3101 (w), 3052 (w), 3029 (w), 2921 (vw), 2852 (vw), 2363 (w), 2332(w), 1588 (w), 1492(w), 1442 (m), 1376 (w), 1324(m), 1075 (m), 1000 (vs, V=O stretching), 952(vs), 853 (m), 801 (s), 756 (s), 721 (s), 697 (s), 659 (w). MALDI-MS (m/z): 603.13 ($M^{\cdot+}$). The experimental PXRD pattern obtained by measuring the microcrystalline powder was compared with the simulated one (**Figure 11.2**).

Synthesis of [VO(TrPP)]$_2$: The synthesis was performed using a slightly modified procedure.[161] In a pre-dried Schlenk flask, **[VO(TrPP)]** (60 mg, 0.10 mmol) was added and solved in 30 mL of dry CH_2Cl_2 under N_2. The solution was cooled to −78°C with an acetone/N_2 bath. Then, a PIFA (86 mg, 0.20 mmol) solution in 10 mL of dry CH_2Cl_2 was slowly added to the reaction mixture. Once the addition was completed, the acetone/N_2 bath was removed, and the reaction mixture was brought to room temperature. After 40 min of stirring at room temperature, UV/Vis and TLC analyses confirmed the full conversion of the precursor. The reaction was quenched with a

$NaBH_4$ (37 mg, 1.00 mmol) solution in 12 mL of MeOH. The resulting solution was further stirred for an extra 15 min. Afterward, deionized H_2O (20 mL) was added to the reaction mixture, and the organic phase was collected and washed twice with sat. $NaHCO_3$ solution (30 mL x 2). The combined water phases were extracted thrice with CH_2Cl_2 (30 mL) to recover the residual product. After drying the combined organic phases with anhydrous $NaSO_4$, CH_2Cl_2 was removed under reduced pressure. The crude product was purified by column chromatography (flash silica gel) using toluene as eluent. The overall procedure yielded 65 mg (0.47 mmol) of pure **[VO(TrPP)]$_2$**·$3C_7H_8$ (final yield = 94%) as a microcrystalline powder. We should mention that after the purification of the dimer by column chromatography adopting toluene as an eluting solvent (see Experimental and Theoretical Methods), one always obtains microcrystalline powder samples of **m-[VO(TrPP)]$_2$**. Furthermore, faster crystallization from toluene or acetone/toluene solutions led to **m-[VO(TrPP)]$_2$**. The comparison between the experimental and simulated PXRD patterns (**Figure 11.2** highlights that the cell parameters are comparable to those of **m-[VO(TrPP)]$_2$**. R_f (toluene) = 0.52; $\lambda_{max}(CH_2Cl_2)$ 308 nm, 422 nm, 456 nm, 556 nm, 594 nm; MALDI-MS (m/z): 1204.67 ($M^{\cdot+}$); v_{max}/cm^{-1}: 3055 w and 3020 w (C=C stretching), 2960 m and 2854 m (CH_3 stretching from co-solvent), 1596 m (N=C stretching), 1486 w, 1438 m, 1367 w, 1326 m, 1261 m, 1204 m, 1175 m, 1000 s (V=O stretching), 803 s, 744 m, 729 s, 721 s, 696 s, 660 m, 444 m

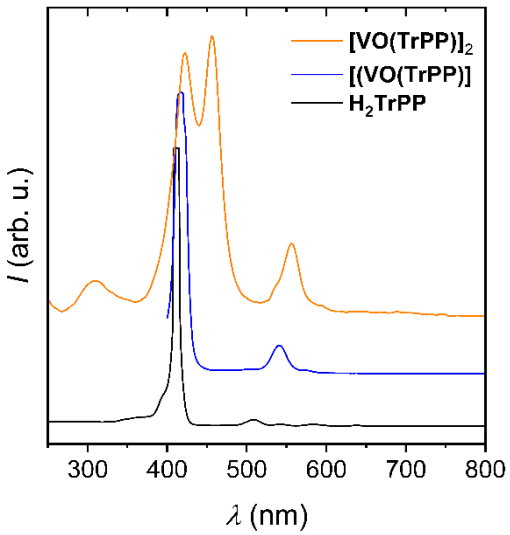

Figure 11.1. UV/Vis spectra of **[VO(TrPP)]$_2$** (orange line), **[VO(TrPP)]** (blue line) and H_2(TrPP) (black line).

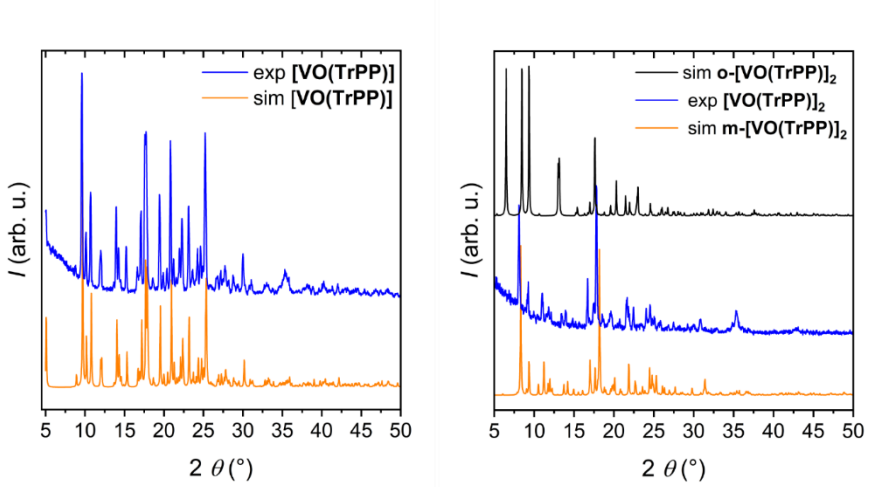

Figure 11.2: Simulated (orange) and experimental (blue) PXRD pattern of **[VO(TrPP)]** (left), and **m-[VO(TrPP)]$_2$** (right). In addition to the simulated **m-[VO(TrPP)]$_2$** powder pattern, the simulated powder pattern of **o-[VO(TrPP)]$_2$** (black line) is reported in the right panel to highlight the difference between the two structures. Only **m-[VO(TrPP)]$_2$** powders are obtained by fast crystallization in toluene.

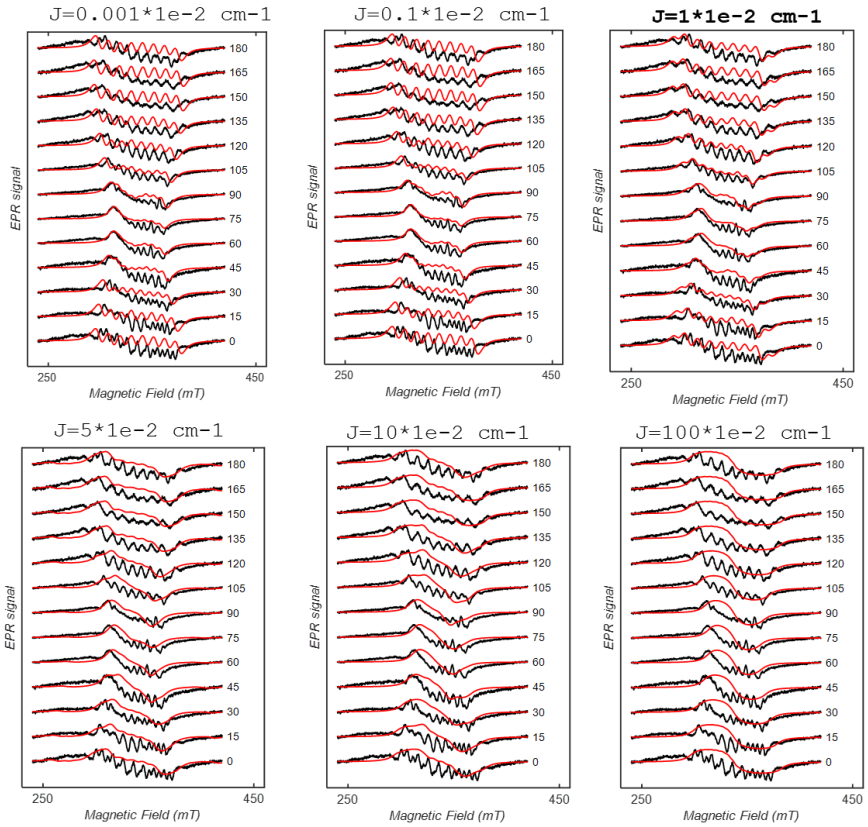

Figure 11.3. Simulations of the angular dependency of the EPR spectrum of the **m-[VO(TrPP)]$_2$** crystal for the rotation along the b-axis obtained by using different $|J_{12}|$ exchange coupling constants. In all cases, we assumed the same **g**- and **A**- tensors as the solution molecule. We considered the through-space dipolar interaction (intra- and inter-molecular) as a linewidth broadening of 8 mT. The best agreement between data and simulations is obtained using $|J_{12}|$=0.01 (0.005) cm^{-1}.

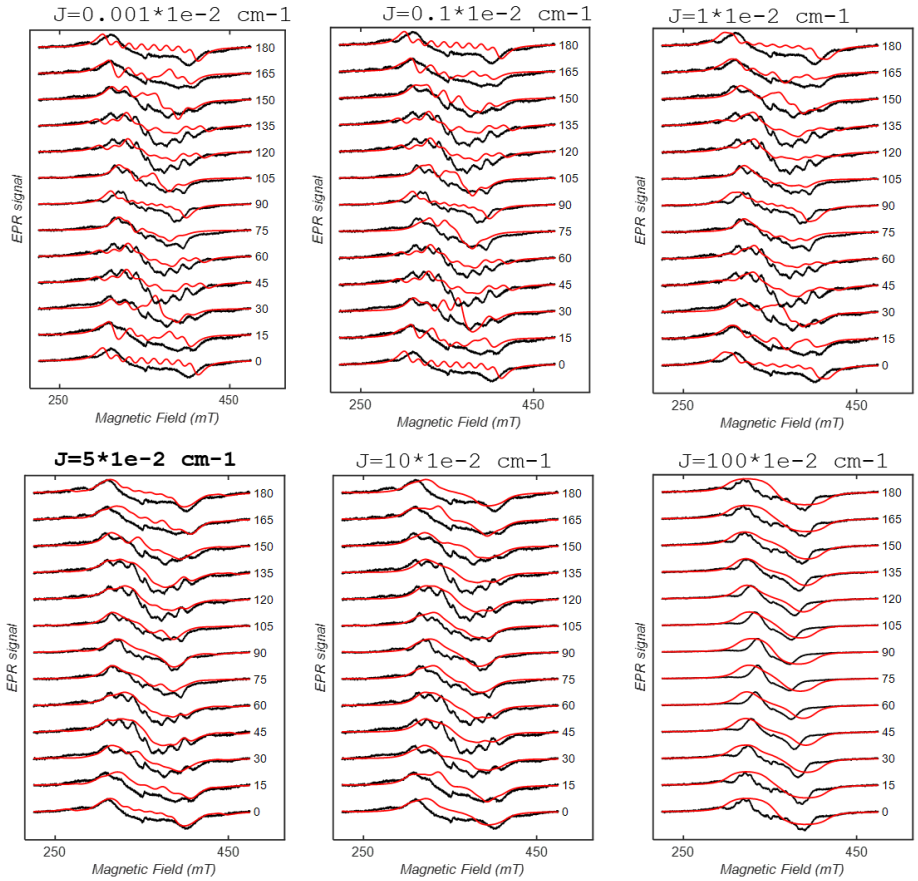

Figure 11.4. Simulations of the angular dependency of the EPR spectrum of the **o-[VO(TrPP)]$_2$** crystal for the rotation along the b-axis using different $|J_{12}|$ exchange coupling constants. We considered the through-space dipolar interaction (intra- and inter-molecular) as a linewidth broadening of 13 mT. The best agreement between data and simulations is obtained using $|J_{12}|$=0.05 (0.01) cm^{-1}.

Table 11.1. Most important crystallographic data was obtained from single crystal X-ray diffraction analysis of **[VO(TrPP)]**, **m-[VO(TrPP)]$_2$**, and **o-[VO(TrPP)]$_2$**.[241]

Sample	**[VO(TrPP)]**	**m-[VO(TrPP)]$_2$**	**o-[VO(TrPP)]$_2$**
Empirical Formula	$VON_4C_{38}H_{24}$	$V_2O_2N_8C_{97}H_{46}$	$V_2O_2N_8C_{76}H_{46}$
Formula weight (g mol^{-1})	603.58	1457.34	1205.11
Crystal system	monoclinic	monoclinic	orthorhombic
Space group	$P2_1/c$	$C2/c$	$Ccc2$
Z	4	4	4
a (Å)	18.9568(9)	29.2955(12)	20.8648(13)
b (Å)	8.0830(3)(2)	11.3883(5)	27.1717(13)
c (Å)	19.9282(9)	22.5512(9)	11.4881(6)
α (°)	90	90	90
β (°)	114.250(2)	96.942(2)	90
γ (°)	90	90	90
V (Å^3)	2784.1(2)	7468.5(5)	6513.0(6)
ρ (calc.) (Mg/m^3)	1.440	1.296	1.229
μ (mm^{-1})	3.294	2.557	2.816
T (K)	100	100	100
Radiation	CuK_α (λ = 1.514178 Å)	CuK_α (λ = 1.514178 Å)	CuK_α (λ = 1.514178 Å)
θ range (°)	2-56 – 68.36	3.95 – 68.54	5.33 – 72.83
F(000)	1244	2984	2480
GooF	1.066	1.104	1.049
R1 (%)[a]	8.31	6.38	7.33
wR2 (%)[a]	22.46	16.55	21.88
Intramolecular Porphyrin dihedral angle (°)	-	66	77
Intramolecular VO-VO torsion angle (°)	-	64	72
Intramolecular VO-VO distance (Å)	-	8.52	8.37
Intermolecular VO-VO distance (Å)	9.42	10.44	7.78

11.2 SI: The quest of finding a suitable diamagnetic dilutant for **[VO(TrPP)]$_2$**

Synthesis of [TiO(TrPP)]:

The synthesis was performed using a slightly modified procedure.[97] Phenol (PhOH, 6 g, 0.06 mol) was heated to 80 °C and degassed by vacuum/N2 cycles in a pre-dried flask. H_2TrPP (50 mg, 0.09 mmol) and TiO(acac)$_2$ (70 mg, 0.27 mmol, 3 eq.) were added to the PhOH solution, and the reaction mixture was heated to 175 °C under N_2 for 48 h. The reaction was checked by UV/Vis spectroscopy. Afterward, PhOH was removed by distillation under a constant N2 flow while the temperature was kept at 140 °C – 150 °C. The crude product was then solved in 200 mL of CH_2Cl_2, filtered, and purified by column chromatography (SiO_2 flash, CH_2Cl_2, R_f = 0.38). The overall process yielded 2.7 mg (0.0045 mmol, 5 %) of a microcrystalline powder identified as the target **[TiO(TrPP)]** product; $\lambda_{max}(CH_2Cl_2)$ = 418 nm, 547 nm, 576 nm; ^{1}H NMR (400 MHz, $CDCl_3$): δ 10.70 (s, 1H, *m*-H), 9.67 (d, 2H, 4.5 Hz, β-H), 9.35 (d, 2H, 4.5 Hz, β-H), 9.23 (m, 4H, β-H), 8.58 (br, 4 H, Ph), (br, 4H, Ph), (m, 7H, Ph). X-ray quality crystals were obtained, as reported in Chapter 7.

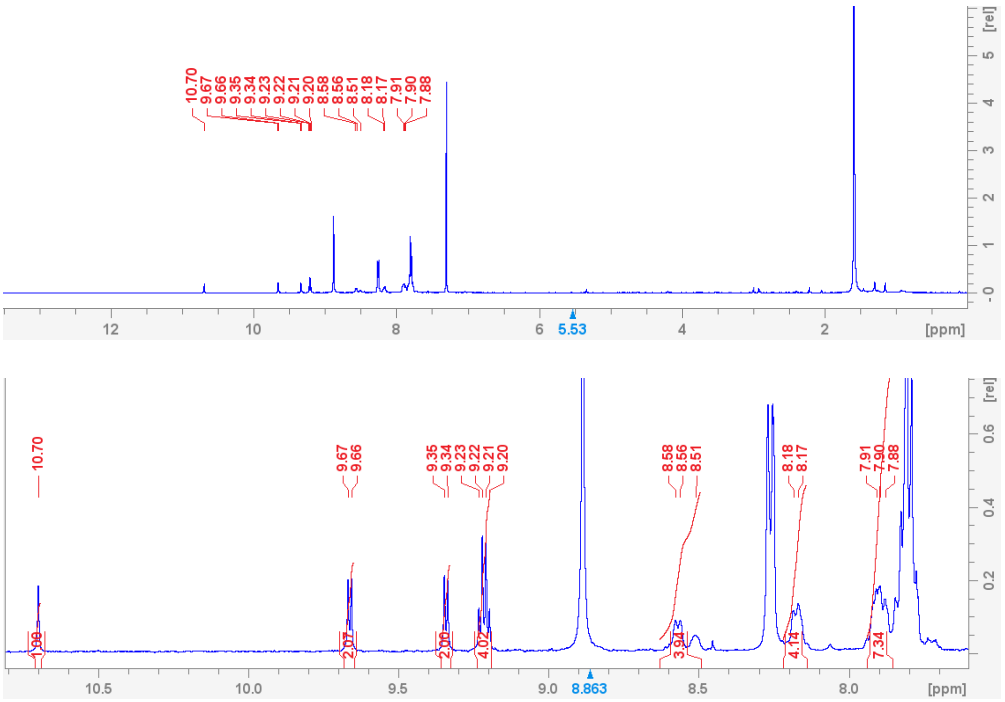

Figure 11.5: ^{1}H-NMR spectrum ($CDCl_3$, 400 MHz) of **[TiO(TrPP)]** in the full scan (top) and aromatic (bottom) region.

Synthesis of [TiO(TrPP)]$_2$:

The synthesis was performed using a slightly modified procedure.[161] In a pre-dried Schlenk flask, **[TiO(TrPP)]** (10 mg, 0.017 mmol) was added and solved in 5 mL of dry CH_2Cl_2 under N_2. The solution was cooled to −78°C with an acetone/N_2 bath. Then, a PIFA (36 mg, 0.085 mmol, 5 eq.) solution in 6 mL of dry CH_2Cl_2 was slowly added to the reaction mixture. Once the addition was completed, the acetone/N_2 bath was removed, and the reaction mixture was brought to room temperature. After 16 h of stirring at room temperature, TLC analyses confirmed the full conversion of the precursor. The reaction was subsequently quenched with 10 mL of a saturated $NaHCO_3$ solution. The resulting solution was further stirred for an extra 15 min. Afterward, the organic phase was collected and washed twice with sat. $NaHCO_3$ solution (10 mL x 2). The combined water phases were extracted thrice with CH_2Cl_2 (10 mL) to recover the residual product. After drying the combined organic phases

with anhydrous $NaSO_4$, CH_2Cl_2 was removed under reduced pressure. The crude product was purified by column chromatography (flash SiO_2, Et_2O, $R_f = 0.82$) for the separation of **[TiO(TrPP)]$_2$** with **[TiO(TrPP)]**, and another column (flash SiO_2, CH_2Cl_2:hexane 1:1, $R_f = 0.47$) to separate **[TiO(TrPP)]$_2$** from **[H$_2$ (TrPP)]$_2$**. The overall procedure yielded 65 mg (0.47 mmol) of pure **[TiO(TrPP)]$_2$** (9 mg, 0.075 mmol, 92%) as an amorph purple powder. $\lambda_{max}(CH_2Cl_2)$ 308 nm, 423 nm, 457 nm, 560 nm, 599 nm; ESI-MS (m/z): (exp) 1199.27 (M^+), calcd: 1199.28 (M^+); ^{1}H NMR (400 MHz, $CDCl_3$): δ 9.24 (m, 8H, β-H), 8.97 (d, 2H, 4.8 Hz, β-H), 8.79 (d, 4H, 4.8 Hz, β-H), 8.65 (br, 2H, β-H), 8.52 (m, 4H, Ph), 8.17 (m, 6H, Ph), 7.96 (m, 20H, Ph)

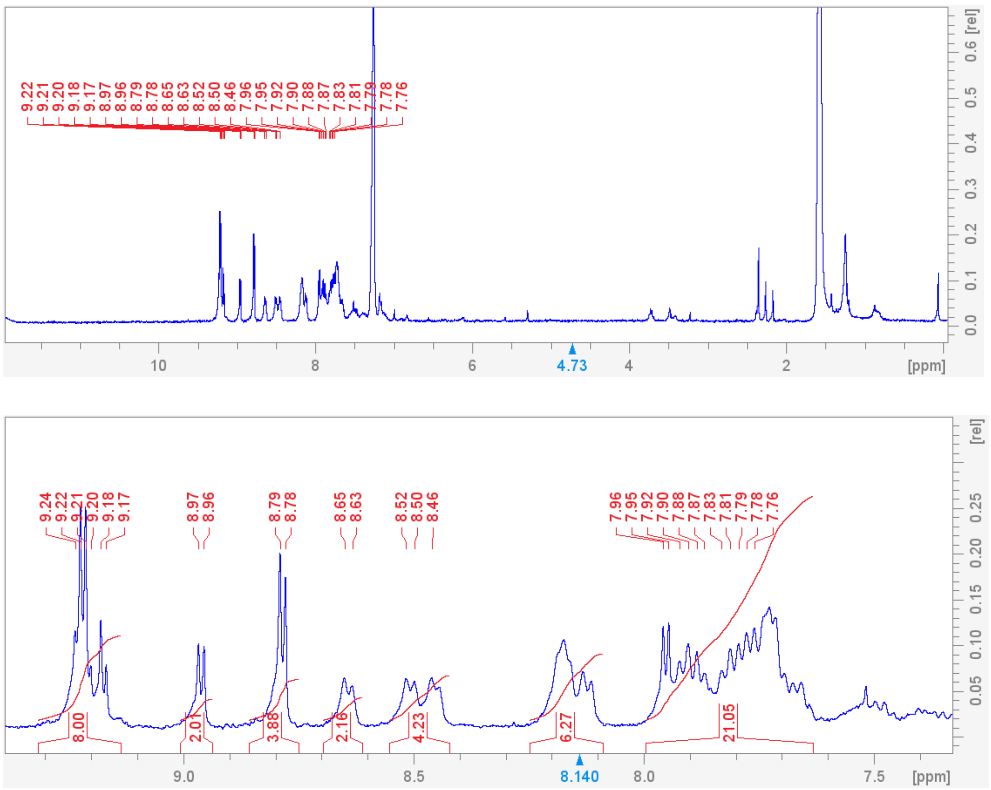

Figure 11.6: ^{1}H-NMR spectrum ($CDCl_3$, 400 MHz) of **[TiO(TrPP)]$_2$** in the full scan (top) and aromatic (bottom) region.

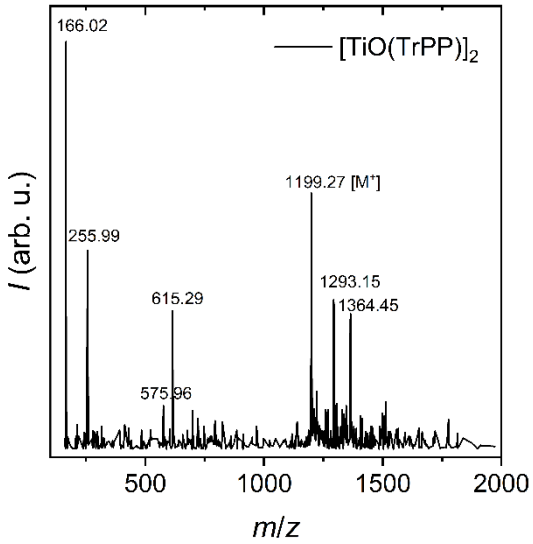

Figure 11.7: ESI-MS spectra measured between 1250-2000 m/z of **[TiO(TrPP)]$_2$**.

Synthesis of [Zn(TrPP)]$_2$:

The synthesis was performed using the procedure from.[161] In a pre-dried Schlenk flask, **[Zn(TrPP)]** (20 mg, 0.033 mmol) was added and solved in 6 mL of dry CH_2Cl_2 under N_2. The solution was cooled to −78°C with an acetone/N_2 bath. Then, a PIFA (7 mg, 0.017 mmol, 0.5 eq.) solution in 6 mL of dry CH_2Cl_2 was slowly added to the reaction mixture. Once the addition was completed, the acetone/N_2 bath was removed. After 5 min of stirring, the reaction was quenched with a $NaBH_4$ (12.5 mg, 0.33 mmol, 10 eq.) solution in 4 mL of MeOH. The resulting solution was further stirred for an extra 15 min. Afterward, deionized H_2O (5 mL) was added to the reaction mixture, and the organic phase was collected and washed twice with sat. $NaHCO_3$ solution (10 mL x 2). The combined water phases were extracted thrice with CH_2Cl_2 (10 mL) to recover the residual product. After drying the combined organic phases with anhydrous $NaSO_4$, CH_2Cl_2 was removed under reduced pressure. The crude product was purified by column chromatography (flash SiO_2, CH_2Cl_2:hexane: $HNEt_3$ 1:1:0.01, R_f = 0.27). The overall procedure yielded 19 mg (0.016 mmol, 96 %) of **[Zn(TrPP)]$_2$** as a red microcrystalline powder. λ_{max}(CH_2Cl_2) 312 nm, 417 nm, 454 nm, 559 nm, 598

nm. ^{1}H NMR (400 MHz, $CDCl_3$): δ 9.04 (m, 8H β-H), 8.68 (d, 4H, 4.7 Hz, β-H), 8.32 (m, 4H, β-H), 8.225 (m, 8H, Ph), 8.14 (d, 4H, 4.7 Hz, Ph), 7.82 (m, 6H, Ph), 7.68 (m, 12H, Ph).

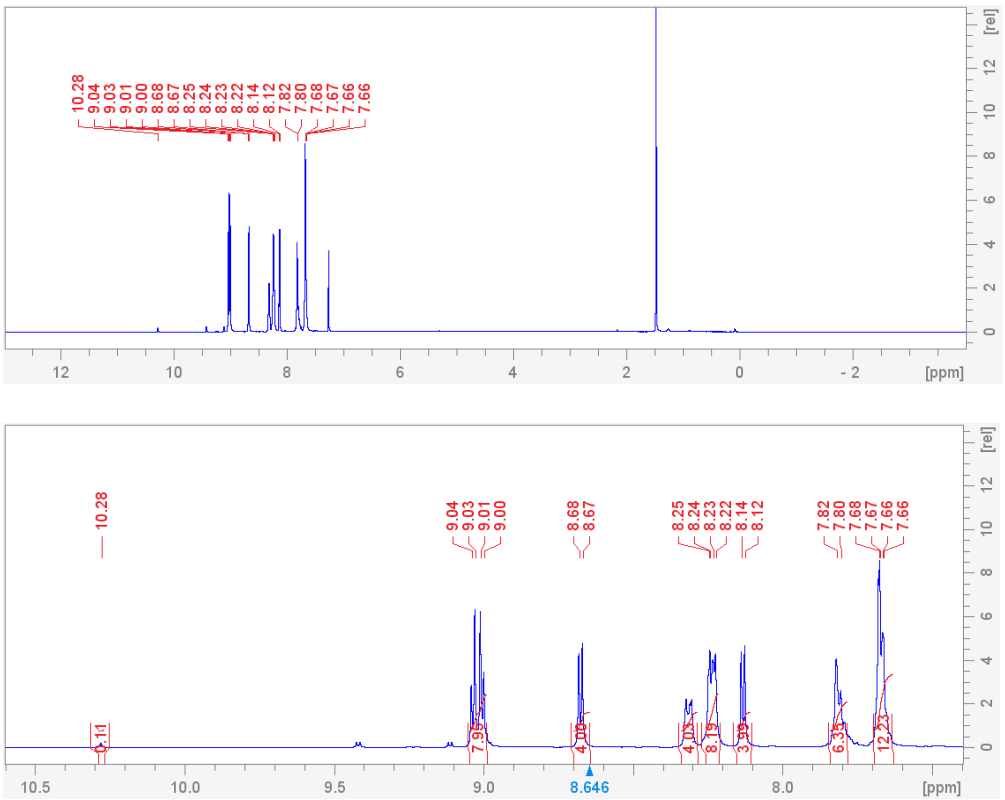

Figure 11.8: ^{1}H-NMR spectrum ($CDCl_3$, 400 MHz) of **[Zn(TrPP)]$_2$** in the full scan (top) and aromatic (bottom) region. Approximately, the product is contaminated with 2.5 % of **[Zn(TrPP)]**.

Synthesis of [H$_2$(TrPP)]$_2$:

In a 50 mL round-bottom flask, **[Zn(TrPP)]$_2$** (10 mg, 0.0083 mmol) powders were inserted and solved in 10 mL of CH_2Cl_2. The solution was stirred at room temperature, and 5 mL of trifluoroacetate was added. The solution turned from orange to yellow. After 2 h, the reaction was poured into a 250 mL beaker, diluted with 10 mL CH_2Cl_2, and portionwise a solution containing sat. $NaHCO_3$ was added until the organic phase turned orange again. The organic phase was separated from the water phase, and the

organic phase dried over anhydrous $NaSO_4$. The solution was evaporated under reduced pressure to yield **$[H_2(TrPP)]_2$** (8 mg, 0.0074 mmol, 89 %). $\lambda_{max}(CH_2Cl_2)$ 304 nm, 413 nm, 450 nm, 524 nm, 594 nm, 653 nm. ^{1}H NMR (400 MHz, $CDCl_3$): δ 8.94 (m, 8H, β-H), 8.60 (d, 2H, 4.7 Hz, β-H), 8.30 (m, 4H, β-H), 8.23 (m, 8H, Ph), 8.09 (4H, 4.7 Hz, Ph), 7.82 (m, 6H, Ph), 7.68 (m, 12H, Ph), −2.21 (s, 4H, N-H).

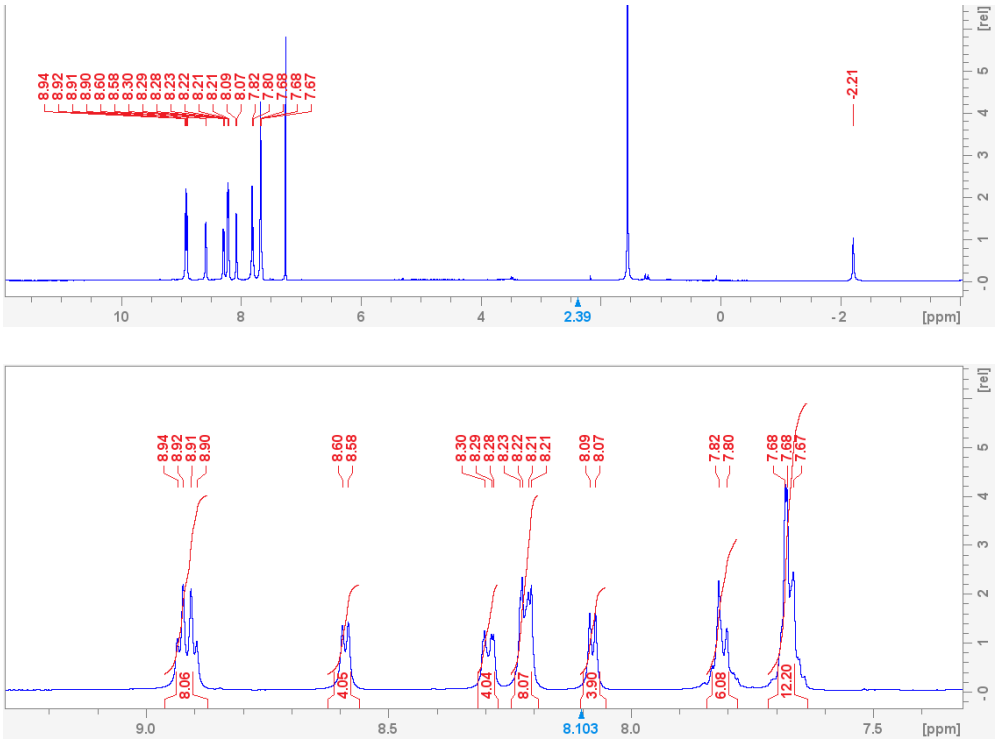

Figure 11.9: ^{1}H-NMR spectrum ($CDCl_3$, 400 MHz) of **$[H_2(TrPP)]_2$** in the full scan (top) and aromatic (bottom) region.

Preparation of $[VO_{0.01}H_{2(0.99)}(TrPP)]_2$ dilutions:

An $8.3 \cdot 10^{-2}$ mmol stock solution of **$[VO(TrPP)]_2$** in CH_2Cl_2 was prepared. 0.56 mL (n(**$[VO(TrPP)]_2$**) = $4.7 \cdot 10^{-5}$ mmol) of this stock solution was added to a flask containing **$[H_2(TrPP)]_2$** (5 mg, 0.0047 mmol, 100 eq.) solved in 3 mL CH_2Cl_2. **$[VO_{0.01}H_{2(0.99)}(TrPP)]_2$** powders were obtained after adding 1 mL of methanol and fast evaporation of this solution.

Preparation of $[H_2(TrPP)]_2$-pyr & $[VO_{0.01}H_{2(0.99)}(TrPP)]_2$ single crystals:

5 mg of **$[H_2(TrPP)]_2$** (**$[VO_{0.01}H_{2(0.99)}(TrPP)]_2$**) powders were put in a vial with a diameter of 3 cm. The powder was solved in 3 mL of CH_2Cl_2 (HPLC-grade), to which 0.3 mL of pyridine was added. To this solution, 9 mL of CH_3OH (HPLC-grade) was added. The screw cap of the vial was first fully closed and then slightly re-opened (90° turn). Three different batches of these solutions were prepared and stored in the chemistry laboratory, which, at that time, had a temperature between 16-18°C. After 5-6 days, needle-like crystals were visible. The evaporation of CH_2Cl_2 from the vial was stopped by closing the screw cap and taping the border (cap and glass) with parafilm® and with a black friction tape. This was done to avoid the complete loss of solvent and prevent crystal degradation.

Table 11.2: Crystal data and structure refinement for the **$[Zn(TrPP)]_2$** solvatomorphs and **[TiO(TrPP)]**.

Name	**$[Zn(TrPP)]_2$-MeOH**	**$[Zn(TrPP)]_2$-Pyr**	**[TiO(TrPP)]**
Formula weight	2642.17	1390.63	600.50
Temperature	110	293(2)	185
Wavelength	1.54178	1.54178 Å	1.54178 Å
Crystal system	monoclinic	monoclinic	monoclinic
Space group	$P2_1/n$	$P2_1/c$	$P2_1/c$
Unit cell dimensions	a = 13.1517(11)Å b = 31.432(3)Å c = 31.390(3) Å α= γ = 90° β = 96.254(4)	a = 11.3378(14) b = 35.941(6) c = 17.742(4) α= γ = 90° β = 108.307(11)	a = 19.163(6) b = 8.185(2) c =20.037(6) α = γ = 90 β = °
Volume	12898.9	6863.8(3)	2857.6 $Å^3$
Z	4	4	4
Density (calculated)	1.419 g cm^{-3}	1.346 g cm^{-3}	1.396 g cm^{-3}
Absorption coefficient	1.387 mm^{-1}	1.322 mm^{-1}	2.845
F(000)	5472	2866	1240
Crystal size	0.200x0.300x0.400 mm^3	0.250 x 0.130 x 0.02 mm^3	0.14x0.10x0.02 mm^3

Theta range for data collection	3.16 to 68.44°	2.90 to 58.36°	2.5341° to 61.1377°
Index ranges	-15<=h<=15, -34<=k<=37, -37<=l<=37	-12<=h<=12, -39<=k<=39, -19<=l<=19	−16≤h≤23, −9≤k≤8, −24≤l≤20
Reflections collected	23728	9671	14352
Independent reflections	9836 [R(int) = 0.0631]	8604 [R(int) = 0.0571]	4874 [R(int) = 0.063]
Completeness to theta = 63.898°	99.4 %	99.6 %	93.3 %
Absorption correction	Multi-Scan	Multi-Scan	Multi-scan
Refinement method	Full-matrix least-squares on F^2	Full-matrix least-squares on F^2	Full-matrix least-squares on F^2
Goodness-of-fit on F^2	0.769	1.088	1.066
Final R indices [I>2σ(I)]	R1 = 0.0537, wR2 = 0.1580	R1 = 0.0644, wR2 = 0.1655	R1 = 0.1133, wR2 = 0.1783
R indices (all data)	R1 = 0.0562, wR2 = 0.1621	R1 = 0.0637, wR2 = 0.1747	R1 = 0.0804, wR2 = 0.2327

11.3 SI: **[VOCu(DPP)$_2$]**: The heterometallic version of a two-qubit quantum logic gate

Dipyrromethane *(DPM),* 5,15-diphenylporphyrin (DPP), 5-bromo-10,20-diphenylporphyrin (BrDPP), (5,15-diphenylporphyrinato)copper(II) (**[Cu(DPP)]**), 5-iodo-10,20-diphenylporphyrin (H_2IDPP), and 5,15-diphenyl-(10-pinacoleboryl)porphyrin (BpinDPP) were synthesized according to literature procedures.[142,242–246]

Oxo(5,15-diphenylporphyrinato)vanadium(IV) (**[VO(DPP)]**):[97] A pre-dried Schlenk flask was charged with phenol (6 g, 6.37 mmol), DPP (200 mg, 0.43 mmol), and $VO(acac)_2$ (200 mg, 0.75 mmol). The solids were heated at 165 °C under an Ar atmosphere for 18 h. Afterward, the reaction mixture was cooled to 150 °C and

distilled under a constant N_2 flow until all phenol was removed. The crude product was diluted with 300 mL of CH_2Cl_2, filtered, and the solution was concentrated under reduced pressure. Compound **[VO(DPP)]** was purified with column chromatography (flash SiO_2 hexane: CH_2Cl_2, 1:1, R_f = 0.22). The desired fraction was collected, the eluent removed under reduced pressure, and the product recrystallized from a 1:5 acetonitrile: CH_2Cl_2 mixture to yield 190 mg (0.36 mmol, 84%) of needle-like purple crystals of **[VO(DPP)]**. APCI-MS (*m/z*): 528.1150 ($M+H^+$, calcd), 528.1151 ($M+H^+$, found). UV/Vis (CH_2Cl_2): λ_{max} (log(ε)) = 414 (5.7), 536 (4.4), 572 nm (3.7).

Oxo(5-iodo-10,20-diphenylporphyrinato)vanadium(IV) (**[VO(IDPP)]**):[142] In a Schlenk flask, [**VO(DPP)]** (100 mg, 0.19 mmol) was dissolved in 60 mL CH_2Cl_2 under N_2 flow. To this solution, pyridine (0.3 mL, 296 mg, 3.8 mmol) was added, and the reaction mixture was degassed with N_2. Subsequently, I_2 (96 mg, 0.38 mmol) and PIFA (245 mg, 0.57 mmol) were added, and the reaction mixture was stirred at rt and in the dark for 2 h. The reaction mixture was quenched with 30 mL of an aqueous solution of $Na_2S_2O_3$. The water and organic phase were separated, and the organic phase was washed with a 30 mL sat. $NaHCO_3$ solution three times. The organic phase was dried with Na_2SO_4, and the solvent was evaporated under reduced pressure. The crude product was purified with column chromatography (flash SiO_2, 1:2 hexane: CH_2Cl_2, R_f = 0.55). Polycrystalline powders of **[VO(IDPP)]** were obtained by the slow evaporation of the eluent (26 mg, 0.04 mmol, 21 %). APCI-MS (*m/z)*: 653.0116 ($M+H^+$, calcd), 654.0043 ($M+H^+$, found). UV/Vis (CH_2Cl_2): λ_{max} (log(ε)) = 423 (5.5), 547 nm (4.1),

(5-Iodo-10,20-diphenylporphyrinato)copper(II) (**[Cu(IDPP)]**): A solution of $Cu(OAc)_2$ (1.14 g, 6.3 mmol) in methanol was added to a solution of free base 5-iodo-10,20-diphenylporphyrin (371 mg, 0.63 mmol) in $CHCl_3$. The resulting mixture was stirred at 65°C for 2 h, concentrated *in vacuo,* and subjected to column chromatography on silica gel, eluting with DCM. A red powder was obtained by precipitation with *n*-hexane. Yield: 397 mg, 0.61 mmol, 97%. APCI-MS (*m/z*):

649.9825 ($M+H^+$, calcd.), 650.0027 ($M+H^+$, found), UV/Vis (CH_2Cl_2): λ_{max} (log(ε)) = 412 (5.40), 537 nm (4.15).

(5-[Oxo(10,20-diphenylporphyrinato-5-yl)vanadium(IV)]-10,20-diphenylporphyrin, V(IV)O-free base dimer (**[VOH_2(DPP)$_2$]**):[149,213] To a pre-dried double-necked round bottom flask, **[VO(IDPP)]** (10 mg, 0.015 mmol) and BpinDPP (9 mg, 0.015 mmol) were added among with Cs_2CO_3 (0.04 mmol, 13 mg) under an Ar flow. The solids were solved in 5 mL of dry DMF and 10 mL of dry toluene. The solution was degassed with Ar for about 30 min. After the degassing, $Pd(PPh_3)_4$ (1.2 mg, 0.001 mmol) was added. The reaction mixture was heated to 80 °C and stirred for 18 h (TLC-check). The reaction was quenched by adding 10 mL of water. The water and organic phase were separated, and the organic phase was washed three times with 10 mL water. The organic phase was collected and dried with Na_2SO_4. The solvent was evaporated using a rotatory evaporator, and the crude product was purified with column chromatography (flash SiO_2, 1:1 hexane:CH_2Cl_2, R_f = 0.24). After slow evaporation of the eluent, violet needles of **[VOH_2(DPP)$_2$]** (12 mg, 0.012 mmol, 83 %) were obtained. To remove residual [**VO(DPP)]**, an additional column using toluene as eluent was performed (flash SiO_2, toluene, R_f = 0.67). ^{1}H NMR (400 MHz, $CDCl_3$): δ 10.39 (s, 1H), 9.44 (br, 2H), 9.08 (br, 2H), 8.22 (br, 4H), 7.69 (m, 10H), −1.58 ppm (s, 2H). ESI-MS (*m/z*): 988.2843 ($M+H^+$, calcd), 988.2849 ($M+H^+$, found). IR $\tilde{\nu}_{max}$/cm^{-1}: 3302 (w, N-H, stretching), 3050 (w, C=C stretching), 3020 (w), 1597 (w, N=C stretching), 1317 (m), 1152 (w), 1065 (m), 997 (s, V=O stretching), 967 (m), 957 (m), 856 (m), 792 (s), 722 (s), 697 (m), 655 (m). UV/Vis (CH_2Cl_2): λ_{max} (log(ε)) = 416 (5.3), 447 (5.3), 513 (4.7), 548 (4.7), 586 (4.3), 642 nm (3.4).

(5-[10,20-Diphenylporphyrinato-5-yl)copper(II)]-10,20-diphenylporphyrin, Cu(II)-free base dimer (**[CuH_2(DPP)$_2$]**):[149,213] In a pre-dried double-necked round bottom flask, **[Cu(IDPP)]** (10 mg, 0.015 mmol) and BpinDPP (9 mg, 0.015 mmol) were added together with Cs_2CO_3 (13 mg 0.04 mmol,) under an Ar flow. The solids were dissolved in 5 mL of dry DMF and 10 mL of dry toluene. The solution was degassed

with Ar for about 30 min. After the degassing, $Pd(PPh_3)_4$ (1.2 mg, 0.001 mmol) was added. The reaction mixture was heated to 80 °C and stirred for 18 h (TLC-check). The reaction was quenched by adding 10 mL of water. The water and organic phase were separated, and the organic phase was washed three times with 10 mL water. The organic phase was collected and dried with Na_2SO_4. The solvent was evaporated at the rotatory evaporator, and the crude product was purified with column chromatography (flash SiO_2, 3:1 hexane:CH_2Cl_2, R_f = 0.24). To remove residual **[Cu(DPP)]**, an additional size exclusion chromatography (SEC) can be performed using toluene:CH_2Cl_2:CH_3OH 70:20:10 mixture as eluent. ^{1}H NMR (400 MHz, $CDCl_3$): δ 10.34 (s, 1H), 9.40 (br, 2H), 9.03 (br, 2H), 8.22 (br, 4H), 7.72 (br, 6H), 7.56 (br, 2H), 7.42 (br, 4H) −2.61 ppm (s, 2H). MALDI-orbitrap (*m/z*): 984.2745 ($M+H^+$, calcd), 984.2732 ($M+H^+$, found). IR: $\tilde{\nu}_{max}$/cm^{-1}: 3294 (w, N-H, stretching), 3037 (w, C=C stretching), 3018 (w), 1598 (m, N=C stretching), 1442 (m), 1376 (m), 1312 (m), 1218 (w), 1091 (m), 912 (m), 957 (m), 856 (m), 791 (s), 699 (m). UV/Vis (CH_2Cl_2): λ_{max} (log(ε)) = 410 (5.1), 440 (5.0), 512 (4.2), 539 (4.3), 586 (3.9), 642 nm (3.4).

(5-[10,20-Diphenylporphyrinato-5-yl)copper(II)]-[oxo(10,20-diphenylporphyrinato)vanadium(IV) , Cu(II)-V(IV)O dimer (**[VOCu(DPP)$_2$]**): **[VOH$_2$(DPP)]** (10 mg, 0.010 mmol) was dissolved in 5 mL of CH_2Cl_2. To this solution, $Cu(acac)_2$ (10 mg, 0.038 mmol) dissolved in 5 mL CH_2Cl_2 was added dropwise at rt while stirring. After 16 h, the reaction mixture was poured into a short silica pad (flash SiO_2, 1:1 hexane:CH_2Cl_2, R_f = 0.32). Small violet needles of **[VOCu(DPP)$_2$]** (9.4 mg, 0.009 mmol, 90 %) were obtained by recrystallization from a MeOH: CH_2Cl_2 1:5 mixture. APCI-MS (*m/z*): 1049.1983 ($M+H^+$, calcd), 1049.1995 ($M+H^+$, found). IR: $\tilde{\nu}_{max}$/cm^{-1}: 3092 (w), 3048 (w, C=C stretching), 2925 (w), 2854 (w), 1811 (w), 1599 (m, N=C stretching), (1528 m, N=C stretching), 1440 (m), 1381 (m), 1319 (s), 1298 (s), 1210 (m), 1179 (m), 1153 (m), 1064 (s), 996 (V=O stretching), 859 (m), 830 (m), 796 (s), 721 (s), 697 (s), 658 (s), 510 (vs). UV/Vis (CH_2Cl_2): λ_{max} (log(ε)) = 415 (5.3), 442 (5.2), 548 (4.6), 586 nm (4.0). EA (%); (calcd): N 10.64, C 73.24, H 3.65. (found): N 10.30, C 73.26, H 3.44

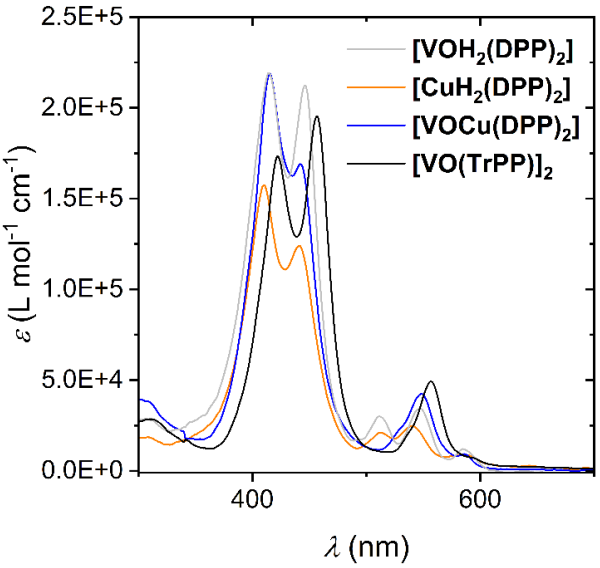

Figure 11.10: UV/Vis spectra of the compounds **[VOH₂(DPP)₂]** (orange line), **[CuH₂(DPP)₂]** (black line), **[VOCu(DPP)₂]** (blue line), and **[VO(TrPP)]₂**[217] (light gray line) in CH_2Cl_2.When comparing the UV/Vis spectra of the dimers presented in this work with the homometallic dimer,[217] one can see that the bands are broader and red-shifted.

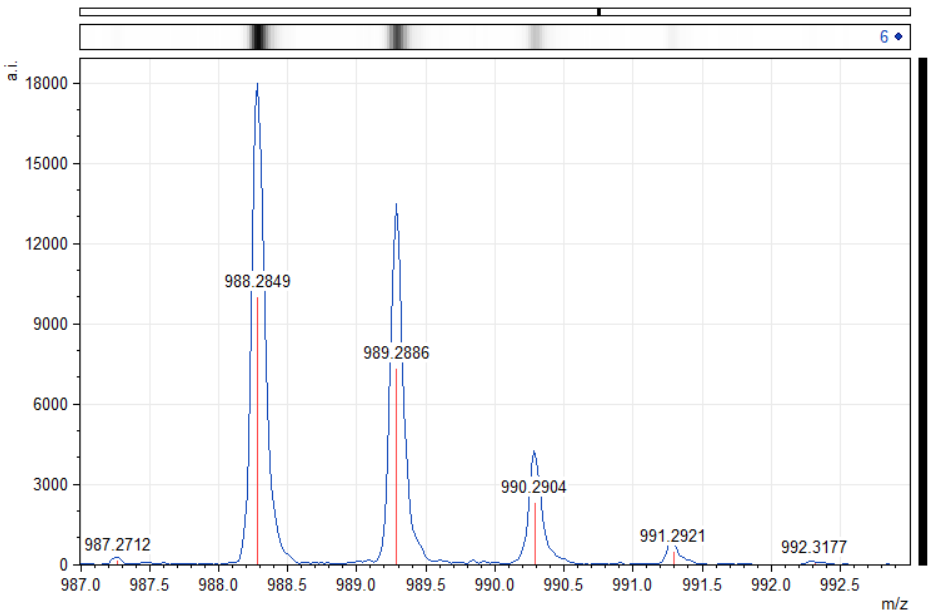

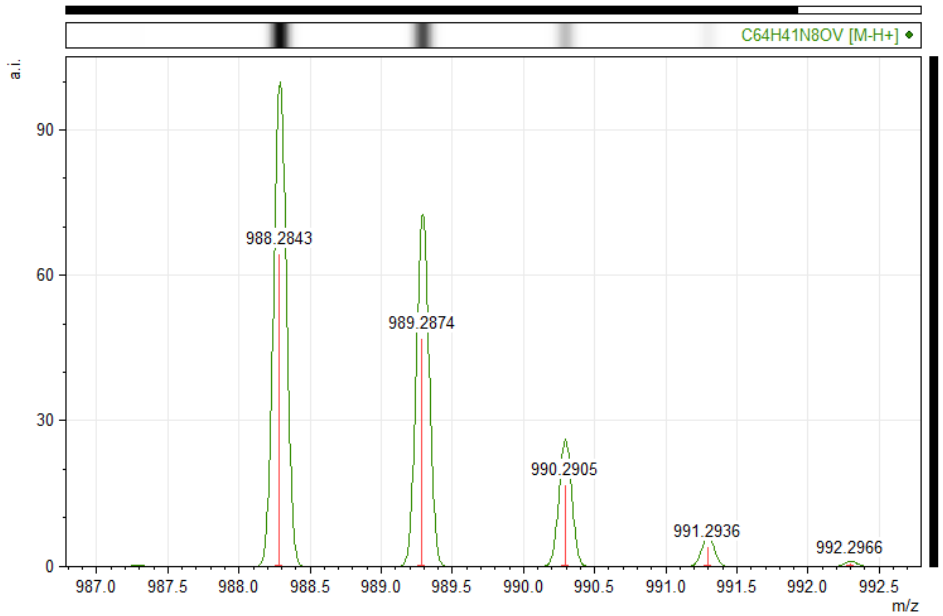

Figure 11.11: Experimental (top, blue line) and simulated (bottom, orange line) APCI-MS signals of **c**ompound **[VOH$_2$(DPP)$_2$]**

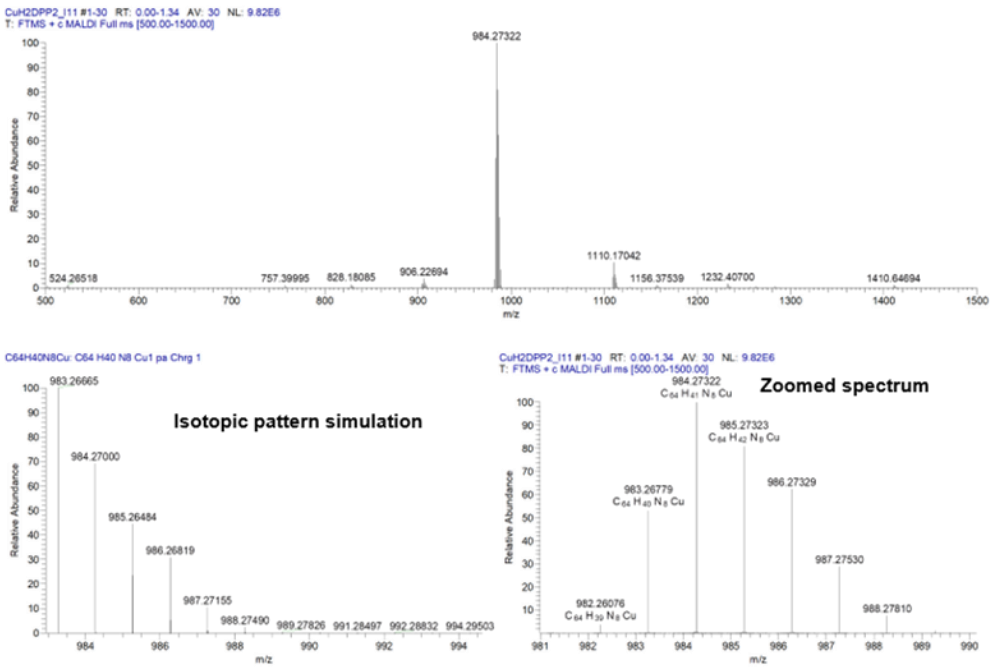

Figure 11.12: MALDI-Orbitrap signals of **c**ompound **[$CuH_2(DPP)_2$]**, full range (top), compared with the simulated pattern (bottom, left) in the zoomed region between 981-990 *m/z* (bottom, right)

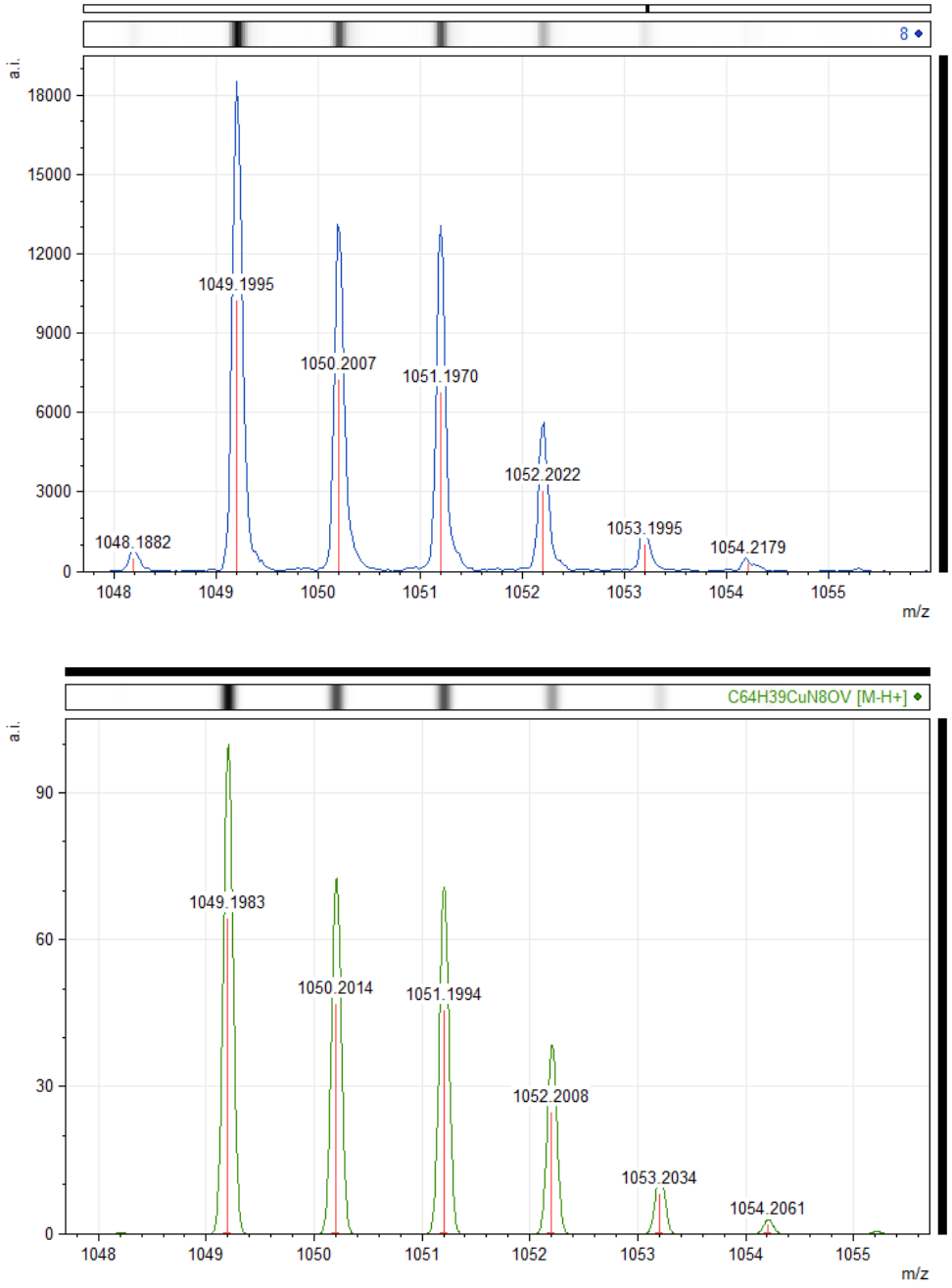

Figure 11.13: Experimental (top, blue line) and simulated (bottom, orange line) APCI-MS signals of compound **[VOCu(DPP)$_2$]**.

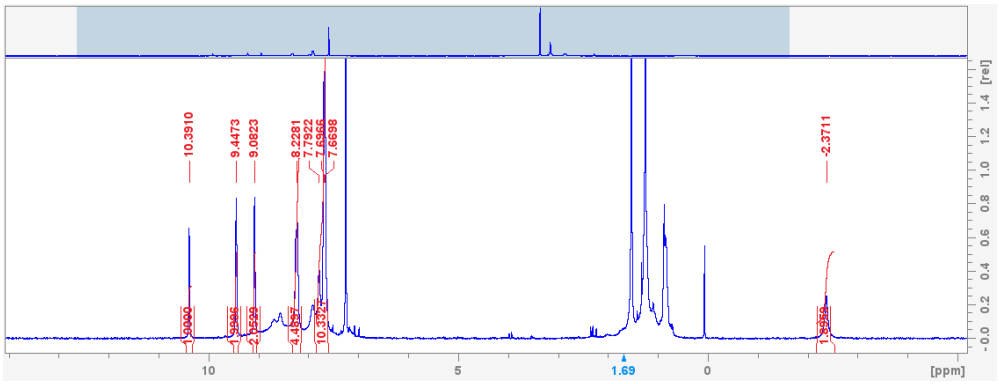

Figure 11.14: ^{1}H-NMR spectrum in $CDCl_3$ of compound **[VOH_2(DPP)$_2$]** (from δ = −3 to 12 ppm). The signals between 0 and 3 ppm correspond to H_2O and grease contamination.[247]

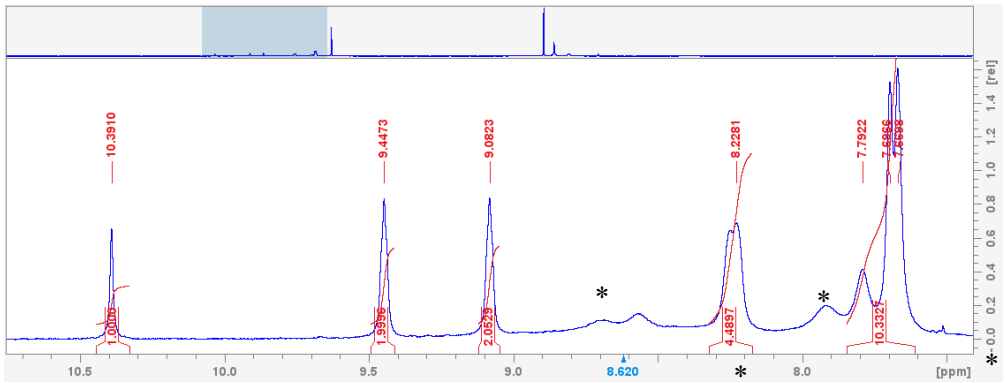

Figure 11.15: ^{1}H-NMR signals in $CDCl_3$ of compound **[VOH_2(DPP)$_2$]** in the aromatic region. Only the signals allocable to the free base porphyrin unit were integrated. The broad signals marked with * correspond to ^{1}H-signals of the VO^{IV}porphyrin unit.

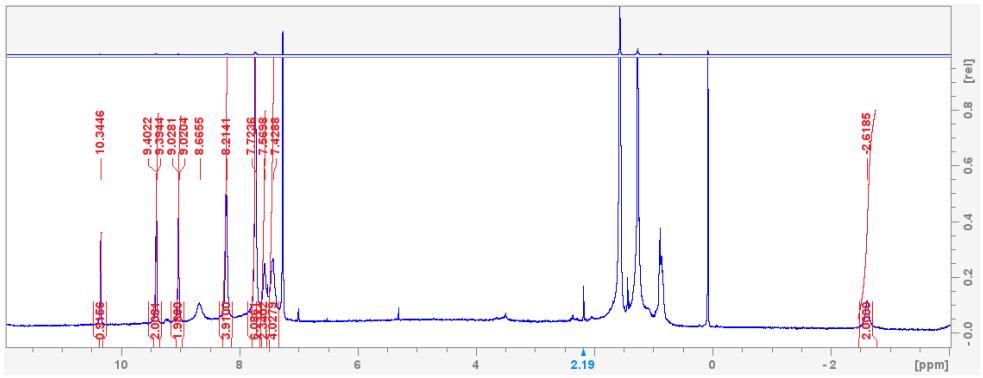

Figure 11.16: ^{1}H-NMR spectrum in $CDCl_3$ of compound **[CuH_2(DPP)$_2$]** (from δ = −3 to 12 ppm). The signals between 0 and 3 ppm correspond to H_2O and grease contamination.[247]

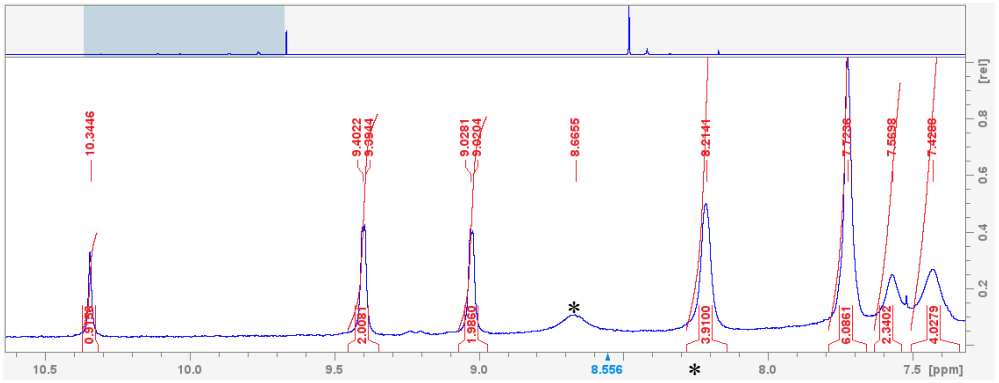

Figure 11.17: ^{1}H-NMR signals in $CDCl_3$ of compound **[CuH_2(DPP)$_2$]** in the aromatic region. Only the signals allocable to the free base porphyrin unit were integrated. The broad signals marked with * correspond to ^{1}H-signals of the Cu^{II}porphyrin unit.

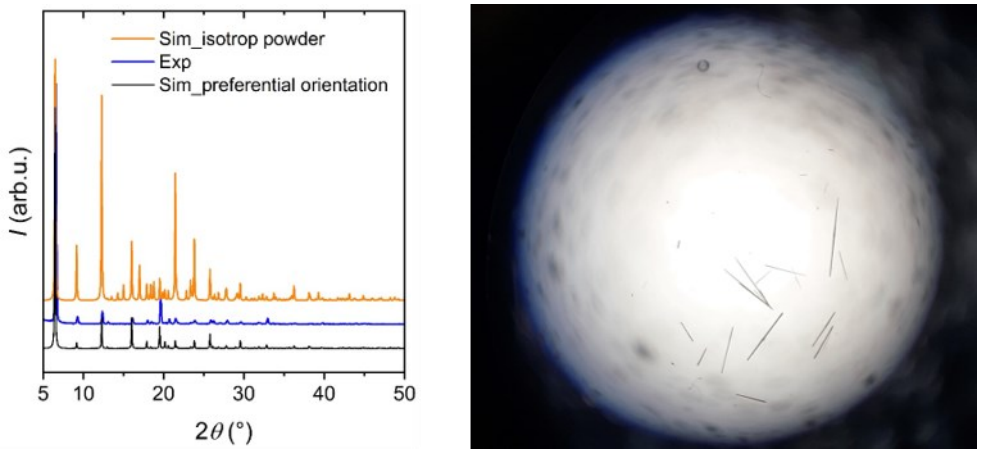

Figure 11.18: Experimental PXRD pattern (blue line) of **[VOCu(DPP)$_2$]**. The PXRD pattern was simulated using the crystallographic data obtained from the crystal structure of **[VOCu(DPP)$_2$]** assuming a perfectly isooriented powder (orange line) and assuming a preferential orientation of the powders along the (112) direction (black line) with a March-Dollase parameter of 4.[248] Due to the morphology of the small needle-like microcrystals, diffraction patterns belonging to the reflexes parallel to the *c*-axes are visible with a lower intensity. On the right side, the needle-like crystals of **[VOCu(DPP)$_2$]** are shown under a light microscope.

Table 11.3: Crystal data and structure refinement for compounds **[VO(DPP)]**, **[Cu(DPP)]**, **[$VOH_2(DPP)_2$]**, and **[$VOCu(DPP)_2$]**.

Empirical formula	$C_{32}H_{20}N_4OV$	$C_{33}H_{21}N_4Cl_3Cu$	$C_{64}H_{40}N_8OV$	$C_{64}H_{38}CuN_8OV$
Formula weight	527.46	643.43	987.98	1049.50
Temperature	100(2) K	110(2) K	100(2) K	100(2) K
Wavelength	1.54178 Å	1.54176 Å	1.54178 Å	1.54178 Å
Crystal system	Monoclinic	Monoclinic	Tetragonal	Tetragonal
Space group	$P2_1/c$	$P2_1/c$	P4cc	P4/ncc
Unit cell dimensions	a = 6.8212(2) Å b = 19.0316(6) Å c = 9.6358(3) Å α= γ = 90°. β = 105.9111(13)°	a = 18.299(3) Å b = 13.7344(16) Å c = 10.8108(14) Å α= γ = 90°. β = 99.422(9)°.	a = b = 19.130(9) Å c = 13.044(6) Å α = β = γ= 90°.	a = b = 19.275(2) Å c = 13.084(3) Å α = β= γ= 90°
Volume	1202.98(6) $Å^3$	2680.4(6)	4774(5) $Å^3$	4861.3(17) $Å^3$
Z	2	4	4	4
Density (calculated)	1.456 mg/m^3	1.594 mg/m^3	1.375 mg/m^3	1.434 mg/m^3
Absorption coefficient	3.722 mm^{-1}	4.158 mm^{-1}	2.176 mm^{-1}	2.587 mm^{-1}
F(000)	542	1308	2044	2152
Crystal size	0.115 x 0.047 x 0.04 mm^3	0.200 x 0.130 x 0.07 mm^3	0.151 x 0.041 x 0.028 mm^3	0.246 x 0.038 x 0.029 mm^3
Theta range for data collection	4.647 to 69.947°.	2.45 to 69.03°	2.309 to 63.898°.	3.242 to 60.615°.
Index ranges	-8≤h≤8, -23≤k≤23, -11≤l≤11	-22<=h<=21, -16<=k<=16, -12<=l<=13	-22≤h≤22, -22≤k≤22, -15≤l≤15	-12≤h≤21, -21≤k≤16, -14≤l≤14
Reflections collected	22000	24644	58671	1828
Independent reflections	2276 [R(int) = 0.0551]	4802 [R(int) = 0.0731]	3962 [R(int) = 0.1447]	1828 [R(int) = 0.2816]
Completeness to theta = 63.898°	100.0 %	96.3%	100.0 %	99.1 %
Absorption correction	Semi-empirical from	Multi-Scan	Semi-empirical	Semi-empirical from equivalents

	equivalents		from equivalents	
Max. and min. transmission	0.7533 and 0.6237	0.7531 and 0.4123	0.7524 and 0.6457	0.7518 and 0.3390
Refinement method	Full-matrix least-squares on F^2	Full-matrix least-squares on F^2	Full-matrix least-squares on F^2	Full-matrix least-squares on F^2
Data/restraints/parameters	2276 / 0 / 182	4802 / 0 / 370	3962 / 703 / 512	1828 / 315 / 248
Goodness-of-fit on F^2	1.157	1.102	1.018	1.066
Final R indices [I>2σ(I)]	R1 = 0.0473, wR2 = 0.1045	R1 = 0.1175, wR2 = 0.2979	R1 = 0.0727, wR2 = 0.1725	R1 = 0.1211, wR2 = 0.2936
R indices (all data)	R1 = 0.0509 wR2 = 0.1058	R1 = 0.1327, wR2 = 0.3092	R1 = 0.1297, wR2 = 0.2094	R1 = 0.1807, wR2 = 0.3378
Largest diff. peak and hole	0.258 and -0.281 e.Å^{-3}	1.948 and -1.536 eÅ^{-3}	0.166 and -0.189 e.Å^{-3}	0.468 and -0.531 e.Å^{-3}

11.4 SI: The chemical versatility of porphyrins

5,15-diphenyl-(10,20-dipinacoleboryl)porphyrin ($Bpin_2DPP$) was synthesized according to a literature procedure.[246]

Synthesis of [{VO}$_2$(DPP)$_2$(H$_2$DPP)]:

In a pre-dried double-necked round bottom flask, **Bpin$_2$DPP** (5 mg, 0.007 mmol) and **[VO(IDPP)]** (9 mg, 0.014 mmol, 2 eq.) were added together with Cs_2CO_3 (18 mg 0.056 mmol, 4 eq.) under an Ar flow. The solids were dissolved in 6 mL of dry DMF and 12 mL of dry toluene. The solution was degassed with Ar for about 30 min. After the degassing, $Pd(PPh_3)_4$ (0.8 mg, $7 \cdot 10^{-4}$ mmol. 0.1 eq.) was added. The reaction mixture was heated to 80 °C and stirred for 18 h (TLC-check). The reaction was quenched by adding 10 mL of water. The water and organic phase were separated,

and the organic phase was washed three times with 10 mL water. The organic phase was collected and dried with Na_2SO_4. The solvent was evaporated at the rotatory evaporator, and the crude product purified with column chromatography twice (flash SiO_2, petrol ether:CH_2Cl_2:NEt_3 1:1:0.01, R_f = 0.21, and flash SiO_2, hexane:CH_2Cl_2 1:2, R_f = 0.42) to yield red **[VOH$_2$VO(DPP)$_3$]** powder (1.6 mg, 0.001 mmol, 15 %). λ_{max}(CH_2Cl_2) 414 nm, 469 nm, 521 nm, 549 nm, 597 nm, 654 nm. MALDI-orbitrap (*m/z*): 1514.3791 ($M+H^+$, calcd), 1514.3822 ($M+H^+$, found).

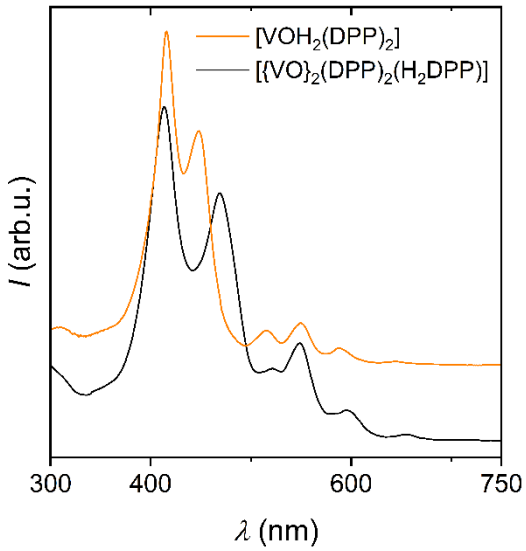

Figure 11.19: UV/Vis spectrum comparison of **[VOH$_2$(DPP)$_2$]** (orange spectrum) and **[{VO}$_2$(DPP)$_2$(H$_2$DPP)]** (black spectrum).

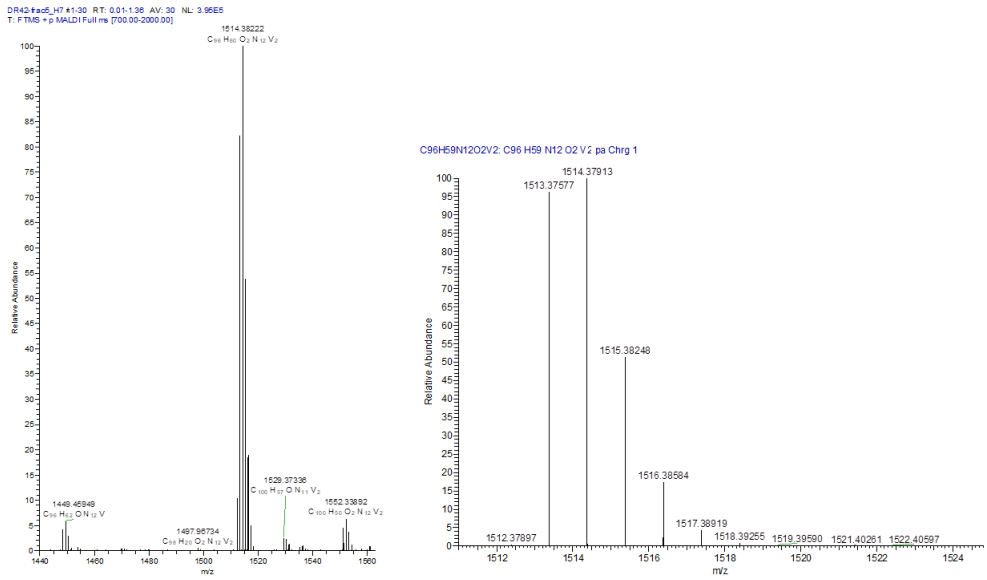

Figure 11.20: Experimental MALDI-orbitrap of **[VOH$_2$VO(DPP)$_3$]** (left), compared to the simulated one (right).

Synthesis of [VO(ITrPP)]:

In a Schlenk flask, **[VOTrPP)]** (40 mg, 0.067 mmol) was dissolved in 30 mL CH_2Cl_2 under N_2 flow. To this solution, pyridine (0.5 mL, 490 mg, 6.2 mmol, 92 eq.) was added and the reaction mixture was degassed with N_2. Subsequently, I_2 (50 mg, 0.198 mmol, 3 eq.) was added to the mixture. In the meantime, a PIFA (85 mg, 0.198 mmol, 3 eq.) solution in10 mL of CH_2Cl_2 was prepared and this solution was added dropwise to the solution containing **[VOTrPP)]**. After all the PIFA solution was added, the reaction mixture was stirred at rt and in the dark for 1 h. The reaction mixture was quenched with 15 mL of an aqueous solution of $Na_2S_2O_3$. The water and organic phase were separated, and the organic phase washed with a 15 mL sat. $NaHCO_3$ solution three times. The organic phase was dried with Na_2SO_4, and the solvent was evaporated under reduced pressure. The crude product was purified with column chromatography (flash SiO_2, hexane:CH_2Cl_2:NEt_3, 1:1:0.01, R_f = 0.27). Polycrystalline powders of **[VO(ITrPP)]** (34 mg, 0.047 mmol, 70 %) were obtained by the slow evaporation of the eluent mixture λ_{max}(CH_2Cl_2) 428 nm, 552 nm, 589 nm. MALDI-orbitrap (*m/z*): 729.0350 (M, calcd), 729.0342 (M, found).

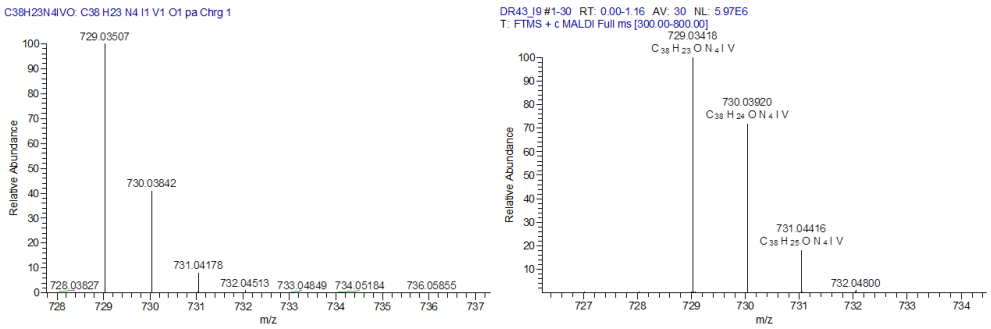

Figure 11.21: Experimental MALDI-orbitrap of **[VO(ITrPP]** (left), compared to the simulated one (right).

Synthesis of [{VO}$_2$(TrPP)$_2$(H$_2$DPP)]:

In a pre-dried double-necked round bottom flask, Bpin$_2$DPP (12 mg, 0.016 mmol) and **[VO(ITrPP)]** (24 mg, 0.033 mmol, 2 eq.) were added together with Cs_2CO_3 (22 mg 0.068 mmol, 4 eq.) under an Ar flow. The solids were dissolved in 10 mL of dry DMF and 20 mL of dry toluene. The solution was degassed with Ar for about 30 min. After the degassing, $Pd(PPh_3)_4$ (2 mg, 0.0017 mmol. 0.1 eq.) was added. The reaction mixture was heated to 80 °C and stirred for 5 h (TLC-check). The reaction was quenched by adding 15 mL of water. The water and organic phase were separated, and the organic phase was washed three times with 20 mL water. The organic phase was collected and dried with Na_2SO_4. The solvent was evaporated at the rotatory evaporator, and the crude product purified with column chromatography (flash SiO_2, hexane:CH_2Cl_2:NEt_3 1:1:0.01, R_f = 0.22) to yield red **[{VO}$_2$(TrPP)$_2$(H$_2$DPP)]** powder (16 mg, 0.0096 mmol, 60 %).. λ_{max}(CH_2Cl_2) 311 nm, 420 nm, 473 nm, 521 nm, 556 nm, 597 nm, 655 nm. MALDI-orbitrap (*m/z*): 1665.43390 ($M+H^+$, calcd), 1665.43626 ($M+H^+$, found).

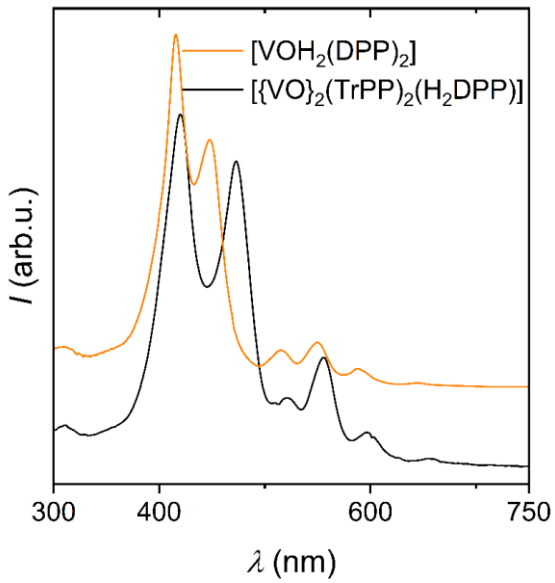

Figure 11.22: UV/Vis spectrum comparison of **[VOH$_2$(DPP)$_2$]** (orange spectrum) and **[{VO}$_2$(TrPP)$_2$(H$_2$DPP)]** (black spectrum).

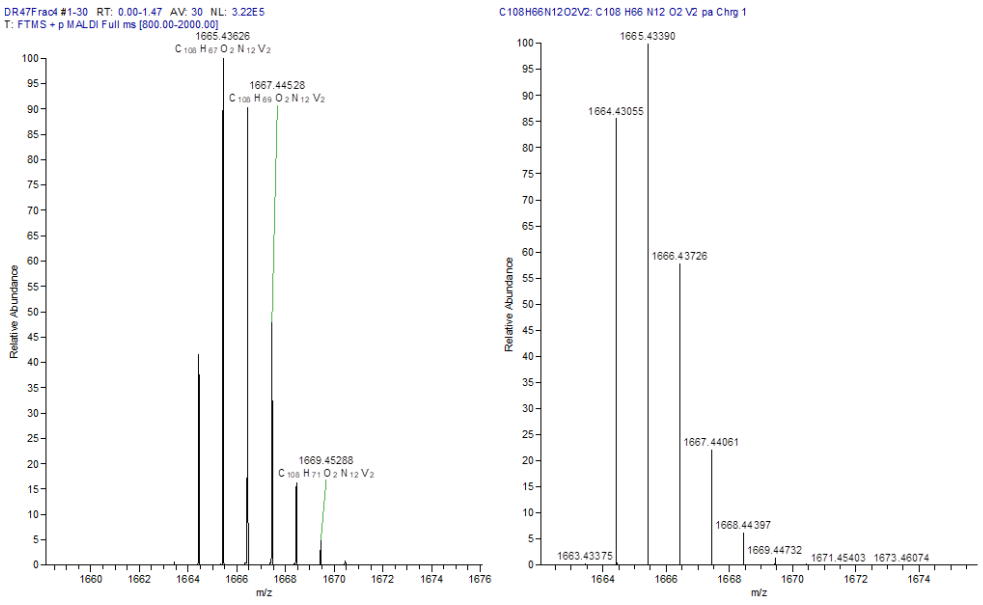

Figure 11.23: Experimental MALDI-orbitrap of **[{VO}$_2$(TrPP)$_2$(H$_2$DPP)]** (left), compared to the simulated one (right).

Synthesis of [Cu(BrTrPP)]:

In this synthesis, 100 mg (0.147 mmol) of BrTrPP were solved in 12 mL of $CHCl_3$. Then, 146 mg (0.735 mmol, 5 eq.) of $Cu(OAc)_2 \cdot H_2O$ in 6 mL MeOH were successively added to the solution and the reaction mixture was stirred for two hours (check UV/VIS spectroscopy and TLC check (petroleum ether/ethyl acetate 4:1). After that, 10 mL of water was poured to the reaction mixture and the organic phase was separated from the water phase. The water phase was washed three times with 20 mL $CHCl_3$. The organic phases were collected and dried with $NaSO_4$ and afterward $CHCl_3$ was removed under reduced pressure. The precipitation was collected and washed with water and MeOH. After drying for two days in the desiccator, 89 mg (0.124 mmol, 77 %) of **[Cu(BrTrPP)]** as a dark red powder was obtained. $\lambda_{max}(CHCl_3)$ = 412 nm, 540 nm; EA: $C_{38}H_{23}N_4BrCu$ (calc, %) = C 67.21 %, H 3.41, N 8.25; (exp, %) = C 71.54, H 3.27, N 8.16.

Synthesis of [VO(BrTrPP)]:

[VO(TrPP)] powders (30 mg, 0.05 mmol) were dissolved in 15 mL $CHCl_3$, and pyridine was added (0.08 mL, 0.99 mmol, 20 eq.). The solution was cooled to 0°C with an ice-bath. To this solution, NBS (17 mg, 0.1 mmol, 2 eq.) solved in 5 mL $CHCl_3$ was added dropwise, and the reaction mixture stirred at 0°C for 10 min. The reaction mixture was quenched with 10 mL acetone. The solvent was evaporated under the rotatory evaporator, and the crude product purified with column chromatography (flash SiO_2, CH_2Cl_2:hexane 1:1). After recrystallization in a mixture of CH_2Cl_2:CH_3CN 5:1, polycrystalline powders of **[VO(BrTrPP)]** (28 mg, 0.04 mmol, 80 % yield) were obtained. $\lambda_{max}(CHCl_3)$ = 425 nm, 551 nm; EA: $C_{38}H_{23}N_4BrVO \cdot 2\ CH_2Cl_2$ (calc, %) = C 56.37, H 3.19, N 6.57; (exp, %) = C 55.58, H 2.84, N 6.58.

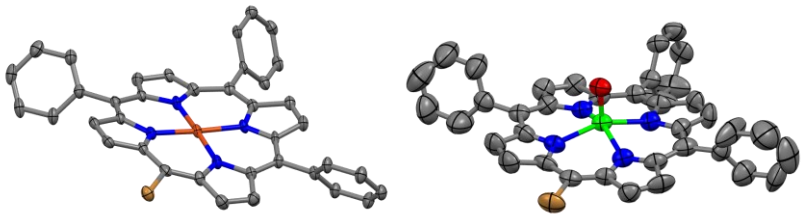

Figure 11.24: Crystal structures of **[Cu(BrTrPP)]** (left) and **[VO(BrTrPP)]** (right). Atoms are shown as thermal ellipsoids (50 % probability). Color code: C = dark grey, N = blue, O = red, Br = light brown, Cu = orange, V = green. Hydrogens are omitted for clarity.

Table 11.4: Crystal data and structure refinement for **[Cu(BrTrPP)]** and **[VO(BrTrPP)]**.

Empirical formula	$C_{38}H_{23}N_4BrCu$	$C_{38}H_{23}N_4BrOV$
Formula weight	679.05	686.88
Temperature	100 (2) K	293(2) K
Wavelength	1.54184	0.71073 Å
Crystal system		monoclinic
Space group	$P2_1/n$	C2/c
Unit cell dimensions	a = 14.452(6) Å b = 9.609(3) Å c = 20.298(7) Å α= γ = 90°. β = 91.810(15)°.	a = 23.938(7) Å b = 11.2555(16) Å c = 26.683(6) Å α= γ = 90°. β = 116.19(3)°.
Volume	2817.4(16)	6451(3)
Z	4	8
Density (calculated)	1.601	1.414 mg/m^3
Absorption coefficient	3.037	4.158 mm^{-1}
F(000)	1372	2777
Crystal size	1.00 x 0.300 x 0.250 mm^3	0.200 x 0.130 x 0.07 mm^3
Theta range for data collection	3.6995 to 72.0982°	4.307 to 35.008°

Index ranges	-17<=h<=17, -11<=k<=11, -24<=l<=25	-33<=h<=37, -16<=k<=16, -40<=l<=39
Reflections collected	6318	11173
Independent reflections	5506 [R(int) = 0.1301]	3677 [R(int) = 0.1401]
Completeness to theta = 63.898°	98.7 %	99.62 %
Absorption correction	Multi-Scan	Multi-Scan
Max. and min. transmission	0.7536 and 0.4933	1.00 and 0.66291
Refinement method	Full-matrix least-squares on F^2	Full-matrix least-squares on F^2
Goodness-of-fit on F^2	1.061	1.249
Final R indices [I>2σ(I)]	R1 =0.0962, wR2 = 0.1603	R1 = 0.0432, wR2 = 0.2901
R indices (all data)	R1 = 0.0637, wR2 = 0.1832	R1 = 0.1410, wR2 = 0.3751

XPS-Characterization

[VO(BrTrPP)] deposits: XPS analyses were carried out in an UHV chamber with a base pressure lower than 10^{-9} mbar. The chamber was equipped with a non-monochromatized Mg Kα radiation ($h\nu$ = 1253.6 eV) and a hemispherical electron/ion energy analyzer (VSW mounting a 16-channel detector).

[Cu(BrTrPP)] deposits: XPS measurements were performed using a micro-focused monochromatic Al Kα radiation source (1486.6 eV, model SPECS XR-MS Focus 600) and a multichannel detector electron analyzer (model SPECS Phoibos 150 1DLD)

Both **[VO(BrTrPP)]** and **[Cu(BrTrPP)]** molecules evaporate at a temperature of around 250°C, with a deposition rate of approximately 0.7 nm/h. Deposition rates were monitored by a quartz microbalance. The XPS-spectrum shows the intensity expressed as counts per second (CPS) of the detected photoelectrons against the binding energy (*B.E*) of electrons in the first substrate layers. Signal attribution of components affected by SOC were allocated according to the *Handbook*

of X-ray Photoelectron Spectroscopy.[249] The *Casa* XPS software was used to fit XPS signals using mixed *Gaussian* and *Lorentzian* functions, and using a Shirley or linear type background. The Lorentzian and Gaussian contributions to the fit were weighted with 70 % *Lorentzian* contribution and 30 % *Gaussian* contribution. Signal areas were used to perform a semi-quantitative elemental analysis and evaluate the intactness of the molecular deposit after the deposition. Indeed, XPS signal areas are proportional to the number of atoms on the surface and allow a quantitative elemental analysis to be compared with the compound stoichiometry. All the XPS-spectra were calibrated to the Au*4f* signal at 84 eV. For the semiquantitative analysis, signal areas were corrected for the elemental cross-section, considering instrument sensitivity of each element.[250] Then, the corrected area of each element (N*1s*, C*1s*, Cu*2p*, and Br*3p*) was divided by the total area given by the sum of all peak areas of the elements.

11.5 Cw-EPR spectrometer

Figure 11.25 shows a schematic drawing of a cw-EPR spectrometer. With the EPR spectrometer, the absorption of electromagnetic waves in a static magnetic field by a paramagnetic sample can be detected and measured. The theoretical background that causes the absorption and the obtained spectra were explained in Chapter 2. Samples can be cooled down to 4 K when a cryostat is available. The sample can be measured in solid-state, as a single crystal, microcrystalline powders or in solution (frozen or liquid).[251] Small amounts of sample are usually necessary to detect the signal. Since the linewidth of the EPR-spectrum increases with decreasing T_2, too high concentrations of a paramagnetic sample enhance the linewidth and suppress smaller contributions in the spectrum, thus diluted samples provide more resolution. The sample is put in a thin quartz tube and is inserted into the sample holder.

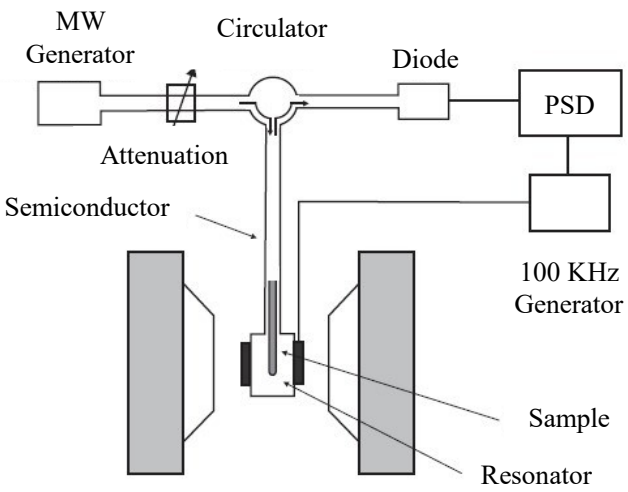

Figure 11.25: Schematic drawing of a simple cw-EPR spectrometer.[252]

The EPR-spectrometer used in this thesis is the Bruker Elexsys E500 spectrometer equipped with an SHQ cavity (υ = 9.39 GHz). Low-temperature measurements were obtained using an Oxford Instruments ESR900 continuous flow helium cryostat. The MW generator generates the microwave, which passes through an attenuator that can attenuate the microwave power. The attenuation is important, because if T_1 is too high, saturation is reached when the microwave power is also too high. From the attenuator, the microwave passes through the circulator that directs the microwave into the resonator. Due to a mirror on the top and bottom of the resonator, the microwave can be held in the resonator, creating a stationary wave. Destructive interference occurs when the resonator length is long enough so that the phases of the arriving microwave and the leaving microwave are shifted to 180°. The mirror between the top and bottom of the resonator can be adjusted before a measurement so that the resonator has the same length as the wavelength of the microwave (~ 3cm). When the sample is put in the resonator, the magnetic field will be varied and when the field-dependent *Zeeman* splitting is the same as the energy of the microwave, some of the microwaves will be absorbed from the sample, and the microwave can leave the resonator and go to a diode where a current is produced. The current is proportional to the reflected microwave and creates a signal on the monitor. To improve the sensitivity, the static magnetic field is modulated. This is done by adding a Cu-spool on the resonator, which creates a varying magnetic field parallel to the quasi-static magnetic field. The modulation appears in the diode current when the sample absorbs the microwave. This current is filtered out and rectified. The obtained voltage is proportional to the absorption signal. The modulation amplitude can be adjusted before a measurement. Note that the modulation amplitude must be smaller than the resonance linewidth. Otherwise, the signal will be distorted and eventually disappear for too high modulation. Due to the modulation, the signal appearing on the monitor is the first derivative of the absorption signal. The most common used cw-EPR spectrometers are in the X-band region. This type of spectrometer works in a 0.37-1 T magnetic field range, with a microwave of 8-12 GHz. Other regions are the Q-band (~ 35 GHz) and the W-band (~ 95 GHz). Spectrometers working with a frequency above 70 GHz are considered High-frequency EPR spectrometers. The cw-EPR spectrometer works

with a variable H_0-field and a constant microwave frequency. Resonance can also occur if the frequency is changed, and the field is constant. This is done in pulsed-EPR spectroscopy. With pulsed-EPR spectroscopy, the relaxation times T_1 and T_2 can be determined. Pulsed-EPR also has a better resolution at higher fields and frequencies.[34]

Figure 11.26, top, shows the EPR spectrum of a Cu^{2+} complex with hyperfine coupling, and as explained earlier, the two dominant signals correspond to the g values of $g_\parallel$, and $g_\perp$. The difference in signal intensity can be explained by statistical means, because the surface area of a sphere is larger around the xy-plane and therefore the number of spins is higher as well, thus increasing the intensity of the signal.

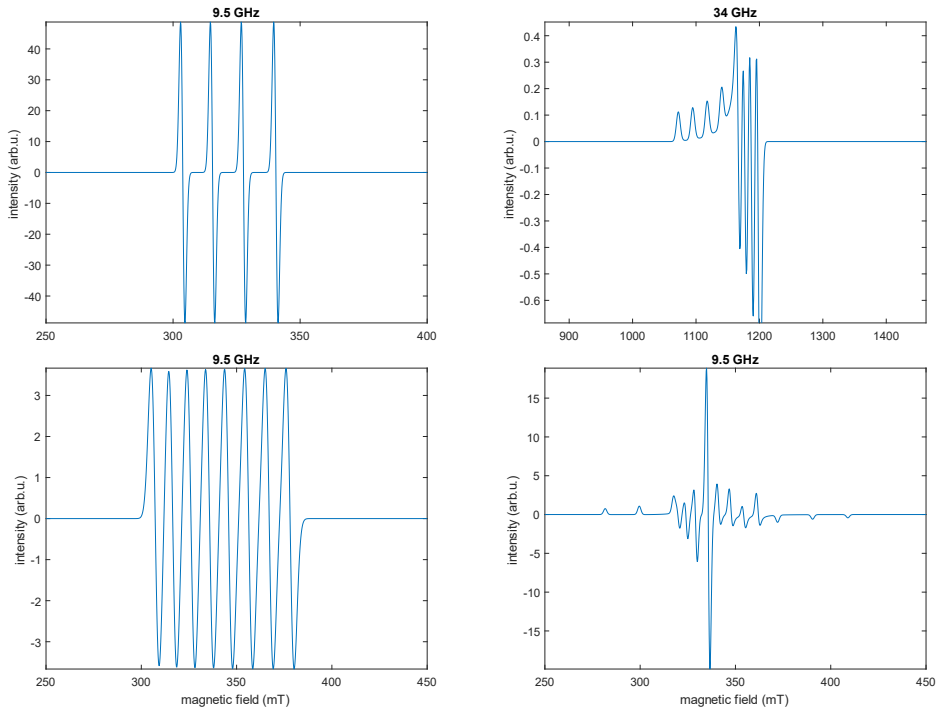

Figure 11.26: Simulated EPR-spectra in a liquid solution (isotropic A and g values, left) and frozen solution (right) for a Cu^{2+} (top) and V^{4+} complex (bottom). The parameters used for the simulations are: g = 1.989, A = 250 MHz (isotropic, V^{4+} complex); g = [1.985 1.985 1.964], A = [250 250 500] MHz (axial, V^{4+}-complex); g = 2.1, A = 430 MHz (isotropic, Cu^{2+}-complex); g = [2.051 2.051 2.195], A= [300 300 700] MHz (axial, Cu^{2+}-complex).

Acknowledgments

To my Family and Friends:

It's time to acknowledge the people who have been my pillars of support during this PhD journey. First and foremost, I want to express my deepest gratitude to my parents, who have been with me through every step of my academic journey, from Bachelor's to Master of Science, and now through my PhD. Their unwavering support allowed me to focus on my studies without financial pressures.

I owe a special thanks to my brother, *Vincenzo*, who ignited my scientific curiosity during my childhood. It was he who gifted me my first book on scientific experiments, setting the stage for my academic journey. My sister, Marianna, played a significant role in expanding my knowledge by introducing me to literature and some heavy-handed films (remember *Schlafes Bruder* & *Marlene Dietrich*?).

I want to extend my gratitude to my other sister, *Francesca*, who was a source of comfort during my time in Florence. Being able to visit her was a pleasant break from my PhD pursuits.

My heartfelt thanks go to my girlfriend, *Magdalena*, who shared many engaging conversations with me about electron spins and intriguing historical topics, sparking my interest.

Finally, I want to thank my fellow friends in Florence. *Alberto*, thank you for the memorable trips to the Apuane and the Appenino Tosco-Emiliano. To *Gabriel*, thank you for our thought-provoking conversations about life, politics, and even esoteric subjects like Taoism. To *Kailin*, your insights into Chinese culture and art opened up a new world for me. And to *Antonio*, I appreciated our scientific discussions. Your contributions have enriched my academic journey.

To the LAMM-group:

I'd like to express my heartfelt gratitude to everyone in our research group who played a role in the successful completion of my PhD Thesis. Your support, guidance, and hard work were essential throughout this journey.

Roberta Sessoli: My “Doktormutter”, your unwavering support and problem-solving skills were precious. You were the driving force behind my decision to pursue a PhD.

Lorenzo Sorace: My “Doktorvater”, co-supervisor, and detail-oriented mentor, your meticulous approach to research and dedication have been a great source of inspiration for me.

Alberto Privitera: My “Doktoronkel”: Not only my trekking friend, but also the guy who made the cw-EPR experiments. He also simulated the solid-state spectra shown in Chapter 6. I remember all the discussions we had with Prof. Roberta Sessoli and Prof. Lorenzo Sorace on how to simulate the single crystal spectra. So much trouble, but at the end, you did it!

Fabio Santanni: My “Doktorbruder”: Probably the smartest PhD Student (now post-doc) I ever met. He gave me so many recommendations in the synthetic lab, but also solved most structures shown in this PhD Thesis (especially in Chapter 7). He also wrote the MatLab program for the identification of suitable computational states (Chapter 6 & 8).

Federico Totti & Andrea Albino: your expertise in DFT calculations provided valuable support for our experimental findings. I really appreciated the fact that you (Federico!) tried to teach me with simple words orbital interaction in porphyrins, on surface, and in general with everything. Thanks for the fruitful conversations!

Giulia Serrano: Your mentorship in on-surface experiments was precious, introducing me to a completely new research area and helping me analyzing XPS data.

Lorenzo Poggini & Andrea Luigi Sorrentino: Your efficiency, accuracy, and unwavering dedication in setting up on-surface experiments are commendable. The

depositions you carried out with my molecules were flawless Andrea even had to endure my present at the CeTechs for some time. At least we had some fun right?

Additionally, I want to show my gratitude to all the LAMM group. It was a pleasure meeting you.

To the external collaborators:

I want to acknowledge the opportunity Prof. Mathias Senge gave me to work in his synthesis laboratory at Trinity College Dublin. I also want to thank Karolina Urbanska, Grant Starchan, and Brendan Twamley who supported me during my stay in Dublin. Furthermore, I want to thank our collaborators at the Department of Chemistry and NIS in the University of Turin (Prof. Mario Chiesa, Prof. Enrico Salvadori, and Dr. Yu-Kai Liao) in performing all the pulsed-EPR measurements.

References

[1] J. P. Dowling, G. J. Milburn, *Phil. Trans. R. Soc. A.* **2003**, *361*, 1655–1674.

[2] M. Atzori, R. Sessoli, *J. Am. Chem. Soc.* **2019**, *141*, 11339–11352.

[3] D. Garisto, "The second quantum revolution," can be found under https://www.symmetrymagazine.org/article/the-second-quantum-revolution?language_content_entity=und#:~:text=In 1994%2C combining new insight,superposition and can be entangled., **2022**.

[4] T. P. Spiller, *Fortschr. der Phys.* **2000**, *48*, 1075–1094.

[5] M. H. Abobeih, Y. Wang, J. Randall, S. J. H. Loenen, C. E. Bradley, M. Markham, D. J. Twitchen, B. M. Terhal, T. H. Taminiau, *Nature* **2022**, *606*, 884–889.

[6] L. Fedichkin, M. Yanchenko, K. A. Valiev, *Proc. 8th Int. Symp. Nanostructures Phys. Technol.* **2000**, 538–541.

[7] B. Trauzettel, D. V. Bulaev, D. Loss, G. Burkard, *Nat. Phys.* **2007**, *3*, 192–196.

[8] M. Pivoluska, M. Plesch, *Sci. Rep.* **2022**, 5841.

[9] P. K. Vishnu, D. Joy, B. K. Behera, P. K. Panigrahi, *Quantum Inf. Process.* **2018**, *17*, 1–17.

[10] F. Arute, K. Arya, R. Babbush, D. Bacon, J. C. Bardin, R. Barends, R. Biswas, S. Boixo, F. G. S. L. Brandao, D. A. Buell, B. Burkett, Y. Chen, Z. Chen, B. Chiaro, R. Collins, W. Courtney, A. Dunsworth, E. Farhi, B. Foxen, A. Fowler, C. Gidney, M. Giustina, R. Graff, K. Guerin, S. Habegger, M. P. Harrigan, M. J. Hartmann, A. Ho, M. Hoffmann, T. Huang, T. S. Humble, S. V. Isakov, E. Jeffrey, Z. Jiang, D. Kafri, K. Kechedzhi, J. Kelly, P. V. Klimov, S. Knysh, A. Korotkov, F. Kostritsa, D. Landhuis, M. Lindmark, E. Lucero, D. Lyakh, S. Mandrà, J. R. McClean, M. McEwen, A. Megrant, X.

Mi, K. Michielsen, M. Mohseni, J. Mutus, O. Naaman, M. Neeley, C. Neill, M. Y. Niu, E. Ostby, A. Petukhov, J. C. Platt, C. Quintana, E. G. Rieffel, P. Roushan, N. C. Rubin, D. Sank, K. J. Satzinger, V. Smelyanskiy, K. J. Sung, M. D. Trevithick, A. Vainsencher, B. Villalonga, T. White, Z. J. Yao, P. Yeh, A. Zalcman, H. Neven, J. M. Martinis, *Nature* **2019**, *574*, 505–510.

[11] F. Luis, A. Repollés, M. J. Martínez-Pérez, D. Aguilà, O. Roubeau, D. Zueco, P. J. Alonso, M. Evangelisti, A. Camón, J. Sesé, L. A. Barrios, G. Aromí, *Phys. Rev. Lett.* **2011**, *107*, 117203.

[12] E. Moreno-Pineda, C. Godfrin, F. Balestro, W. Wernsdorfer, M. Ruben, *Chem. Soc. Rev.* **2018**, *47*, 501–513.

[13] F. Troiani, M. Affronte, *Chem. Soc. Rev.* **2011**, *40*, 3119–3129.

[14] C. H. Bennett, *IBM J. Res. Dev.* **1973**, *17*, 525–532.

[15] R. P. Feynman, *Int. J. Theor. Phys.* **1982**, *21*, 467–488.

[16] D. Deutsch, *Proc. R. Soc. London A* **1985**, *400*, 97–117.

[17] C. E. Shannon, *Bell Syst. Tech. J.* **1948**, *27*, 379–423.

[18] S. W. Amos, *Principles of Transistor Circuits*, Elsevier, **1994**.

[19] T. Mor, R. Renner, *Nat. Comput.* **2014**, *13*, 447–452.

[20] A. Barenco, C. H. Bennett, R. Cleve, D. P. DiVincenzo, N. Margolus, P. W. Shor, T. Sleator, J. A. Smolin, H. Weinfurter, *Phys. Rev. A* **1995**, *52*, 3457–3467.

[21] D. P. DiVincenzo, *Proc. R. Soc. A Math. Phys. Eng. Sci.* **1998**, *454*, 261–276.

[22] P. A. . Dirac, *Math. Proc. Cambridge Philos. Soc.* **1939**, *35*, 416–418.

[23] Micheal A. Nielsen and Isaac L. Chuang, *Quantum Computation and Quantum Information*, Cambridge University Press, Cambridge, **2000**.

[24] M. Hayashi, S. Ishizaka, A. Kawachi, G. Kimura, T. Ogawa, *Introduction to*

Quantum Information Science, Springer Berlin Heidelberg, Heidelberg, **2014**.

[25] G. W. Mackey, *Am. Math. Mon.* **1957**, *64*, 45.

[26] M. D. Lechner, *Einführung in Die Quantenchemie; Aufbau Der Atome Und Moleküle, Spektroskopie*, Springer Spektrum, **2017**.

[27] D. P. DiVincenzo, *Fortschr. Phys.* **2000**, *48*, 771–783.

[28] T. Sleator, H. Weinfurter, *Phys. Rev. Lett.* **1995**, *74*, 4087–4090.

[29] A. Einstein, B. Pololsky, N. Rosen, *Phys. Rev.* **1935**, *47*, 777–780.

[30] J. S. Bell, *Phys. Phys. Физика* **1964**, *1*, 195–200.

[31] C. H. Bennett, S. J. Wiesner, *Phys. Rev. Lett.* **1992**, *69*, 2881–2884.

[32] W. Gerlach, O. Stern, *Zeitschrift für Phys.* **1922**, *9*, 349–352.

[33] S. Blundell, *Magnetism in Condensed Matter*, Oxford University Press, New York, **2001**.

[34] A. Schweiger, G. Jeschke, *Principles of Pulse Electron Paramagnetic Resonance*, Oxford University Press, New York, **2001**.

[35] D. J. Griffiths, D. F. Schroeter, *Introduction to Quantum Mechanics*, Cambridge University Press, New York-Melbourne-New Delhi-Singapore, **2018**.

[36] W. Heisenberg, *Zeitschrift für Phys.* **1926**, *38*, 411–426.

[37] P. Atkins, R. Friedman, *Molecular Quantum Mechanics*, Oxford University Press, New York, **2005**.

[38] S. M. Harvey, M. R. Wasielewski, *J. Am. Chem. Soc.* **2021**, *143*, 15508–15529.

[39] S. Stoll, A. Schweiger, *J. Magn. Reson.* **2006**, *178*, 42–55.

[40] A. B. D. Gatteschi, *EPR of Exchange Coupled Systems*, Springer Berlin

Heidelberg, **1990**.

[41] O. Kahn, Y. Journaux, I. Morgenstern-Badarau, J. Galy, J. Jaud, *J. Am. Chem. Soc.* **1982**, *104*, 2165–2176.

[42] G. R. Eaton, S. S. Eaton, *J. Magn. Reson.* **1999**, *136*, 63–68.

[43] C. Finazzo, C. Calle, S. Stoll, S. Van Doorslaer, A. Schweiger, *Phys. Chem. Chem. Phys.* **2006**, *8*, 1942–1953.

[44] A. Wolberg, J. Manassen, *J. Am. Chem. Soc.* **1970**, *92*, 2982–2991.

[45] D. Gatteschi, R. Sessoli, J. Villain, *Molecular Nanomagnets*, Oxford University Press, Oxford, **2006**.

[46] A. Lunghi, *arXiv:2202.03776v1* **2022**, DOI doi.org/10.48550/arXiv.2202.03776.

[47] A. Lunghi, S. Sanvito, *Sci. Adv.* **2019**, *5*, 1–8.

[48] K. W. H. Stevens, H. A. M. van Eekelen, *Proc. Phys. Soc.* **1967**, *92*, 680–696.

[49] J. B. Goodenough, *Phys. Rev.* **1955**, *100*, 564–573.

[50] J. B. Goodenough, *J. Phys. Chem. Solids* **1958**, *6*, 287–297.

[51] J. Kanamori, *J. Phys. Chem. Solids* **1959**, *10*, 87–98.

[52] O. Kahn, R. Hoffmann, M. Verdaguer, *Molecular Magnetism*, VCH, New York, **1993**.

[53] F. E. Mabbs, D. Collison, *Studies in Inorganic Chemistry | Electron Paramagnetic Resonance of d Transition Metal Compounds*, Elsevier, Amsterdam-London-New York-Tokyo, **1992**.

[54] P. A. . Dirac, *Proc. R. Soc. A Math. Phys. Eng. Sci.* **1927**, *114*, DOI https://doi.org/10.1098/rspa.1927.0039.

[55] G. Wolfowicz, J. J. L. Morton, *eMagRes* **2016**, *5*, 1515–1528.

[56] H. A. Kramers, *Proc. R. Netherlands Acad. Arts Sci.* **1930**, *33*, 959–972.

[57] M. Atzori, L. Tesi, E. Morra, M. Chiesa, L. Sorace, R. Sessoli, *J. Am. Chem. Soc.* **2016**, *138*, 2154–2157.

[58] S. Lenz, K. Bader, H. Bamberger, J. Van Slageren, *Chem. Commun.* **2017**, *53*, 4477–4480.

[59] C. J. Yu, M. J. Graham, J. M. Zadrozny, J. Niklas, M. D. Krzyaniak, M. R. Wasielewski, O. G. Poluektov, D. E. Freedman, *J. Am. Chem. Soc.* **2016**, *138*, 14678–14685.

[60] K. Bader, M. Winkler, J. Van Slageren, *Chem. Commun.* **2016**, *52*, 3623–3626.

[61] R. Sessoli, D. Gatteschi, A. Caneschi, M. A. Novak, *Nature* **1993**, *365*, 141–143.

[62] M. N. Leuenberger, D. Loss, *Nature* **2001**, *410*, 789–793.

[63] D. Gatteschi, R. Sessoli, A. Cornia, *Chem. Commun.* **2000**, 725–732.

[64] D. N. Woodruff, R. E. P. Winpenny, R. A. Layfield, *Chem. Rev.* **2013**, *113*, 5110–5148.

[65] F. K. Larsen, E. J. L. McInnes, H. El Mkami, J. Overgaard, S. Piligkos, G. Rajaraman, E. Rentschler, A. A. Smith, G. M. Smith, V. Boote, M. Jennings, G. A. Timco, R. E. P. Winpenny, *Angew. Chem. Int. Ed.* **2003**, *42*, 101–105.

[66] F. Meier, D. Loss, *Phys. Rev. B* **2001**, *64*, 224411.

[67] F. Troiani, A. Ghirri, M. Affronte, S. Carretta, P. Santini, G. Amoretti, S. Piligkos, G. Timco, R. E. P. Winpenny, *Phys. Rev. Lett.* **2005**, *94*, 207208.

[68] C. J. Wedge, G. A. Timco, E. T. Spielberg, R. E. George, F. Tuna, S. Rigby, E. J. L. McInnes, R. E. P. Winpenny, S. J. Blundell, A. Ardavan, *Phys. Rev. Lett.* **2012**, *108*, 107204.

[69] F. Moro, D. Kaminski, F. Tuna, G. F. S. Whitehead, G. A. Timco, D.

Collison, R. E. P. Winpenny, A. Ardavan, E. J. L. McInnes, *Chem. Commun.* **2014**, *50*, 91–93.

[70] J. Ferrando-Soria, *Magnetochemistry* **2016**, *2*, 36.

[71] V. Corradini, R. Biagi, U. del Pennino, V. De Renzi, A. Gambardella, M. Affronte, C. A. Muryn, G. A. Timco, R. E. P. Winpenny, *Inorg. Chem.* **2007**, *46*, 4937–4943.

[72] A. Ghirri, V. Corradini, C. Cervetti, A. Candini, U. del Pennino, G. Timco, R. J. Pritchard, C. A. Muryn, R. E. P. Winpenny, M. Affronte, *Adv. Funct. Mater.* **2010**, *20*, 1552–1560.

[73] T. Lis, *Acta Crystallogr. Sect. B Struct. Crystallogr. Cryst. Chem.* **1980**, *36*, 2042–2046.

[74] K. Yang, W. Paul, S.-H. Phark, P. Willke, Y. Bae, T. Choi, T. Esat, A. Ardavan, A. J. Heinrich, C. P. Lutz, *Science* **2019**, *366*, 509–512.

[75] K. Bader, D. Dengler, S. Lenz, B. Endeward, S.-D. Jiang, P. Neugebauer, J. van Slageren, *Nat. Commun.* **2014**, *5*, 5304.

[76] J. M. Zadrozny, J. Niklas, O. G. Poluektov, D. E. Freedman, *ACS Cent. Sci.* **2015**, *1*, 488–492.

[77] G. R. Lewis, I. Dance, *J. Chem. Soc. Dalt. Trans.* **2000**, 3176–3185.

[78] M. Atzori, S. Benci, E. Morra, L. Tesi, M. Chiesa, R. Torre, L. Sorace, R. Sessoli, *Inorg. Chem.* **2018**, *57*, 731–740.

[79] A. Lunghi, *ArXiv* **2019**, 1–8.

[80] M. Atzori, E. Morra, L. Tesi, A. Albino, M. Chiesa, L. Sorace, R. Sessoli, *J. Am. Chem. Soc.* **2016**, *138*, 11234–11244.

[81] M. Atzori, A. Chiesa, E. Morra, M. Chiesa, L. Sorace, S. Carretta, R. Sessoli, *Chem. Sci.* **2018**, *9*, 6183–6192.

[82] I. Borilovic, P. J. Alonso, O. Roubeau, G. Aromí, *Chem. Commun.* **2020**, *56*,

3139–3142.

[83] S. Nakazawa, S. Nishida, T. Ise, T. Yoshino, N. Mori, R. D. Rahimi, K. Sato, Y. Morita, K. Toyota, D. Shiomi, M. Kitagawa, H. Hara, P. Carl, P. Höfer, T. Takui, *Angew. Chem. Int. Ed.* **2012**, *51*, 9860–9864.

[84] D. Aguilà, L. A. Barrios, V. Velasco, O. Roubeau, A. Repollés, P. J. Alonso, J. Sesé, S. J. Teat, F. Luis, G. Aromí, *J. Am. Chem. Soc.* **2014**, *136*, 14215–14222.

[85] D. Maniaki, D. Garay-Ruiz, L. A. Barrios, D. O. T. A. Martins, D. Aguilà, F. Tuna, D. Reta, O. Roubeau, C. Bo, G. Aromí, *Chem. Sci.* **2022**, *13*, 5574–5581.

[86] M. Warner, S. Din, I. S. Tupitsyn, G. W. Morley, A. M. Stoneham, J. A. Gardener, Z. Wu, A. J. Fisher, S. Heutz, C. W. M. Kay, G. Aeppli, *Nature* **2013**, *503*, 504–508.

[87] C. J. Brown, *J. Chem. Soc. A* **1968**, 2488–2493.

[88] R. F. Ziolo, C. H. Griffiths, J. M. Troup, *J. Chem. Soc. Dalt. Trans.* **1980**, 2300.

[89] Y. Suzuki, M. Fujimori, H. Yoshikawa, K. Awaga, *Chem. Eur. J.* **2004**, *10*, 5158–5164.

[90] M. G. B. Drew, P. C. H. Mitchell, C. E. Scott, *Inorganica Chim. Acta* **1984**, *82*, 63–68.

[91] L. Malavolti, M. Briganti, M. Hänze, G. Serrano, I. Cimatti, G. McMurtrie, E. Otero, P. Ohresser, F. Totti, M. Mannini, R. Sessoli, S. Loth, *Nano Lett.* **2018**, *18*, 7955–7961.

[92] I. Cimatti, L. Bondì, G. Serrano, L. Malavolti, B. Cortigiani, E. Velez-Fort, D. Betto, A. Ouerghi, N. B. Brookes, S. Loth, M. Mannini, F. Totti, R. Sessoli, *Nanoscale Horiz.* **2019**, *4*, 1202–1210.

[93] H. Adler, M. Paszkiewicz, J. Uihlein, M. Polek, R. Ovsyannikov, T. V.

Basova, T. Chassé, H. Peisert, *J. Phys. Chem. C* **2015**, *119*, 8755–8762.

[94] K. Eguchi, Y. Takagi, T. Nakagawa, T. Yokoyama, *J. Phys. Chem. C* **2013**, *117*, 22843–22851.

[95] P. J. Blowey, R. J. Maurer, L. A. Rochford, D. A. Duncan, J. H. Kang, D. A. Warr, A. J. Ramadan, T. L. Lee, P. K. Thakur, G. Costantini, K. Reuter, D. P. Woodruff, *J. Phys. Chem. C* **2019**, *123*, 8101–8111.

[96] F. Santanni, A. Albino, M. Atzori, D. Ranieri, E. Salvadori, M. Chiesa, A. Lunghi, A. Bencini, L. Sorace, F. Totti, R. Sessoli, *Inorg. Chem.* **2021**, *60*, 140–151.

[97] T. Yamabayashi, M. Atzori, L. Tesi, G. Cosquer, F. Santanni, M. E. Boulon, E. Morra, S. Benci, R. Torre, M. Chiesa, L. Sorace, R. Sessoli, M. Yamashita, *J. Am. Chem. Soc.* **2018**, *140*, 12090–12101.

[98] S. Hiroto, Y. Miyake, H. Shinokubo, *Chem. Rev.* **2017**, *117*, 2910–3043.

[99] S. Von Kugelgen, M. D. Krzyaniak, M. Gu, D. Puggioni, J. M. Rondinelli, M. R. Wasielewski, D. E. Freedman, *J. Am. Chem. Soc.* **2021**, *143*, 8069–8077.

[100] N. Wili, S. Richert, B. Limburg, S. J. Clarke, H. L. Anderson, C. R. Timmel, G. Jeschke, *Phys. Chem. Chem. Phys.* **2019**, *21*, 11676–11688.

[101] T. Ikeue, K. Furukawa, H. Hata, N. Aratani, H. Shinokubo, T. Kato, A. Osuka, *Angew. Chem. Int. Ed.* **2005**, *44*, 6899–6901.

[102] C. J. Kingsbury, M. O. Senge, *Coord. Chem. Rev.* **2021**, *431*, 213760.

[103] J. A. Shelnutt, X. Z. Song, J. G. Ma, S. L. Jia, W. Jentzen, C. J. Medforth, *Chem. Soc. Rev.* **1998**, *27*, 31–41.

[104] M. O. Senge, *Chem. Commun.* **2006**, 243–256.

[105] L. D. Sparks, J. R. Chamberlain, J. A. Shelnutt, M. S. Park, M. R. Ondrias, C. J. Medforth, M. O. Senge, K. M. Smith, *J. Am. Chem. Soc.* **1993**, *115*,

581–592.

[106] T. Ishizuka, N. Grover, C. J. Kingsbury, H. Kotani, M. O. Senge, T. Kojima, *Chem. Soc. Rev.* **2022**, *51*, 7560–7630.

[107] H.-S. He, *Acta Crystallogr. Sect. E Struct. Reports Online* **2007**, *63*, m976–m977.

[108] E. B. Fleischer, *J. Am. Chem. Soc.* **1963**, *85*, 1353–1354.

[109] R. Harada, H. Ōkawa, T. Kojima, *Inorg. Chim. Acta* **2005**, *358*, 489–496.

[110] I. Bischoff, X. Feng, M. O. Senge, *Tetrahedron* **2001**, *57*, 5573–5583.

[111] Y. Bian, J. Jiang, Y. Tao, M. T. M. Choi, R. Li, A. C. H. Ng, P. Zhu, N. Pan, X. Sun, D. P. Arnold, Z. Y. Zhou, H. W. Li, T. C. W. Mak, D. K. P. Ng, *J. Am. Chem. Soc.* **2003**, *125*, 12257–12267.

[112] A. Takenaka, Y. Sasada, H. Ogoshi, T. Omura, Z. Yoshida, *Acta Crystallogr. Sect. B Struct. Crystallogr. Cryst. Chem.* **1975**, *31*, 1–6.

[113] M. Kielmann, M. O. Senge, *Angew. Chem. Int. Ed.* **2019**, *58*, 418–441.

[114] D. Dolphin, *The Porphyrins Vol.3: Physical Chemistry, Part A*, Academic Press, New York San Francisco London, **2012**.

[115] R. Giovannetti, in *Macro To Nano Spectrosc.*, InTech, **2012**.

[116] M. Gouterman, *J. Chem. Phys.* **1959**, *30*, 1139–1161.

[117] M. Gouterman, *J. Mol. Spectrosc.* **1961**, *6*, 138–163.

[118] M. Kasha, *Radiat. Res.* **1963**, *20*, 55–70.

[119] A. Osuka, K. Maruyama, *J. Am. Chem. Soc.* **1988**, *110*, 4454–4456.

[120] S. G. Telfer, T. M. McLean, M. R. Waterland, *Dalton Trans.* **2011**, *40*, 3097.

[121] C. A. Hunter, J. K. M. Sanders, A. J. Stone, *Chem. Phys.* **1989**, *133*, 395–404.

[122] Y. Won, R. A. Friesner, M. R. Johnson, J. L. Sessler, *Photosynth. Res.* **1989**, *22*, 201–210.

[123] A. Tsuda, A. Osuka, *Science* **2001**, *293*, 79–82.

[124] K. Gao, S. B. Jo, X. Shi, L. Nian, M. Zhang, Y. Kan, F. Lin, B. Kan, B. Xu, Q. Rong, L. Shui, F. Liu, X. Peng, G. Zhou, Y. Cao, A. K. -Y. Jen, *Adv. Mater.* **2019**, *31*, DOI 10.1002/adma.201807842.

[125] H. L. Anderson, *Chem. Commun.* **1999**, 2323–2330.

[126] J. L. Du, G. R. Eaton, S. S. Eaton, *J. Magn. Reson. Ser. A* **1996**, *119*, 240–246.

[127] D. K. Lavallee, *Comments Inorg. Chem.* **1986**, *5*, 155–174.

[128] P. Hambright, *Inorg. Chem.* **1977**, *16*, 2987–2988.

[129] S. Funahashi, Y. Yamaguchi, M. Tanaka, *Bull. Chem. Soc. Jpn.* **1984**, *57*, 204–208.

[130] A. Kumar, S. Maji, P. Dubey, G. J. Abhilash, S. Pandey, S. Sarkar, *Tetrahedron Lett.* **2007**, *48*, 7287–7290.

[131] D. Dolphin, *The Porphyrins, Vol. 1: Structure and Synthesis, Part A*, Academic Press, New York San Francisco London, **1978**.

[132] A. D. Adler, F. R. Longo, F. Kampas, J. Kim, *J. Inorg. Nucl. Chem.* **1970**, *32*, 2443–2445.

[133] T. E. Shubina, H. Marbach, K. Flechtner, A. Kretschmann, N. Jux, F. Buchner, H.-P. Steinrück, T. Clark, J. M. Gottfried, *J. Am. Chem. Soc.* **2007**, *129*, 9476–9483.

[134] J. E. Merritt, K. L. Loening, *Pure Appl. Chem.* **1979**, *51*, 2251–2304.

[135] L. E. Webb, E. B. Fleischer, *J. Am. Chem. Soc.* **1965**, *87*, 667–669.

[136] S. G. DiMagno, V. S. Y. Lin, M. J. Therien, *J. Org. Chem.* **1993**, *58*, 5983–

5993.

[137] D. E. Chumakov, A. V. Khoroshutin, A. V. Anisimov, K. I. Kobrakov, *Chem. Heterocycl. Compd.* **2009**, *45*, 259–283.

[138] Y. Bai, F. Buchner, I. Kellner, M. Schmid, F. Vollnhals, H. P. Steinrück, H. Marbach, J. M. Gottfried, *New J. Phys.* **2009**, *11*, 125004.

[139] P. Bhyrappa, V. Krishnan, *Inorg. Chem.* **1991**, *30*, 239–245.

[140] G.-Y. Gao, J. V. Ruppel, D. B. Allen, Y. Chen, X. P. Zhang, *J. Org. Chem.* **2007**, *72*, 9060–9066.

[141] F. A. Carey, R. J. Sundberg, *Advanced Organic Chemistry Part B: Reaction and Synthesis*, Springer US, Boston, MA, **2007**.

[142] R. W. Boyle, C. K. Johnson, D. Dolphin, *J. Chem. Soc. Chem. Comm.* **1995**, 527–528.

[143] A. Nakano, H. Shimidzu, A. Osuka, *Tetrahedron Lett.* **1998**, *39*, 9489–9492.

[144] I. K. Thomassen, H. Vazquez-Lima, K. J. Gagnon, A. Ghosh, *Inorg. Chem.* **2015**, *54*, 11493–11497.

[145] M. Tian, S. Chen, W. Sheng, H. Huang, C. Guo, *Chem. Lett.* **2015**, *44*, 1383–1385.

[146] A. G. Hyslop, M. A. Kellett, P. M. Iovine, M. J. Therien, *J. Am. Chem. Soc.* **1998**, *120*, 12676–12677.

[147] N. Miyaura, A. Suzuki, *J. Chem. Soc. Chem. Comm.* **1979**, 866.

[148] T. Tanaka, B. S. Lee, N. Aratani, M. C. Yoon, D. Kim, A. Osuka, *Chem. Eur. J.* **2011**, *17*, 14400–14412.

[149] N. Aratani, A. Osuka, *Org. Lett.* **2001**, *3*, 4213–4216.

[150] G. Bringmann, S. Rüdenauer, D. C. G. Götz, T. A. M. Gulder, M. Reichert, *Org. Lett.* **2006**, *8*, 4743–4746.

[151] G. Bringmann, D. C. G. Götz, T. A. M. Gulder, T. H. Gehrke, T. Bruhn, T. Kupfer, K. Radacki, H. Braunschweig, A. Heckmann, C. Lambert, *J. Am. Chem. Soc.* **2008**, *130*, 17812–17825.

[152] Cyril Chappaz-Gillot, G. Canard, F. Andreoli, N. Vanthuyne, M. Giorgi, J.-V. Naubron, V. Monnier, R. Rosas, C. Roussel, T. S. Balaban, *Eur. J. Org. Chem.* **2012**, 6526–6536.

[153] I. Funes-Ardoiz, F. Maseras, *ACS Catal.* **2018**, *8*, 1161–1172.

[154] A. Osuka, H. Shimidzu, *Angew. Chemie (International Ed. English)* **1997**, *36*, 135–137.

[155] H. S. Cho, D. H. Jeong, S. Cho, D. Kim, Y. Matsuzaki, K. Tanaka, A. Tsuda, A. Osuka, *J. Am. Chem. Soc.* **2002**, *124*, 14642–14654.

[156] D. H. Yoon, S. B. Lee, K.-H. Yoo, J. Kim, J. K. Lim, N. Aratani, A. Tsuda, A. Osuka, D. Kim, *J. Am. Chem. Soc.* **2003**, *125*, 11062–11064.

[157] M. Kamo, A. Tsuda, Y. Nakamura, N. Aratani, K. Furukawa, T. Kato, A. Osuka, *Org. Lett.* **2003**, *5*, 2079–2082.

[158] A. Tsuda, A. Osuka, *J. Incl. Phenom.* **2001**, *41*, 77–81.

[159] A. Tsuda, A. Nakano, H. Furuta, H. Yamochi, A. Osuka, *Angew. Chem. Int. Ed.* **2000**, *39*, 558–561.

[160] L.-M. Jin, L. Chen, J.-J. Yin, C.-C. Guo, Q.-Y. Chen, *Eur. J. Org. Chem.* **2005**, *2005*, 3994–4001.

[161] Q. Ouyang, Y. Z. Zhu, C. H. Zhang, K. Q. Yan, Y. C. Li, J. Y. Zheng, *Org. Lett.* **2009**, *11*, 5266–5269.

[162] T. Ogawa, Y. Nishimoto, N. Yoshida, N. Ono, A. Osuka, *Angew. Chem. Int. Ed.* **1999**, *38*, 176–179.

[163] S. Hiroto, A. Osuka, *J. Org. Chem.* **2005**, *70*, 4054–4058.

[164] H. S. Ali, R. H. Henchman, S. P. Visser, *ChemCatChem* **2021**, *13*, 3054–

3066.

[165] C.-M. Feng, Y.-Z. Zhu, Y. Zang, Y.-Z. Tong, J.-Y. Zheng, *Org. Biomol. Chem.* **2014**, *12*, 6990–6993.

[166] L. Grill, M. Dyer, L. Lafferentz, M. Persson, M. V. Peters, S. Hecht, *Nat. Nanotechnol.* **2007**, *2*, 687–691.

[167] S. Haq, F. Hanke, M. S. Dyer, M. Persson, P. Iavicoli, D. B. Amabilino, R. Raval, *J. Am. Chem. Soc.* **2011**, *133*, 12031–12039.

[168] Q. Sun, L. M. Mateo, R. Robles, P. Ruffieux, N. Lorente, G. Bottari, T. Torres, R. Fasel, *J. Am. Chem. Soc.* **2020**, *142*, 18109–18117.

[169] Q. Sun, L. M. Mateo, R. Robles, N. Lorente, P. Ruffieux, G. Bottari, T. Torres, R. Fasel, *Angew. Chem. Int. Ed.* **2021**, *60*, 16208–16214.

[170] L. M. Mateo, Q. Sun, K. Eimre, C. A. Pignedoli, T. Torres, R. Fasel, G. Bottari, *Chem. Sci.* **2021**, *12*, 247–252.

[171] P. Fournari, R. Guilard, M. Fontesse, J.-M. Latour, J.-C. Marchon, *J. Organomet. Chem.* **1976**, *110*, 205–217.

[172] R. Bonnett, P. Brewer, K. Noro, T. Noro, *Tetrahedron* **1978**, *34*, 379–385.

[173] G. R. Eaton;, S. S. Eaton, in *Distance Measurements in Biological Systems by EPR* (Eds.: L.J. Berliner, G.R. Eaton, S.S. Eaton), Kluwer Academic/Plenum Publishers, New York (Ny), **2000**, pp. 29–154.

[174] S. Chicco, A. Chiesa, G. Allodi, E. Garlatti, M. Atzori, L. Sorace, R. De Renzi, R. Sessoli, S. Carretta, *Chem. Sci.* **2021**, *12*, 12046–12055.

[175] T. Tanaka, A. Osuka, *Chem. Soc. Rev.* **2015**, *44*, 943–969.

[176] K. Yamashita, S. Tazawa, K. Sugiura, *Inorganica Chim. Acta* **2016**, *439*, 173–177.

[177] C. M. Álvarez, H. Barbero, S. Ferrero, D. Miguel, *J. Org. Chem.* **2016**, *81*, 6081–6086.

[178] C. Lee, W. Yang, R. G. Parr, *Phys. Rev. B* **1988**, *37*, 785.

[179] S.-Y. Wong, R. Wai-Yin Sun, N. P.-Y. Chung, C.-L. Lin, C.-M. Che, *Chem. Commun.* **2005**, 3544.

[180] W. T. Chen, Y. Yamada, G. N. Liu, A. Kubota, T. Ichikawa, Y. Kojima, G. C. Guo, S. Fukuzumi, *Dalton Trans.* **2011**, *40*, 12826–12831.

[181] G. Nandi, H. M. Titi, I. Goldberg, *Cryst. Growth Des.* **2014**, *14*, 3557–3566.

[182] M. Gouterman, *J. Mol. Spectrosc.* **1961**, *6*, 138–163.

[183] W. Jentzen, X. Z. Song, J. A. Shelnutt, *J. Phys. Chem. B* **1997**, *101*, 1684–1699.

[184] A. Stone and B. Everly, *J. Am. Chem. Soc.* **1968**, *90*, 2735–2748.

[185] Y. Jun-i, N. Fukui, K. Furukawa, A. Osuka, *Chem. Eur. J.* **2018**, *24*, 1528–1532.

[186] A. K. D. Dime, C. H. Devillers, H. Cattey, B. Habermeyer, D. Lucas, *Dalton Trans.* **2012**, *41*, 929–936.

[187] Y. Inokuma, N. Ono, H. Uno, D. Y. Kim, S. B. Noh, D. Kim, A. Osuka, *Chem. Commun.* **2005**, 3782–3784.

[188] T. D. Smith, J. R. Pilbrow, *Coord. Chem. Rev.* **1974**, *13*, 173–278.

[189] I. V. Ovchinnikov, V. N. Konstantinov, *J. Magn. Reson.* **1978**, *32*, 179–190.

[190] J. L. Du, G. R. Eaton, S. S. Eaton, *J. Magn. Reson. Ser. A* **1995**, *115*, 236–240.

[191] I. Pozo, F. Lombardi, D. Alexandropoulos, F. Kong, J-R. Deng, P. Horton, S. Coles, W. Myers, L. Bogani, H. Anderson, *ChemRxiv* **2022**, DOI 10.26434/chemrxiv-2022-1v5b4.

[192] J. Ferrando-Soria, E. Moreno Pineda, A. Chiesa, A. Fernandez, S. A. Magee, S. Carretta, P. Santini, I. J. Vitorica-Yrezabal, F. Tuna, G. A. Timco, E. J. L.

McInnes, R. E. P. Winpenny, *Nat. Commun.* **2016**, *7*, 11377.

[193] A. Bencini, D. Gatteschi, *Electron Paramagnetic Resonance of Exchange Coupled Systems*, Springer Berlin Heidelberg, Berlin, Heidelberg, **1990**.

[194] L. Noodleman, J. G. Norman, *J. Chem. Phys.* **1979**, *70*, 4903–4906.

[195] F. Neese, *Wiley Interdiscip. Rev. Comput. Mol. Sci.* **2018**, *8*, e1327.

[196] A. D. Becke, *J. Chem. Phys.* **1993**, *98*, 5648–5652.

[197] S. Grimme, J. Antony, S. Ehrlich, H. Krieg, *J. Chem. Phys.* **2010**, *132*, 154104–154123.

[198] S. Grimme, S. Ehrlich, L. Goerigk, *J. Comput. Chem.* **2011**, *32*, 1456–1465.

[199] A. Bencini, F. Totti, *J. Chem. Theory Comput.* **2009**, *5*, 144–154.

[200] C. Adamo, V. Barone, A. Bencini, F. Totti, I. Ciofini, *Inorg. Chem.* **1999**, *38*, 1996–2004.

[201] B. Röder, M. Büchner, I. Rückmann, M. O. Senge, *Photochem. Photobiol. Sci.* **2010**, *9*, 1152–1158.

[202] C. J. Kingsbury, K. J. Flanagan, H. G. Eckhardt, M. Kielmann, M. O. Senge, *Molecules* **2020**, *25*, 3195.

[203] A. Osuka, S. Nakajami, T. Nagata, K. Maruyama, K. Torium, *Angew. Chem. Int. Ed. Engl.* **1991**, *30*, 582–584.

[204] I. Gimeno, A. Urtizberea, J. Román-Roche, D. Zueco, A. Camón, P. J. Alonso, O. Roubeau, F. Luis, *Chem. Sci.* **2021**, *12*, 5621–5630.

[205] S. Van Doorslaer, A. Schweiger, *Phys. Chem. Chem. Phys.* **2001**, *3*, 159–166.

[206] X. Feng, I. Bischoff, M. O. Senge, *J. Org. Chem.* **2001**, *66*, 8693–8700.

[207] P. Esser, *J. Mol. Catal. A Chem.* **1999**, *140*, 13–24.

[208] S. Ito, T. Ito, D. Makihata, Y. Ishii, Y. Saito, T. Oba, *Tetrahedron Lett.* **2014**,

55, 4390–4394.

[209] R. M. Moriarty, O. Prakash, *ChemInform* **2003**, *34*, DOI 10.1002/chin.200319241.

[210] W. R. Scheidt, J. U. Mondal, C. W. Eigenbrot, A. Adler, L. J. Radonovich, J. L. Hoard, *Inorg. Chem.* **1986**, *25*, 795–799.

[211] N. Miyaura, K. Yamada, A. Suzuki, *Tetrahedron Lett.* **1979**, *20*, 3437–3440.

[212] R. K. Al-Shewiki, M. Korb, A. Hildebrandt, S. Zahn, S. Naumov, R. Buschbeck, T. Rüffer, H. Lang, *Dalton Trans.* **2019**, *48*, 1578–1585.

[213] L. A. Fendt, H. Fang, M. E. Plonska-Brzezinska, S. Zhang, F. Cheng, C. Braun, L. Echegoyen, F. Diederich, *Eur. J. Org. Chem.* **2007**, 4659–4673.

[214] J. M. O. Brien, E. Sitte, K. J. Flanagan, H. Ku, L. J. Hallen, M. O. Senge, *J. Org. Chem* **2019**, *84*, 6158–6173.

[215] S. Horn, B. Cundell, M. O. Senge, *Tetrahedron Lett.* **2009**, *50*, 2562–2565.

[216] Deposition Numbers 2257145 (for **[VO(DPP)]**), 2260447 (for **[Cu(DPP)]**), 2257146 (for **[$VOH_2(DPP)_2$]**), and 2257147 (for **[$VOCu(DPP)_2$]**) Contain the Supplementary Crystallographic Data for This Paper. These Data Are Provided Free of Charge by the Joint Cambridge Crystallographic Data Centre and Fachinformazionszentrum Karlsruhe, **2023**.

[217] D. Ranieri, F. Santanni, A. Privitera, A. Albino, E. Salvadori, M. Chiesa, F. Totti, L. Sorace, R. Sessoli, *Chem. Sci.* **2023**, *14*, 61–69.

[218] S. Takahashi, J. Van Tol, C. C. Beedle, D. N. Hendrickson, L. C. Brunel, M. S. Sherwin, *Phys. Rev. Lett.* **2009**, *102*, 087603.

[219] I. Pozo, Z. Huang, F. Lombardi, D. Alexandropoulos, F. Kong, M. Slota, J.-R. Deng, W. Stawski, P. Horton, S. Coles, *ChemRxiv* **2023**, DOI 10.26434/chemrxiv-2022-1v5b4-v2.

[220] G. A. Timco, S. Carretta, F. Troiani, F. Tuna, R. J. Pritchard, C. A. Muryn,

E. J. L. McInnes, A. Ghirri, A. Candini, P. Santini, G. Amoretti, M. Affronte, R. E. P. Winpenny, *Nat. Nanotechnol.* **2009**, *4*, 173–178.

[221] J. Ferrando-Soria, S. A. Magee, A. Chiesa, S. Carretta, P. Santini, I. J. Vitorica-Yrezabal, F. Tuna, G. F. S. Whitehead, S. Sproules, K. M. Lancaster, A.-L. Barra, G. A. Timco, E. J. L. McInnes, R. E. P. Winpenny, *Chem* **2016**, *1*, 727–752.

[222] S. Gorgon, K. Lv, J. Grüne, B. H. Drummond, W. K. Myers, G. Londi, G. Ricci, D. Valverde, C. Tonnelé, P. Murto, A. S. Romanov, D. Casanova, V. Dyakonov, A. Sperlich, D. Beljonne, Y. Olivier, F. Li, R. H. Friend, E. W. Evans, *Nature* **2023**, *620*, 538–544.

[223] T. Quintes, M. Mayländer, S. Richert, *Nat. Rev. Chem.* **2023**, *7*, 75–90.

[224] N. Grzegorzek, H. Mao, P. Michel, M. J. Junge, E. R. Lorenzo, R. M. Young, M. D. Krzyaniak, M. R. Wasielewski, E. T. Chernick, *J. Phys. Chem. A* **2020**, *124*, 6168–6176.

[225] M. S. Asano, K. Ishizuka, Y. Kaizu, *Mol. Phys.* **2006**, *104*, 1609–1618.

[226] A. van der Est, M. Asano-Someda, P. Ragogna, Y. Kaizu, *J. Phys. Chem. A* **2002**, *106*, 8531–8542.

[227] M. Asano-Someda, T. Ichino, Y. Kaizu, *J. Phys. Chem. A* **1997**, *101*, 4484–4490.

[228] L. M. Jin, J. J. Yin, L. Chen, C. C. Guo, Q. Y. Chen, *Synlett* **2005**, *2*, 2893–2898.

[229] K. Diller, F. Klappenberger, M. Marschall, K. Hermann, A. Nefedov, C. Wöll, J. V. Barth, *J. Chem. Phys.* **2012**, *136*, 014705.

[230] L. Poggini, A. L. Sorrentino, D. Ranieri, A. Calloni, F. Santanni, N. Giaconi, G. Cucinotta, E. Otero, D. Longo, B. Cortigiani, A. Caneschi, G. Bussetti, R. Sessoli, M. Mannini, G. Serrano, *Adv. Phys. Res.* **2023**, *submitted*.

[231] O. Jankovský, P. Šimek, K. Klimová, D. Sedmidubský, S. Matějková, M.

Pumera, Z. Sofer, *Nanoscale* **2014**, *6*, 6065–6074.

[232] M. Nardi, R. Verucchi, C. Corradi, M. Pola, M. Casarin, A. Vittadini, S. Iannotta, *Phys. Chem. Chem. Phys.* **2010**, *12*, 871–880.

[233] I. Reid, Y. Zhang, A. Demasi, A. Blueser, L. Piper, J. E. Downes, A. Matsuura, G. Hughes, K. E. Smith, *Appl. Surf. Sci.* **2009**, *256*, 720–725.

[234] I. Mazov, D. Krasnikov, A. Stadnichenko, V. Kuznetsov, A. Romanenko, O. Anikeeva, E. Tkachev, *J. Nanotechnol.* **2012**, *2012*, 1–5.

[235] A. Urtizberea, E. Natividad, P. J. Alonso, L. Pérez-Martínez, M. A. Andrés, I. Gascón, I. Gimeno, F. Luis, O. Roubeau, *Mater. Horizons* **2020**, *7*, 885–897.

[236] X. Zhang, C. Wolf, Y. Wang, H. Aubin, T. Bilgeri, P. Willke, A. J. Heinrich, T. Choi, *Nat. Chem.* **2022**, *14*, 59–65.

[237] P. Willke, T. Bilgeri, X. Zhang, Y. Wang, C. Wolf, H. Aubin, A. Heinrich, T. Choi, *ACS Nano* **2021**, *15*, 17959–17965.

[238] J. Zhu, Y. Zhou, W. Wu, Y. Deng, Y. Xiang, *ChemistrySelect* **2019**, *4*, 11853–11861.

[239] J. Jiang, X. X. Liu, J. Han, K. Hu, J. S. Chen, *Processes* **2021**, *9*, 680.

[240] D. J. Miller, M. C. Biesinger, N. S. McIntyre, *Surf. Interface Anal.* **2002**, *33*, 299–305.

[241] *Dep. Numbers 2202805 ([VO(TrPP]) 2203176 (o-[VO(TrPP]2) and 2203175 (m-[VO(TrPP]2) Contain the Cryst. Data for This Paper. These Data Are Provided Free of Charge by the Joint Cambridge Crystallographic Data Centre and Fachinformationszentrum Karlsruhe*, **2022**.

[242] B. J. Littler, M. A. Miller, C. H. Hung, R. W. Wagner, D. F. O'Shea, P. D. Boyle, J. S. Lindsey, *J. Org. Chem.* **1999**, *64*, 1391–1396.

[243] J. S. Lindsey, H. C. Hsu, I. C. Schreiman, *Tetrahedron Lett.* **1986**, *27*, 4969–

4970.

[244] T. Hasobe, K. Ida, H. Sakai, K. Ohkubo, S. Fukuzumi, *Chem. Eur. J.* **2015**, *21*, 11196–11205.

[245] T. Morotti, M. Pizzotti, R. Ugo, S. Quici, M. Bruschi, P. Mussini, S. Righetto, *Eur. J. Inorg. Chem.* **2006**, *2006*, 1743–1757.

[246] M. A. Bakar, N. N. Sergeeva, T. Juillard, M. O. Senge, *Organometallics* **2011**, *30*, 3225–3228.

[247] G. R. Fulmer, A. J. M. Miller, N. H. Sherden, H. E. Gottlieb, A. Nudelman, B. M. Stoltz, J. E. Bercaw, K. I. Goldberg, *Organometallics* **2010**, *29*, 2176–2179.

[248] E. Zolotoyabko, *J. Appl. Crystallogr.* **2009**, *42*, 513–518.

[249] D. Briggs, *Surf. Interface Anal.* **1981**, *3*, 190.

[250] J. J. Yeh, I. Lindau, *At. Data Nucl. Data Tables* **1985**, *32*, 1–155.

[251] A. Abragam, B. Bleaney, *Electron Paramagnetic Resonance of Transition Ions*, Oxford University Press, Oxford, **1970**.

[252] H. Dilger, T. Sottman, *Skript Zum PCII-Praktikum*, Universität Stuttgart, **2016**.

Appendix

Volume 14
Number 1
7 January 2023
Pages 1–216

Chemical Science

rsc.li/chemical-science

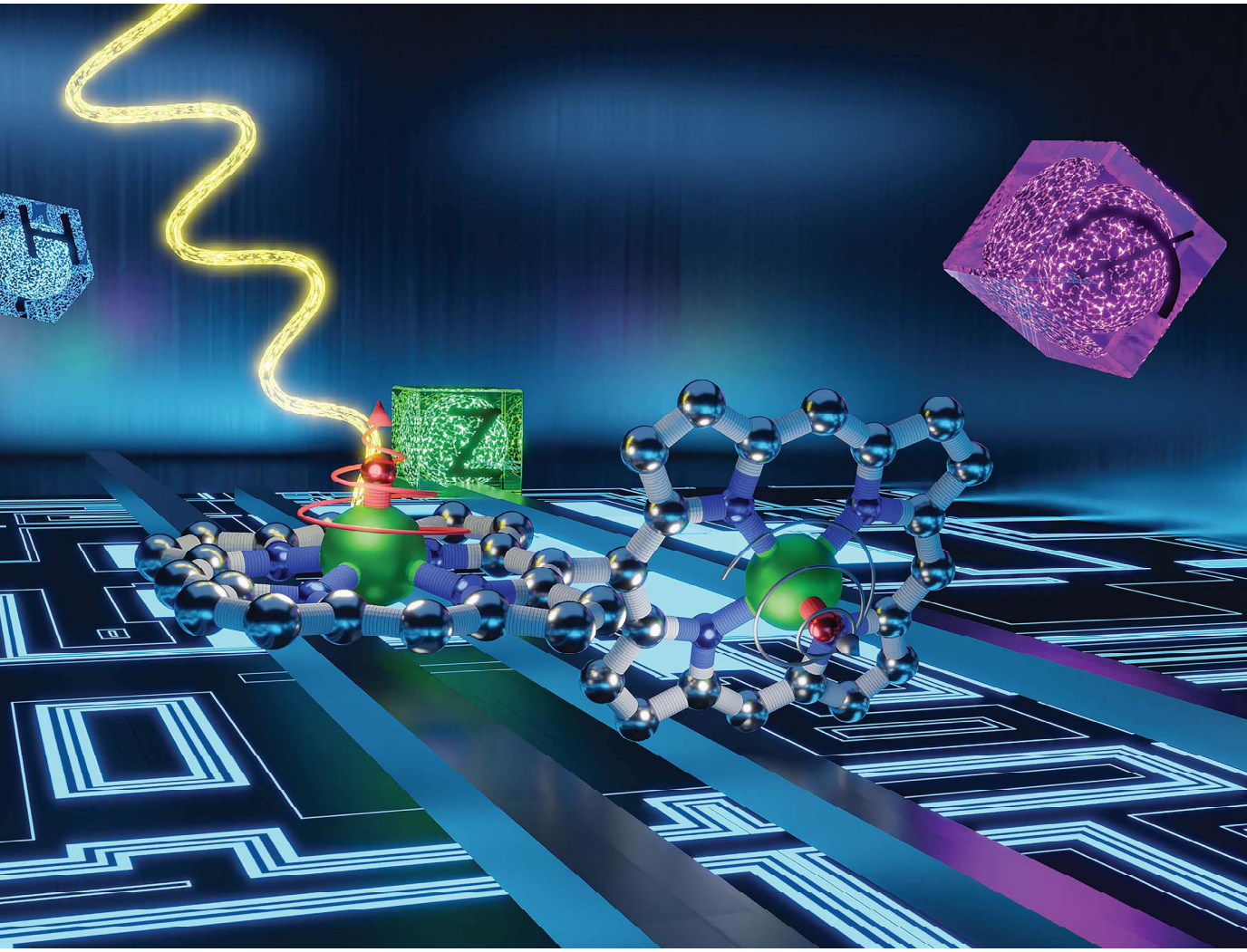

ISSN 2041-6539

ROYAL SOCIETY OF CHEMISTRY

EDGE ARTICLE

D. Ranieri, F. Santanni *et al.*

An exchange coupled *meso–meso* linked vanadyl porphyrin dimer for quantum information processing

Chemical Science

ROYAL SOCIETY OF CHEMISTRY

EDGE ARTICLE

View Article Online
View Journal | View Issue

Cite this: *Chem. Sci.*, 2023, **14**, 61

All publication charges for this article have been paid for by the Royal Society of Chemistry

An exchange coupled *meso–meso* linked vanadyl porphyrin dimer for quantum information processing†

Davide Ranieri, ‡[a] Fabio Santanni, ‡[a] Alberto Privitera, [a] Andrea Albino, [a] Enrico Salvadori, [b] Mario Chiesa, [b] Federico Totti, [a] Lorenzo Sorace *[a] and Roberta Sessoli [a]

Received 6th September 2022
Accepted 13th November 2022

DOI: 10.1039/d2sc04969d

rsc.li/chemical-science

We report here the synthesis of a new *meso–meso* (*m–m*) singly linked vanadyl–porphyrin dimer that crystallizes in two different pseudo-polymorphs. The single crystal continuous-wave electron paramagnetic resonance investigation evidences a small but crucial isotropic exchange interaction, *J*, between the two tilted, and thus distinguishable, spin centers of the order of 10^{-2} cm^{-1}. The experimental and DFT studies evidence a correlation between *J* values and porphyrin plane tilting angle and distortion. Pulsed EPR analysis shows that the two vanadyl dimers maintain the coherence time of the monomer. With the obtained spin Hamiltonian parameters, we identify suitable transitions that could be used as computational basis states. Our results, coupled with the evaporability of porphyrin systems, establish this class of dimers as extremely promising for quantum information processing applications.

Introduction

A qubit is a quantum object suitable to define a superposition state in which the information is encoded.[1] For a physical system to act as a qubit, its coherence time T_m (*i.e.*, the lifetime of its superposition state) must be long enough to allow manipulability.[2] For this reason, electron or nuclear spins, either as solid-state systems[3] or quantum dots,[4] are appealing platforms for encoding qubits.[3,5] More recently, electron spin-based molecular qubits gained interest in this field because of the chemical tunability of their properties.[6,7] In these systems, magnetic exchange interaction between spin centers, either dipolar or isotropic, is crucial to establish the entanglement condition needed for implementing quantum logic gates. However, for this aim, the interqubit interaction should be finely tuned to avoid a strong-exchange regime[6,8] thus maintaining the individual addressability of each qubit.

Various molecular systems have been investigated and proposed as multi-qubit platforms.[9–13] Here, addressability has been achieved through two different molecular design strategies: (i) inclusion of paramagnetic centers with different electronic and magnetic properties (*e.g.*, two different Landé factors, *g*);[9,10,13,14] (ii) inclusion of the same paramagnetic moiety characterized by significant magnetic anisotropy and different orientation in space.[11] Most of these systems were also designed to minimize the hyperfine interactions detrimental to T_m.

In the quest for molecular systems acting as potential qubits, our groups mainly focused on $V^{IV}O$ metal complexes, which show good coherence times and can be operated as a nuclear qubit with an electronic spin ancilla.[15,16] More recently, dinuclear $V^{IV}O$-based complexes with weakly coupled electron spins were proposed as an electron-mediated nuclear quantum simulator.[17,18] However, these complexes were of no use as quantum logic gates since the two $V^{IV}O$ ions were iso-oriented and thus not singly addressable. To harness the potential of $V^{IV}O$ dimers as potential quantum gates, it is crucial to introduce a tilting angle between two interacting spins.

Singly-linked porphyrin dimers are appealing candidates to solve this issue since the two macrocycle units adopt a tilted geometry imparting different orientations to the two spin centers.[19,20] Furthermore, their marked thermal stability and excellent deposition properties on various metal and semiconducting surfaces[21–23] make them interesting for engineering prototypical devices. However, little is still known about the magnetic interactions in paramagnetic porphyrin dimers.[24,25] Osuka and coworkers investigated the isotropic exchange interaction in *meso–meso* (*m–m*) singly linked, *m*-β β-*m* doubly linked, and β–β *m–m* β–β triply linked Cu^{II} and Ag^{II} porphyrin dimers.[24] They found that the magnitude of the antiferromagnetic superexchange interaction between the spins

[a]*Department of Chemistry "Ugo Schiff" & INSTM RU, University of Florence, Via della Lastruccia 3, 50019 Sesto Fiorentino, Italy. E-mail: lorenzo.sorace@unifi.it*

[b]*Department of Chemistry, NIS, University of Turin, Via P. Giuria 7, I10125 Torino, Italy*

† Electronic supplementary information (ESI) available: Synthetic procedures, experimental details, additional crystallographic and EPR characterization, DFT computational details. CCDC 2202805 ([**VO(TrPP)**]), 2203175 (***m***-[**VO(TrPP)**]$_2$), and 2203176 (***o***-[**VO(TrPP)**]$_2$). For ESI and crystallographic data in CIF or other electronic format see DOI: **https://doi.org/10.1039/d2sc04969d**

‡ These authors contributed equally to this work.

increases by three orders of magnitude for β–β linked systems, compared to *m*–*m* linked systems, because of the larger conjugation between the two quasi coplanar porphyrin rings. In agreement with this, an ELDOR-detected NMR study revealed very weak exchange interactions compatible with a dipolar origin in *m*–*m* singly linked Cu^{II} complexes *vs.* a significant exchange interaction for the triply linked analog.[25] A very recent report on triply linked vanadyl dimers[26] suggests two orders of magnitude reduction of the exchange interaction compared to Cu^{II} dimers,[25] as expected for the different symmetry of the magnetic orbital.

Following these results, we decided to synthesize and investigate a novel *m*–*m* linked bis vanadyl 5,10,15-triphenylporphyrin ([**VO(TrPP)**]$_2$) to combine the interesting magnetic properties of porphyrins with the good coherence times characteristic of their vanadyl complexes.[15,16] Since porphyrin units in *m*–*m* linked porphyrin dimers are tilted to each other, they might also be singly addressable by exploiting the large anisotropy of hyperfine coupling in vanadyl complexes. Angular-dependent continuous-wave electron paramagnetic resonance (CW EPR) measurements were performed on oriented single crystals along with CW and pulsed X- (*ca.* 9 GHz) and Q-band (*ca.* 34 GHz) EPR experiments on frozen solutions. Our experimental investigation indicates that [**VO(TrPP)**]$_2$ maintains a coherence time comparable to its monomer building block while showing an exchange interaction comparable to that of triply linked species.[26] The presence of a non-negligible magnetic exchange is a counterintuitive result that we rationalized by DFT calculations. The latter suggest that optimal coupling between distinguishable vanadyl qubits can be achieved. Combined with the evaporability of porphyrin systems, these results establish this class of dimers as extremely promising for quantum information processing applications.

Results and discussion

Synthesis

Compound [**VO(TrPP)**] was synthesized by a slight modification of a previously reported procedure.[15] The reaction of the free H_2TrPP ligand with the vanadyl precursor [VO(acac)$_2$] (acac = acetylacetonate) was conducted in phenol (PhOH) as reported in Scheme 1a. The dimer [**VO(TrPP)**]$_2$ was then obtained by performing an oxidative coupling reaction on [**VO(TrPP)**], in analogy to literature reports for other metal derivatives.[27] Among the different strategies reported in the literature to obtain *m*–*m* linked metal porphyrin complexes,[24,28] the use of (bis(trifluoroacetoxy)iodo)benzene (PIFA) as an oxidative coupling reagent recently turned out to be a good alternative to commonly used Ag^{I} hexafluorophosphate ($AgPF_6$),[29] Sc^{III} triflate ($Sc(OTf)_3$),[30] and Au^{III} chloride/Ag^{I} triflate ($AuCl_3$/AgOTf) mixtures.[31] Indeed, the PIFA reactant is cheaper and, being metal-free, it does not interfere in the magnetic characterization of the final product. Previous studies showed that PIFA leads to highly selective reactions characterized by almost quantitative yields in the case of the reaction of Zn^{II} and Ni^{II} porphyrin dimers.[27] The reaction reported in Scheme 1b was then conducted in dry CH_2Cl_2 under an inert atmosphere by adding PIFA. The exact stoichiometric amount of PIFA added during the reaction turned out to be crucial for the efficiency and overall yield of the reaction. The use of 2 eq. of PIFA and 40′ reaction time at room temperature gave the desired porphyrin dimer in almost quantitative yields.

Structural characterization

Details of the X-ray diffractometry characterization on single crystals of [**VO(TrPP)**] and [**VO(TrPP)**]$_2$ are reported in the ESI.† Needle-shaped X-ray quality crystals of the monomeric unit [**VO(TrPP)**] (Fig. S1†) were grown by slow evaporation of a CH_2Cl_2/CH_3CN (98 : 2) solution. This system crystallizes in the $P2_1/c$ space group (no. 14) with two pairs of centrosymmetrically related molecules per unit cell (Fig. S1 and Table S1†). The asymmetric unit is a single [**VO(TrPP)**] molecular complex, in which V^{IV} presents a square pyramidal coordination geometry comprising the four porphyrin N atoms and the apical O atom of the V=O moiety. To better characterize the porphyrin plane distortion modes, the normal-coordinate structure decomposition (NSD) tool was used.[32,33] As evidenced in Fig. S1,† the porphyrin ring assumes a distorted ruffle shape,[32,34] B_{1u}. This ruffle shape distortion differs from the planar structure of some *m*- and β substituted vanadyl–porphyrin complexes.[15,35–37] On the other hand, the distance of the V atom from the plane individuated by the four N atoms, 0.51 Å, is the same as that

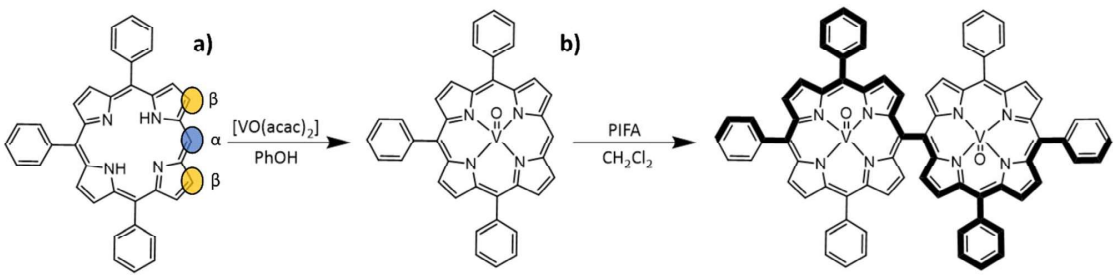

Scheme 1 Sketch of the reaction strategies to obtain [VO(TrPP)] (a) and [VO(TrPP)]$_2$ (b). (a) in PhOH, 165 °C, N_2, 12 h; (b) anhydrous CH_2Cl_2, −78 °C to room temperature, N_2, 40 min. The ellipsoids on the porphyrin rings highlight the carbons where oxidative coupling reactions are possible in β (orange) and *m* (blue) positions.

observed in tetraphenyl derivatives.[28] The mean V–N and V–O distances of 2.06 Å and 1.58 Å are comparable with those observed in similar vanadyl complexes, while the shortest intermolecular VO–VO distance is 9.42 Å. This is about 1.2 Å shorter than in the tetraphenyl analogous, as expected for the reduced hindering. The dimeric compound **[VO(TrPP)]$_2$** is highly soluble in various solvents, including acetonitrile, ethers, and toluene. Single crystals of **[VO(TrPP)]$_2$** suitable for X-ray measurements were obtained using two strategies involving toluene as crystallization solvent. Prism-shaped red to violet crystals were grown by very slow evaporation (~1 month) of a toluene solution dispersed in Sephadex® gel. In this case, the dimer (hereafter, ***m*-[VO(TrPP)]$_2$**, Fig. 1b) crystallizes in the monoclinic *C*2/*c* space group (no. 15), with three crystallization toluene molecules per dimer molecule. The molecular structure is composed by two **[VO(TrPP)]** units, symmetry-related by the C_2 axis (Fig. 1a). The asymmetric unit is thus composed of half a dimer unit, one disordered toluene molecule, and half of a disordered toluene molecule lying in a special position (Fig. 1b and S3†). The dihedral angle θ, formed by the planes passing through C1–C2–C2′ and C2–C2′–C3′ (see Fig. 1a) at the porphyrin ring, is about 69° (Fig. 1b). The molecular structure presents an intrinsic disorder of the vanadyl moieties below and above the porphyrin planes, not observed for **[VO(TrPP)]**, with occupancy factors of 85 : 15 (Fig. S2†). The O1–V1–V1′–O1′ tilting angle, δ, is *ca.* 64° (red dashed line in Fig. 1b). The intramolecular VO–VO distance is of 8.37 Å, while the minimum intermolecular VO–VO distance of 9.70 Å is found between parallel molecules on adjacent layers (Fig. S3 left, ESI†). The porphyrin molecules in ***m*-[VO(TrPP)]$_2$** are not aligned to any crystallographic axes.

As a second crystallization strategy, X-ray quality crystals of **[VO(TrPP)]$_2$** were grown by very slow evaporation of a toluene/acetone (95 : 5) solution. These crystals were similar in shape, size, and color to those grown in toluene, but the system crystallized in the acentric orthorhombic *Ccc*2 (no. 37) space group without cocrystallized solvent molecules (hereafter ***o*-[VO(TrPP)]$_2$**, Fig. 1c and S4†). Even in this case, the asymmetric unit is composed of one vanadyl–porphyrin unit, and the dimer is generated by the C_2 axis parallel to *c* and perpendicular to the C2–C2′ *meso*-bridging bond. The structure presents solvent-accessible voids of about 302 Å^3 along the *c* crystallographic direction (Fig. S5, ESI†). The absence of significative residual electron density suggests an intrinsic porous nature of the material. The molecules are oriented with the C2–C2′ bridging bond direction along the crystallographic *b* axis (Fig. S4, ESI†). An intrinsic disorder in the VO center is also observed in this case, with estimated occupancy factors of 75 : 25. The tilting of the two porphyrin moieties is higher in ***o*-[VO(TrPP)]$_2$**, as indicated by both θ and δ angles, of about 77° and 72°, respectively. On the other hand, the first coordination sphere does not present any major difference with respect to ***m*-[VO(TrPP)]$_2$**, and the intramolecular VO–VO distance (8.37 Å) is also comparable. The closest intermolecular contact for the ***o*-[VO(TrPP)]$_2$** is instead shorter than in the previous case, with an average distance of 7.78 Å considering the VO disorder (Fig. S3, right, ESI†). The shorter distance can be related to the absence of crystallization solvent molecules in ***o*-[VO(TrPP)]$_2$**.

The dominant distortion mode in both porphyrin dimers is the saddle distortion B_{2u}, also found in other A_3B type porphyrins.[38–40] The average dihedral angle among the pyrrole planes is 7.41° for ***o*-[VO(TrPP)]$_2$**, while it is 4.36° for ***m*-[VO(TrPP)]$_2$**, indicating a larger deviation from planarity and a higher degree of distortion in the solvent-free crystal structure ***o*-[VO(TrPP)]$_2$** than in ***m*-[VO(TrPP)]$_2$**.

The observation of tilting angles significantly different from 90° is not unprecedented in linked porphyrins. At least two reported structures of pentacoordinated Zn^{II}–porphyrin dimers, including bulky *t*-Bu groups on peripheral positions, are characterized by a dihedral angle of about 72°.[41,42] The dihedral angle, however, cannot be directly correlated to the coordination number of the central ion since at least one previous result reports a pentacoordinated Zn^{II} system showing a dihedral angle of about 90°.[43]

EPR experiments

We investigated the electronic structure and magnetic interactions in both **[VO(TrPP)]** and **[VO(TrPP)]$_2$** compounds by using

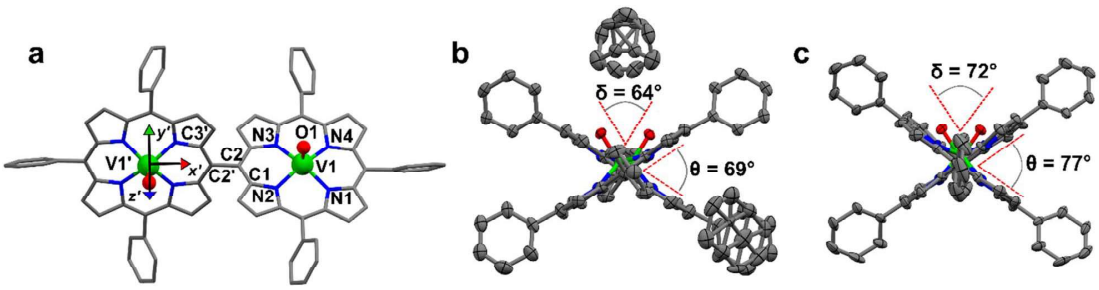

Fig. 1 (a) Molecular structure of [VO(TrPP)]$_2$ with labeled atoms. The local *xyz* (not shown for clarity's sake) and *x′y′z′* reference frames are those diagonalizing ***g***- and ***A***-tensors of the two vanadyl moieties. Primed labels indicate atoms related to non-primed ones by the C_2 symmetry axis bisecting the *m*–*m* bond. (b and c) View along the *m*–*m* bond of the ***m***-[VO(TrPP)]$_2$ and ***o***-[VO(TrPP)]$_2$ molecules. The dihedral angle, θ, between the porphyrin planes and the torsion angle, δ, between the vanadyl moieties' directions are highlighted by red dashed lines; atoms in (b and c) are represented as thermal ellipsoids at 50% probability level. Color code: C = gray; N = blue; V = green; O = red. Only the majority configuration of the V=O groups is reported. H-atoms are omitted for clarity.

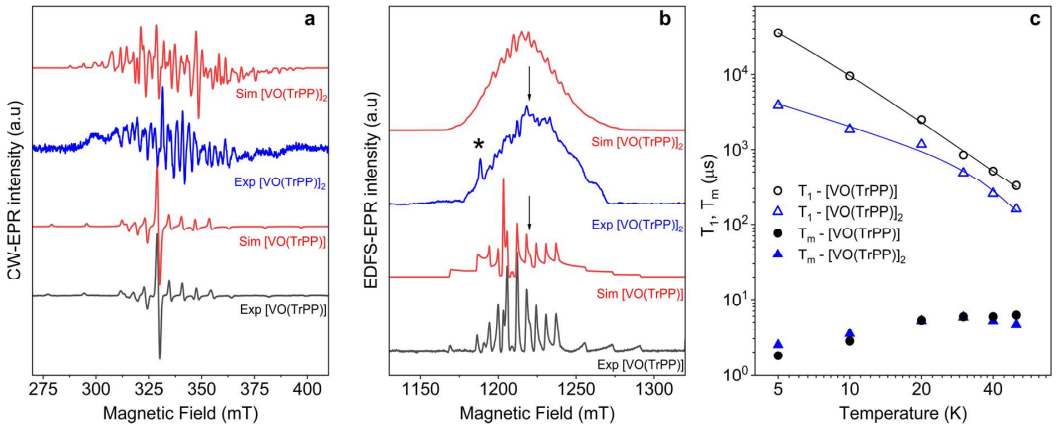

Fig. 2 (a) X-band (ν = 9.40 GHz) CW-EPR spectra of **[VO(TrPP)]** and **[VO(TrPP)]$_2$** in frozen toluene solution (T = 30 K) together with their best simulations obtained using spin Hamiltonian parameters reported in Table 1. (b) Q-band (ν = 33.8 GHz) ESE-EPR spectra of **[VO(TrPP)]** and **[VO(TrPP)]$_2$** in frozen – toluene/CH_2Cl_2 1 : 1 solution (T = 5 K). The arrows indicate the magnetic field settings at which pulse EPR experiments were performed. The asterisk indicates the signal of background impurities. (c) Temperature dependence of T_1 (open symbols) and T_m (full symbols) for **[VO(TrPP)]** (circles) and **[VO(TrPP)]$_2$** (triangles) measured at 1214 mT at Q-band frequency in a 0.5 mM frozen d_8-toluene solution. Error bars are within the size of the symbols. The continuous lines represent the best fit curves obtained using model and parameters reported in the text and ESI.†

EPR spectroscopy. The low temperature (T = 30 K) CW-EPR X-band spectrum of a frozen 1 mM solution of the monomer **[VO(TrPP)]** is shown in Fig. 2a (black trace), while the Q-band (ν = 33.8 GHz) Electron Spin Echo (ESE) detected EPR spectrum, corresponding to the absorption spectrum, is shown in Fig. 2b (black trace). Both spectra show the characteristic EPR powder pattern due to the anisotropic hyperfine coupling of the electron spin to the I = 7/2 nuclear spin of ^{51}V. Spectral simulations, shown in Fig. 2a and b, were performed based on the following Hamiltonian:[44]

$$\hat{H}_{\mathbf{[VO(TrPP)]}} = \mu_B \vec{B}\cdot\boldsymbol{g}\cdot\hat{S} + \hat{S}\cdot\boldsymbol{A}\cdot\hat{I} \quad (1)$$

assuming collinear and axial $\boldsymbol{g}$ and $\boldsymbol{A}$ tensors, indicating, within the spectral resolution, a local C_{4v} symmetry. The spin-Hamiltonian parameters extracted from the simulations of the spectra recorded at the two frequencies are listed in Table 1 and closely match those already reported in the literature for $[VO]^{2+}$ porphyrins consistently with a magnetic d_{xy} vanadium orbital.[15] The X-band CW-EPR spectrum of the **[VO(TrPP)]$_2$** dimer (blue trace in Fig. 2a), recorded under the same conditions, shows a complex hyperfine pattern, incompatible with two identical, non-interacting **[VO(TrPP)]** units, thereby indicating the presence of magnetic interactions between the two VO units.

Table 1 Spin-Hamiltonian parameters for **[VO(TrPP)]** and **[VO(TrPP)]$_2$** obtained from the simulation of frozen solution and single crystal experimental EPR spectra. For the simulation of the frozen solution spectra, a VO–VO tilting angle δ = 64°, corresponding to the monoclinic structure, has been considered

Simulation parameters	**[VO(TrPP)]**	Single crystal **[VO(TrPP)]$_2$**	Frozen solution **[VO(TrPP)]$_2$**
g_z	1.985 (1)	1.985	1.985
$g_{x,y}$	1.962 (1)	1.962	1.962
A_z (MHz)	168 (2)	168	168
$A_{x,y}$ (MHz)	480 (2)	480	480
$\lvert J\rvert$ (cm^{-1})		1.0(5) × 10^{-2} (***m***-) 5(1) × 10^{-2} (***o***-)	>1.0 × 10^{-2}
$\boldsymbol{D}$ (cm^{-1})			[2.8, –5.6, 2.8] 10^{-3}

The same complex spectral profile is observed in Q-band ESE-EPR experiments (blue trace in Fig. 2b) and suggests that the two vanadyl units in **[VO(TrPP)]$_2$** are coupled through an exchange interaction smaller than the microwave quantum of energy ($h\nu \approx 0.3$ cm^{-1} for X-band). Under these circumstances, magnetic coupling of the two S = 1/2 electron spins results in four states, which are neither pure "triplet" nor pure "singlet", leading to $4(2I_1 + 1)(2I_2 + 1) = 256$ $\Delta M_s = 1$ allowed EPR transitions, where $I_1 = I_2 = 7/2$ are the nuclear spin quantum numbers of the two coupled ^{51}V nuclei.[45] In the case of a randomly oriented sample (frozen solution), the spectrum will contain overlapping peaks from those orientations corresponding to $\partial B/\partial\theta = 0$ or $\partial B/\partial\varphi = 0$. Such conditions occur along principal directions, although extra peaks may occur at other orientations (off-axis turning points),[46] leading to the intricate spectral pattern reported in Fig. 2a and b. Single crystal CW-EPR experiments were performed to simplify the problem and determine the spin-Hamiltonian parameters for the coupled dimers. Studies on oriented single crystals of coupled porphyrins were never reported before, despite their capability to characterize weak magnetic interactions. The angular dependence of the EPR spectra on both the ***m***-**[VO(TrPP)]$_2$** and ***o***-**[VO(TrPP)]$_2$** crystals was studied by performing crystal rotations along three orthogonal directions (Fig. 3). For the monoclinic case, the rotations were performed along the crystallographic

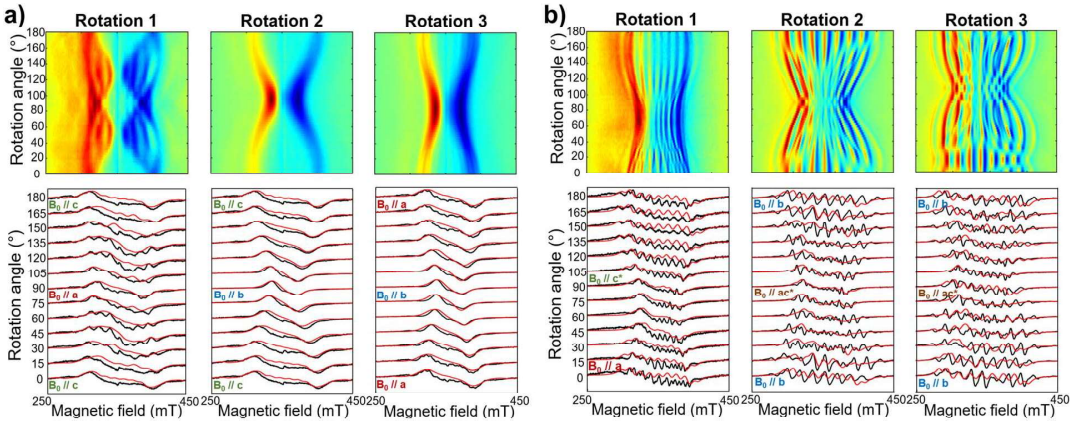

Fig. 3 Room temperature angular-dependent CW EPR X-band spectra of (a) *m*-[VO(TrPP)]$_2$ and (b) *o*-[VO(TrPP)]$_2$ for crystal rotations around three orthogonal axes. For both panels, the upper row shows the 2D experimental EPR contour plots for the three rotations, acquired with a 3° step; the lower row shows representative EPR spectra (black lines) for the three rotations – from 0° to 180° every 15° – together with the best spectral simulations (red lines) obtained by using $|J| = 0.01$ (0.005) cm^{-1} and $|J| = 0.05$ (0.01) cm^{-1} for (a) and (b), respectively. Experimental frequency: 9.40 GHz for (a), 9.87 GHz for (b).

b axis (Rotation 1) and two orthogonal axes (Rotations 2 and 3) in the *ac** plane, clockwise tilted by 14° with respect to the *a* and *c** axes (Fig. S7†). For the orthorhombic crystal, the rotations were performed along directions collinear to the crystallographic *a* (Rotation 2), *b* (Rotation 1), and *c* (Rotation 3) axes.

The experimental EPR spectra of the two forms are characterized by a different linewidth, most likely attributable to different intermolecular through-space dipolar coupling in the two crystals. The spectra were simulated based on the spin Hamiltonian shown in eqn (2):

$$\hat{H}_{[\mathbf{VO(TrPP)}]_2} = \sum_{i=1,1'} \mu_B \vec{B} \cdot \boldsymbol{g}^{V_i} \cdot \hat{S}^{V_i} + \sum_{i=1,1'} \left(\hat{S}^{V_i} \cdot \boldsymbol{A}^{V_i} \cdot \hat{I}^{V_i} + \hat{S}^{V_i} \cdot \boldsymbol{J} \cdot \hat{S}^{V_i} \right) \quad (2)$$

This includes the Zeeman and hyperfine interaction terms for both VO porphyrin units (first and second term) and an interaction term described by a general matrix $\boldsymbol{J}$,[47] which comprises the isotropic component J of the exchange interaction and a through-space dipolar coupling $\boldsymbol{D}$ (eqn (3)):

$$\boldsymbol{J} \approx J\boldsymbol{I} + \boldsymbol{D} = \begin{bmatrix} J + D_X & 0 & 0 \\ 0 & J + D_Y & 0 \\ 0 & 0 & J + D_Z \end{bmatrix} \quad (3)$$

Intramolecular dipolar interaction was fixed at the value calculated by point-dipole approximation (see Table 1). The antisymmetric and the anisotropic exchange contribution to the $\boldsymbol{J}$ matrix were neglected since both are expected to be negligible due to the small orbital contribution of vanadyl ions.[47]

Based on the results of the crystallographic study, two different tilting angles between the magnetic tensors of the two VO units were considered for *m*-[VO(TrPP)]$_2$ and *o*-[VO(TrPP)]$_2$, of 64° and 72° respectively. The molecular reference framework that we adopted for the simulation has the *Z*-axis parallel to the C_2 axis of the molecule, the *Y*-axis parallel to the *m*–*m* bond direction, and the *X*-axis perpendicular to these two directions. The principal values of the $\boldsymbol{g}$ and $\boldsymbol{A}$ tensors of the two vanadyl centers were kept fixed to the values obtained by the best simulation of the [VO(TrPP)] monomer, with their local *z* direction oriented along the V=O bond. Intermolecular through-space dipolar interactions were included as a broadening of the linewidth. Specifically, we used a peak-to-peak Lorentzian linewidth of 8 mT for *m*-[VO(TrPP)]$_2$ and 13 mT for *o*-[VO(TrPP)]$_2$, which highlights a stronger dipolar interaction in the latter, consistent with the shorter intermolecular distance. In Fig. S8 and S9,† we survey simulated EPR spectra for the two crystals to assess the effect of $|J|$ magnitudes ranging from 1.0×10^{-5} to 1 cm^{-1}. Our analysis shows that for *m*-[VO(TrPP)]$_2$, the $|J|$ value that best simulates the angular dependence of the EPR spectra is about 0.01 (0.005) cm^{-1} while for *o*-[VO(TrPP)]$_2$ $|J|$ is about 0.05 (0.01) cm^{-1}. The simulated spectra are shown in Fig. 3a and b (red traces), while the extracted spin-Hamiltonian parameters are listed in Table 1.

The same parameters provide a convincing simulation of the frozen solution spectra at both X- and Q-band frequencies (Fig. 2a and b, S10†, and Table 1), confirming the consistency of the determined values. A survey of the simulation parameters allows defining a lower limit of $|J| = 10^{-2}$ cm^{-1} to simulate the spectra, consistent with the spanned range in the crystalline phases.

Inversion recovery and echo decay experiments at Q-band frequency were performed to get insight into the temperature dependence (T = 5–50 K) of the spin-lattice relaxation time T_1 and the coherence time T_m, respectively. In Fig. 2c and Table S2,† we report the T_1 and T_m values for both [VO(TrPP)] and [VO(TrPP)]$_2$ in 0.5 mM deuterated d_8-toluene obtained from the fit of the inversion recovery and echo decay traces. The temperature dependence of T_1 shows a slight divergence

between the monomer and the dimer below 20 K but is in essential agreement with previous reports of T_1 in vanadyl porphyrins. The temperature dependent data for T_1 were fitted by assuming a combination of direct and Raman process:

$$T_1^{-1} = aT + bT^n \quad (4)$$

The best fit parameters (Table S3†) suggest that the direct process is more efficient in the dimer than in the monomer, and that the two Raman processes show low values of the exponent n (2.2 for **[VO(TrPP)]** and 4.2 for **[VO(TrPP)]$_2$**), in the range reported for vanadyl complexes.[48–51] We note however that due to the limited temperature range in which the investigation is possible, the number of experimental points is small compared to the number of parameters of eqn (4). The numerical values of the obtained best-fit parameters should then be considered with caution. The experimental coherence times T_m are very similar for the two samples and of the order of few μs in the 5–50 K range; the small decrease in T_m observed on decreasing temperature has already been reported for other $S = 1/2$ molecular species.[49] The decoherence times reported here are comparable to or even higher than those reported for weakly interacting vanadyl moieties[16,25] or molecular dimers based on either Cr_7Ni rings[52] or lanthanide complexes.[9]

DFT calculations

It is interesting to highlight two counterintuitive results of our investigation. First, the exchange interaction is larger in vanadyl than in copper *m*–*m* dimers,[25] despite the weaker overlap (π *vs.* σ interaction) of the magnetic orbital with the ligand scaffold. Notably, for triply linked dimers, the exchange is stronger in the copper derivative, as expected.[24,25] Second, the exchange interaction increases with the VO tilting angle, which is also counterintuitive when considering the extent of conjugation between the two porphyrin units.

To elucidate the nature of the observed exchange interaction and establish magneto-structural correlations, we performed DFT Broken-Symmetry (BS) calculations (technical details can be found in ESI†).[53] First, we focus on the crystallographic structures: the computed J values for ***m***- and ***o***-**[VO(TrPP)]$_2$** are both antiferromagnetic and in striking agreement with their experimental estimated magnitude: 1.4×10^{-2} and 4.7×10^{-2} cm^{-1}, respectively. The computed magnetic orbitals (labeled according to the standard reference system for vanadyls) for both derivatives are localized on the V^{IV} centers (d_{xy}) with in-plane π contributions from the N–$C_{2,5}$ sp components for each of the four pyrrole subunits (see Fig. S11†). Next, we investigated the J variation as a function of the dihedral angle θ, keeping the other structural parameters fixed to those of the orthorhombic structure. Calculated J values for θ angles in the 17–157° range are reported in Table S4.† The results (see Fig. 4) show an asymmetric double-well behavior with the absolute minimum for $\theta \sim 60°$ and a less pronounced one for $\theta \sim 125°$. The double-well asymmetry originates from the non-planarity of each vanadyl–porphyrin moiety, which alters the overlap between their π–π systems for the clock- and the anti-clockwise rotation around $\theta = 90°$.

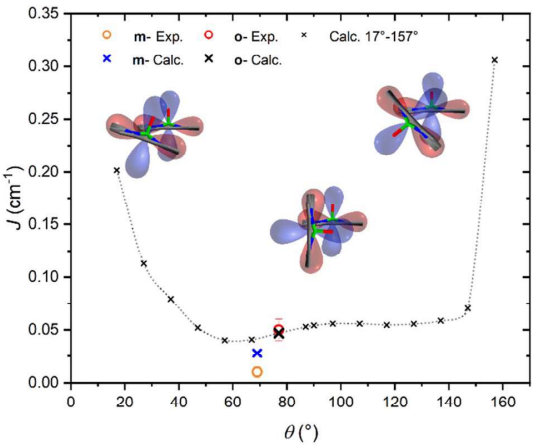

Fig. 4 Magneto-structural correlation of the exchange parameter J (cm^{-1}), *vs.* θ(°). The in-plane sp and out-of-plane π densities of the two porphyrins are sketched by red and blue lobes, respectively. The black line across the red density indicates the porphyrin planes. Large crosses refer to values computed for the two crystallographic structures, while small crosses refer to simulated geometries obtained varying the tilting angle in *o*-[VO(TrPP)]$_2$.

The highest J values were computed for the smallest and largest accessible θ values ($\theta = 17°$ and 157°), *i.e.*, close to coplanarity where the largest overlap between two out-of-plane π porphyrins systems is expected. The relative maximum for $\theta \sim 90°$ is achieved when the overlap between the sp system of one porphyrin and the out-of-plane π system of the other is largest. The computed angular dependence is, however, not sufficient to justify the different J magnitude in the two derivatives, otherwise well reproduced when using the real structures. This observation points to the key role of the saddle distortion of the single porphyrin unit that alters the mixing of the local sp (in-plane) and delocalized π (out-of-plane) contributions: indeed, the average dihedral angle between pyrrole planes is larger for the ***o***- than the ***m***- derivative (7.4° *vs.* 4.4°, see structural characterization).

As discussed in other works,[54–56] the distortion of the porphyrin plane indeed alters their chemical and physical properties. The change in electronic properties of the porphyrins is reflected by the red-shift of the Q and B-bands in the UV/vis spectrum and their respective broadening, which is also visible in our spectra (see Fig. S12†). Although the red-shift in the UV/vis spectrum can be exclusively attributed to the plane distortion, in porphyrin dimers, the conjugation between two porphyrin rings might be the dominant cause.[56,57] Discrimination between these two hypotheses would require more detailed calculations which are beyond the scope of this study.

The DFT analysis confirmed the magnitude of the interaction and allowed us to disclose its antiferromagnetic nature and explain the reason for the larger coupling in the orthorhombic form. Both the deviation from the planarity of the single porphyrin units and the vanadyl magnetic orbital lying slightly above/below the porphyrin plane are responsible for the not

negligible J value. These geometrical features contribute to the involvement of the out-of-plane π systems providing a more efficient superexchange interaction. These considerations also explain the negligible exchange coupling recently observed for the similar *m*–*m* linked Cu–porphyrin dimer.[25]

That system is indeed characterized by high planarity of the porphyrins and an in-plane nature of the magnetic orbitals. Moreover, in **[VO(TrPP)]$_2$**, access to the out-of-plane π system can occur *via* spin polarization processes through the oxygen atom in the VO group, as witnessed by a non-negligible spin density on it (see Fig. S11†). Therefore, the VO systems present intrinsic properties that make them more appealing than the copper ones for their exploitation as multi-qubit systems in *m*–*m* porphyrin systems.

Computational states

As a final step, we illustrate in the following that **[VO(TrPP)]$_2$** fulfils the conditions that allow individual addressing of the spins. The presence of a sizeable exchange interaction and the small homogeneous linewidths estimated by the measured T_m indicate that selective excitation is possible, *i.e.*, at a given field the frequency difference between spin transitions on the two electronic sites is larger than the decoherence rate.

To analyse this issue in more detail we performed simulations of frequency-swept EPR spectra on an oriented crystal of ***o*-[VO(TrPP)]$_2$**. We assumed a static magnetic field of 1.3 T applied along the local z direction of $\boldsymbol{A}$ and $\boldsymbol{g}$ tensors of one of the vanadyl moieties (Fig. 5) and swept the frequency in the Q-band region (see Fig. S13 and S14†). This configuration has been chosen to maximise the difference between the resonant frequencies of the two sites. However, the operative conditions in two-frequency experiments implementing logic gates can be easily matched by aligning the field closer to the two-fold symmetry axis of the dimer. To better reproduce the initialization process of our system we performed our simulation at 10 mK.

The direction of the field establishes the so-called "target" (T) qubit, while the other unit, tilted by 72°, is defined as the "control" one (C). Under these conditions the ground state of the system is given by $|m_S^T, m_S^C, m_I^T, m_I^C\rangle = \left|-\frac{1}{2}, -\frac{1}{2}, +\frac{7}{2}, +\frac{7}{2}\right\rangle$ (with minor contributions from states with different m_I), and the system is initialized as $|00\rangle$. We selected spin transitions among almost completely factorized states following the selection rules $\Delta m_s = \pm 1$ and $\Delta m_I = 0$, so that the computational basis can be roughly defined by the electronic spin states of the two moieties (*i.e.*, $|0\rangle = \left|-\frac{1}{2}\right\rangle$ and $|1\rangle = \left|+\frac{1}{2}\right\rangle$). This option guarantees a unique computational basis for the two-qubit architecture given by the four states $|00\rangle$, $|10\rangle$, $|01\rangle$ and $|11\rangle$, where the first label indicates C and the second T.

A scheme of the transitions involved in the quantum computing process, together with the zoom on spectral region of interest, are visible in Fig. 5. By using the spin Hamiltonian parameters reported in Table 1, the transition $|00\rangle \rightarrow |10\rangle$ and $|00\rangle \rightarrow |01\rangle$ are separated by an energy of 1.575 GHz, far exceeding the decoherence rate. Furthermore, no other

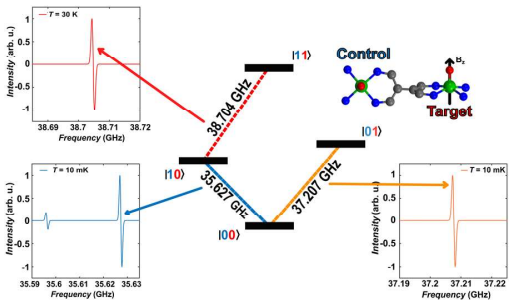

Fig. 5 Plots of the calculated frequency-swept spectra with a magnetic field of 1.3 T applied along the local z axis of the target vanadyl moiety in three different regions, corresponding to inverting the electronic spin of the control (blue line, bottom left corner), of the target without inverting the control (orange plot, bottom right corner) and of the target once the control is inverted (red plot, upper left corner). A temperature of 10 mK is employed to simulate thermal initialization in the ground state, while $T = 30$ K is employed to have a sizeable intensity of the transition of the target once the control is flipped (red).

transitions are visible close to the $|00\rangle \rightarrow |01\rangle$ (Fig. 5, bottom right corner), while a much less intense peak is observed in proximity of $|00\rangle \rightarrow |10\rangle$. However, this minor transition involves a higher lying initial state, with different nuclear spin projection compared to those of $|00\rangle$; thus, this would not interfere with the quantum computational process. This means that it is possible to excite selectively either C or T moiety once the system is properly initialized in the $|00\rangle$ state.

The computational process requires that the spin state of T must be selectively changed only when C is set to $|1\rangle$, *i.e.*, the spin transition $|10\rangle \rightarrow |11\rangle$ must be selectively probed. This implies to first excite our system from $|00\rangle \rightarrow |10\rangle$ and only then to invert the target spin by promoting the transition $|10\rangle \rightarrow |11\rangle$. Our simulation, performed at 30 K to obtain a reasonable population of the excited $|10\rangle$ state, indicates that the transition occurs at 38.704 GHz (red dashed lines in Fig. 5). This is the only allowed transition in the probed frequency range, and it can be selectively excited without involving sides transitions.

We notice here that, on increasing temperature from 10 mK, further nuclear transitions would appear because of the 16×16 dimension of the electronuclear spin space. While this might be seen as detrimental for quantum information applications, the possibility to exploit the nuclear spin degrees of freedom has been highlighted as a further advantage of vanadyl over other systems.[16,58]

Conclusions

In summary, we obtained **[VO(TrPP)]$_2$** by an oxidative coupling reaction in almost quantitative yields. Its high solubility made it possible to obtain two pseudo polymorph single crystals (monoclinic ***m*-[VO(TrPP)$_2$]** and orthorhombic ***o*-[VO(TrPP)]$_2$**). These two compounds showed significant intramolecular exchange interactions, generally not observed for paramagnetic

singly linked *m*–*m* porphyrin dimers. The possibility to perform single crystal magnetic studies of two polymorphs slightly differing in the molecular structure also allowed us to investigate the dependence of the exchange coupling constant on the molecular geometry. Indeed, DFT calculations showed that the dependence of the antiferromagnetic exchange interaction on the dihedral angle between porphyrin planes, is mainly determined by the saddle-like distortion of the porphyrin plane. These new magneto-structural correlations open the possibility of chemically tuning the magnetic interaction in this platform, which presents unique and appealing features for quantum technology applications. Indeed, we showed here that, thanks to the anisotropic hyperfine interaction, the two tilted but exchange coupled vanadyl units are individually addressable as requested for quantum logic gate implementation. Furthermore, the coherence time of the dimer turned out to be comparable to that of monomeric vanadyl porphyrins. Since the latter have a relatively long coherence time up to room temperature when diluted in a diamagnetic host,[15,16,59] we foresee that coherent properties in the dimer can be improved by working on single crystals of diamagnetic hosts, which are currently under investigation. Multi-porphyrin structures are also synthetically accessible[28,60–63] to extend the number of coupled spins, thus offering a solution to the crucial issue of scalability in quantum architectures. Additionally, deposition on a surface to perform single qubit addressing *via* scanning tunnel microscopy combined with microwaves[64–66] appears also within reach.

Data availability

All data associated with this article have been included in the main text and ESI.†

Author contributions

D. R.: investigation, formal analysis, writing – original draft, writing review and editing. F. S.: investigation, formal analysis, writing – original draft, writing review and editing. A. P.: investigation, formal analysis, writing – original draft. A. A.: investigation. E. S.: investigation, formal analysis, writing – original draft. M. C.: supervision, writing review and editing. F. T.: investigation, formal analysis, writing – original draft. L. S.: supervision, project administration, writing review and editing. R. S.: conceptualization, supervision, fund acquisition, writing review and editing.

Conflicts of interest

There are no conflicts to declare.

Acknowledgements

The support of EC through EU Commission through the FETOPEN project FATMOLS (GA 862893) and Italian MIUR for Progetto Dipartimenti di Eccellenza 2018–2022 (ref. B96C1700020008) is acknowledged. National Recovery and Resilience Plan, Mission 4 Component 2 – Investment 1.4 – National Center for HPC, Big Data and Quantum Computing – funded by the European Union – NextGenerationEU – CUP (B83C22002830001) is acknowledged. We acknowledge the support of Dr S. Ciattini, Dr L. Chelazzi and Dr E. Fantechi (CRIST – University of Florence), for the crystallographic data analysis and Prof. S. Carretta and Dr A. Chiesa (Univ. of Parma) for fruitful discussion.

Notes and references

1 J. P. Dowling and G. J. Milburn, *Philos. Trans. R. Soc., A*, 2003, **361**, 1655–1674.
2 D. P. Di Vincenzo, *Fortschr. Phys.*, 2000, **48**, 771–783.
3 M. H. Abobeih, Y. Wang, J. Randall, S. J. H. Loenen, C. E. Bradley, M. Markham, D. J. Twitchen, B. M. Terhal and T. H. Taminiau, *Nature*, 2022, **606**, 884–889.
4 A. Morello, J. J. Pla, P. Bertet and D. N. Jamieson, *Adv. Quantum Technol.*, 2020, **3**, 2000005.
5 A. Barenco, C. H. Bennett, R. Cleve, D. P. Di Vincenzo, N. Margolus, P. W. Shor, T. Sleator, J. A. Smolin and H. Weinfurter, *Phys. Rev. A*, 1995, **52**, 3457–3467.
6 F. Troiani and M. Affronte, *Chem. Soc. Rev.*, 2011, **40**, 3119–3129.
7 M. Atzori and R. Sessoli, *J. Am. Chem. Soc.*, 2019, **141**, 11339–11352.
8 S. L. Bayliss, D. W. Laorenza, P. J. Mintun, B. D. Kovos, D. E. Freedman and D. D. Awschalom, *Science*, 2020, **370**, 1309–1312.
9 D. Aguilà, L. A. Barrios, V. Velasco, O. Roubeau, A. Repollés, P. J. Alonso, J. Sesé, S. J. Teat, F. Luis and G. Aromí, *J. Am. Chem. Soc.*, 2014, **136**, 14215–14222.
10 S. Von Kugelgen, M. D. Krzyaniak, M. Gu, D. Puggioni, J. M. Rondinelli, M. R. Wasielewski and D. E. Freedman, *J. Am. Chem. Soc.*, 2021, **143**, 8069–8077.
11 S. Nakazawa, S. Nishida, T. Ise, T. Yoshino, N. Mori, R. D. Rahimi, K. Sato, Y. Morita, K. Toyota, D. Shiomi, M. Kitagawa, H. Hara, P. Carl, P. Höfer and T. Takui, *Angew. Chem., Int. Ed.*, 2012, **51**, 9860–9864.
12 A. Ardavan, A. M. Bowen, A. Fernandez, A. J. Fielding, D. Kaminski, F. Moro, C. A. Muryn, M. D. Wise, A. Ruggi, E. J. L. McInnes, K. Severin, G. A. Timco, C. R. Timmel, F. Tuna, G. F. S. Whitehead and R. E. P. Winpenny, *Npj Quantum Inf.*, 2015, **1**, 15012.
13 D. Maniaki, D. Garay-Ruiz, L. A. Barrios, D. O. T. A. Martins, D. Aguilà, F. Tuna, D. Reta, O. Roubeau, C. Bo and G. Aromi, *Chem. Sci.*, 2022, **13**, 21–25.
14 F. Luis, A. Repollés, M. J. Martínez-Pérez, D. Aguilà, O. Roubeau, D. Zueco, P. J. Alonso, M. Evangelisti, A. Camón, J. Sesé, L. A. Barrios and G. Aromí, *Phys. Rev. Lett.*, 2011, **107**, 117203.
15 T. Yamabayashi, M. Atzori, L. Tesi, G. Cosquer, F. Santanni, M.-E. Boulon, E. Morra, S. Benci, R. Torre, M. Chiesa, L. Sorace, R. Sessoli and M. Yamashita, *J. Am. Chem. Soc.*, 2018, **140**, 12090–12101.
16 S. Chicco, A. Chiesa, G. Allodi, E. Garlatti, M. Atzori, L. Sorace, R. De Renzi, R. Sessoli and S. Carretta, *Chem. Sci.*, 2021, **12**, 12046–12055.

17 M. Atzori, A. Chiesa, E. Morra, M. Chiesa, L. Sorace, S. Carretta and R. Sessoli, *Chem. Sci.*, 2018, **9**, 6183–6192.
18 I. Borilovic, P. J. Alonso, O. Roubeau and G. Aromí, *Chem. Commun.*, 2020, **56**, 3139–3142.
19 A. A. Ryan and M. O. Senge, *Eur. J. Org. Chem.*, 2013, **2013**, 3700–3711.
20 S. Hiroto, Y. Miyake and H. Shinokubo, *Chem. Rev.*, 2017, **117**, 2910–3043.
21 K. Eguchi, T. Nakagawa, Y. Takagi and T. Yokoyama, *J. Phys. Chem. C*, 2015, **119**, 9805–9815.
22 A. Urtizberea, E. Natividad, P. J. Alonso, L. Pérez-Martínez, M. A. Andrés, I. Gascón, I. Gimeno, F. Luis and O. Roubeau, *Mater. Horiz.*, 2020, **7**, 885–897.
23 Q. Sun, L. M. Mateo, R. Robles, P. Ruffieux, N. Lorente, G. Bottari, T. Torres and R. Fasel, *J. Am. Chem. Soc.*, 2020, **142**, 18109–18117.
24 T. Ikeue, K. Furukawa, H. Hata, N. Aratani, H. Shinokubo, T. Kato and A. Osuka, *Angew. Chem., Int. Ed.*, 2005, **44**, 6899–6901.
25 N. Wili, S. Richert, B. Limburg, S. J. Clarke, H. L. Anderson, R. Timmel and G. Jeschke, *Phys. Chem. Chem. Phys.*, 2019, **21**, 11676–11688.
26 I. Pozo, F. Lombardi, D. Alexandropoulos, F. Kong, J.-R. Deng, P. Horton, S. Coles, W. Myers, L. Bogani and H. Anderson, ChemRxiv, 2022, preprint, DOI: **10.26434/chemrxiv-2022-1v5b4**.
27 Q. Ouyang, Y.-Z. Zhu, C.-H. Zhang, K.-Q. Yan, Y.-C. Li and J.-Y. Zheng, *Org. Lett.*, 2009, **11**, 5266–5269.
28 T. Tanaka and A. Osuka, *Chem. Soc. Rev.*, 2015, **44**, 943–969.
29 A. Osuka and H. Shimidzu, *Angew. Chem., Int. Ed. Engl.*, 1997, **36**, 135–137.
30 M. Kamo, A. Tsuda, Y. Nakamura, N. Aratani, K. Furukawa, T. Kato and A. Osuka, *Org. Lett.*, 2003, **5**, 2079–2082.
31 S. Hiroto and A. Osuka, *J. Org. Chem.*, 2005, **70**, 4054–4058.
32 C. Lee, W. Yang and R. G. Parr, *Phys. Rev. B: Condens. Matter Mater. Phys.*, 1988, **37**, 785.
33 C. J. Kingsbury and M. O. Senge, *Coord. Chem. Rev.*, 2021, **431**, 213760.
34 R. Harada, H. Ōkawa and T. Kojima, *Inorg. Chim. Acta*, 2005, **358**, 489–496.
35 S.-Y. Wong, R. Wai-Yin Sun, N. P.-Y. Chung, C.-L. Lin and C.-M. Che, *Chem. Commun.*, 2005, 3544.
36 W.-T. Chen, Y. Yamada, G.-N. Liu, A. Kubota, T. Ichikawa, Y. Kojima, G.-C. Guo and S. Fukuzumi, *Dalton Trans.*, 2011, **40**, 12826.
37 G. Nandi, H. M. Titi and I. Goldberg, *Cryst. Growth Des.*, 2014, **14**, 3557–3566.
38 M. Gouterman, *J. Mol. Spectrosc.*, 1961, **6**, 138–163.
39 W. Jentzen, X. Z. Song and J. A. Shelnutt, *J. Phys. Chem. B*, 1997, **101**, 1684–1699.
40 A. Stone and B. Everly, *J. Am. Chem. Soc.*, 1968, **90**, 2735–2748.
41 Y. Jun-i, N. Fukui, K. Furukawa and A. Osuka, *Chem.–Eur. J.*, 2018, **24**, 1528–1532.
42 A. K. D. Dime, C. H. Devillers, H. Cattey, B. Habermeyer and D. Lucas, *Dalton Trans.*, 2012, **41**, 929–936.
43 Y. Inokuma, N. Ono, H. Uno, D. Y. Kim, S. B. Noh, D. Kim and A. Osuka, *Chem. Commun.*, 2005, 3782.
44 S. Stoll and A. Schweiger, *J. Magn. Reson.*, 2006, **178**, 42–55.
45 T. D. Smith and J. R. Pilbrow, *Coord. Chem. Rev.*, 1974, **13**, 173–278.
46 I. V. Ovchinnikov and V. N. Konstantinov, *J. Magn. Reson.*, 1978, **32**, 179–190.
47 A. Bencini and D. Gatteschi, *Electron Paramagnetic Resonance of Exchange Coupled Systems*, Springer Berlin Heidelberg, 1st edn, 1990.
48 M. Atzori, E. Morra, L. Tesi, A. Albino, M. Chiesa, L. Sorace and R. Sessoli, *J. Am. Chem. Soc.*, 2016, **138**, 11234–11244.
49 M. Atzori, S. Benci, E. Morra, L. Tesi, M. Chiesa, R. Torre, L. Sorace and R. Sessoli, *Inorg. Chem.*, 2018, **57**, 731–740.
50 J. L. Du, G. R. Eaton and S. S. Eaton, *J. Magn. Reson., Ser. A*, 1995, **115**, 236–240.
51 J. L. Du, G. R. Eaton and S. S. Eaton, *J. Magn. Reson., Ser. A*, 1996, **119**, 240–246.
52 J. Ferrando-Soria, E. Moreno Pineda, A. Chiesa, A. Fernandez, S. A. Magee, S. Carretta, P. Santini, I. J. Vitorica-Yrezabal, F. Tuna, G. A. Timco, E. J. L. McInnes and R. E. P. Winpenny, *Nat. Commun.*, 2016, **7**, 11377.
53 L. Noodleman and J. G. Norman, *J. Chem. Phys.*, 1979, **70**, 4903–4906.
54 B. Röder, M. Büchner, I. Rückmann and M. O. Senge, *Photochem. Photobiol. Sci.*, 2010, **9**, 1152–1158.
55 M. O. Senge, *Chem. Commun.*, 2006, 243–256.
56 C. J. Kingsbury, K. J. Flanagan, H. G. Eckhardt, M. Kielmann and M. O. Senge, *Molecules*, 2020, **25**, 3195.
57 A. Osuka, S. Nakajami, T. Nagata, K. Maruyama and K. Torium, *Angew. Chem., Int. Ed. Engl.*, 1991, **30**, 582–584.
58 I. Gimeno, A. Urtizberea, J. Román-Roche, D. Zueco, A. Camón, P. J. Alonso, O. Roubeau and F. Luis, *Chem. Sci.*, 2021, **12**, 5621–5630.
59 M. Atzori, L. Tesi, E. Morra, M. Chiesa, L. Sorace and R. Sessoli, *J. Am. Chem. Soc.*, 2016, **138**, 2154–2157.
60 N. Aratani and A. Osuka, *Org. Lett.*, 2001, **3**, 4213–4216.
61 C. Schissler, E. K. Schneider, B. Felker, P. Weis, M. Nieger, M. M. Kappes and S. Bräse, *Chem.–Eur. J.*, 2021, **27**, 3047–3054.
62 M. Rickhaus, A. Vargas Jentzsch, L. Tejerina, I. Grübner, M. Jirasek, T. D. W. Claridge and H. L. Anderson, *J. Am. Chem. Soc.*, 2017, **139**, 16502–16505.
63 A. K. Sahoo, Y. Nakamura, N. Aratani, K. S. Kim, S. B. Noh, H. Shinokubo, D. Kim and A. Osuka, *Org. Lett.*, 2006, **8**, 4141–4144.
64 D. Serrate, P. Ferriani, Y. Yoshida, S. W. Hla, M. Menzel, K. Von Bergmann, S. Heinze, A. Kubetzka and R. Wiesendanger, *Nat. Nanotechnol.*, 2010, **5**, 350–353.
65 K. Yang, W. Paul, S. H. Phark, P. Willke, Y. Bae, T. Choi, T. Esat, A. Ardavan, A. J. Heinrich and C. P. Lutz, *Science*, 2019, **366**, 509–512.
66 W. Ko, C. Ma, G. D. Nguyen, M. Kolmer and A. P. Li, *Adv. Funct. Mater.*, 2019, **29**, 1903770.

How to cite: Angew. Chem. Int. Ed. 2023, e202312936
doi.org/10.1002/anie.202312936

Molecular Qubits

A Heterometallic Porphyrin Dimer as a Potential Quantum Gate: Magneto-Structural Correlations and Spin Coherence Properties

Davide Ranieri, Alberto Privitera, Fabio Santanni, Karolina Urbanska, Grant J. Strachan, Brendan Twamley, Enrico Salvadori, Yu-Kai Liao, Mario Chiesa, Mathias O. Senge, Federico Totti, Lorenzo Sorace,* and Roberta Sessoli**

Abstract: In the development of two-qubit quantum gates, precise control over the intramolecular spin-spin interaction between molecular spin units plays a pivotal role. A weak but measurable exchange coupling is especially important for achieving selective spin addressability that allows controlled manipulation of the computational basis states $|00\rangle$ $|01\rangle$ $|10\rangle$ $|11\rangle$ by microwave pulses. Here, we report the synthesis and Electron Paramagnetic Resonance (EPR) study of a heterometallic meso-meso (m-m) singly-linked $V^{IV}O$–Cu^{II} porphyrin dimer. X-band continuous wave EPR measurements in frozen solutions suggest a ferromagnetic exchange coupling of ca. $8 \cdot 10^{-3}$ cm^{-1}. This estimation is supported by Density Functional Theory calculations, which also allow disentangling the ferro- and antiferromagnetic contributions to the exchange. Pulsed EPR experiments show that the dimer maintains relaxation times similar to the monometallic Cu^{II} porphyrins. The addressability of the two individual spins is made possible by the different **g**-tensors of V^{IV} and Cu^{II}-ions, in contrast to homometallic dimers where tilting of the porphyrin planes plays a key role. Therefore, single-spin addressability in the heterometallic dimer can be maintained even with small tilting angles, as expected when deposited on surface, unlocking the full potential of molecular quantum gates for practical applications.

Introduction

The electronic spin is an appealing candidate for the physical realization of qubits, the core units of the quantum computer.[1] It has an intrinsic quantum nature and can be coherently manipulated with microwave radiation, as commonly done in pulsed electron paramagnetic resonance (EPR).[2] Even if most efforts have been devoted to spin impurities in semiconductors and inorganic lattices,[3,4] molecular spins are an attractive alternative because of their chemical versatility and ease of processing.[5–7] Molecules are also ideal candidates for realizing multiple qubits and quantum logic gates.[6,8] A controlled-NOT (C-NOT) two-qubit gate is indeed sufficient, in combination with single qubit gates, to form a universal set for quantum computation.[9] The four necessary computational basis states, namely $|00\rangle$ $|01\rangle$ $|10\rangle$ $|11\rangle$, can be realized with two spins $^1/_2$ as in a bimetallic paramagnetic complex. On one hand, the two spins must be appropriately coupled to differentiate the energy gaps and, thus, the excitation frequency of each transition inside the four-level space. On the other hand, too strong exchange interactions do not allow single-spin addressability, which requires that the two coupled spins are distinguishable.[6,8] The electron spins can either be different in nature, e.g., having different true or effective g values,[10,11] or they can be identical but with their anisotropic magnetic tensors oriented differently in space.[12] Considering the other fundamental requirement, i.e., the long lifetime of the coherence of any superposition state,[9]

[*] D. Ranieri, Dr. A. Privitera, Dr. F. Santanni, Prof. Dr. F. Totti, Prof. Dr. L. Sorace, Prof. Dr. R. Sessoli
Department of Chemistry "Ugo Schiff" & INSTM RU, University of Florence
Via della Lastruccia 3, 50019 Sesto Fiorentino (Italy)
E-mail: lorenzo.sorace@unifi.it
roberta.sessoli@unifi.it

Dr. A. Privitera
Department of Industrial Engineering & INSTM RU, University of Florence
Via Santa Marta 3, 50139 Firenze (Italy)

Dr. K. Urbanska, Dr. G. J. Strachan, Prof. Dr. M. O. Senge
School of Chemistry, Chair of Organic Chemistry, Trinity Biomedical Sciences Institute, Trinity College Dublin, The University of Dublin, 152-160 Pearse Street, D02R590 Dublin (Ireland)
E-mail: sengem@tcd.ie

Dr. B. Twamley
School of Chemistry, Trinity College Dublin, The University of Dublin, Dublin 2 (Ireland)

Prof. Dr. E. Salvadori, Dr. Y.-K. Liao, Prof. Dr. M. Chiesa
Department of Chemistry and NIS, University of Turin,
Via P. Giuria 7, 10125 Torino (Italy)

Prof. Dr. M. O. Senge
Institute for Advanced Study (TUM-IAS), Technical University of Munich, Focus Group—Molecular and Interfacial Engineering of Organic Nano-systems
Lichtenberg-Str.2a, 85748 Garching (Germany)

3d metal ions are very appealing. Record coherence times have been obtained for vanadium(IV) ions (V^{IV}) with nuclear spin-free ligands, while coherence persists up to room temperature in copper(II) (Cu^{II}) and V^{IV} complexes. An interesting example of spectral addressability and long relaxation times is a Cu^{II} porphyrin complex functionalized with a carboxylate group coordinating a $[Ti^{III}Cp_2]^+$ unit.[11]

Multi-porphyrin systems offer the advantage of superior chemical stability compared to ligands hitherto used to develop molecular quantum gates. When neutral, they can be deposited by sublimation on various surfaces,[13–15] making their embedding in devices more feasible. In addition, surface-induced reactivity has been exploited to produce flat triply-linked porphyrin nano tapes.[16–18] Studies on the exchange-coupling in porphyrin metal dimers evidenced moderate antiferromagnetic interactions promoted by the conjugation in doubly- and triply-linked porphyrins,[19–23] while meso-meso singly-linked homometallic Cu^{II} dimers exhibit negligible exchange interactions.[19] We recently demonstrated that the vanadyl analog shows a measurable exchange interaction of the order of 10^{-2} cm^{-1}.[23] Interestingly, due to the tilting of the two porphyrin planes and the anisotropy of the vanadyl ***g***- and ***A***- tensors, the two spin centers in this complex are distinguishable in almost all orientations of the external magnetic field. In addition, the good coherence properties of the monomeric units are retained in the dimer, a finding that has been recently generalized to vanadyl dimers coupled through a delocalized π-system.[22] The increased exchange coupling in the vanadyl complex was justified by the fact that the vanadyl magnetic orbital lies slightly above the porphyrin plane. The saddle-like distortion of the porphyrin ring,[24] when coordinated to the $V^{IV}O$ unit, further induces the mixing of the in-plane porphyrin orbitals with the out-of-plane ones.

Here, we investigated whether the key role of the vanadyl unit in promoting a significant magnetic exchange interaction is maintained even when coupled to a different paramagnetic center in a heterometallic $V^{IV}O$–Cu^{II} bisporphyrin using H_2DPP (5,15-diphenylporphyrin). This porphyrin ligand was selected as a compromise between solubility and decoherence induced by hydrogen magnetic nuclei on the ligand and is also suited for thermal sublimation experiments. Moreover, this choice also represents a good building block for extended arrays of porphyrin rings. Additionally, we focused on singly-linked porphyrin to avoid the stronger coupling promoted by triply linked porphyrins.[19] We found that the exchange interaction, though weaker than in the homometallic vanadyl dimer, clearly impacts the EPR spectrum, causing a sizeable splitting of the resonance lines. The difference in the *g*-factors of the two metal centers suggests that individual spin addressability will also be retained when depositing the dimer on a surface, where flattening of the molecules is expected.[25]

Results and Discussion

Retrosynthetically, the synthesis of unsymmetric m-m and/or β-β directly-linked bisporphyrins requires a stepwise approach, ideally using precursors with two different but complementary functional groups.[26] This was exemplified in *Osuka* and co-workers' synthesis of hybrid porphyrins, e.g., heterobimetallic Ni^{II}-Zn^{II} and free base-Zn^{II} hybrids.[27,28]

Following this strategy, the monomeric porphyrin complexes (Scheme 1) were synthesized by reacting H_2DPP with $VO(acac)_2$[29] or $Cu(AcO)_2$[30] to yield the respective metalloporphyrin **1** or **2** (Scheme 1, A). The oxidative coupling step employing brominated porphyrins in the dimerization procedure[31] did not yield the dimer and therefore we used iodinated derivatives obtained by following published procedures.[31,32] Monomer **1** was used to obtain the iodinated derivative **3**, while the free base H_2DPP was first iodinated, to yield 5-iodo-10,20-diphenylporphyrin (H_2IDPP) and subsequently metalated with $Cu(OAc)_2$ to obtain monomer **4** (Scheme 1, A). The yield of the iodination did not change significantly upon using various oxidative agents such as $CuCl_2$, PIFA ((bis(trifluoroacetoxy)iodo)benzene), or $AgPF_6$. PIFA was then chosen as the oxidizing agent to reduce metal contamination of the final products, which were purified by column chromatography. The borylated compound **5** (Scheme 1, B) was synthesized according to a literature procedure.[31] The synthesis of compounds **3**, **4**, and **5**, allowed an entry into the hybrid porphyrin dimers. For the synthesis of the hybrid dimers **6** and **7**, a *Suzuki–Miyaura* coupling[33] was performed between the pinacolborane **5** and iodinated porphyrins **3** or **4** (Scheme 1, B).[34,35] Finally, the

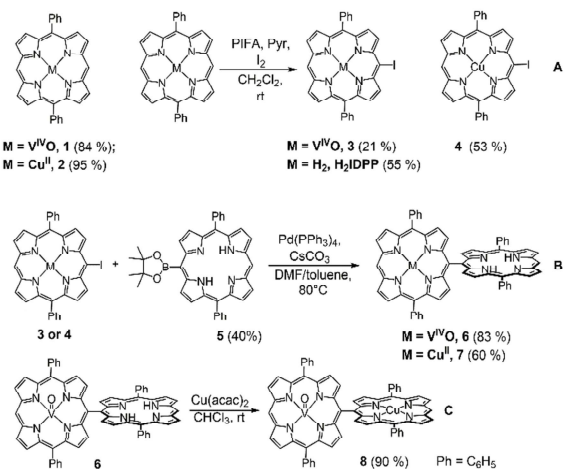

Scheme 1. (A) Chemical structures of the synthesized monomeric porphyrins, along with the iodination reaction. (B) Scheme of the reaction of the iodinated $V^{IV}O$ (**3**) or Cu^{II} (**4**) porphyrin with the borylated porphyrin **5** to obtain hybrid porphyrin dimers **6** or **7**. (C) The free base porphyrin unit in **6** is metalated with $Cu(acac)_2$ to yield the heterometallic porphyrin dimer **8**. Experimental yields are given in parentheses.

metalation of the free base porphyrin unit in compound **6** with $Cu(acac)_2$ in $CHCl_3$ at room temperature afforded compound **8** (Scheme 1, C). To obtain **8**, metalation of **6** was preferred over that of **7** due to the milder reaction conditions required for the former. Detailed synthetic procedures and chemical characterization for all molecules prepared in this work can be found in the Supporting Information (Section S1, Figures S1–S8).

Purple single crystals of monomers **1** and **2** were obtained by slow evaporation of a CH_2Cl_2/MeCN (10:1) mixture and a $CHCl_3$/heptane (7:1) mixture, respectively. Both compounds crystallized in the monoclinic space group $P2_1/c$ (see Table S1 for details of crystallographic data collections). For **1**, the asymmetric unit is half of the molecule, the V=O group being disordered over inversion above and below the porphyrin plane (Figure S9).[36] For **2**, the asymmetric unit includes the porphyrin unit with one $CHCl_3$ molecule of solvation (Figure S9). The porphyrin plane in compound **2** exhibits out-of-plane ruffled distortion.

Crystallization of the dimers **6–8** was hampered by their low solubility in toluene and ethers and only limited solubility in $CHCl_3$ or CH_2Cl_2. This resulted in fast precipitation during the slow evaporation process, thus limiting the sizes of the crystals obtained and the quality of the data collection. However, the basic features of the molecular structures were obtained, providing crucial information on the chemical identity, connectivity of the complexes, and on the tilting angle between the two moieties. A detailed discussion on disorder modeling is reported in Section S2. In the case of compound **7**, attempts to get single crystals were unsuccessful.

Compound **6** crystallized in the tetragonal space group P4cc (n. 103), and the refined structure evidences a high degree of disorder (see Figure S10). The asymmetric unit consists of one porphyrin moiety with 50% metal occupancy, the dimer showing a C_2-axis perpendicular to the meso-meso bond. The resulting tilt angle between the porphyrin planes θ, defined as the dihedral angle about the meso-meso bond, is 78°, close to that observed in a homometallic $V^{IV}O$-dimer;[23] a similar saddle-like distortion is also observed. The shortest intermolecular VO–VO distance is around 8.5 Å. The structure shows solvent-accessible voids occupying 4.1% of the unit cell volume, which are visible along the *c* axis (Figure S11). Compound **8** crystallizes in the tetragonal space group P4/ncc (n.130). The asymmetric unit is half a porphyrin unit, with partial $V^{IV}O$ and Cu^{II} occupancy, and the former being disordered above and below the porphyrin plane. A C_2-axis passing through the meso carbon atoms and an S_4-axis bisecting the meso-meso bond generates the dimeric unit. The tilting angle θ between porphyrin planes is around 78° (Figure 1b) and the intramolecular V–Cu distance is around 8.4 Å, which compares well with the 8.37 Å observed in the homometallic vanadyl dimer.[23] Despite the low quality of the crystal structure, the simulated Powder X-Ray Diffraction pattern compares well with the experimental one (see Figure S12).

X-band continuous wave (cw) EPR measurements were carried out to gain insight into the magnetic interactions in compounds **1**, **2**, **6**, **7**, and **8**. All spectra were recorded in a frozen solution of a 0.2 mM 1:1 toluene/CH_2Cl_2 mixture at 30 K. The experimental and simulated spectra of the monomers **1** and **2** and their monometallic dimers **6** and **7** are shown in the Supporting Information (Figures S13 and S14) and Figure 2 (left, turquoise and red lines). The simulations of the monometallic porphyrins were performed based on the spin-Hamiltonian:[37]

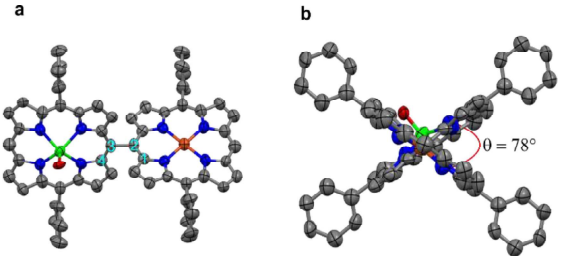

Figure 1. (**a**) Molecular structure of compound **8** in the crystal. (**b**) Molecular structure of compound **8** viewed along the meso-meso linkage. The angle θ, describing the tilting between the porphyrin units, is defined as the dihedral angle between the carbon atoms 1–4 labeled in **a**.

$$\hat{H}_M = \mu_B \vec{\boldsymbol{B}} \cdot \boldsymbol{g}_M \cdot \hat{\boldsymbol{S}}_M + \hat{\boldsymbol{S}}_M \cdot \boldsymbol{A}_M \cdot \hat{\boldsymbol{I}}_M + \sum_{i=1}^{4} \hat{\boldsymbol{S}}_M \cdot \boldsymbol{A}_N \cdot \hat{\boldsymbol{I}}_{N,i} \qquad (1)$$

where $\boldsymbol{g}_M$ is the $\boldsymbol{g}$-tensor of the metal porphyrin, and $\boldsymbol{A}_M$ and $\boldsymbol{A}_N$ are the hyperfine coupling tensors for the metal and the pyrrolic nitrogen nuclei. In our simulations we assumed a local electronic C_{4v} symmetry, $\boldsymbol{g}_M$ and $\boldsymbol{A}_M$ tensors being collinear and axial.

The spectrum of **6** in Figure 2 (left), as that of **1** in Figure S13, shows the characteristic EPR powder pattern of vanadyl porphyrins due to the anisotropic hyperfine coupling of the electron spin with the ^{51}V ($I=7/2$) nucleus. No sign of coupling with the four nearby nitrogen atoms of the porphyrin unit is observed since the d_{xy} magnetic orbital of the vanadyl ion is not pointing directly toward the nitrogen donors. The last term of the Hamiltonian (1) can therefore be neglected. Similarly, the spectra of **2** and **7** (see Figure 2 and S14) show the typical pattern of Cu^{II} porphyrins due to the anisotropic hyperfine interaction of the electron spin with nuclei of Cu (^{63}Cu, natural abundance, NA = 69.17%; ^{65}Cu, NA = 30.83%; both $I=3/2$) and the four coordinated ^{14}N ($I=1$). The simulation parameters for all the monometallic porphyrins (Table 1) agree with values in the literature.[29,38,39] Notably, the simulation values of the monometallic dyads **6** and **7** are very similar to their monomeric counterparts **1** and **2**. This highlights that even after the introduction of an additional porphyrin unit, both $\boldsymbol{A}_M$ and $\boldsymbol{g}_M$ tensors remain axial within the spectral resolution of X-band cw-EPR spectroscopy.

The EPR spectrum of compound **8** (Figure 2 left, black line, other spectra available as Figure S15–S16) differs from the superposition of the spectra of the two metal ions. It is also characterized by a larger linewidth than the monome-

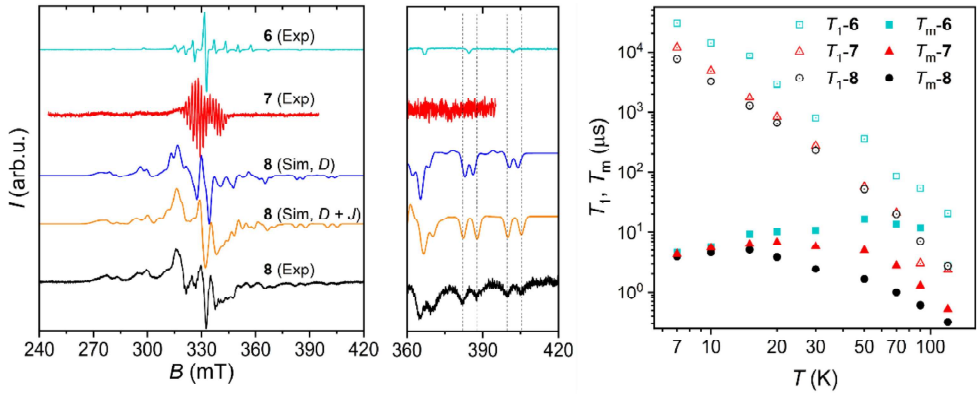

Figure 2. Left: Experimental X-band cw-EPR spectra ($T=30$ K, frozen solution 0.2 mM in 1:1 toluene/CH_2Cl_2) of the compounds **6** ($\nu=9.392$ GHz, magenta line), **7** ($\nu=9.402$ GHz, brown line), and **8** ($\nu=9.394$ GHz, black line) together with two relevant spectral simulations of compound **8**. The reported simulations were performed at two different values of J (0 and $-8.0\cdot10^{-3}$ cm^{-1}) by keeping the dipolar interaction and $\theta=78°$ constant to highlight the effect of the exchange interaction. The parameters of the simulations are reported in Table 1. Right: Temperature dependence of T_1 (dotted symbols) and T_m (solid symbols) for compounds **6** (turquoise squares), **7** (red triangles), and **8** (black circles) measured at 340 mT at X-band frequency in a 0.2 mM d_8-toluene frozen solution.

Table 1: Principal values of the Spin-Hamiltonian tensors for compounds **1**, **2**, **6**, **7**, and **8** and isotropic exchange coupling constant obtained from the simulation of frozen solution samples. For the simulation of the spectra of **8**, a tilting angle of 78° was assumed between Cu^{II} and V^{IV} tensors. ***D*** has been calculated in the point-dipole approximation with z perpendicular to the Cu-porphyrin plane and y along the meso-meso bond.

	1, 2, 8		6, 7, 8			8	
	g_V	A_V (MHz)	g_{Cu}	A_{Cu} (MHz)	A_N (MHz)	D (cm^{-1})	J (cm^{-1})
x	1.985	162	1.985	60	54	$3.0\cdot10^{-3}$	
y	1.985	162	1.985	60	43	$-6.2\cdot10^{-3}$	$-8\cdot10^{-3}$
z	1.964	475	1.964	626	45	$3.2\cdot10^{-3}$	

tallic dimers, most likely attributable to the dipolar coupling interaction between the two unpaired electron spins of the dyad and a possible distribution of dihedral angles between the two porphyrin units in the frozen solution. The EPR spectrum was simulated using the following Spin-Hamiltonian:

$$\hat{\boldsymbol{H}}_{V-Cu}=\mu_B\vec{\boldsymbol{B}}\cdot\boldsymbol{g}_V\cdot\hat{\boldsymbol{S}}_{VO}+\hat{\boldsymbol{S}}_{VO}\cdot\boldsymbol{A}_V\cdot\hat{\boldsymbol{I}}_V+\mu_B\vec{\boldsymbol{B}}\cdot\boldsymbol{g}_{Cu}\cdot\hat{\boldsymbol{S}}_{Cu}+\hat{\boldsymbol{S}}_{Cu}\cdot\boldsymbol{A}_{Cu}\cdot\hat{\boldsymbol{I}}_{Cu}+\sum_{i=1}^{4}\hat{\boldsymbol{S}}_{Cu}\cdot\boldsymbol{A}_{N,i}\cdot\hat{\boldsymbol{I}}_N+\hat{\boldsymbol{S}}_{VO}\cdot\boldsymbol{J}_{V-Cu}\cdot\hat{\boldsymbol{S}}_{Cu} \quad (2)$$

that adds to the Zeeman and hyperfine interaction terms of the single centers the interaction contribution described by the matrix $\boldsymbol{J}_{V-Cu}$. The latter comprises the isotropic component of the exchange interaction J and the through-space dipolar coupling $\boldsymbol{D}$, while we neglected the antisymmetric term:[40]

$$\boldsymbol{J}_{V-Cu}\approx J\boldsymbol{I}+\boldsymbol{D}=\begin{bmatrix}J+D_X & 0 & 0\\ 0 & J+D_Y & 0\\ 0 & 0 & J+D_Z\end{bmatrix} \quad (3)$$

To reduce the number of free parameters, the $\boldsymbol{g}_M$ and $\boldsymbol{A}$ tensors principal values were fixed at those of their respective monometallic dimers, and their local z axis assumed to be perpendicular to the porphyrin planes. Further, the tilting angle between the two porphyrin units was fixed at the experimental value of $\theta=78°$, and $\boldsymbol{D}$ was calculated in the point-dipole approximation using the X-ray data and relative $\boldsymbol{g}$-tensor orientations.[23] We note that, due to the relatively small g-anisotropy, the calculated $\boldsymbol{D}$ tensor is essentially axial, with the main axis being directed along the V–Cu direction. Thus, it is not affected by variation of the dihedral angle.[40] Consequently, the only variable parameter was the exchange interaction J. The splitting of the outermost lines, corresponding to the parallel transitions of the $V^{IV}O$ unit, provides a first clue as to the magnitude of the exchange interaction. The splitting simulated by assuming a purely dipolar coupling (i.e., fixing $J=0$) is clearly smaller than that observed in the experiment. A preliminary survey (Figure S17) indicates that the correct splitting of those lines can be obtained with either $J=2\cdot10^{-3}$ (antiferromagnetic, AF) or $J=-8\cdot10^{-3}$ cm^{-1} (ferromagnetic, FM). The reason for this difference is that in the direction of V=O bond (i.e., the direction of those EPR transitions) the dipolar interaction is AF. FM exchange interactions larger than AF ones are therefore necessary to obtain the same splitting, which is proportional to $|J+D_z|$. The survey further shows that the central part of the spectrum is much better reproduced using $J=-8\cdot10^{-3}$ cm^{-1} than $J=+2\cdot10^{-3}$ cm^{-1}. This is also the case for the simulation of

pseudomodulated Q-band spectrum (Figure S18). Notably, in contrast to the homometallic vanadyl dimer,[23] the simulated spectra of the heterometallic dimer **8** do not change significantly with the g_M and A_M- tensors tilting angle, as shown in Figure S19.

The EPR data clearly show that the VO–Cu exchange coupling is weakly FM (the best simulation is reported in Figure 2 and corresponding parameters in Table 1). Its magnitude falls between those reported for structurally similar meso-meso linked Cu–Cu[19] and VO–VO[23] homometallic dimers, albeit being of opposite sign.

This confirms our prediction, based on the deformations brought in by $V^{IV}O$ coordination, that local σ (in-plane) and delocalized π (out-of-plane) contributions are responsible for the super-exchange interaction.[23] A comparison between the UV/Vis spectra of VO–Cu and VO–VO dimers (Figure S1) confirms the higher conjugation in the latter, which shows larger line broadening and more red-shifted Q-bands.[41,42]

The spin relaxation properties of compounds **6–8** were studied by pulsed EPR spectroscopy at X-band frequency. Temperature-dependent inversion recovery and primary echo decay experiments were used to determine the longitudinal (T_1) and transverse (T_m) relaxation times in the interval between 7 and 120 K. The samples were dissolved in d_8-toluene (0.2 mM) and measured as frozen solutions. All measurements were performed at a magnetic field setting corresponding to the maximum intensity of echo detected EPR spectrum (Figure S20). T_m values were extracted by fitting the experimental decay traces using a stretched exponential function, while T_1 values were obtained by a biexponential fitting of the inversion recovery traces (Figure S21–S23 and Table S2). In Figure 2, only the slow component of the biexponential fit, usually taken to represent the spin-lattice relaxation (T_1), is plotted; the fast component[43,44] is associated with spectral diffusion effects[43,44] (i.e., excitation bandwidth smaller than the spectral width) and, thus, is not shown.

Compound **6** has T_1 and T_m values longer than compound **7**. In both cases, these values are comparable with the relaxation times of other monomeric $V^{IV}O$[29,45,46] or Cu^{II} complexes.[46–48] The faster spin-lattice relaxation of Cu^{II} can be attributed to the larger spin-orbit coupling that makes the spin system more sensitive to molecular vibrations. Compound **8** has T_1 values very similar to **7**, suggesting that the presence of the nearby slower relaxing vanadyl unit does not negatively impact the spin-lattice relaxation. T_m values of **8** are instead slightly faster than those of **6** and **7** and also lower than those reported for dimeric $V^{IV}O$ bimetallic complexes, including the homometallic vanadyl porphyrin dimer.[11,22,49,50]

The accurate determination of the Spin-Hamiltonian parameters of **8** allows us to envision the microwave operation of the dimeric unit as a C-NOT quantum gate. This is fundamental for realizing a universal quantum computer. We define the computation states by choosing the V and Cu electronic spins as control and target qubits, respectively (Figure 3a). By applying a field of 1.3 T, the nuclear and electronic spin states are factorized, and the microwave radiation in the Q-band range (ca. 30 GHz) induces transition from the $m_s=-1/2$ to the $m_s=+1/2$ states (labelled as computational states $|0\rangle$ and $|1\rangle$ in Figure 3b).

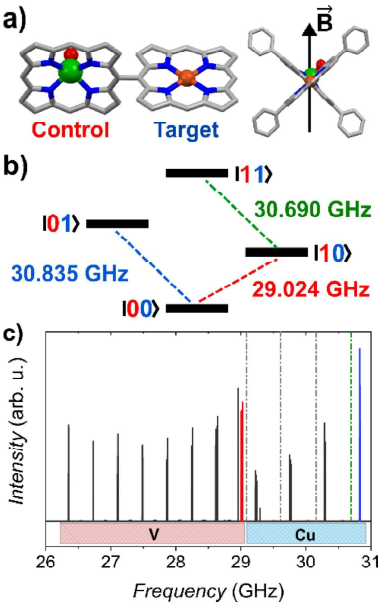

Figure 3. a) Orientation of the static magnetic field with respect to the control and target qubits; b) Computed energy differences between states involving control (red) and target qubit (blue and green) electronic spin transitions highlighted with the same color in the frequency-swept absorption spectrum (c) simulated for $B=1.3$ T, $T=100$ mK and the Spin-Hamiltonian parameters reported in Table 1. Gray dashed lines refer to other possible choices of hyperfine levels of the target.

In difference to the homometallic vanadyl dimer, addressability of the two spins in **8** is warranted for most orientations of the static magnetic field, including along the bisector of the two porphyrin planes. Figure 3c shows the frequency-swept absorption spectrum computed for this orientation at 100 mK (see Figure S24 for simulation at 10 K). The spectrum can be divided into a low-frequency region where the eight hyperfine transitions of the ^{51}V are visible and a high-frequency region where four transitions (shown only for the ^{65}Cu isotope for clarity) can be identified. The nuclear spins are not polarized at this temperature and the intensity is almost equally distributed over the different hyperfine lines. Focusing on the highest hyperfine transition of the target qubit, we compute that the transition occurs at 30.835 GHz if the control qubit is in its ground state ($|00\rangle\rightarrow|01\rangle$, blue line in Figure 3b and 3c). Upon excitation of the control qubit—for instance irradiating at 29.024 GHz (red line)—absorption of microwaves at 30.690 GHz occurs, corresponding to the $|10\rangle\rightarrow|11\rangle$ transition (green line). Different hyperfine lines of the target can be selected to reduce the frequency separation between the control and the target absorptions, while maintaining ca. 200 MHz of separation induced by the control (gray dashed

lines in Figure 3c), as commercial low-Q cavities have a bandwidth of ca. 400 MHz.

Interestingly, the scenario described in Figure 3 is rather robust against different operating conditions. If the static magnetic field is aligned along the target z axis, the target and control transitions are slightly more separated in frequency (see Figure S25–S26), while a separation similar to that in Figure 3c is observed upon reduction of the tilting angle between the two porphyrin units (see Figure S27–S28).

Density Functional Theory (DFT) geometry optimization in gas-phase was carried out to shed light on the structural properties of compound **8** because of the low quality of the experimental structure determination. The results are reported in Figure S29 and some selected distances are given in Table S3. The tilting angle of the optimized structure, $\theta \approx 84°$, is close to the value $\theta \approx 78°$ of the X-ray structure. The corresponding calculated J value ($-1.2 \cdot 10^{-2}$ cm^{-1}) is in very good agreement with the one estimated from the EPR simulations and confirms the trend expected upon substituting vanadyl with copper ions in singly-linked porphyrin dimers, i.e., a reduction in the magnitude of the coupling and a change of the nature of the coupling from AF to FM.[23]

This observation corresponds to the behavior of the seminal copper/vanadyl dimer reported by Kahn et al.,[51] but at a different level of complexity. The magnetic orbitals of the $Cu^{II}(d_{x^2-y^2})$ and $V^{IV}O$ (d_{xy}) ions are orthogonal by symmetry (see Figure 4), justifying the FM nature of the interaction in **8** and its smaller value in comparison to the homometallic $V^{IV}O$-dimer.[23] Moreover, as the Cu^{II} ion lies in the plane of the porphyrin ligand, the overlap of the magnetic orbital with the porphyrin out-of-plane orbitals (π-system) is minimal. This significantly reduces the antiferromagnetic contributions that are active when the porphyrin rings are tilted.

To analyze this point in more depth, we performed single-point J value calculations on two additional geometries. The first corresponds to the tilting angle set to the value determined by single crystal X-ray analysis, while the second represents a possible critical point where the tilting angle is set to 90°. No significant difference in J between the X-ray and optimized structures is computed, while a small reduction in the magnitude of J is derived for $\theta = 90°$ (see Table S4). The presence of two pathways, the FM one through σ porphyrin orbitals and the AF one involving π orbitals, nicely explains the different angular dependence of the computed exchange interaction in **8** compared to the homometallic $V^{IV}O$-dimer. For the latter, angles close to 90° correspond to a relative maximum of $|J|$. The exchange interaction mediated by out-of-porphyrin-plane orbitals is expected to be AF and maximum at $\theta = 90°$, where the overlap with the in-plane orbital of the metal unit is highest. In the case of the Cu–VO dimer, this AF contribution adds to the FM one with the opposite sign, thus slightly reducing $|J|$ for $\theta = 90°$.

We also computed the exchange coupling for an optimized structure of a triply-fused dimer (Figure S30 and S31). As expected, a much stronger FM coupling of $J = -0.36$ cm^{-1} is calculated, which would hamper the single spin addressability. Similar to the singly-linked case, the sign of the coupling is consistent with Kahn's model. Its magnitude is intermediate between triply-fused Cu[19] and VO homometallic dimers,[22] the former being the largest.

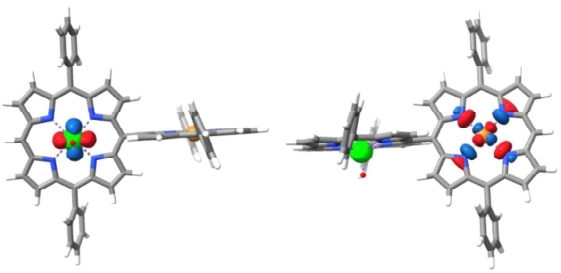

Figure 4. Two orthogonal views of the isodensity ($\psi = 0.05$ (e bohr^{-3})$^{1/2}$) surfaces of magnetic orbitals for compound **8** computed at the B3LYP level. The code color is V (green), Cu (orange), N (blue), O (red), C (gray), and H (white).

Conclusion

The combined results in this and our previous work[23] show that paramagnetic bimetallic $V^{IV}O$ bisporphyrins are promising candidates for developing two-qubit quantum gates. It is possible to obtain paramagnetic singly metalated bisporphyrins (compounds **6** and **7**) through a *Suzuki–Miyaura* coupling.[31,52] By metallating compound **6**, we obtained a paramagnetic and heterometallic porphyrin dimer in very good yields. We demonstrated by means of cw-EPR and DFT calculations that J is smaller than in the vanadyl homometallic dimer,[23] but still strong enough to be measured with a standard X-band cw-EPR spectrometer. With this set of parameters, single spin addressability, a fundamental prerequisite for the realization of a C-NOT quantum gate, is possible, in principle, over a wide range of experimental conditions.

Furthermore, both spectral simulations and DFT calculations revealed that the weak exchange interaction is ferromagnetic. The magnitude and sign of J are explained by the competitive in-plane and out-of-plane super-exchange pathways made possible by the pentacoordinate $V^{IV}O$ unit. Our study identifies the $V^{IV}O$ unit as a key ingredient to enhance the magnetic exchange interaction in oligo-porphyrin structures, and similar J values are expected in other heterometallic combinations containing $V^{IV}O$ porphyrins. Interestingly, the relaxation times T_m and T_1 of the dimer do not vary significantly from monomeric Cu^{II}[46–48] or $V^{IV}O$ porphyrins,[29,45,46] suggesting that the additional paramagnetic unit does not substantially affect decoherence. The combined exchange and coherence properties of this system form a sound starting point to investigate its single-molecule properties once deposited on surfaces.

Supporting Information

Additional details on the synthetic procedures, crystal structure determination, and EPR spectroscopy investigation. Further information on the DFT calculations and selected parameters of the optimized molecular structures. The authors have cited additional references within the Supporting Information..[53–70]

Acknowledgements

This work was supported by the European Union through the FETOPEN project FATMOLS (GA 862893) and by the NextGenerationEU funds through the Italian MUR National Recovery and Resilience Plan, Mission 4 Component 2—Investment 1.4—National Center for HPC, Big Data and Quantum Computing—CUP B83C22002830001), Investment 1.3 (PE0000023-NQSTI), and Investment 1.2—Project ID: SOE_0000064—PHOTOCODE (A. P.). The support of MUR through Progetto Dipartimenti di Eccellenza 2018–2022 (CUP B96 C1700020008) and 2023–2027 (CUP B97G22000740001—DICUS 2.0 for F. T., L. S., R. S. and CUP D13C22003520001—Project CH4.0 for E. S. and M. C.) is acknowledged. The work was supported by the Science Foundation Ireland (SFI award 21/FFP-A/9469) and the Irish Research Council (GOIPD/2021/479). The support of the Technical University of Munich—Institute for Advanced Study through a Hans Fischer Senior Fellowship (M. O. S.) is also acknowledged. We thank the Centro di Servizi di Spettrometria di Massa (CISM) of the University of Florence.

Conflict of Interest

The authors declare no conflict of interest.

Data Availability Statement

The data that support the findings of this study are available from the corresponding author upon reasonable request.

Keywords: DFT Calculations · EPR-Spectroscopy · Hybrid Porphyrin Dimers · Molecular Spin Qubits

[1] J. P. Dowling, G. J. Milburn, *Philos. Trans. R. Soc. A* **2003**, *361*, 1655–1674.
[2] G. Wolfowicz, J. J. L. Morton, *eMagRes* **2016**, *5*, 1515–1528.
[3] A. Chatterjee, P. Stevenson, S. De Franceschi, A. Morello, N. P. de Leon, F. Kuemmeth, *Nat. Rev. Phys.* **2021**, *3*, 157–177.
[4] L. M. K. Vandersypen, M. A. Eriksson, *Phys. Today* **2019**, *72*, 38–45.
[5] F. Luis, S. Hill, E. Coronado, *Nat. Chem.* **2019**, *11*, 301–309.
[6] M. Atzori, R. Sessoli, *J. Am. Chem. Soc.* **2019**, *141*, 11339–11352.
[7] M. R. Wasielewski, M. D. E. Forbes, N. L. Frank, K. Kowalski, G. D. Scholes, J. Yuen-Zhou, M. A. Baldo, D. E. Freedman, R. H. Goldsmith, T. Goodson, M. L. Kirk, J. K. McCusker, J. P. Ogilvie, D. A. Shultz, S. Stoll, K. B. Whaley, *Nat. Chem. Rev.* **2020**, *4*, 490–504.
[8] F. Troiani, M. Affronte, *Chem. Soc. Rev.* **2011**, *40*, 3119–3129.
[9] D. P. DiVincenzo, *Fortschr. Phys.* **2000**, *48*, 771–783.
[10] D. Aguilà, L. A. Barrios, V. Velasco, O. Roubeau, A. Repollés, P. J. Alonso, J. Sesé, S. J. Teat, F. Luis, G. Aromí, *J. Am. Chem. Soc.* **2014**, *136*, 14215–14222.
[11] S. Von Kugelgen, M. D. Krzyaniak, M. Gu, D. Puggioni, J. M. Rondinelli, M. R. Wasielewski, D. E. Freedman, *J. Am. Chem. Soc.* **2021**, *143*, 8069–8077.
[12] S. Nakazawa, S. Nishida, T. Ise, T. Yoshino, N. Mori, R. D. Rahimi, K. Sato, Y. Morita, K. Toyota, D. Shiomi, M. Kitagawa, H. Hara, P. Carl, P. Höfer, T. Takui, *Angew. Chem. Int. Ed.* **2012**, *51*, 9860–9864.
[13] I. Cimatti, L. Bondì, G. Serrano, L. Malavolti, B. Cortigiani, E. Velez-Fort, D. Betto, A. Ouerghi, N. B. Brookes, S. Loth, M. Mannini, F. Totti, R. Sessoli, *Nanoscale Horiz.* **2019**, *4*, 1202–1210.
[14] L. Malavolti, M. Mannini, P. E. Car, G. Campo, F. Pineider, R. Sessoli, *J. Mater. Chem. C* **2013**, *1*, 2935–2942.
[15] T. Lukasczyk, K. Flechtner, L. R. Merte, N. Jux, F. Maier, J. M. Gottfried, H. P. Steinrück, *J. Phys. Chem. C* **2007**, *111*, 3090–3098.
[16] Q. Sun, L. M. Mateo, R. Robles, N. Lorente, P. Ruffieux, G. Bottari, T. Torres, R. Fasel, *Angew. Chem. Int. Ed.* **2021**, *60*, 16208–16214.
[17] L. M. Mateo, Q. Sun, S. X. Liu, J. J. Bergkamp, K. Eimre, C. A. Pignedoli, P. Ruffieux, S. Decurtins, G. Bottari, R. Fasel, T. Torres, *Angew. Chem. Int. Ed.* **2020**, *59*, 1334–1339.
[18] L. M. Mateo, Q. Sun, K. Eimre, C. A. Pignedoli, T. Torres, R. Fasel, G. Bottari, *Chem. Sci.* **2021**, *12*, 247–252.
[19] N. Wili, S. Richert, B. Limburg, S. J. Clarke, H. L. Anderson, C. R. Timmel, G. Jeschke, *Phys. Chem. Chem. Phys.* **2019**, *21*, 11676–11688.
[20] Y. Inokuma, N. Ono, H. Uno, D. Y. Kim, S. B. Noh, D. Kim, A. Osuka, *Chem. Commun.* **2005**, 3782–3784.
[21] T. Ikeue, K. Furukawa, H. Hata, N. Aratani, H. Shinokubo, T. Kato, A. Osuka, *Angew. Chem. Int. Ed.* **2005**, *44*, 6899–6901.
[22] I. Pozo, Z. Huang, F. Lombardi, D. Alexandropoulos, F. Kong, M. Slota, J.-R. Deng, W. Stawski, P. Horton, S. Coles, *ChemRxiv.* **2023**, https://doi.org/10.26434/chemrxiv-2022-1v5b4-v2.
[23] D. Ranieri, F. Santanni, A. Privitera, A. Albino, E. Salvadori, M. Chiesa, F. Totti, L. Sorace, R. Sessoli, *Chem. Sci.* **2023**, *14*, 61–69.
[24] C. J. Kingsbury, M. O. Senge, *Coord. Chem. Rev.* **2021**, *431*, 213760.
[25] R. D. McCurdy, P. H. Jacobse, I. Piskun, G. C. Veber, D. J. Rizzo, R. Zuzak, Z. Mutlu, J. Bokor, M. F. Crommie, F. R. Fischer, *J. Am. Chem. Soc.* **2021**, *143*, 4174–4178.
[26] A. Ryan, A. Gehrold, R. Perusitti, M. Pintea, M. Fazekas, O. B. Locos, F. Blaikie, M. O. Senge, *Eur. J. Org. Chem.* **2011**, 5817–5844.
[27] N. Aratani, A. Osuka, *Org. Lett.* **2001**, *3*, 4213–4216.
[28] T. Tanaka, B. S. Lee, N. Aratani, M. C. Yoon, D. Kim, A. Osuka, *Chem. Eur. J.* **2011**, *17*, 14400–14412.
[29] T. Yamabayashi, M. Atzori, L. Tesi, G. Cosquer, F. Santanni, M.-E. Boulon, E. Morra, S. Benci, R. Torre, M. Chiesa, L. Sorace, R. Sessoli, M. Yamashita, *J. Am. Chem. Soc.* **2018**, *140*, 12090–12101.
[30] R. K. Al-Shewiki, M. Korb, A. Hildebrandt, S. Zahn, S. Naumov, R. Buschbeck, T. Rüffer, H. Lang, *Dalton Trans.* **2019**, *48*, 1578–1585.
[31] L. A. Fendt, H. Fang, M. E. Plonska-Brzezinska, S. Zhang, F. Cheng, C. Braun, L. Echegoyen, F. Diederich, *Eur. J. Org. Chem.* **2007**, 4659–4673.

[32] R. W. Boyle, C. K. Johnson, D. Dolphin, *J. Chem. Soc. Chem. Commun.* **1995**, 527–528.
[33] N. Miyaura, K. Yamada, A. Suzuki, *Tetrahedron Lett.* **1979**, *20*, 3437–3440.
[34] J. M. O'Brien, E. Sitte, K. J. Flanagan, H. Ku, L. J. Hallen, M. O. Senge, *J. Org. Chem.* **2019**, *84*, 6158–6173.
[35] S. Horn, B. Cundell, M. O. Senge, *Tetrahedron Lett.* **2009**, *50*, 2562–2565.
[36] Deposition numbers 2257145 (for **1**), 2260447 (for **2**), 2257146 (for **6**), and 2257147 (for **8**) contain the supplementary crystallographic data for this paper. These data are provided free of charge by the joint Cambridge Crystallographic Data Centre and Fachinformationszentrum Karlsruhe Access Structures service.
[37] S. Stoll, A. Schweiger, *J. Magn. Reson.* **2006**, *178*, 42–55.
[38] C. Finazzo, C. Calle, S. Stoll, S. Van Doorslaer, A. Schweiger, *Phys. Chem. Chem. Phys.* **2006**, *8*, 1942–1953.
[39] A. Wolberg, J. Manassen, *J. Am. Chem. Soc.* **1970**, *92*, 2982–2991.
[40] A. Bencini, D. Gatteschi, *Electron Paramagnetic Resonance of Exchange Coupled Systems*, Springer, Berlin, **1990**.
[41] A. Osuka, S. Nakajami, T. Nagata, K. Maruyama, K. Torium, *Angew. Chem. Int. Ed. Engl.* **1991**, *30*, 582–584.
[42] C. J. Kingsbury, K. J. Flanagan, H. G. Eckhardt, M. Kielmann, M. O. Senge, *Molecules* **2020**, *25*, 3195.
[43] S. Takahashi, J. Van Tol, C. C. Beedle, D. N. Hendrickson, L. C. Brunel, M. S. Sherwin, *Phys. Rev. Lett.* **2009**, *102*, 087603.
[44] G. R. Eaton, S. S. Eaton, in *Distance Measurements in Biological Systems by EPR* (Eds.: L. J. Berliner, G. R. Eaton, S. S. Eaton), Kluwer Academic/Plenum Publishers, New York, **2000**, pp. 29–154.
[45] M. Atzori, L. Tesi, E. Morra, M. Chiesa, L. Sorace, R. Sessoli, *J. Am. Chem. Soc.* **2016**, *138*, 2154–2157.
[46] J. L. Du, G. R. Eaton, S. S. Eaton, *J. Magn. Reson. Ser. A* **1996**, *119*, 240–246.
[47] F. Santanni, A. Albino, M. Atzori, D. Ranieri, E. Salvadori, M. Chiesa, A. Lunghi, A. Bencini, L. Sorace, F. Totti, R. Sessoli, *Inorg. Chem.* **2021**, *60*, 140–151.
[48] M. Warner, S. Din, I. S. Tupitsyn, G. W. Morley, A. M. Stoneham, J. A. Gardener, Z. Wu, A. J. Fisher, S. Heutz, C. W. M. Kay, G. Aeppli, *Nature* **2013**, *503*, 504–508.
[49] I. Borilovic, P. J. Alonso, O. Roubeau, G. Aromí, *Chem. Commun.* **2020**, *56*, 3139–3142.
[50] M. Atzori, S. Benci, E. Morra, L. Tesi, M. Chiesa, R. Torre, L. Sorace, R. Sessoli, *Inorg. Chem.* **2018**, *57*, 731–740.
[51] O. Kahn, Y. Journaux, I. Morgenstern-Badarau, J. Galy, J. Jaud, *J. Am. Chem. Soc.* **1982**, *104*, 2165–2176.
[52] S. Hiroto, A. Osuka, *J. Org. Chem.* **2005**, *70*, 4054–4058.
[53] B. J. Littler, M. A. Miller, C. H. Hung, R. W. Wagner, D. F. O'Shea, P. D. Boyle, J. S. Lindsey, *J. Org. Chem.* **1999**, *64*, 1391–1396.
[54] J. S. Lindsey, H. C. Hsu, I. C. Schreiman, *Tetrahedron Lett.* **1986**, *27*, 4969–4970.
[55] F. Neese, *Wiley Interdiscip. Rev.: Comput. Mol. Sci.* **2018**, *8*, e1327.
[56] A. D. Becke, *J. Chem. Phys.* **1993**, *98*, 5648–5652.
[57] C. Lee, W. Yang, R. G. Parr, *Phys. Rev. B* **1988**, *37*, 785.
[58] S. Grimme, S. Ehrlich, L. Goerigk, *J. Comput. Chem.* **2011**, *32*, 1456–1465.
[59] S. Grimme, J. Antony, S. Ehrlich, H. Krieg, *J. Chem. Phys.* **2010**, *132*, 154104–154123.
[60] L. Noodleman, J. G. Norman, *J. Chem. Phys.* **1979**, *70*, 4903–4906.
[61] A. Bencini, F. Totti, *J. Chem. Theory Comput.* **2009**, *5*, 144–154.
[62] C. Adamo, V. Barone, A. Bencini, F. Totti, I. Ciofini, *Inorg. Chem.* **1999**, *38*, 1996–2004.
[63] T. Hasobe, K. Ida, H. Sakai, K. Ohkubo, S. Fukuzumi, *Chem. Eur. J.* **2015**, *21*, 11196–11205.
[64] T. Morotti, M. Pizzotti, R. Ugo, S. Quici, M. Bruschi, P. Mussini, S. Righetto, *Eur. J. Inorg. Chem.* **2006**, *2006*, 1743–1757.
[65] M. A. Bakar, N. N. Sergeeva, T. Juillard, M. O. Senge, *Organometallics* **2011**, *30*, 3225–3228.
[66] G. R. Fulmer, A. J. M. Miller, N. H. Sherden, H. E. Gottlieb, A. Nudelman, B. M. Stoltz, J. E. Bercaw, K. I. Goldberg, *Organometallics* **2010**, *29*, 2176–2179.
[67] O. V. Dolomanov, L. J. Bourhis, R. J. Gildea, J. A. K. Howard, H. Puschmann, *J. Appl. Crystallogr.* **2009**, *42*, 339–341.
[68] G. M. Sheldrick, *Acta Crystallogr. Sect. A* **2015**, *71*, 3–8.
[69] C. F. MacRae, I. Sovago, S. J. Cottrell, P. T. A. Galek, P. McCabe, E. Pidcock, M. Platings, G. P. Shields, J. S. Stevens, M. Towler, P. A. Wood, *J. Appl. Crystallogr.* **2020**, *53*, 226–235.
[70] E. Zolotoyabko, *J. Appl. Crystallogr.* **2009**, *42*, 513–518.

Manuscript received: September 1, 2023
Accepted manuscript online: October 9, 2023
Version of record online: ■■, ■■

Research Articles

Molecular Qubits

D. Ranieri, A. Privitera, F. Santanni, K. Urbanska, G. J. Strachan, B. Twamley, E. Salvadori, Y.-K. Liao, M. Chiesa, M. O. Senge,* F. Totti, L. Sorace,* R. Sessoli* **e202312936**

A Heterometallic Porphyrin Dimer as a Potential Quantum Gate: Magneto-Structural Correlations and Spin Coherence Properties

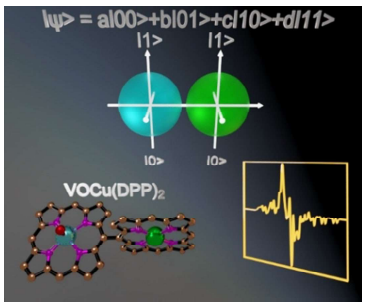

Electron paramagnetic resonance (EPR) shows that a vanadyl-copper meso-meso linked bisporphyrin complex has good spin coherence and a sizeable magnetic exchange interaction, making it suitable for operating two-qubit molecular spin-based quantum gates over a wide range of operation conditions. Theoretical calculations show that the super-exchange interaction is granted by the out-of-plane component of the vanadyl magnetic orbital despite the tilting angle of the two rings.